Tânia Sofia dos Santos Vieira

Mestre em Ciências Biomédicas

Development of a new nanostructured scaffold for neural stem/progenitor cell transplantation

Dissertação para a obtenção do grau de Doutor em
Bioengineering Systems – MIT Portugal Program

Orientador: Dr Célia Henriques, Profª auxiliar, FCT-UNL
Co-orientador: Dr João Paulo Borges, Prof auxiliar, FCT-UNL
Co-orientador: Dr Ana Sofia Falcão, Pos-doc, CEDOC

Júri:

Presidente: Prof.Doutor Luís Paulo da Silva Nieto Marques Rebelo

Arguentes: Profª. Doutora Maria Helena Mendes Gil
Doutor Hugo Agostinho Machado Fernandes

Vogais: Prof. Doutor António Alfredo Coelho Jacinto
Profª. Doutora Maria Helena Figueiredo Godinho
Prof. Doutor Frederico Castelo Ferreira
Prof. Doutora Célia Maria Reis Henriques
Doutora Ana Paula Gomes Moreira Pêgo

FACULDADE DE CIÊNCIAS E TECNOLOGIA
UNIVERSIDADE NOVA DE LISBOA

Outubro de 2017

Development of a new nanostructured scaffold for neural stem/progenitor cell transplantation

Acknowledgments

First of all I want to express my gratitude to my thesis advisors, professor Célia Henriques, professor João Paulo Borges and Ana Sofia Falcão for the presentation of this fascinating project and their effort to ensure all the necessary conditions for their development. I also thank their guidance, encouragement and time during these years. I would like to thank to Professor Jorge Silva for the availability and teaching during the development of this project.

I appreciate the financial support from Fundação para a Ciência e Tecnologia – FCT that funded the PhD grant - SFRH/BD/90682/2012.

I also want to thank the members of the thesis committee, professor Helena Godinho and professor Domingos Henrique for their suggestions throughout the development of the work.

I would like to thank to Professor Elvira Fortunato for the opportunity to use the CENIMAT/i3N research facilities: thanks to Ana Pimentel and Alexandra Gonçalves for DSC/TGA acquisition; Joana Pinto for XRD acquisition and Daniela Gomes for SEM acquisition.

I would like to express my gratitude to Doctor Cecília Bonifácio, from REQUIMTE – FCT/UNL, for NMR acquisition and to Professor Ana Rego, from IST, for the XPS acquisition and for their guidance and help in the interpretation of the results.

I am especially grateful to all the GREAT LAB students that provided moments of fun and laughs and helped to overcome the difficulties. However, I am indebted to Luisa Fialho, Ana Fradinho, Zeliha Güler, Carolina Rufino and Ana Nogueira for their friendship and support beyond the lab.

In the Polymers lab, I'd like to thank to Paula Soares, Susete Fernandes and Coro Echeverria for scientific support and advices, you were always available to help. Augusta thanks for your affection and happy guffaws. Ana Almeida thanks for the help in contact angle measurements. I´d like to thank to all the colleagues and students that passed the Polymers Lab for their contribution to a great lab atmosphere. Special thanks to Mariana Amaro for all the support, encouragement and friendship.

I am especially grateful to Dr Sharka Kubinova for the opportunity to work in the laboratory of biomaterials and biophysical methods at Institute of Experimental Medicine AS CR and for their guidance and teaching. I also would like to thank to Lenka for the help in the lab integration and in MSCs culture and to Klara for the guidance with the SPC-01 cultures. Thanks to the desktop colleagues Barbora, Monika, Kristina, Serguei, Jiří and Zuska for support and "oběd" time. "Děkuji" to all laboratory group.

I want to thank to the MIT Portugal colleagues, especially Andreia Pimenta, Cláudia Saraiva and Marta Costa, for learning, support and happy moments during the first year of the PhD program.

I also thank to my friends Sara, Magda and Carla and my sister Ângela for their support and patience during these last years. Special thanks to my parents for the education, advices, support and love. Finally, special thanks go to Ricardo for the love, support and understanding. Thank you for believe in me even when myself did not. Thank you for give me strength and help me to be a better person.

Abstract

Tissue engineering investigates new therapeutic approaches for spinal cord regeneration. Biodegradable scaffolds are employed aiming at creating an appropriate environment to support cell regrowth and transplantation. The transplantation of neural stem/progenitor cells (NSPCs) is a promising strategy under investigation. The main objective of this work was the synthesis of new soft materials for the production of nanostructured scaffolds able to support NSPCs transplantation and enable spinal cord regeneration.

Polyurethanes (PUs) are segmented polymers, with tunable properties. PUs were synthesized using polycaprolactone-diol (PCL-diol) as soft segment, and isophorone diisocyanate and dimethylol propionic acid (DMPA) as hard segment. To introduce biological cues in the polymer backbone, chitosan (CS) and gelatin (Gel) were used to substitute DMPA as chain extender. The PUs were characterized regarding their chemical composition and thermal properties.

Electrospun fibrous mats are convenient structures for cell support. In particular, aligned nanofibers provide a guidance cue to axon regrowth. Electrospinning was used to produce scaffolds of randomly oriented and aligned fibers from the different PU formulations. Scaffolds were characterized regarding their morphology, mechanical behavior, crystallinity, surface properties and hydrolytic degradation. Their impact on cells was evaluated *in vitro* using human fibroblasts. Cell adhesion and proliferation was highest for scaffolds produced from PUs containing CS or Gel as the only chain extender.

Stem cell interaction with PU-CS and PU-Gel scaffolds was studied using human umbilical cord mesenchymal stem cells (MSCs) and human fetal spinal cord neural stem cells (NSCs). MSCs proliferated best on PU-Gel randomly oriented fibers whereas NSCs proliferated best on PU-CS with aligned fiber morphology. Neuronal differentiation of NSCs was confirmed using neuronal markers. Neurites aligned along the fibers direction.

The physical, chemical and biological properties of PU-CS and PU-Gel fibrous mats make them promising substrates for NSPC in order to promote neural regeneration.

Keywords: Polyurethanes, Chitosan, Gelatin, Electrospinning, Neural Stem/progenitor Cells.

Resumo

A engenharia de tecidos investiga novas abordagens para a regeneração da espinal medula. Estruturas biodegradáveis são usadas para criar um ambiente que suporte o crescimento e transplante de células. O transplante de células neurais estaminais/progenitoras (NSPCs) é uma estratégia promissora sob investigação. O principal objetivo deste trabalho foi a síntese de novos materiais macios para produzir matrizes nano-estruturadas capazes de suportar o transplante de NSPCs e permitir a regeneração da espinal medula.

Poliuretanos (PUs) são polímeros segmentados, com propriedades ajustáveis. Foram sintetizados PUs utilizando policaprolactona-diol como segmento macio, e diisocianato de isoforona e ácido dimetilol propiónico (DMPA) como segmento duro. Para introduzir sítios para interação biológica na estrutura do polímero, foram utilizados quitosano (CS) e gelatina (Gel) substituindo o DMPA. Os PUs foram caracterizados química e termicamente.

Matrizes fibrosas eletrofiadas, são estruturas convenientes para o suporte celular. Em particular, nanofibras alinhadas guiam o crescimento dos axônios. Matrizes de fibras orientadas aleatoriamente e alinhadas dos diferentes Pus foram obtidas por eletrofiação e caracterizadas quanto à morfologia, comportamento mecânico, cristalinidade, propriedades de superfície e degradação hidrolítica. O seu impacto nas células foi avaliado *in vitro* utilizando fibroblastos humanos. A adesão e proliferação celular foram mais elevadas nas matrizes de PUs contendo CS ou Gel como único extensor de cadeia.

A interação de células estaminais com matrizes de PU-CS e de PU-Gel foi estudada usando células humanas estaminais mesenquimais do cordão umbilical (MSCs) e células estaminais neurais da espinal medula fetal (NSCs). As MSCs proliferaram melhor nas fibras orientadas aleatoriamente de PU-Gel, enquanto as NSCs proliferaram melhor em matrizes de fibras alinhadas de PU-CS. A diferenciação neuronal das NSCs foi confirmada usando marcadores neuronais. As neurites alinharam ao longo das fibras.

As propriedades físicas, químicas e biológicas das matrizes de PU-CS e PU-Gel tornam-nas substratos promissores para NSPCs, na promoção da regeneração neural.

Palavras-chave: Poliuretanos, Quitosano, Gelatina, Electrofiação, Células Neurais Estaminais/progenitoras.

Table of Contents

List of Figures

Chapter 2

Chapter 3

Chapter 4

Chapter 5

List of Tables

Chapter 2

Chapter 3

Chapter 4

Chapter 5

List of Acronyms

3D	Three dimensional space
3T3	3-day transfer, inoculum 3×10^5 cells
AFM	Atomic force microscopy
ATR	Attenuated total reflectance
ATP	Adenosine triphosphate
BD	Butanediol
BDNF	Brain-derived neurotrophic factor
BMP4	Bone morphogenic protein
bFGF	Basic fibroblast growth factor
cAMP	Cyclic adenosine monophosphate
CH_3COOH	Acetic acid
CH_3COONa	Sodium acetate
ChABC	Chondroitinase ABC
CNS	Central nervous system
CNTF	Ciliary neurotrophic factor
CNTs	Carbon nanotubes
CS	Chitosan
CSPGs	Chondroitin sulfate proteoglycans
DAPI	4,6-Diamidino-2-Phenylindole dihydrochloride
DD	Degree of deacetylation
DHD	2,5-dimethyl-3-hexine-2,5-diol
DMAc	Dimethylacetamide
DMEM	Dulbecco's modified Eagle's medium
DMF	N,N-dimethylformamide
DMPA	Dimethylol proprionic acid
DOPA	3,4-diihydroxy-L-phenylalanine
DSC	Differential scanning calorimetry
DTG	Derivative thermo-gravimetric
ECM	Extracellular matrix
EDTA	Ethylenediaminetetraacetic acid
EGF	Epidermal growth factor
EGFR	Epidermal growth factor receptor
eFGF	Epidermal fibroblast growth factor
ESCs	Embryonic stem cells
FAK	Focal adhesion kinase
FBS	Fetal bovine serum
FFT	Fast Fourier Transform

FGF-2	Fibroblast growth factor 2
FTIR	Fourier transform infrared spectroscopy
FWHM	Full width at half maximum
GDNF	Glial cell line-derived neurotrophic factor
GPC	Gel permeation chromatography
HFFF2	Caucasian foetal foreskin fibroblasts
HFP	1,1,1,3,3,3-hexafluoro-2-propanol
^{1}H NMR	Proton nuclear magnetic resonance
HPSG	Heparan Sulfate proteoglycan
HS	Hard segments
IgG	Immunoglobulin G
IPDI	Isophorone diisocyanate
IKVAV	Ile-Lys-Val-Ala.Val amino acid sequence
iPSCs	Induced pluripotent stem cells
LDH	Lactate dehydrogenase
MAP2	Microtubule-associated protein 2
MAPK	Mitogen-activated protein kinase
MDI	Methyl di-p-phenyl diisocyanate
MEM	Alpha-minimum essential medium
MIDE	2,2'-(methylimino) diethanol
MSCs	Mesenchymal stem cells
$NaHSO_3$	Sodium bisulfite
$NaNO_2$	Sodium nitrite
NaOH	Sodium hydroxide
NF70	70 kDa Neurofilament
NGF	Nerve Growth factor
NMP	N-methylpyrrolidone
Nogo-A	Neurite outgrowth inhibitor
NSCs	Neural stem cells
NSPCs	Neural stem/progenitor cells
NT-3	Neurothophin-3
OHT	4-hydroxytamoxifen
PBS	Phosphate buffer saline
PCL	Polycaprolactone
PCL-diol	Polycaprolactone-diol
PDL	Poly-D-lysine
PDMS	Poly(dimethylsiloxane)
PEDOT	Poly(3,4-ethylenedioxythiophene)
PEG	Polyethylene glycol
PES	Polyethersulfone

PHEMA	Poly(2-hydroxyethyl methacrylate)
PHPMA	Poly[N-2-(hydroxypropyl) methacrylamide]
PL	Platelet lysate
PLA	Poly(lactic acid)
PLCL	Poly[(L-lactide)-*co*-(Ɛ-caprolactone)]
PLGA	Poly(lactic-co-glycolic acid)
PLL	Poly-L-lysine
PLLA	Poly(L-lactic acid)
PU-CS	Polyurethane extended with chitosan
PU-CS/DMPA	Polyurethane extended with dimethylol proprionic acid and chitosan
PU-DMPA	Polyurethane extended with dimethylol proprionic acid
PU-Gel	Polyurethane extended with gelatin
PUs	Polyurethanes
RADA-16	Ac-(Asp-Ala-Asp-Ala)4-$CONH_2$ peptide
REST	RE-1 silencing transcriptional factor
SCI	Spinal cord Injury
SEM	Scanning electron microscopy
SiRNA	Small interference ribonucleic acid
SPC-01	Conditionally immortalized neural stem cell line derived from human fetal spinal cord tissue
SS	Soft segments
STEP	Spinneret based tunable engineered parameters
TCP	Tissue culture plate
TEA	Triethylamine
TGA	Thermogravimetric analysis
THF	Tetrahydrophuran
TMS	Tetramethylsilane
TrkC	Tropomyosin receptor kinase C
UV	Ultraviolet
VEGF	Vascular endothelial growth factor
WCA	Water contact angle
WST-1	[2-(2-methoxy-4-nitrophenyl)-3-(4-nitrophenyl)-5-(2,4-disulfophenyl)-2H-tetrazolium, monosodium salt]
XPS	X-ray photoelectron spectroscopy
XRD	X-ray diffraction

Symbols

A_{1655}	Absorption band at 1655 cm^{-1}
A_{3450}	Absorption band at 3450 cm^{-1}
α	Constant dependent on the solution (solute-solvent system) and temperature

β	Full width at half maximum
Y	Young modulus
ΔH_m	Enthalpy of fusion
ε_r	Elongation at break
[η]	Intrinsic viscosity,
θ	Diffraction angle
I_a	Area of the diffraction peaks resulting from the amorphous reflections
I_c	Area of the diffraction peaks resulting from the crystalline reflections
K	Constant dependent on the solution (solute-solvent system) and temperature
λ	Wavelength
M_v	Viscosimetric molecular weight
σ_{600}.	Tensile stress at 600% strain
ρ	Density
τ	Crystallite size
T_g	Glass transition temperature
T_{hard}	Degradation temperatures of soft segments
T_m	Melting temperature
T_{soft}	Degradation temperatures of soft segments
W_1	Specific gravity bottle weight filled with water
W_2	Specific gravity bottle weight with water and scaffold
W_3	Specific gravity bottle weight after removal of water-saturated matrix from W2
$W_{c,x}$	Crystalline degree
Wi	Initial mass
Wk	Remaining mass
W_s	Scaffold weight

Chapter 1

Introduction

1. Introduction

Spinal cord injury (SCI), either traumatic or non-traumatic in origin, represent a major health problem affecting not only the patient but also their family and the community. After the injury, loss of nervous tissue and consequently loss of motor and sensory function often produce permanent disabilities such as respiratory failure, pressure sores and autonomic dysreflexia, resulting in complete or partial paralysis (Thuret, Moon et al. 2006; Madigan, McMahon et al. 2009). Worldwide, it is estimated that 2.5 million people live with SCI, with more than 130,000 new SCI reported each year (International Campaign for Cures of Spinal Cord Injury Paralysis, website: http://www.campaignforcure.org/). The main causes of SCI are road traffic accidents, falls, violence and sports activities (Injury 2005), which affects mainly young people with ages between 15 and 29 years (Van den Berg, Castellote et al. 2010). Less than 1% of people who suffered from some type of SCI can recover complete neurological function (Injury 2005).

Unfortunately, there are no actual clinical treatment for this disability. Pain reliefs and surgical decompression are the only procedures realized in clinics, depending on the type of injury, but they are far from ideal to promote the functional regeneration. The transplantation of functional stem cells, mainly neural stem cells (NSCs), to the injury site can lead to minimal improvements at the sensory-motor functions (Tsukamoto, Uchida et al. 2013). However, a few cells survive in the inhospitable injury environment and their differentiation is not controlled. Tissue engineering has been working out in a new therapeutic regenerative approach for the treatment of damaged or missing tissues or organs. In this approach, engineered scaffolds are aimed at creating an appropriate environment to support endogenous cell regrowth and a possible cell transplantation from exogenous sources. Recent studies have point out the implantation of scaffolds as a vehicle for NSCs transplantation as a promising therapeutic strategy to fill in the injury site and promote the spinal cord regeneration (Saglam, Perets et al. 2013; Li, Liu et al. 2016). However, the role of the scaffolds is far beyond that. A scaffold may provide chemical cues (type of polymer and/or functionalization) (Ren, Zhang et al. 2009), mechanical properties (Leipzig and Shoichet 2009) and topographical cues (nano and micro scale topographies) (Kerativitayanan, Carrow et al. 2015) to influence stem cell behavior. Therefore, gather in a scaffold all the characteristics that act in synergy to support the differentiation of NSCs in functional neurons that extent axons over significant distances and form synapses with the host neurons around the injury site is still a challenge.

The goal of this project was to develop a tissue engineering approach to produce an electrospun mat to guide the NSCs. The stem cells respond to the substrate chemical cues as well as to the micro and nanotopography, similar to the extracellular matrix (ECM), which determine their fate. With this idea, three main tasks were performed: (1) develop new biocompatible and biodegradable polyurethanes, (2) process those polyurethanes with the electrospinning technique to get fibrous mats, and (3) evaluate the effect of the chemical and topographic cues on the NSPCs.

In chapter 2 the SCI problem is described and an overview of the polymers used in tissue engineering scaffolds for spinal cord repair are exposed. The benefits of use scaffolds seeded with NSCs were also detailed. Finally, the effect of the scaffolds topographic and chemical cues were also addressed.

Different techniques were used to create scaffolds with a structure similar to the ECM: phase separation, self-assembly peptide nanofibers and electrospinning. From those, electrospinning has been investigated in the construction of conduits that not only fill in the injury and bridge the lesion site but also contain the topographical signals essential to provide contact guidance to host cells infiltration and axonal outgrowth (Liu, Houle et al. 2012). The easy control over the fiber alignment and diameter as well as their functionalization, make the fibrous substrates suitable to support NSCs (Lim, Liu et al. 2010). The polyurethanes (PUs) are polymers whose their properties can be easily tunable. Therefore, PUs can be designed to have customized chemistry and mechanical properties, resulting in promising biomaterials for a wide range of tissue engineering applications (Guelcher 2008). Electrospun mats from designed PUs are promising substrates for stem cell support in order to promote blood vessels replacement (Wang, Li et al. 2013) and tendon/ligament regeneration (Cardwell, Dahlgren et al. 2012). However, for spinal cord, there are no reports designing and processing through electrospinning a tunable PU to get mats that support and induce the differentiation of NSCs.

To overcome this gap, in chapter 3 is described the synthesis of PUs extended with dimetlylol proprionic acid (DMPA), DMPA and chitosan (CS) and CS, which were characterized with spectroscopic techniques and thermal analysis. CS is widely used in biomedical applications due to its biocompatibility, biodegradability and antimicrobial, antimicrobial, antioxidant and hemostatic properties (Dash, Chiellini et al. 2011). In neural regeneration, CS has been explored as a suitable biomaterial for neural differentiation (Du, Tan et al. 2014). It is also described the optimization of the electrospinning process in order to get mats from the synthetized PUs with random and aligned morphology. Their morphology, mechanical properties, degradation profile, wettability and cytotoxicity were evaluated. The mats were also seeded with caucasian foetal foreskin fibroblasts (HFFF2) cells and the adhesion and proliferation of the cells on the mats was evaluated.

In the chapter 4, and similarly to the chapter 3, is described the synthesis and characterization of the PUs extended with gelatin. The gelatin quantity was adjusted to render a polymer suitable for electrospinning. Gelatin is a biocompatible and biodegradable natural polymer derived from the hydrolysis and denaturation of collagen, with motifs for cell adhesion and prolileration (Kang, Tabata et al. 1999). However, gelatin is water soluble and their use as scaffold requires an additional crosslinking step. The crosslinking agents are toxic and can left toxic residues in the gelatin scaffolds, which can also impair their structure (Amadori, Torricelli et al. 2015). The incorporation of the gelatin in the PU structure prevent that. The electrospinning parameters for the synthetized PUs were optimized. The resulting mats with random and aligned

morphology were characterized according to mechanical properties, degradation profile, wettability and cytotoxicity. The adhesion and proliferation of HFFF2 fibroblasts in the mats was also studied.

In the chapter 5, the ability of the mats from PUs extended with either chitosan or gelatin to support human mesenchymal stem cells (MSCs) and NSCs is evaluated. Mats were seeded with human MSCs and adhesion and proliferation assay as well as fluorescent staining was performed to evaluate the viability of those cells on the mats. Human NSCs were also seeded on the mats and their proliferation was evaluated. In addition, the ability of the cells to differentiate in neurons on the mats, without additional biomolecules, was evaluated by immnufluorescent analysis.

Finally, the conclusions of this study are described in chapter 6. The results demonstrate the feasibility of the electrospun mats to support human mesenchymal and neural stem cells. Further research on the field is also described.

References

Amadori, S., P. Torricelli, et al. (2015). "Effect of sterilization and crosslinking on gelatin films." Journal of Materials Science: Materials in Medicine **26**(2): 1-9.

Cardwell, R. D., L. A. Dahlgren, et al. (2012). "Electrospun fibre diameter, not alignment, affects mesenchymal stem cell differentiation into the tendon/ligament lineage." Journal of tissue engineering and regenerative medicine **8**(12): 937–945.

Dash, M., F. Chiellini, et al. (2011). "Chitosan—A versatile semi-synthetic polymer in biomedical applications." Progress in polymer science **36**(8): 981-1014.

Du, J., E. Tan, et al. (2014). "Comparative evaluation of chitosan, cellulose acetate, and polyethersulfone nanofiber scaffolds for neural differentiation." Carbohydrate polymers **99**: 483-490.

Guelcher, S. A. (2008). "Biodegradable polyurethanes: synthesis and applications in regenerative medicine." Tissue Engineering Part B: Reviews **14**(1): 3-17.

National Spinal Cord Injury Statistical Center. (2005). "Spinal Cord Ijury. Facts and Figures at a Glance." The Journal of Spinal Cord Medicine **28**(4): 379:380.

Kang, H.-W., Y. Tabata, et al. (1999). "Fabrication of porous gelatin scaffolds for tissue engineering." Biomaterials **20**(14): 1339-1344.

Kerativitayanan, P., J. K. Carrow, et al. (2015). "Nanomaterials for engineering stem cell responses." Advanced healthcare materials **4**(11): 1600-1627.

Leipzig, N. D. and M. S. Shoichet (2009). "The effect of substrate stiffness on adult neural stem cell behavior." Biomaterials **30**(36): 6867-6878.

Li, X., S. Liu, et al. (2016). "Training Neural Stem Cells on Functional Collagen Scaffolds for Severe Spinal Cord Injury Repair." Advanced Functional Materials **26**(32): 5835-5847.

Lim, S. H., X. Y. Liu, et al. (2010). "The effect of nanofiber-guided cell alignment on the preferential differentiation of neural stem cells." Biomaterials **31**(34): 9031-9039.

Liu, T., J. D. Houle, et al. (2012). "Nanofibrous collagen nerve conduits for spinal cord repair." Tissue Engineering Part A **18**(9-10): 1057-1066.

Madigan, N. N., S. McMahon, et al. (2009). "Current tissue engineering and novel therapeutic approaches to axonal regeneration following spinal cord injury using polymer scaffolds." Respiratory physiology & neurobiology **169**(2): 183-199.

Ren, Y.-J., H. Zhang, et al. (2009). "In vitro behavior of neural stem cells in response to different chemical functional groups." Biomaterials **30**(6): 1036-1044.

Saglam, A., A. Perets, et al. (2013). "Angioneural crosstalk in scaffolds with oriented microchannels for regenerative spinal cord injury repair." Journal of Molecular Neuroscience **49**(2): 334-346.

Thuret, S., L. D. Moon, et al. (2006). "Therapeutic interventions after spinal cord injury." Nature Reviews Neuroscience **7**(8): 628-643.

Tsukamoto, A., N. Uchida, et al. (2013). "Clinical translation of human neural stem cells." Stem Cell Res Ther **4**(4): 102.

Van den Berg, M., J. Castellote, et al. (2010). "Incidence of spinal cord injury worldwide: a systematic review." Neuroepidemiology **34**(3): 184-192.

Wang, F., Z. Li, et al. (2013). "Fabrication of mesenchymal stem cells-integrated vascular constructs mimicking multiple properties of the native blood vessels." Journal of Biomaterials Science, Polymer Edition **24**(7): 769-783.

Chapter 2

Literature Review

2. Literature Review

2.1 Spinal Cord Injury

Spinal cord has well-characterized descending and ascending tracts. The ascending tracts are the ones that receive the sensorial inputs and the descending tracts are responsible for a rich variety of quantifiable motor outputs, ranging from simple reflexes to more complex motor patterns, such as scratching, fast paw shake and locomotion (Rossignol and Frigon 2011). In a devastating condition (physical or mechanical trauma) the ascending and/or descending pathways, which connects the brain to the rest of the body, are disrupted. This phenomenon results in a large damage to the spinal cord, leading to paralysis and loss of sensation below the level of injury (Ghosh, Haiss et al. 2009). The initial trauma – primary injury is followed by the secondary injury, consisting of several events including the loss of neuronal and glial cells, which culminates with the formation of cystic cavities and glial scars (Figure 2.1).

2.1.1 Primary injury

The primary injury emerges from the initial physical and/or mechanical trauma to the spinal cord and surrounding vertebral column, caused by blunt impact, compression and penetrating trauma. Blunt impact comes mainly from falls or collisions; compression from hyperflexion, hyperextension, axial loading and severe rotation; and penetrating trauma usually arise from gunshots and stab wounds (Viano, King et al. 1989; Dubendorf 1999; Hulsebosch 2002). After immediate mechanical damage, a cascade of events such as blood vessel damage, dislocation of bones, rupture of intervertebral discs, injury to ligaments and cease of blood flow that deprive the spinal cord of oxygen and nutrients takes place, leading to immediate cell necrosis at the point of impact (Hulsebosch 2002). Without any treatment, the cells and axons in the spinal cord that were not affected by the primary injury can be damaged by secondary injury events spreading to the surrounding tissue (Wang, Zhai et al. 2011).

2.1.2 Secondary injury

The secondary injury is characterized by the events that take place within the spinal cord in response to the primary injury. Those events propagate from the site of injury to unaffected areas of the spinal cord and include:

1- Ischemia and micro-vascular damage, comprising vasospasm, thrombosis, hemorrhage and increased permeability that combined with edema lead to hypoperfusion and necrosis (Tator and Fehlings 1991; Winkler, Sharma et al. 2002; Samadikuchaksaraei 2007).

2- Glutamatergic excitotoxicity, resulting from the accumulation of excitatory neurotransmitters due to the failure of the adenosine triphosphate (ATP)-dependent ion pumps,

conducting to the depolarization of the neuronal membrane potential (McDonald and Sadowsky 2002; Park, Velumian et al. 2004).

3- Oxidative stress, resulting from free radical formation and lipid peroxidation that can attack membranes and other cell components, disturbing unaffected neurons and oligodendrocytes (Braughler and Hall 1989; McDonald and Sadowsky 2002).

4- Inflammation, recruitment and activation of inflammatory cells associated with secretion of cytokines, which contribute to further tissue damage (Dusart and Schwab 1994; Takami, Oudega et al. 2002).

5- Loss of ionic intracellular balance, increase of the opioids at the injury site, depletion of energy metabolites, conducting to an anaerobic metabolism, an increase of lactate dehydrogenase (LDH) activity and an activation of calpains and caspases, culminating in cellular apoptosis (Samadikuchaksaraei 2007).

After days to weeks from the injury, a fluid filled cystic cavity is formed due to the removal of injured neurons, their axons and necrotic debris. The cyst is expanded to adjacent spinal cord areas, increasing the cell dead and loss of neuronal function, mainly the dead of oligodendrocytes that lead to malfunction and degeneration of the intact axons.

Finally, due to the absence of phagocytic macrophages, a scar is formed not only to promote wound healing but also to limit the spreading of the injury to unaffected areas. In the central nervous system (CNS), two types of scar tissue were identified, the fibrous scar in the core and the glial scar in the surrounding parenchyma. The glial scar is constituted by reactive astrocytes from self-duplication, oligodendrocyte progenitors and astrocytes derived from the ependymal cells (presented at the central canal of the spinal cord with the ability of neural stem cells), which are activated after a lesion (Sabelström, Stenudd et al. 2014). On the other hand, the fibrotic/inflammatory scar is formed from collagen IV, which result in a meshwork basement membrane where other ECM compounds and inhibitory molecules can bind. It also has perivascular fibroblasts that deposit on the basal lamina and form a barrier between the lesion core and the penumbra (Soderblom, Luo et al. 2013).

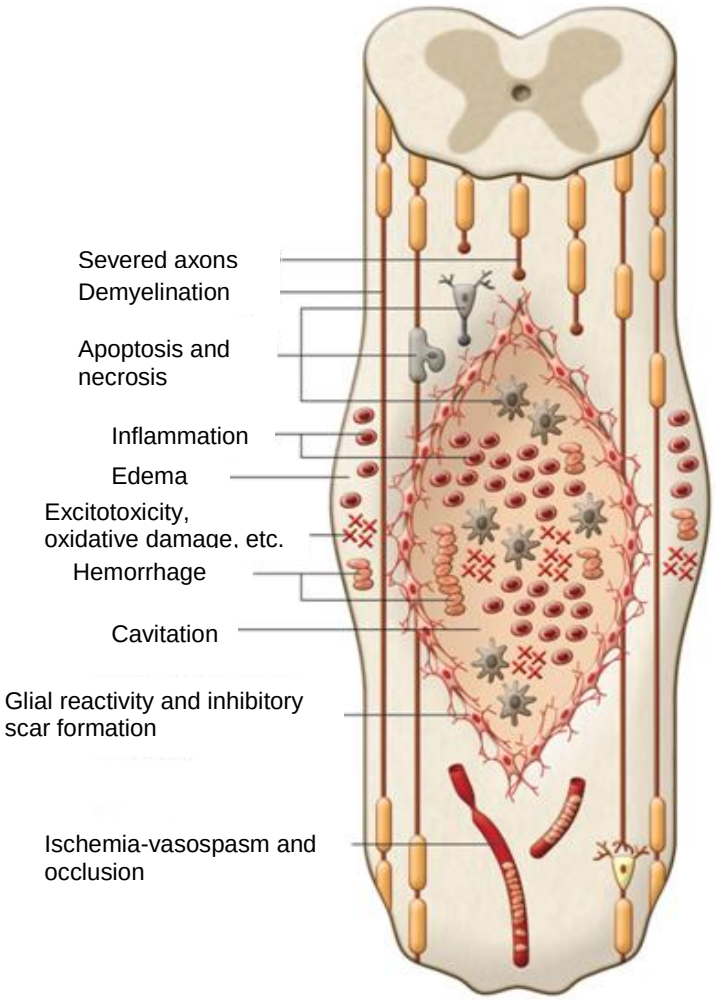

Figure 2.1 – Pathophysiological events occurring after SCI, including the primary, secondary and chronic phases. (reproduced with permission from (Mothe and Tator 2013))

2.2 Limited spinal cord regeneration capacity

The inflammatory events in the acute phase are necessary to prevent infections, clear the debris tissue and close the blood-brain barrier, restraining the lesion site. However, in the chronic stage, inflammation, myelin debris and glial scar formation limit the axonal regeneration and consequently, the capacity of the spinal cord to restore their functions after an injury. The scar formed after the injury is a hostile environment with inhibitory molecules and proteoglycans without the ability to support the neuronal cells; therefore, acting as a chemical and physical barrier to the axonal regeneration (Yiu and He 2006).

The inhibitory molecules released after SCI that limit the spinal cord regeneration are: myelin-associated proteins that inhibit axonal growth such as, oligodendrocyte myelin protein – neurite outgrowth inhibitor (Nogo-A), (GrandPré, Nakamura et al. 2000); netrin-1 (Löw, Culbertson et al. 2008); transmembrane semaphoring Sema4D/CD100 (Moreau-Fauvarque, Kumanogoh et al. 2003) and ephrin-B3 (Benson, Romero et al. 2005). In addition, new

compounds are formed to help the propagation of the inflammation and the remodeling of the ECM. The deposition of inhibitory ECM molecules around the injury sites such as, inhibitory chondroitin sulfate proteoglycans (CSPGs) secreted by reactive astrocytes on the glial scar will impair the spinal cord regeneration and induces the formation of dystrophic cones on injured neurons (Smith-Thomas, Stevens et al. 1995; Niederöst, Zimmermann et al. 1999).

Nevertheless, there are also some endogenous regeneration events that take place after SCI, such as the upregulation of some proteins related to axonal growth at the lesion site contributing to axonal sprouting in short distances and the migration of Schwann cells from spinal roots to the damaged tissue to promote the myelination of spinal cord axons. However, the recovery of the spinal cord is very limited (Duncan and Hoffman 1997; Zawadzka, Rivers et al. 2010). Although it is not a regenerative event, the glial scar formed by the astrocytes derived from ependymal cells is needed to restrict secondary damage on the lesion site (Sabelström, Stenudd et al. 2013). In addition, the ependymal cells also provide neurotrophic effects essential to the survival of the intact neurons after a spinal cord injury. Also, the presence of oligodendrocyte progenitor cells on the glial scar can generate myelinating oligodendrocytes after SCI (Sabelström, Stenudd et al. 2014).

Plasticity within intrinsic spinal cord circuits has been reported as a phenomenon that help in the spinal cord repair. The spinal cord inputs, from descending and peripheral sources, experience functional and anatomical changes that contribute to recovery, mainly by accessing and modulating the modified spinal network in a meaningful way (Raineteau and Schwab 2001; Blesch and Tuszynski 2009). However, these events are almost negligible compared to all the obstacles that prevent the complete spinal cord regeneration.

2.3 Therapeutic/regenerative strategies

Nowadays, there is no treatment for SCI. The standard therapies consist in surgical stabilization and decompression of the spinal cord associated with the use of some drugs such as methylprednisolone, to reduce inflammation and consequently, to minimize secondary damage (Hyun and Kim 2010) and Pregabalin to neuropathic pain relief (Sadosky, Parsons et al. 2016). However, the disabilities arising from the SCI such as paraplegia or tetraplegia, respiratory failure and absence of sphincter control, are still a concern as they drastically reduce the patient's life quality.

In an attempt to regain the walking ability, various types of exercises and supporting strategies have been developed such as, physiotherapy, functional electrical stimulation to strength muscles, condition of heart and pain control, and robot-assistive devices (Colombo, Wirz et al. 2001; McDonald and Sadowsky 2002; Wirz, Zemon et al. 2005; Ragnarsson 2007). These strategies may improve the quality of life of the patient, minimizing the disabilities arising from such devastating condition but, complete functional recovery was not attained yet.

The complex mechanism involving SCI requires strategies that can overcome the inhibitory environment at the injury, and at the same time can also prevent neuronal loss, promote axonal myelinationn regeneration and the reconnection of the interrupted spinal cord signal, leading to the complete spinal cord regeneration.

2.3.1 Drugs

Several drugs have been tested to limit the spinal cord secondary injury, facilitating regeneration. Riluzole, which have been used in the treatment of amyotrophic lateral sclerosis, is in phase IIB/III clinical trials for the treatment of acute SCI, demonstrating neuroprotective benefits (Fehlings, Nakashima et al. 2016). Rolipram, a phosphodiesterase 4 inhibitor that elevated the cyclic adenosine monophosphate (cAMP) levels, demonstrated anti-inflammatory effects, enhanced axonal growth and functional recovery when administered in rats with SCI (Nikulina, Tidwell et al. 2004; Costa, Pereira et al. 2013). Epothilone B, which is a microtubule-stabilizing drug, encourage the polymerization of microtubules, inducing the axonal growth and functional recovery (Ruschel, Hellal et al. 2015). The bacterial enzyme chondroitinase ABC (chABC), which digests CSPG (contribute to the inhibitory environment), was investigated in a rat SCI model and was effective in the restoration of electrophysiological activities and in the promotion of functional recovery (Bradbury, Moon et al. 2002). When the delivery of the ChABC was carried out via gene therapy into a cervical contusion injury rat model, it was observed improvements in the upper limb and hands function (James, Shea et al. 2015). However, the ChABC therapy combined with treadmill rehabilitation was more effective in promoting tissue regeneration of rats with chronic severe spinal cord contusion by changing neural plasticity (Shinozaki, Iwanami et al. 2016). Purified anti-Nogo-A monoclonal immunoglobulin G (IgG) antibodies, which block the myelin protein Nogo-A, enhanced the neurite outgrowth and axonal regeneration in rat SCI model (Liebscher, Schnell et al. 2005). A Rho GTPase, central regulators of actin reorganization, antagonist – VX-210 – is in phase I/IIA trial and led to motor improvements without safety concerns in SCI (Fehlings, Theodore et al. 2011). Other compounds such as antiserum to dynorphin A (Faden 1990), omega-3 polyunsaturated fatty acids alphalinolenic acid and docosahexaenoic acid (King, Huang et al. 2006) and 4-aminopyridine (Hayes, Blight et al. 1993) were also investigated to prevent the inhibitory environment inside the SCI to facilitate the regeneration process.

Neurotrophic factors such as, neurotrophin-3 (NT-3), nerve growth factor (NGF), brain-derived neurotrophic factor (BDNF), ciliary neurotrophic factor (CNTF) and glial cell line-derived neurotrophic factor (GDNF), enhance neuronal survival, proliferation, migration and differentiation, axonal growth and synaptic plasticity, promoting the repair and recovery at some extent of the central nervous system after injury (Nomura, Tator et al. 2006; Hyun and Kim 2010).

The drugs can be used after the SCI to limit the secondary events and to create an environment inside the lesion most appropriate for regeneration. However, in the chronic phase,

the focus should be in the regenerative therapies such as stem cells transplantation and tissue engineering to achieve functional recovery.

2.3.2 Stem cells therapy

Stem cell transplantation has been widely studied in the treatment of several disabilities, including the treatment of spinal cord. Stem cells (embryonic or adult in origin) are cells with the ability to self-renew and differentiate into multiple lineages. Embryonic stem cells (ESCs) and recently, induced pluripotent stem cells (iPSCs) are able to differentiate into the three germ layers (endoderm, ectoderm and mesoderm). Although their high self-renewal and differentiation ability, the *in vivo* transplantation of ESCs can induce teratomas, indicating the need to strictly control the proliferation/differentiation processes of those cells. Even more, the use of these cells is related with some ethical issues. On the other hand, the adult stem cells such as mesenchymal stem cells (MSCs) and neural stem cells (NSCs) are more restricted and can only differentiate into specific lineages.

Examples of stem cells that have been investigated for the SCI regeneration include: embryonic or fetal stem cells, NSPCs, oligodendrocyte progenitor cells, MSCs from umbilical cord blood and bone marrow, olfactory ensheathing glia and recently, iPSCs (Romanyuk, Amemori et al. 2015). Several reviews summarized the benefits/effects of employing different stem cells types both *in vitro* and *in vivo* in the central nervous system regeneration (Kabu, Gao et al. 2015; Iyer, Wilems et al. 2017; Zhu, Uezono et al. 2017). Briefly, the stem cells implanted in rats with SCI were able to differentiate into neurons and helped to bridge and restore the signaling in the spinal cord, resulting in sensory- and motor-level improvements (Lu, Woodruff et al. 2014; Iyer, Wilems et al. 2017). In addition, the stem cells secreted factors, which have neuroprotective effects and promote regeneration of the damage axons (Raspa, Pugliese et al. 2016).

From the different stem cells, the NSPCs, found in mammalian brain and spinal cord, were the most promising cell source since they are committed to the neural lineage. The transplanted NSCPs to SCI have the potential to repopulate the damaged area with new neurons, to remielinate the axons and to modulate the environment to neural repair (permitting neural plasticity, trophic factor support and controlling the inflammatory response) (Bonner and Steward 2015). NSPCs, mainly from fetal sources, are in phase I/II clinical trials to the treatment of SCI, improving the sensorial responses (Tsukamoto, Uchida et al. 2013).

Despite of the great potential of stem cells to differentiate into neuronal lineage and improve spinal cord regeneration, some drawbacks have been reported arising from the transplantation of the cells. The hostile environment inside the lesion site conducted to the low rate of cell survival and uncontrolled cell differentiation. In addition, the lack of a physical support led to insufficient cell reinnervation with few axons crossing the injury gap to the distal host tissue. Therefore, the stem cells were preferentially differentiated into astrocytes and not into oligodendrocytes and mature neurons (Vroemen, Aigner et al. 2003; Mothe, Kulbatski et al. 2008).

2.3.3 Tissue engineering

Tissue engineering has been working out in a new therapeutic approach of regenerative medicine for the treatment of damaged or missing tissues or organs. It combines several strategies such as cell transplantation, scaffolds, and biomolecules/drug delivery systems. Therefore, tissue engineering has been investigated in spinal cord regeneration.

After SCI, a structure suitable to connect the two injury ends and to create a suitable environment for cell transplantation is needed. Tissue engineered scaffolds can act as structures that bridges the lesion site and fill in the necrotic areas, creating the suitable cues to provide axonal guidance through the lesion site and connection with the host tissue as well as support the transplanted and endogenous cells and drugs/biomolecules (Cheng, Huang et al. 2007; Potter, Kalil et al. 2008; Olson, Rooney et al. 2009).

The scaffolds seeded with stem cells and transplanted in rat SCI models, improved behavioral recovery and graft survival, reduced the cavitation and increased oligodendrocytic differentiation, compared to cells transplanted without any substrate (Mothe, Tam et al. 2013). The presence of the physical support, facilitate the exchange of oxygen, nutrients, growth factors, and cytokines from the cells with the surrounding environment, improving the cell survival inside the lesion (Bozkurt, Mothe et al. 2010).

Scaffolds can control the delivery of biomolecules such as BDNF (Patist, Mulder et al. 2004; Stokols and Tuszynski 2006) and NT3 (Piantino, Burdick et al. 2006; Fan, Zhang et al. 2011) in the SCI site, which have beneficial effects in spinal cord regeneration, disrupting the inhibitory environment inside the lesion and leading to better axonal growth and improved locomotion. Several reviews are available in the literature explaining the effects of the controlled release of drugs and bioactive agents from scaffolds for spinal cord regeneration (Kwon, Okon et al. 2011; Tator, Hashimoto et al. 2012; Kabu, Gao et al. 2015).

2.3.3.1 Scaffold properties

A scaffold to be applied in spinal cord regeneration must fulfill a number of requirements: 1) biocompatible, integrating the host tissue without triggering a major immune response (reduced astrocytic reaction and fibroblastic gliosis) (Madigan, McMahon et al. 2009); 2) possess high porosity and interconnected pores improving cell attachment and in-growth, as well as the capacity of vascularization (Dinan, Bhattarai et al. ; Pham, Sharma et al. 2006; Lim and Mao 2009); 3) biodegradable to avoid a second surgery for their removal, with a controlled degradation rate mimicking the rate of tissue formation and non-toxic degradation products; 4) have adequate permeability to various molecular sizes in order to supply adequate oxygen and nutrients to cells and the removal of waste products; 5) have a favorable surface chemistry to allow cellular attachment, differentiation, proliferation, and orientation (direction of the neural cell behavior); 6) should possess mechanical properties similar to the ones of the native spinal cord, with a similar

elastic moduli in order to minimize mechanical parenchymal damage at points in contact between the scaffolds and the host; and 7) be produced on large scale and in a reproducible way (Straley, Foo et al. 2010; Wang, Zhai et al. 2011; He, Wang et al. 2012).

2.3.3.2 **Materials used in scaffold's preparation**

The physico-chemical properties of a scaffold and the interaction of the biological environment with it, depend on the physico-chemical properties of the raw material. Both synthetic and natural polymers have been investigated as materials for the production of scaffolds for spinal cord regeneration.

2.3.3.2.1 *Natural polymers*

Natural polymers are extracted from the natural ECM of humans and animals. They are biocompatible, biodegradable and have motifs to promote cell adhesion, proliferation, and even differentiation. However, the use of natural polymers is associated with some drawbacks such as variability in fabrication and risk of immunogenicity due to the incomplete polymer purification (Straley, Foo et al. 2010; Kubinová and Syková 2012). Moreover, natural polymers usually own weak mechanical properties and rapid degradation rate, which can be advantageous or not depending on the application (Kai, Jin et al. 2013).

Scaffolds from natural polymers, such as collagen, agarose, fibrin and/or fibronectin, silk fibroin and chitosan, were evaluated in the regeneration of the spinal cord. Scaffolds from collagen, which is the main structural protein of connective tissue, improved the forelimb-hindlimb locomotion when implanted into cat spinal cord transection (Goldsmith, Fonseca et al. 2005). Yoshii et al. produced collagen filaments which were implanted in a rabbit spinal cord with a 3 mm transected defect, promoting not only the axonal regeneration but also the function restoration of the transected spinal cord (Yoshii, Ito et al. 2009). Fibrous collagen nerve conduits were repopulated with host cells and prevented astrocyte accumulation in SCI rat models (Liu, Houle et al. 2012). Porous honeycomb collagen sponges filled with PuraMatrix hydrogel conducted to regeneration, migration and differentiation of neural cells in rats with complete SCI transection, resulting in locomotors recovery (Kaneko, Matsushita et al. 2015). Linearly ordered collagen scaffolds surface modified with a collagen biding epidermal growth factor receptor (EGFR) antibody, reduced the glial scar formation and promoted the neuronal differentiation as well as myelination of endogenous NSCs in a transverse thoracic rat SCI, which result in functional neurons exhibiting synaptic activity and conducting functional recovery (Fan, Li et al. 2017).

Fibronectin is also a protein of the ECM, which is important in cellular adhesion, growth and migration. Scaffolds from fibronectin combined with fibrin had a good integration within the knife-cut cavity in a rat spinal cord. Moreover, those scaffolds supported the axonal growth and ingrowth (King, Alovskaya et al. 2010). Aligned fibrin hydrogels reduced the scarring and inflammatory response in hemisection SCI canine model, leading to the infiltration of regenerating nerve fibers through the lesion and improving the functional recovery (Zhang, Yao et al. 2017).

Agarose is extracted from seaweed and has a particular characteristic: the gelling temperature around 37 ºC – the human body temperature. Agarose scaffolds that gels *in situ* filled in a hemisection spinal cord defect in adult rats. The gels supported the three dimensional space (3D) neurite extension *in vivo*, controlled the delivery of trophic factors and anti-scar agents, enhancing the regeneration (Jain, Kim et al. 2006).

Silk fibroin, a protein found in the silk produced by spiders and other insects, was processed into multichannel scaffolds with hierarchical pore structure and coated with laminin. The construct when implanted in hemisection SCI rat model enhanced the ECM and blood vessels formation guiding the extension of the axons through the injury, with benefits in the locomotor function (Zhang, Yan et al. 2016).

Chitosan is a polysaccharide derived from chitin, which is extracted from the exoskeleton of crustaceans. It was been applied in the medical field due to the hemostatic and antibacterial properties. Chitosan nerve conduits, fabricated by lyophilization, with an internal structure of open channels and coated with laminin were implanted in a rat SCI model to observe the axonal re-growth. The axons growth around the channels, requiring further scaffold optimization (Cheng, Huang et al. 2007).

2.3.3.2.2 *Synthetic polymers*

Synthetic polymers can be processed in large quantities and their chemical and physical properties can be easily controlled. They own good mechanical properties and stability in the body, overcoming the drawbacks of natural polymers. However, synthetic polymers usually are hydrophobic and lack the biological motifs for cell adhesion and proliferation found in the natural polymers (Kubinová and Syková 2012; Kai, Jin et al. 2013).

Synthetic polymers such as, poly(2-hydroxyethyl methacrytale) (PHEMA), poly[N-2-(hydroxypropyl) methacrylamide] (PHPMA), poly (lactic-co-glycolic acid) (PLGA) and poly(caprolactone) (PCL) have been processed into hydrogels or microchannel tubes and their effect evaluated into SCI animal models. A PHPMA hydrogel reduced the glial scar formation and the myelin degradation and promoted the formation of new blood vessels when implanted into a cat spinal cord transection (Woerly, Doan et al. 2004). Kubinová et al. produced a cholesterol modified PHEMA hydrogel with a superporous structure and with an elastic modulus between 10 and 19 kPa. When implanted into rats with hemisection SCI, the hydrogels were well-integrated into the surrounding tissue, bridging the lesion site and the porous structure enable the axons and Schwann cells infiltration as well as the angiogenesis process (Kubinová, Horak et al. 2011). PHEMA was also modified with poly(lactic acid) (PLA) rendering a copolymer of PLA-b-PHEMA, which formed hydrogels that allowed the infiltration of neurofilament fibers of regenerating axons and improve partially the locomotor function of rats with a spinal cord hemi-transection (Pertici, Trimaille et al. 2014). A multi-channel PLGA scaffold with high channel number and interconnected pores was produced combining a gas foaming technique with a sacrificial template of sucrose fibers and salt particles. The scaffold implanted in a rat SCI model induced the re-growth of axons and the infiltration of other cells (including oligodendrocytes) but did not improve the myelination (Thomas, Kubilius et al. 2013). Porous scaffolds from PLGA (Pritchard, Slotkin et

al. 2010) and PLGA/poly-L-lysine (PLL) (Slotkin, Pritchard et al. 2017) improved the remodeling of the tissue into complete lateral thoracic hemisection spinal cord injury of African green monkeys. In the scaffolds with PLL, the recovery of the monkey's locomotion was observed because the benefic effects of the positive charges of PLL, promoting a positive environment for survival and growth of the axons (Slotkin, Pritchard et al. 2017). Recently, a PCL scaffold was designed to maximize open pore volume using a modified salt-leaching technique. The scaffold is composed of several microtubules inserted into a larger tube. The space into the microtubules as well as the interstitial space between the tubes were filled with neurons and the axonal growth was linear to the scaffolds into transected rat spinal cord model (Shahriari, Koffler et al. 2017).

2.3.3.2.3 *Polyurethanes*

Polyurethanes (PUs), the major class of synthetic elastomers, have been recently investigated as suitable biomaterials to produce scaffolds for tissue engineering. They have three main constituents, a macrodiol or polyol, a diisocyanate, and a chain extender (Figure 2.2).

Usually the synthesis of PUs is realized in two steps. In the first step, the pre-polymer is formed by reacting the hydroxyl groups of a polyol with the isocyanate groups of a polyisocyanate (usually a diisocyanate). The polyisocyanates used in the synthesis can be aromatic, aliphatic or lysine-derived. The polyols are macrodiols with a polyether, polyester or polycarbonate backbone, and hydroxyl functional groups (at least two groups). The second step consists in the extension of the pre-polymer with a short polyol or polyamide extender, resulting in polyurethane or polyurethane urea, respectively (Guelcher 2008; Bagdi, Molná et al. 2011).

In PUs, all components react in order to form segmented copolymers composed of soft and hard segments (thermoplastic polyurethanes) that microphase separate due to the thermodynamic incompatibility between them (Oprea 2010). The soft segment is derived from the polyol and the hard one is derived from the polyisocyanate and the chain extender. The hard segments are organized in discrete domains resulting from hydrogen bonds and van der Walls interactions between the N-H groups of urethane and urea linkages, acting as reinforcing fillers of the soft segment matrix. However, the hydrogen bonds can be established with the carbonyl or ester/ether oxygen groups of the soft segment, which disturb the phase separation and drive the phase mixing.

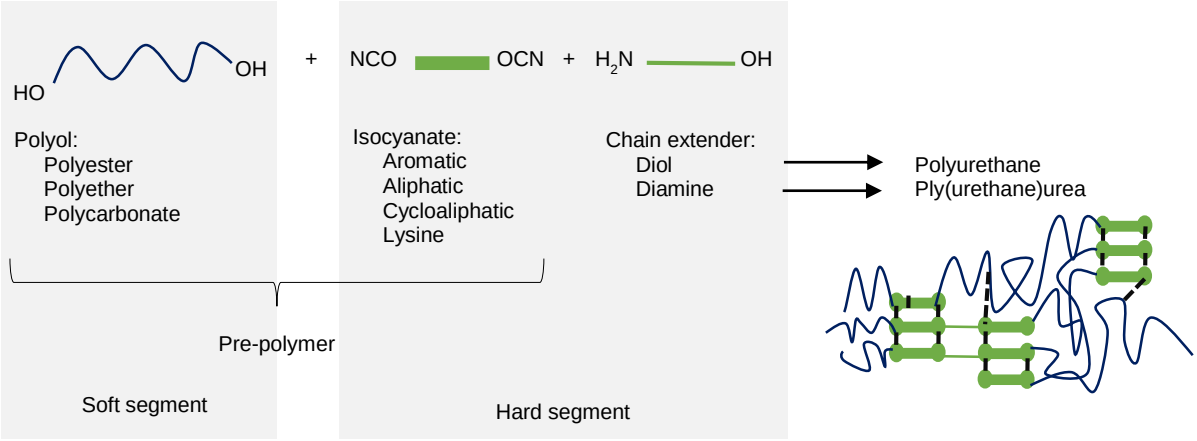

Figure 2.2 – Constituents and route of production of PUs.

By changing the type and ratio of the PUs constituents, PUs with different physico-chemical properties (mechanical, thermal, and physical), degradation rates and biocompatibility can be obtained and used as biomaterials in different fields (Tatai, Moore et al. 2007; Li, Li et al. 2013).

Mechanical Properties

Soft tissues like heart, blood vessels, skeletal muscle, tendon, and so forth, are very elastic and strong, with non-linear stress-strain behavior (Ma, Hong et al. 2011). Unlike soft tissues, the available polymers are too stiff with low elongation or very soft with low strength (Zhang, Zhang et al. 2006). Modulus mismatch between biomaterials and the surrounding tissue can exacerbate inflammatory reactions that prevent and/or impair the tissue regeneration process (Ma, Hong et al. 2011). PUs constituents can be wisely chosen to synthetize PUs with mechanical properties similar to the tissues intended to repair/replace.

The polyol, either polyester, polyether or polycarbonate, has an important effect on the mechanical properties of the PUs. The use of a polycarbonate as soft segment rendered PUs with superior elongation at break and resilience compared to the PUs based polyester (Ma, Hong et al. 2011). The variations in the molecular weight of the soft segment also affected the mechanical moduli of the PUs (Ma, Hong et al. 2011). In PUs with polyester in their structure, the interaction between hard and soft segments was stronger, resulting in PUs with higher strain hardening tendency as well as larger tensile strength and smaller deformations comparing to PUs based on polyethers (Bagdi, Molná et al. 2011).

The choice of the chain extender also influence the final mechanical properties of the PUs. Chan-Chan et al. (2010) produced biodegradable segmented PUs using either butanediol or dithioerythritol as chain extenders. The use of butanediol, which hinder the phase separation, conducted to a PU with lower strain at break and superior Young modulus comparing to PUs using the dithioerythritol as chain extender, which impart phase separation (Chan-Chan, Solis-Correa et al. 2010). The PUs synthetized with different chain extenders such as, 2,5-dimethyl-3-hexine-2,5-diol (DHD), hexaethylene glycol, glycerin, or castor oil, had distinct mechanical properties due to their distinct chemical structure and the presence of hard-segment crosslinking

(Oprea 2010). PUs with longer chain lengths between crosslinks had lower young modulus and high elongation at break (Oprea 2010).

Biodegradation

An appropriate degradation rate is also essential and should be in tune with the rate of new tissue formation: a too fast degradation will compromise the needed support for the forming tissue and a too slow degradation may compromise the healing, contributing to a persistent host inflammatory response (Zhang, Zhang et al. 2006).

The *in vivo* degradation of PUs occur mainly by hydrolytic, enzymatic and oxidative attack (Santerre, Woodhouse et al. 2005). The polyesters are the preferred choice as soft segments for PUs. The ester links are hydrolysable and their degradation can be accelerated by the presence of enzymes existent in the organism, such as the esterases (Tokiwa, Ando et al. 1990; Wang, Labow et al. 1997). On the other hand, the polyethers are less prone to hydrolytic and enzymatic attack. However, they are susceptible to oxidative degradation (Schubert, Wiggins et al. 1995).

The urea and urethane linkages are reasonably stable to either hydrolysis, oxidative stress or enzymatic attack, but still they are degradable *in vivo*. To control the degradation rate of PUs and to get degradation products without toxicity, the naturally-derived chain extenders have been incorporated in PUs. Those include phenylalanine diester chain extender (Skarja and Woodhouse 2001) and lysine or ornithine chain extenders (Marcos-Fernández, Abraham et al. 2006), rendering biodegradable PU with non-toxic and easily metabolized *in vivo* degradation products. The design of enzyme-sensitive chain extenders is another way to control the PUs degradation. The chain extender based on DL-lactic acid and ethylene glycol on the PU backbone accelerated the hydrolytic degradation (Tatai, Moore et al. 2007). A collagenase-sensitive peptide was designed and used as chain extender to control the degradation of PUs through the enzyme collagenase (Fu, Hong et al. 2014).

The choice of the diisocyanate has influence not only on the degradability of the PUs but also, on the toxicity of the degradation products. In order to obtain biodegradable PUs, the aliphatic and lysine-derived diisocyanates have been better choices in detriment of the aromatic ones. The aromatic isocyanates did not meet agreement according to the toxicity of their degradation products. The toxic effects are dependent on the degradation rate of the PUs as well as the clearance rate by the tissue (Guelcher 2008). On the other hand, the biodegradable PUs synthetized with the aliphatic diisocyanates (Park, Gong et al. 2013) and lysine-derived diisocyanates (Wang, Yu et al. 2011) can be easily degraded in phosphate buffer saline (PBS) and enzymatic solution and their degradation products were not toxic in *in vitro* experiments.

Biocompatibility

The controlled degradation rate of PUs, the lack of toxicity of their degradation products and the minimum host inflammatory response are not the only factors to have into account during the synthesis of PUs. To be used as biomaterials in tissue engineering, PUs must be able to support the host and transplanted cells, allowing their adhesion, proliferation, survival, and

differentiation. As synthetic polymers, PUs are destitute of biological recognition sites for cell adhesion and proliferation and have poor hydrophilicity and hemocompatibility (Wang, Feng et al. 2012).

The biological response of PUs can be improved by using hydrophilic, polarized and with biological recognition sites chain extenders. Zhang et al. synthetized PUs with methylene di-p-phenyl-diisocyanate (MDI), PCL-diol and with either butanediol (BD) or 2,2'-(methylimino) diethanol (MIDE) chain extenders. The PU with MIDE had superior hydrophilicity and swelling rate, resulting in superior fibroblast's adhesion and proliferation (Zhang, Zhang et al. 2006). PUs extended with N,N-bis (2-hydorxyethyl)-2-aminoethane-sulfonic acid also supported the adhesion and proliferation of fibroblasts, with additional anticoagulation properties (Zhang, Wen et al. 2008). The use of aminoacids as chain extenders in the PU structures is a way to introduce specific biological functionality, such as enhanced cellular adhesion. Perales-Alcacio and co-workers (Perales-Alcacio, Santa-Olalla Tapia et al. 2013) extended PUs with either glutamic acid, cysteine or glycine aminoacids. The viability of endothelial cells was superior in PUs with either glycine or cysteine in their structure. Endothelial cells were also used to evaluate the compatibility of PUs with glycine, arginine and aspartic acid (Chan-Chan, Tkaczyk et al. 2013) and the PUs extended with arginine support endothelial cells adhesion and viability.

PUs can be processed into scaffolds with tunable mechanical properties and degradation rates as well as with the ability to support the host and/or transplanted cells for tissue engineering. The PUs scaffolds have been widely studied for the cardiovascular and cartilage regeneration, encouraging the formation of new tissue when they are associated with stem cells. For central nervous system regeneration, PUs were used as substrates to guide neuronal differentiation *in vitro* (Carlberg, Axell et al. 2009; Zandén, Erkenstam et al. 2014). *In vivo*, the use of the reverse thermal gel poly(ethylene glycol)-poly(serinol hexamethylene urethane) loaded with bone marrow stromal cells, increased the cells survival inside the lesion, improving the hindlimb motor and sensorimotor recovery in rats with spinal cord contusions (Ritfeld, Rauck et al. 2014). Hsieh et al. 2015 synthetized aqueous PU dispersions with both PCL and PLLA on the soft segment that formed hydrogels at 37 ºC by thermally-induced self-assembly, the gels had an elastic modulus similar to that of the brain tissue. The PU water dispersion was used to embed NSCs before gelation, constituting an ink for 3D printing. The cells proliferate and differentiate properly on the hydrogel, rendering functional recovery of zebrafish neuronal injury (Hsieh, Lin et al. 2015).

2.3.3.2.4 *Electrical conductive polymers*

Special attention has been given to electrically conductive polymers due to their ability to stimulate electrically responsive tissues. Some cells in the body, such as the ones from cardiac and neural tissue, are responsive to electrical stimulus. Therefore, conductive polymers can have a positive role in the spinal cord regeneration mechanism. Two semi-conductive polymers (iodine-doped pyrrole and pyrrole-polyethylene glycol) were synthetized and implanted in rats with spinal cord transection. The polymers were well integrated in the host tissue and prevented tissue destruction (Olayo, Ríos et al. 2008). The polymers also improved the motor function and the

somatosensory evoked potentials, particularly in the presence of iodine-doped pyrrole (Cruz, Mondragón-Lozano et al. 2012). Therefore, iodine-doped pyrrole in a mesoparticles formulation implanted in rats with traumatic SCI were combined with a treadmill training which induced neuroplasticity, promoting the spinal cord functional recovery and preserving the tissues (Alvarez-Mejia, Morales et al. 2015). Recently, poly(3,4-ethylenedioxythiophene) (PEDOT)-coated carbon microfibers functionalized with a multimolecular complex of polylysine, heparin, basic fibroblast growth factor and fibronectin were well integrated into transected rat spinal cord. The construct interacted with the host cells, which provided guidance cues for axonal growth and regeneration and promoted angiogenesis (Alves-Sampaio, García-Rama et al. 2016).

2.4 Interaction of scaffolds with NSPCs

As described before, either the transplantation of NSPCs or the implantation of scaffolds are strategies that lead to improved spinal cord regeneration at some extent. However, using scaffolds seeded with NSCs, improved the axonal regeneration in rat SCI model (Olson, Rooney et al. 2009). Therefore, combining a 3D scaffold with NSCs as a therapeutic approach for SCI, can conduct to better results for spinal cord regeneration, as these structures should support the stem cells, guiding their migration, while supporting phenotype maintenance.

2.4.1 *In vitro* studies

The cell behavior is regulated by cell-matrix and cell-cell interactions. The interactions between the scaffolds and the NSPCs have been evaluated to get a cell-scaffold construct that maximizes spinal cord regeneration (Table 2.1). The scaffolds, mainly hydrogels and guiding tubular structures, had a 3D porous macrostructures to support the NSPCs, which ameliorated the communication between cells compared to flat 2D structures (Wang, Ao et al. 2010).

In general, the 3D porous scaffolds made of synthetic polymers such as polyethylene glycol (PEG) and PLGA and natural polymers such as collagen, gelatin, hyaluronic acid and chitosan owns the ability to support the adhesion, proliferation and differentiation of NPSCs into the three neural lineages by adjusting the culture medium composition with specific growth factors and/or others biomolecules.

The scaffolds should create the appropriate environment to induce the neuronal differentiation, because in the SCI the NSCs without any support or stimulation spontaneously differentiate mainly into astrocytes. Therefore, the scaffolds were designed with bioactive molecules to induce the differentiation of NSPCs into functional neurons. Hydrogels from xyloglucan functionalized with poly-D-lysine (PDL) (Nisbet, Moses et al. 2009), from methacrylamide chitosan immobilized with biotin rat interferon γ (Leipzig, Wylie et al. 2011), from PuraMatrix modified with two short peptide sequences, one derived from laminin and the other

from bone marrow homing, and from PEG modified with adhesive peptide ligands (Zustiak, Pubill et al. 2013) induced the differentiation of NSCs into neurons. In addition, collagen scaffolds functionalized with EGRF not only induce the neuronal differentiation but also inhibited the unwanted astrocytic differentiation (Li, Xiao et al. 2013). Recently, a collagen porous scaffold modified with three neurotrophic factors (BDNF, NT3 and basic fibroblast growth factor – bFGF) and two neutralizing proteins (Epha4LBD and PlexinB1LBD), all modified with a collagen biding domain, induced the differentiation of NSCs into functional mature neurons and had a neuroprotective effect in the presence of myelin derived inhibitory molecules (Li, Liu et al. 2016).

The scaffold itself, free of biomolecules, can control the cellular differentiation. Scaffolds from chitosan (Wang, Ao et al. 2010) or gelatin (Saglam, Perets et al. 2013) with longitudinal oriented microchannels stimulated the neuronal differentiation and also increased the neurites alignment and outgrowth. Furthermore, scaffolds from poly(3,4-ehylenedioxythiophene) doped with PEG, with high conductance (higher than 10^{-4} S/cm^2), induced the differentiation of NSCs and P19 pluripotent embryonic carcinoma cells into neurons due to the downregulation of the Akt signaling pathway and the increase in expression of dual oxidase 1 (Ostrakhovitch, Byers et al. 2012). Moreover, the elastic modulus of the scaffolds can also influence the NSCs differentiation. Thus, soft laminin-coated methacrylamide chitosan hydrogels with elasticity less than 1 kPa (Leipzig and Shoichet 2009) and alginate hydrogels with low elastic modulus (Banerjee, Arha et al. 2009) induced the neuronal differentiation of NSCs. The stiffness of the material regulates the cytoskeletal organization and consequently, the intracellular signaling events, such as the increased activation of the mechanotransductive Rho GTPases (Keung, de Juan-Pardo et al. 2011).

When the NSCs were transfected with vectors carrying the tropomyosin receptor kinase C (TrkC) gene and NT-3 gene, the PLGA macroporous rods provide the right environment to support the differentiation of those cells into functional neurons, that established connections between them and exhibited synaptic activity (Xiong, Zeng et al. 2009). Moreover, the gelatin sponges also supported the differentiation of NSCs carrying the TrkC gene into functional neurons but in the presence of Schwann cells transfected with vectors carrying the NT-3 gene (Lai, Wang et al. 2013). Therefore, the modification of the stem cells rather than the scaffolds was another approach to induce the neuronal differentiation. Neuritogenesis can also be improved using the co-culture of NSCs with endothelial cells in a 3D porous scaffold from gelatin (Saglam, Perets et al. 2013) or in a hydrogel from fibrin with hyaluronic acid and laminin (Arulmoli, Wright et al. 2016).

Table 2.1 – Interaction of 3D scaffolds from different polymers with NSPCs from different sources.

Material	Processing Technique	Seeded cell type	Additional factors	Cells – final state	Reference
Collagen	Gel forming	Embryonic rat NSPCs	bFGF	Cells survive, proliferate and differentiate in neurons	(Ma, Fitzgerald et al. 2004)
Collagen and type I-hyaluronan	Matrix of blended polymers	Adult mice NSPCs	mitogens epidermal growth factor (EGF) and fibroblast growth factor-2 (FGF-2)	Proliferation and differentiation in neurons, astrocytes, and oligodendrocytes	(Brännvall, Bergman et al. 2007)
Collagen	Print hydrogel	C17.2 (immortalized neural progenitor cell line)	Vascular endothelial growth factor (VEGF)-releasing fibrin gel	Cell survival to print and migrated and proliferated	(Lee, Polio et al. 2010)
Collagen and chitosan	Membranes	Spinal cord rat derived NSCs - neurospheres	EGF, bFGF	Cells survive, migrate, and differentiate into astrocytes, neurons and oligodendrocytes. The differentiated cells are also supported by the membrane	(Yang, Mo et al. 2010)
Collagen and heparan sulfate proteoglycan (HPSG)	Freeze-drying porous tubes	Primary rat NSCs	bFGF (from HPSG)	NSCs adhesion and proliferation	(Wang, Zhou et al. 2012)
Collagen chemically conjugated with cetuximab (EGFR antagonist)	Freeze-drying	Rat NPCs	B27 supplement	Scaffold support cells proliferation; promote neuronal differentiation while decrease the differentiation in astrocytes	(Li, Xiao et al. 2013)
Collagen	Freeze-drying (Porous scaffold)	Rat NSCs (from telencephalon of newborn rats)	Scaffolds functionalized with three neurotrophic factors (BDNF, NT3 and bFGF) and two neutralizing proteins (Epha4LBD and PlexinB1LBD), Culture medium with 2% B27 and myelin	NSCs differentiated into functional mature neurons into the functionalized scaffolds that had neuroprotective effects, even in the presence of myelin derived inhibitory molecules.	(Li, Liu et al. 2016)
Gelatin	Gel forming	Human NSCs	Basic fibroblast growth factor (bFGF)	Support adhesion and growth and differentiation in neurons	(Chen, Chiou et al. 2006)
Gelatin	Sponges	Rat NSCs and Schwann cells	NSCs and SCs transfected with vectors carrying TrkC gene and NT-3 gene, respectively	NSCs differentiated into neurons with the capacity to form structural and functional connections with each other	(Lai, Wang et al. 2013)
Gelatin crosslinked with genipin	3D porous scaffold with longitudinal oriented microchannels (freeze-drying technique)	PC12 pheochromocytoma cells; and endothelial cells (co-culture)	NGF	Promote neurite alignment and outgrowth (even without NGF); Without endothelial cells neuritogenesis was not observed	(Saglam, Perets et al. 2013)

Material	Processing Technique	Seeded cell type	Additional factors	Cells – final state	Reference
Chitosan	Films, porous scaffold and multimicrotubule conduit	Rat Embryonic NSCs	Fetal bovine serum (FBS)	Multimicrotubule conduit provide a better neuronal differentiation	(Wang, Ao et al. 2010)
Chitosan	Carriers	Rat spinal cord derived- NSC	NT-3	Support survival, proliferation and induce neuronal differentiation with a reduced quantity of NT3	(Yang, Duan et al. 2010)
Methacrylamide chitosan	Photocrosslinkable hydrogel with different elastic modulus	NSCs from forebrain of adult rats	L-glutamin; Scaffolds coated with laminin	Hydrogels with elasticity less than 1 kPa induced the neuronal differentiation	(Leipzig and Shoichet 2009)
Methacrylamide chitosan	Photocrosslinkable hydrogel	NSCs from forebrain of adult rats	Immobilization of biotin- rat interferon-γ	Differentiation in neurons (lineage specificity)	(Leipzig, Wylie et al. 2011)
Methacrylamide chitosan, perfluorocarbons	Hydrogel	NSCs from forebrain of adult rats	recombinant interferon-γ	Support neuronal differentiation due to the controlled oxygen uptake through perfluorocarbons	(Li, Wijekoon et al. 2013)
Hyaluronic acid	Hydrogel modified with Nogo receptor antibody	Rat fetal pups primary NSCs	Retinoic acid	Support NSCs and differentiation in neurons and glial cells	(Pan, Ren et al. 2009)
Hyaluronic acid and fibroin	Hydrogel (produced by freeze-drying)	Embryonic rat NSCs	EGF, bFGF	Migration and adhesion of NSCs	(Ren, Zhou et al. 2009)
Hyaluronic acid, fibrin and laminin	Hydrogel	Human NSCs (from cerebral cortices of brains) Human cord blood-derived endothelial cells	Neuronal differentiation media with 2% B27, 20 ng/mL BDNF and GDNF and 0.5 µM dibutyryl acidic adenosine monophosphate	NSCs proliferated and differentiated into the scaffolds, express integrins that bound to fibrinogen or laminin The co-culture with endothelial cells increased the vascularization	(Arulmoli, Wright et al. 2016)
Xyloglucan	Termoresponsive hydrogel	Embryonic mice NSCs	Immobilization of poly-D-lysine	Neuronal survival, differentiation and neurite extension	(Nisbet, Moses et al. 2009)
Alginate	hydrogel with different elastic modulus	NSCs from hippocampi of adult rats	N2 supplement, FGF-2	NSCs encapsulated into the hydrogel with low Young modulus induced better neuronal differentiation	(Banerjee, Arha et al. 2009)
PuraMatrix	Hydrogel matrix modified with short peptide sequences (based on bone marrow homing factor and laminin)	Human NPCs	Epidermal fibroblast growth factor (eFGF), bFGF	Differentiation in neurons, with lower number of apoptotic and necrotic neuronal cells	(Liedmann, Frech et al. 2012)
Recombinant spider silk	Films and foams uncoated or coated with poly-L-ornithine and fibronectin	Rat NSCs	Bone morphogenic protein (BMP4), Wnt3a	Scaffolds supported proliferation and neuronal differentiation, reduced differentiation into oligodendrocytes	(Lewicka, Hermanson et al. 2012)
PEG	Hydrogel	Rat NSCs	FGF-2	Cells survive, proliferate and differentiate in neurons and glia	(Mahoney and Anseth 2006)

Material	Processing Technique	Seeded cell type	Additional factors	Cells – final state	Reference
PEG and poly(3,4-ehylenedioxy thiophene) (PEDOT)	Films	Primary NSCs from post-natal mouse brains; P19 pluripotent embryonic carcinoma cells		Differentiation of both cell types into neurons due to the downregulation of the Akt signaling pathway and the increase in expression of dual oxidase 1	(Ostrakhovitch, Byers et al. 2012)
PEG with peptide ligands	Hydrogel (placed over a collagen coated coverslip)	PC12 cells (encapsulated in the hydrogel)	NGF	The hydrolytic degradation release the cells from the hydrogel that proliferate and differentiate into neurons (due to the peptide ligands)	(Zustiak, Pubill et al. 2013)
PLGA	Macroporous rods produced by thermally induced phase separation	Rat pups NSCs	NSCs transfected with NT-3 or its receptor TrkC gene	Differentiation in neurons, establish connections, exhibit synaptic activity	(Xiong, Zeng et al. 2009)
Poly(3-hydroxybutyrate-co-3-hydroxyvalerate)	Microspheres produced by emulsion-solvent-evaporation technique	Embryonic mouse NSCs	Microspheres coated with PLL; Brain derived neurotrophic factor (BDNF)	Differentiation in neurons (with low levels of maturation)	(Chen and Tong 2012)

2.4.2 *In vivo* studies

Scaffolds with NSPCs were implanted in rat and/or mice *in vivo* SCI models, to evaluate the interaction of cell-scaffold constructs with the host tissue. Hydrogels have been widely studied for spinal cord injury repair because they can be directly injected into the lesion site and gel in situ, making those scaffolds less invasive. Hydrogels had beneficial effects in axonal recovery; however, they provided low mechanical support and impaired the infiltration and survival of cells inside their structure. Several reviews have discussed the role of the hydrogels as a vehicle for cell transplantation in spinal cord regeneration (Nomura, Tator et al. 2006; Willerth and Sakiyama-Elbert 2007; Zhong and Bellamkonda 2008; Madigan, McMahon et al. 2009).

Porous sponges and multichannel scaffolds from either natural or synthetic polymers were appropriate vehicles for NSPCs allowing their survival and differentiation in *in vivo* SCI animal models. Scaffolds from PLGA, with an inner part with macroporous structure and an outer part with oriented structure, seeded with NSCs reduced the tissue loss and the glial scar, promoting functional recovery at some extent (Teng, Lavik et al. 2002). A chitosan tubular construct with NSCs bridge the lesion site, connecting the transected cord stumps with integration of host neurons (Zahir, Nomura et al. 2008). Collagen porous scaffolds with oriented pores and NSCs aligned the reparative tissue with the direction of the spinal cord, reducing the formation of fluid-filled cysts and preventing the collapse of musculature and connective tissue into the lesion site (Cholas, Hsu et al. 2012). The same scaffold functionalized with an epidermal growth factor receptor (cetuximab) improved the functional recovery (Li, Xiao et al. 2013). Recently, NSCs in a

collagen porous scaffold modified with three neurotrophic factors (BDNF, NT3 and bFGF) and two neutralizing proteins (Epha4LBD and PlexinB1LBD), all modified with a collagen biding domain, stimulated the endogenous neurogenesis in the lesion and improve the hosted NSCs survival and differentiation into motor and sensory neurons, which can establish synapsis between them and the host neurons (Li, Liu et al. 2016).

Scaffolds with both NSCs and Schwann cells induced spinal cord functional recovery due to the presence of Schwann cells, which released neurotrophic factors to promote survival and axonal regeneration of injured neurons (Chen, Hu et al. 2010). Using those cells but transfected with adenoviral vectors carrying TrkC gene and NT-3 gene into gelatin sponges, created a suitable environment to form a neural network derived from the NSCs that was well integrated into the host neuronal network, which is a way to conduct signals from the brain to the hindlimbs, providing the functional recovery (Lai, Wang et al. 2013) and also increasing the remyelination (Lai, Wang et al. 2013). Ensheathing the gelatin sponges with a thin PLGA film formed a tubular structure, which improved the axonal regeneration, the synaptogenesis and the locomotor function, and decrease the injury site cavity (Du, Zeng et al. 2015). The NT-3 embedded into a tubular scaffold from a block copolymer of poly(Ɛ-caprolactone)-block-poly(l-lactic acid-co-Ɛ-caprolactone) coated with silk fibroin instead of using genetically modified NSCs also promoted functional recovery and axonal regeneration (Tang, Liao et al. 2014).

2.5 Role of scaffold topography in stem cell differentiation

In the last years, the emergence of the nanotechnology/microtechnology allowed the manipulation of the materials at nanometric/micrometric scale. At the submicron scale the scaffolds can be designed to resemble many of the topographical features of the ECM, closely interacting with the cells and influencing their behavior.

The ECM is a fibrous acellular matrix of molecules, which confer structural support to the surrounding cells and modulates cellular activities such as migration, proliferation, differentiation, gene expression and secretion of growth factors. The ECM forms a highly structured local microenvironment that allows the transport of oxygen and nutrients and the removal of waste products, allowing cellular metabolism and communication (Lim and Mao 2009; Zhao, Tan et al. 2012). The ECM of the CNS has a composition different from the ECM in most tissues of the body. In the CNS, the interstitial matrix contains small quantities of fibrillar proteins and glycoproteins. Instead, they are formed by a network of proteoglycans, hyaluronan, tenascins and link proteins, which act not only as the mechanical support to the tissue but also as the scaffold during development of adult neurogenesis (Zimmermann and Dours-Zimmermann 2008). In addition, the soma and dendrites of the neuronal cell are surrounded by a high-density ECM aggregates named perineuronal nets. In their niches, the NSCs were also surrounded by ECM and closely interact with it by expressing adhesion molecules (Bond, Ming et al. 2015).

As the cells sense the scaffolds characteristics at nano/micro-scale level – as an artificial ECM, mechanical signals are generated and translated by intracellular signaling pathways, regulating the genomic expression and the cell fate. This mechanism is called mechanotransduction and integrins and focal adhesions take an important role on it (Figure 2.3) (Lutolf and Hubbell 2005). The integrins mediate the adhesion of the cell to the ECM. When integrins are bounded both conformation and affinity are changed, resulting in integrin clustering and immature focal complexes formation. The focal complexes bind to actin linker proteins, which result in stress fiber formation and increase focal adhesion site and cytoskeletal tension (McMurray, Dalby et al. 2014). The integrin clustering depends on the sensed topography and stiffness, and activate specific signaling pathways important for cellular function (migration, proliferation and differentiation) (Gjorevski and Nelson 2009). Focal adhesions link the actin cytoskeleton to the transmembrane integrins, experiencing forces that actin exerts on the adhesion sites, which varied with the sensed topography and stiffness and resulted in alterations in the cellular differentiation (McMurray, Dalby et al. 2014). The structural organization of the nucleus and gene and protein expression are also influenced by topographical factors (Teo, Ankam et al. 2010). The biophysical signals are transduced to the nucleus by soluble regulatory factors through nuclear pores (Yim and Sheetz 2012).

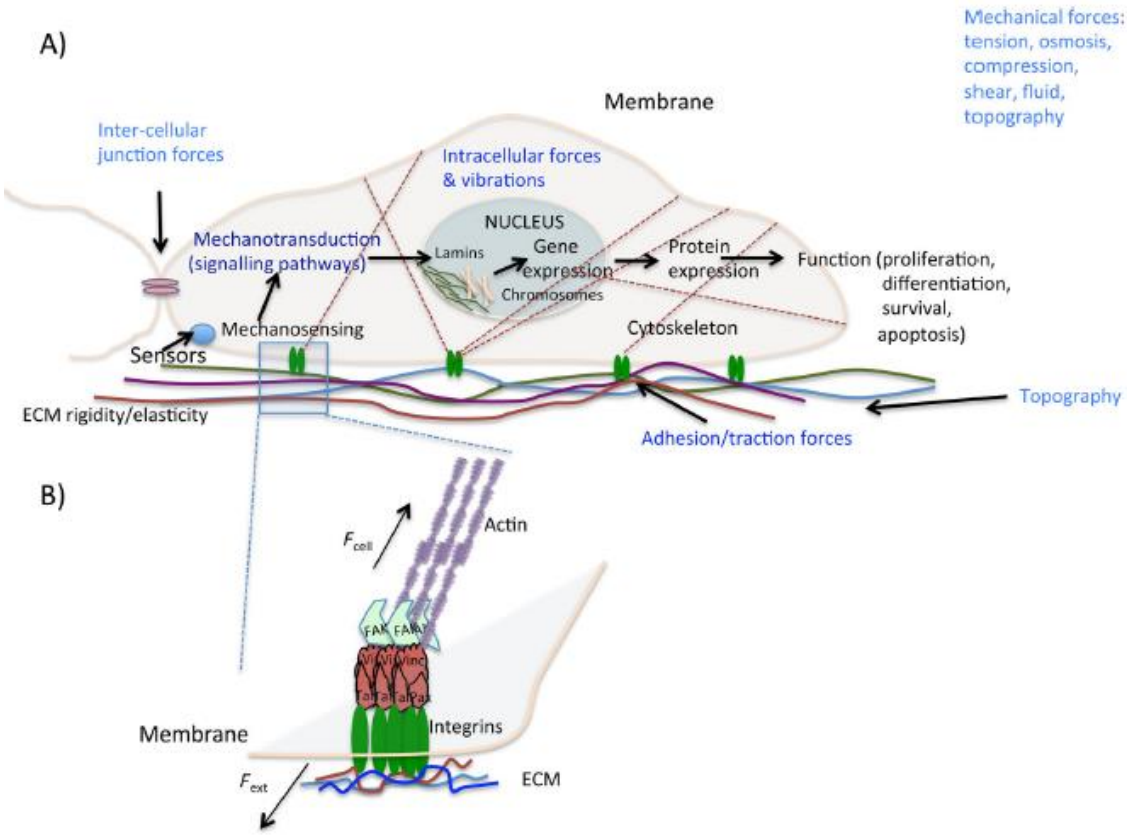

Figure 2.3 – Cells mechanosensors are stimulated by external mechanical forces. (A) Multiple forces activated the signaling pathways, modulating the gene expression, and consequently, protein expression and cellular functions. (B) Focal adhesion experiencing the balance of the external (F_{ext}) and internal forces (F_{cell}) in driving stress at a mechanosensor (reproduced with the permission of McMurray 2014)

The lack of a functional ECM at the lesion site is one of the causes that impair the regeneration of the SCI because the cells (either transplanted or from the host) require a functional ECM to survive and functionally integrate into the tissue (He, Wang et al. 2012; Purcell, Naim et al. 2012). Therefore, a scaffold that mimic the ECM of the NSCs niche will support the NSCs and guide their behavior inside the injury and, consequently, will assist the proper spinal cord regeneration.

2.5.1 Nano/micro-scale scaffolds

Techniques such as, peptide self-assembly, phase separation, lithography and nanoimprinting and electrospinning can modify/produce substrates with nano/micro-scale topographies to guide the NSCs behavior.

2.5.2 Self-assembly nanofibers

Self-assembly technique allows the production of nanofibers from custom-designed peptide-like amphiphiles that spontaneously assemble and organize by using positive and negative L-amino acids (Ellis-Behnke, Liang et al. 2009). Excellent control over the substrate chemistry and the nanoscale features of the resulting fibers are attractive characteristics of this technique. However, it is a very time consuming and expensive technique due to the difficulty in the optimization of the design, structure and stability of the peptide sequences (Rim, Shin et al. 2013).

2.5.2.1 Interaction of NSCs with self-assembly peptide nanofibers and SCI treatment

3D hydrogels of nanofibers formed by self-assembly of peptide amphiphilic molecules were designed to interact with NPCs. The Ac-(Asp-Ala-Asp-Ala)4-$CONH_2$ – RADA-16 is a synthetic amphiphilic peptide of 16 aminoacids that could self-assemble in a well-defined nanofiber structure (~10 nm) and form a 3D hydrogel. Self-assembled structures from this peptide sequence can be easily functionalized with cell adhesion and differentiation motifs, which are better substrates for NSCs than the self-assembled hydrogels without modification. The different motifs such as, functional motifs from bone marrow homing peptides – SKPPGTSS, bone marrow homing peptides – PFSSTKT and fibronectin – arginylglycylaspartic acid (RGD) (Koutsopoulos and Zhang 2012); neural cell adhesion molecule – derived mimetic peptide SIDRVEPYSSTAQ (FRM) (Zou, Liu et al. 2014); motif from neural cell adhesion molecule AcN-EVYVVAENQQGKSKA-$CONH_2$ (FGL) (Wang, Zheng et al. 2015) and clyco-RGD (Gao, Tao et

al. 2017) were used to functionalize the RADA-16 peptide, improving the proliferation and differentiation of NSCs into progenitor neural cells, neurons, astrocytes and oligodendrocytes.

RADA-16 peptide self-assembled nanofiber hydrogels were seeded with NSPCs and implanted in transected rat spinal cord, which supported the migration of host cells, the growth of blood vessels and axons into the scaffolds, providing a true three-dimensional environment for the migration of living cells (Guo, Su et al. 2007). However, encapsulation of the NSCs on the self-assembled peptide nanofiber hydrogels enhanced the survival and differentiation of NSPCs for longer periods (Koutsopoulos and Zhang 2013), which improved the functional recovery or injured rats relatively to hydrogels seeded with NSPCs (Ye, Qin et al. 2016). The encapsulation of NSCs into RADA16 functionalized with RGD and neurite-promoting laminin epitope – amino acid sequence Ile-Lys-Val-Ala-Val (IKVAV) self-assembled peptides survived whereas in RADA16 without modification the cells hardly survived, they also support the differentiation into neurons and astrocytes (Sun, Li et al. 2016).

Other peptide self-assembly nanofibers and motifs were evaluated in the interaction with NSCs. The nanofibers made of four Ala and three Gly residues with a hydrophobic alkyl tail, were functionalized with the IKVAV epitope, which induced faster differentiation of NSCs into neurons, while discouraged the development of astrocytes when compared to laminin or the soluble peptides (Silva, Czeisler et al. 2004). The application of those nanofiber hydrogels into a rat SCI model, conducted to the reduction of astrogliosis and cell death and increased the number of oligodendroglia and the regeneration of both descending and ascending fibers in the lesion site (Tysseling-Mattiace, Sahni et al. 2008).

Self-assembled peptides from LDLK-12 peptide, functionalized with the KLPGWSG sequence which is found in proteins and is responsible for stem cell maintenance an differentiation, was organized into a nanoconstructed hydrogel that supported the *in vitro* differentiation of murine NSCs (from albino mice) (Caprini, Silva et al. 2013). Moreover, the hydrogels with lower stiffness, comparable to the soft tissues, enhanced the neuronal differentiation (Caprini, Silva et al. 2013). Changing the mechanical properties of the hydrogels from silk-fibroin self-assembled nanofibers to ~5 kPa was sufficient to induce the neuronal differentiation without biochemical factors (Bai, Zhang et al. 2014).

Self-assembled peptide molecules $K_2(QL)_6K_2$ (QL6), which attenuate inflammation and glial scar, associated with NSPCs and implanted *in vivo* SCI rat models promoted superior NSCs survival, higher neuronal and oligodendrocyte differentiation, reduction of inflammation and increased in the synaptic activity in the newly formed neurons inside the lesion site, resulting in the recovery of locomotor function at some extent (Iwasaki, Wilcox et al. 2014; Zweckberger, Ahuja et al. 2016).

The self-assembly peptide nanofibrous hydrogels mimic the ECM 3D environment to easily integrate the host tissue and regenerate the tissue. The mechanisms of proliferation and differentiation inside the self-assembly peptide is not truly understand, therefore more research is needed to find the best structure and properties to the neural tissue engineering.

2.5.3 Phase separation fibrillar structures

Phase separation is a technique that renders foam materials that can have a fibrillar structure. It is a simple technique on which the polymer is dissolved in a suitable solvent and rapidly cooled to induce phase separation. Then, the solvent is replaced by water and the construct is freeze-dried, originating a structured material. However, the choice of the appropriate solvent to induce phase separation is a difficult task and this technique is limited to a few polymers (Rim, Shin et al. 2013). Therefore, this technique was not widely used in the construction of scaffolds for spinal cord treatment. However, due to the nanofibrous structure, which resemble the natural ECM, poly (L-lactic acid) (PLLA) (Yang, Murugan et al. 2004) and Polyhydroxyalkanoates (Xu, Li et al. 2010) nanofibrous scaffolds produced by thermal-induced phase separation supported the adhesion and neuronal differentiation of NSCs and induced the neurites outgrowth.

2.5.4 Lithographic patterned substrates

Lithographic technique allow the construction of a variety of topographies with controlled surface geometry. First, a pattern is created and exposed through light, ions, and electrons or imprinted. Then, lithography is done in a polymer or suitable material, which can be used as a mask to pattern other subtracts or used as the final product. Soft lithography is the most diffused lithographic technique to create a master pattern on which an elastomeric material is cast (typically, poly(dimethylsiloxane) (PDMS)). The resulting elastomeric material is cured and can be used as the final substrate or can be used to pattern another surfaces or as a mold to cast other polymers (Purcell, Naim et al. 2012).

2.5.4.1 Interaction of NSCs with surfaces patterned with lithography and SCI treatment

Different pattern arrays (ridges, grooves, pits) with controlled dimension and alignment produced with lithographic techniques can be used to control the NSCs adhesion, proliferation and differentiation. Especial attention has been given to the topographical cues that induce better neuronal differentiation and the axonal extension and elongation.

At the microscale level, PDMS substrates with grooves width between 10 and 20 µm, pre-coated with PLL and laminin, induced both neuronal differentiation of NSCs and the alignment of the forming neurites (Béduer, Vieu et al. 2012). Likewise, silica wafers with other patterns, linear micro-pattern and circular micro-pattern with 10 and 2 µm width and coated with laminin, increased the neuronal differentiation of NSCs and reduced the differentiation in astrocytes compared to the dot micro-pattern. Furthermore, the cell body and the branches followed the direction of the patterns. The topographical cues activated the mitogen-activated protein

kinase/extracellular signaling-regulated kinase (MAPK/ERK) pathway, inducing the neuronal differentiation (Qi, Li et al. 2013). The anisotropic grooved micropatterns were preferred to induce the alignment of the neural cells.

At nanoscale, PU acrylate patterned substrates (treated with oxygen plasma) with anisotropic grooves and isotropic pillar patterns were produced with different dimensions. NSCs differentiate better into the neuronal lineage on the anisotropic grooves with 300 nm, while glial differentiation was higher on isotropic patterns with 300 nm. Both nanopatterns, improved the focal adhesion formation and stimulated the focal adhesion kinase (FAK) signaling pathway in NSCs, when compared to flat substrates (Yang, Jung et al. 2013). The same trend was observed when nanogrooves substrates from PLGA coated with 3,4-dihydroxy-L-phenylalanine (DOPA) to improve the immobilization of PLL and fibronectin proteins on the surface of the patterns were tested with human NSCs. The cells aligned along the nanogrooved pattern, improving the neuronal differentiation, which can be increased by the addition of NGF (Yang, Park et al. 2015). Therefore, anisotropic patterned substrates in the nanoscale were better to induce neuronal differentiation of NSCs while isotropic patterns were favorable to induce the differentiation into astrocytes.

The combined effect of hierarchical pattern with both micropatterns (microgroove patterns with 1.5 µm groove size) and nanopatterns (nanopores with 10 nm diameter) were suitable substrates to induce NSCs alignment, elongation and differentiation into functional neurons in detriment of astrocytes. The presence of the nanoporous pattern brought advantages to NSCs culture, promoting higher expression of focal adhesion proteins in NSCs, which contributed to enhanced neuronal differentiation (Yang, Jung et al. 2014). Nano-roughness graphene oxide (height: ~10 nm) was patterned using photolithography with microgrooves of 5 µm. The hierarchical topographical cues enhanced the differentiation of human NSCs into functional neurons, even without the addition of chemical agents to induce the neurogenesis (Yang, Lee et al. 2016). Recently, (Geisel, Clasohm et al. 2016) copied the microstructures with controlled topography (lines and grids) produced with photolithography and etching to bacterial cellulose, changing their self-oriented fibers structures. In the valleys areas, where random bacterial cellulose fibers are still found, the neurons and glial cells can differentiate and follow the microstructures (Geisel, Clasohm et al. 2016). The microstructures led to cell guidance while nanoscale features influence the differentiation of neurospheres derived from postnatal subventricular zone. The ability to use a natural polymer prevented the use of other coatings and/or surface modifications to enhance the cell adhesion. In addition, the natural nano-fibrillar structure of the cellulose was an advantage to induce the neuronal differentiation of NSCs together with the guidance cues provided by the microstructured pattern. This study opens new opportunities to use other polymers in lithographic techniques.

2.5.5 Carbon-based nanomaterials

The carbon nanotubes (CNTs) have very interesting properties, including electrical and thermal conductivity and high flexibility and tensile strength. As referred before, NSCs react to electrical stimulus leading to improved cell behavior. Therefore, CNTs can be used alone improving the expansion of more neuronal fibers and higher growth cones activity in contact with spinal cord explants (Fabbro, Villari et al. 2012) and supporting the NSCs proliferation and differentiation (Kam, Jan et al. 2008). CNT-polyelectrolyte thin films assembled with layer-by-layer also support the culture of NSCs. The cells can be differentiated into the three neural types (neurons, astrocytes, oligodendrocytes) and the neurites were extended along the substrate, similarly to the control poly-L-ornithine (Jan and Kotov 2007). When the CNTs were integrated into polymeric scaffolds and implanted into SCI rat model, they improved the axonal repair and regeneration into the lesion cavity with modest functional recovery (Roman, Niedzielko et al. 2011). Likewise, the combination of CNTs with Nafion (sulfonated tetrafluorethylene-based tetrafluoroethylene copolymer) and their implantation into transection SCI rat model improved the number of neuronal fibers on the lesion, which resulted in hindlimb locomotor recovery (Imani, Zagari et al. 2016).

Graphene structures have excellent electrical, mechanical and optical properties and have been investigated as substrates for NSCs. Graphene foams were able to electrically stimulate the proliferation and differentiation in defined lineages of NSCs (Li, Zhang et al. 2013). Different hybrid structures using graphene in several forms and other materials such as, arrays of graphene with silica nanoparticles (Solanki, Chueng et al. 2013), graphene nanogrids on a SiO_2 matrix with TiO_2 nanoparticles (Akhavan and Ghaderi 2013), PCL nanofibers with graphene oxide (Shah, Yin et al. 2014) and PEDOT combined with graphene oxide nanosheets (Weaver and Cui 2015) were evaluated as substrates for NSCs. Those hybrids induced better neuronal differentiation of human NSCs and guided the orientation of the differentiated cells. In addition, the structures can also control the differentiation of NSCs into oligodendrocytes.

Recently, Akhavan and colleagues have shown that the reduced graphene oxide nanomeshes were better cell substrates to human NSCs, compared to graphene oxide sheets. The nanosheets induced superior neuronal differentiation, due to the low-energy photoelectrons of the reduced graphene state (Akhavan, Ghaderi et al. 2015). By rolling the reduced graphene oxide foams to get 3D conductive structures, Akhavan verified that the human NSCs can freely go through the pores and interfaces of the structure and, when electrically stimulated, induced superior proliferation and neuronal differentiation (Akhavan, Ghaderi et al. 2016).

2.5.6 Electrospinning

Electrospinning is a simple and cost effective technique that is easy to use, versatile and allows the production of nano/microfibrous matrices from several polymeric solutions with controlled fiber diameter and orientation (Sill and von Recum 2008). The obtained mats have high

porosity, interconnectivity, and unique mechanical properties, resembling the hierarchical structure of the ECM. Therefore, they have been used as subtracts for cell adhesion, proliferation and differentiation, creating an appropriate environment for the diffusion of nutrients and waste products in order to maintain the cellular metabolism. The principal drawback pointed out to this technique is their recognition as a two dimensional and not as a 3D scaffold, due to the small fiber diameter and inter-fiber distance. The reduced pore size impaired the cell penetration on the mats and the vascularization process required in the formation of new tissue (Kai, Jin et al. 2013). Although in most cases the cells do not migrate into the scaffold, the fibrous mesh is still different from a 2D flat surface, since the cells receive nutrients and growth factors three-dimensionally. Strategies such as the dissolution of salts into the polymeric solution or co-electrospun the desired polymeric solution with a sacrificial polymer created pores through the nanofibrous meshes after leaching out the sacrificial salts or polymeric fibers, respectively (Rim, Shin et al. 2013). The treatment of the fiber meshes with aminolysis also improve the penetration of the cells into electrospun fibrous mats (Nisbet, Forsythe et al. 2009).

The electrospinning technique was patented by Formhals in 1934 (Anton 1934) but just recently was used to fabricate scaffolds for tissue engineering applications. The electrospinning setup, depicted in the Figure 2.4, comprises a syringe pump to control the flow rate of the polymer solution held in a syringe that is attached to a needle, a high voltage power supply to stretch the polymeric solution and a grounded collector to collect the fibers. During the electrospinning process (Henriques, Vidinha et al. 2009), a positive high voltage is applied to the needle, establishing an electric field between the needle tip and the grounded collector. Under an electrical field strong enough to overcome the solution surface tension, the drop solution at the needle tip acquires a conical shape, named Taylor Cone (Taylor 1969), and a jet is forced to flow from the tip of the Taylor Cone to the grounded collector. While the jet is travelling, the solvent evaporates and the fibers are deposited in the grounded collector at a settled distance from the needle tip. Typically, a stationary planar target is used to collect the fibers with a random orientation. However, fibers with preferential alignment can be obtained using different collector configurations such as a rotatory mandrel rotating at high rotation speed, parallel electrodes or a rotating disk (Murugan and Ramakrishna 2007).

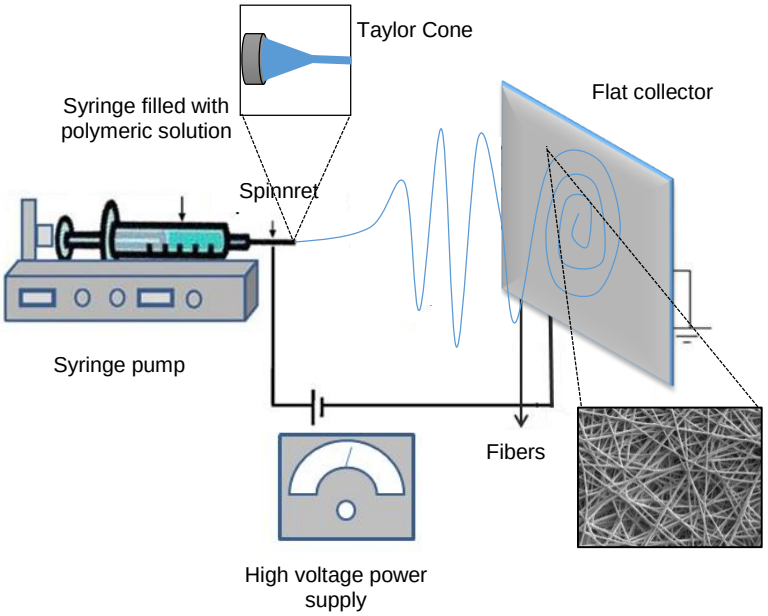

Figure 2.4 – Scheme of the electrospinning setup.

In the electrospinning technique a number of parameters can be adjusted to control the characteristics of the fibers. Those include the intrinsic characteristics of the polymeric solution (concentration, viscosity, surface tension, conductivity and type of solvent), the setup parameters (applied voltage, polymer flow rate, distance between the needle tip and the collector and needle size) and the environmental conditions.

A solution to be electrospinnable should be from a polymer with high molecular weight enough to promote chain entanglement and fiber formation. The polymer concentration in the solution must be adjusted; high concentrations can impart the electrospinning by preventing the jet stretching due to the high solution viscosity while solutions with low concentrations had low solution viscosity and high surface tension, resulting in fibers with beads (Luo, Nangrejo et al. 2010). However, the viscosity and other parameters such as the conductivity and the surface tension also depends on the solvent used in the dissolution of the polymer. Solvents with high dielectric constant, density, boiling point and conductivity reduces the solution viscosity and carry high amounts of charges that electrostatically repel each other, enhancing the continuous stretching of the jet and resulting in fibers with small diameter. On the opposite, less conductive solvents with lower dielectric constant, density and boiling point increase the solution viscosity, resulting in higher diameter fibers (Wannatong, Sirivat et al. 2004; Uyar and Besenbacher 2008).

The influence of each setup parameters on the final fibers morphology is strictly related to the other settled parameters. High solution flow rates resulted in fibers with higher diameter (and mat pore size) since more solution is transferred in the same period of time. However, with high flow rates the solvent cannot properly evaporate before the fibers reach the collector and thus, the fibers can have beaded defects and/or a fused morphology (Bhardwaj and Kundu 2010). Nevertheless, those problems can be circumvented by increasing the distance between the needle tip and the ground collector, increasing the time for solvent evaporation and reducing the diameter of the fibers because of the longer fiber stretching (Khil, Cha et al. 2003). As the distance

between the needle tip and the collector increased, the applied voltage should also increase to maintain the electric field. However, increasing the applied voltage decrease the time of flight of the fiber jet contributing to superior fiber diameters but also increase the electrostatic repulsion inside the jet leading to better stretching and resulting fibers with small diameter (Kidoaki, Kwon et al. 2006).

Environmental factors such as humidity, temperature and air velocity also influence the electrospinning process and the final fibers morphology. High humidity can lead to the formation of pores in the fibers surface, resulting from the absorption of water molecules entrapped on the jet (Casper, Stephens et al. 2004). On the other hand, low humidity can accelerate the solvent evaporation rate preventing the fibers to reach the collector and, consequently, the electrospinning process. High temperatures increase the drying rate of the solvent and the conductivity of the solution, improving the electrospinning process (De Vrieze, Van Camp et al. 2009). Small variations on the air velocity affect the fiber jet resulting in different fiber surface morphologies (Xu, Xu et al. 2011).

A detailed description of the influence of the electrospinning parameters on the fibers morphology can be found in the review from (Murugan and Ramakrishna 2007).

2.5.6.1 **Electrospun fibers in spinal cord regeneration**

The electrospun fibrous mats can be rolled into conduits providing the appropriate physical supports to fill in the injury site and bridge the lesion but also contain the topographical signals essential to provide contact guidance to host cells infiltration and axonal outgrowth for SCI. Conduits from electrospun PLLA aligned microfibers facilitated the infiltration of the host tissue on a thoracic spinal cord gap, which was fully closed after 4 weeks and composed by regenerating axons and glial cells (Hurtado, Cregg et al. 2011). The scaffold guided the tissue regeneration without the administration of cells and biomolecules. PLGA electrospun nanofibers with a different design, a bilayer structure with an inner layer of aligned nanofibers and an outer layer of random nanofibers, were loaded with the rolipram drug (enhance cAMP activity in neurons and suppress inflammatory response) to bridge the lesion site of rats with hemisection lesions. The scaffold increased the axonal growth and angiogenesis as well as decreased the astrocytes and the inhibitory environment in the lesion (Zhu, Wang et al. 2010). 3D spiral constructs from electrospun collagen nanofibers supported extensive cellular penetration, prevented the astrocyte accumulation and supported neural fiber sprouting in a rat hemi-section SCI model (Liu, Houle et al. 2012). The electrospinning system with an air gap collector separated by projecting piers was used to create a tubular scaffold from aligned polydioxinone fibers embedded with alginate beads that are encapsulated with NGF and ChABC. The construct implanted into a hemisection spinal cord rat model supported the vascularization and the axonal regeneration, improving the functional recovery (Colello, Chow et al. 2016). Aligned poly (caprolactone-*co*-ethyl ethylene phosphate) electrospun nanofibers incorporated into a collagen scaffolds formed a hybrid construct able to guide neurite extension, support new vessels formation and integrate well into

the host tissue of rats with hemi-section SCI model (Milbreta, Nguyen et al. 2016). However, the functional recovery was not significant compared to the animals with injuries and without scaffolds. Therefore, the same scaffold was encapsulated with NT3 and miR-22 (that control the local protein synthesis at distal axons), providing not only topographical but also biochemical cues, reducing the excessive inflammatory response and the scar tissue formation in the hemi-sected rats (Nguyen, Gao et al. 2017). However, no functional tests were performed.

2.5.6.2 **Neuronal cell's interaction with electrospun fibrous mats**

Polymeric nano/microfibrous matrices produced by electrospinning closely resemble the topography of the CNS ECM, providing the right guidance cues to the neural/neuronal cells. The electrospun fibrous substrates increased the neuritogenesis and neurite outgrowth of rat spinal cord motor neurons compared to thin films without any topographical cue (Gertz, Leach et al. 2010). Several *in vitro* and *in vivo* studies have explored the use of the electrospun mats to support and guide the development of embryonic neurons as well as the regenerating neurons. Those studies are briefly summarized in Table 2.2.

In neurons, the neurite growth cone at the tip of the axon regulates neurite outgrowth and sense the guidance cues. The nanofibers interact intimately with the growth cone, providing the contact guidance signals to induce the axonal growth (Nisbet, Forsythe et al. 2009). Nanofibrous scaffolds with aligned morphology oriented the neurite outgrowth exactly parallel to the nanofiber axis (Corey, Gertz et al. 2008; Xie, MacEwan et al. 2009). This is an important cue in SCI regeneration, since neurites can reach longer distances from one end to the other of the lesion site (Meiners, Ahmed et al. 2007; Hurtado, Cregg et al. 2011). On the opposite, the misalignment of fibers prevent neurite outgrowth, which delay the axonal extension from one end to the other of the injury, delaying the regeneration process (Wang, Mullins et al. 2008). However, fiber density, surface chemistry and surface properties of the fibrous matrices can have stronger influence than the fiber alignment and the neurites cannot align along the fibers direction (Xie, Liu et al. 2014). In regions with high fiber density, the neurites perfectly align perpendicular to the fiber alignment with in lower densities the fibers neurites follow the fiber alignment, increasing the neurite outgrowth. However, in high density fibers coated with laminin the neurites also extend in the direction of the fiber alignment.

The presence of ECM proteins such as laminin can thus improve the neurite outgrowth. The increased immobilization of laminin on electrospun fibrous mats conducted to superior neurite outgrowth of neuron-like PC12 cells (Zander, Orlicki et al. 2012). The FGF-2 growth factor, which is important in neurogenesis, also conducted to superior neurite outgrowth and axonal extension of rat dorsal root ganglia when immobilized on polyamide nanofibers (Delgado-Rivera, Harris et al. 2009). Collagen nanofibers can adsorb NT-3 and chABC factors, which were controlled release, resulting in superior neurite extension of rat dorsal root ganglia depending on the NT-3 concentration (Liu, Xu et al. 2012).

Another topographical signal that influence the neuronal behavior is the diameter of the fibers. PLLA aligned fibers with smaller diameter (300 nm) impaired neurite outgrowth while larger fibers (700 and 1300 nm) increased their growth (Wang, Mullins et al. 2010). On the opposite, silk fibroin fibers with 400 nm diameter were better substrates for neurite outgrowth of rat cortical neurons relative to fibers with 800 nm and 1200 nm diameters (Qu, Wang et al. 2013). Better neurite outgrowth and the formation of a 3D neuronal network was observed in PU fibers with similar diameter ranges (450 nm) (Puschmann, de Pablo et al. 2014). Although the contradictory results, the chemical structure of the polymer as well as the alignment degree of the fibers were different between the studies, making it difficult to compare the results and define the better diameters range for neurite outgrowth. However, fiber diameters in the range of 400 – 700 nm could be the preferred choice to increase the neurite outgrowth, instead of microfibers or nanofibers with smaller diameters (< 300 nm).

Therefore, fibers with aligned morphology, diameters ranging from 400 nm to 700 nm and a surface presenting ECM proteins or growth factors seems to be appropriate substrates for neuritogenesis and neurite outgrowth.

Table 2.2 – Effects of the electrospun nanofibers on nerve cells.

Material/ scaffold	Nerve cell type	Additional factors	Effects on cells	Reference
PLLA (aligned nanofibers)	Primary motor and sensory neurons (from rat spinal cord)	Coating substrates with PLL and collagen I for motor and sensory neurons, respectively	Directed neurite outgrowth in fiber direction	(Corey, Gertz et al. 2008)
PLLA (aligned nanofibers)	Chicks primary dorsal root ganglia; rat Schwann cells	Coating substrates with PLL	Guided neurite outgrowth in fiber direction; Schwann cells grew along the aligned fibers	(Wang, Mullins et al. 2008)
PLLA (nanofibers vs. films)	Rat spinal cord primary motor neurons	Coating substrates with PLL	Nanofibers accelerated the neuritogenesis and major neurite growth while restricted dendritic maturation and soma spreading	(Gertz, Leach et al. 2010)
PLLA (aligned nanofibers with diameters: 300, 700, and 1300 nm)	Rat dorsal root ganglia and Schwann cells		Higher neurite alignment on fibers with superior diameter and densely packed	(Wang, Mullins et al. 2010)
PCL (aligned nanofibers)	Embryonic chicks primary dorsal root ganglia	Coating fibers with laminin	Neurites preferential extended along the long axis of nanofiber matrice; Increased guidance with laminin	(Xie, MacEwan et al. 2009)
PCL (nanofibers surface modified)	Neuron-like PC12 cells	Covalent attachment of laminin	Neurite outgrowth increase with the increase of the attached laminin	(Zander, Orlicki et al. 2012)
PCL (aligned nanofibers – fiber density, and surface chemistry)	Chick dorsal root ganglion	Coated with poly-L-lysine (PLL) and laminin	Neurites grew parallel to the fiber alignment or perpendicular to it if the fibers were not coated with laminin or coated with PEG	(Xie, Liu et al. 2014)
Polydioxanone nanofibers (aligned vs. random)	Rat dorsal root ganglia; rat astrocytes	Coating substrates with PLL	Both neurites and astrocytes aligned in the direction of the electrospun fibers; Neurites grew more robustly and extended longer processes when co-cultured with astrocytes	(Chow, Simpson et al. 2007)
Polyamide (nanofibers surface modified)	Rat dorsal root ganglia and non-reactive astrocytes	Fibers covalently modified with FGF-2	Higher neurite outgrowth and axonal extension in nanofibers with FGF-2 modification	(Delgado-Rivera, Harris et al. 2009)
Polyurethane (nanofibers with diameters: 450 nm, 1350 nm, 2500 nm)	Mice embryonic hippocampus neurons (Co-culture with astrocytes)	Fibers coated with poly-D-lysine;	Neurite outgrowth was superior in fibers with 450 nm diameter while the astrocytes were less proliferative	(Puschman n, de Pablo et al. 2014)
Collagen nanofibers (aligned vs. random)	Prymary rat astrocytes and dorsal root ganglia neurons		Aligned nanofibers directed the orientation of neurites and astrocytes; In randomly oriented fibers the astrocytes spared radially	(Liu, Houle et al. 2012)
Collagen (nanofibers as drug delivery system)	Rat dorsal root ganglia	Incorporation of NT-3 and chABC in fibers	The neurite extension was increased depending on the NT-3 concentration loaded on the fibers	(Liu, Xu et al. 2012)
Silk fibroin (nanofibers with diameters: 400 nm, 800 nm, 1200 nm)	Prymary rat dorsal root ganglia neurons and astrocytes		Smaller diameter fibers induced better development and maturation of neurons	(Qu, Wang et al. 2013)

2.5.6.3 The influence of fibrous mats on NSPCs

Electrospun fibers were better substrates than flat surfaces for the proliferation and neuronal differentiation of human spinal cord-derived NPCs. Moreover, the differentiated neurons on the fibrous substrates showed improved synaptic maturation involving the β-integrins-ERK1/2-Synapsin pathway (Yin, Huang et al. 2014). Therefore, the resulting functional neurons can help to restore the communication through the SCI, guiding the regeneration.

The fibrous substrates were also able to support the differentiation of other stem cell types into the neural lineage such as, human ESC (Xie, Willerth et al. 2009; Lam, Patel et al. 2010; Mahairaki, Lim et al. 2010; Cherry, Carlson et al. 2012; Wang, Ye et al. 2012; Abbasi, Hashemi et al. 2015), iPSCs (Mohtaram, Ko et al. 2014) and MSCs from bone (Cho, Choi et al. 2010), adipose tissue (Guo, Liu et al. 2015) endometrium (Ebrahimi-Barough, Javidan et al. 2014) and human umbilical cord (Yao, Liu et al. 2016). In the last study human umbilical cord-derived MSCs differentiated into neural and neuronal lineage in aligned fibrillar fibrin hydrogel fabricated using electrospinning and simultaneous molecular self-assembly without soluble inductor factors, just with the combined effect of the aligned morphology and the lower elastic modulus.

However, as NSPCS are the focus of this project, the effect of topographical cues (alignment and fiber diameter) and the chemical groups at the surface of the fibrous mats on the NSPCs will be described in detail hereafter.

2.5.6.3.1 *Fiber alignment and/or diameter*

The aligned electropun nanofibrous affected the behavior of NSPCs (Table 2.3). The underlying aligned fibers provide directionality to the NSPCs. Therefore, fibers with high alignment degree increased the proliferation of spinal cord derived NPCs (Wang, Yao et al. 2011; Zhou, Sui et al. 2013) and also induced superior neuronal differentiation by upregulating the Wnt/β-catenin pathway in adult NSCs (Lim, Liu et al. 2010). The differentiated neurons extend and elongate following the direction of the fiber axis (Yang, Murugan et al. 2005; Ghasemi-Mobarakeh, Prabhakaran et al. 2008). However, (Lins, Wianny et al. 2016) verified that the proliferation and glial differentiation of NSCs were superior in non-aligned fibers when compared to the aligned ones due to the difficulty of the cells to migrate and interact with each other. The alignment was only favorable to induce the neuronal differentiation and to guide the neuronal cells along the fiber alignment.

The interaction of NSCs with the fibrous mats can be optimized by adjusting the fibers diameter (Table 2.3). PLLA aligned nanofibers (300 nm) improved the NSCs differentiation into neurons relatively to the microfibers (1.5 µm) (Yang, Murugan et al. 2005). Likewise, the effect of PLLA aligned fibers with precise diameters ranges (307 ± 47, 500 ± 53, 679 ± 72 and 917 ± 84) on C17.2 cells were studied. The fibers of intermediate diameters (500 ± 53 nm) were better substrates to support the adhesion and proliferation of cells. The neuronal differentiation was also improved on this diameter range as well as the neurite outgrowth (He, Liao et al. 2010). Lim et al. also verified improved neuronal differentiation of rat hippocampal-derived NSCs using PCL

electrospun nanofibers with intermediate diameters (~480 nm) regarding smaller (~260 nm) and larger (~930 nm) diameter fibers (Lim, Liu et al. 2010). Although without an aligned morphology, the relationship between the fiber diameter and the neural differentiation in each one of the three neural lineages (neurons, astrocytes and oligodendrocytes) was investigated by Christopherson et al. Electrospun polyethersulfone (PES) fiber meshes with smaller diameter fibers (around 300 nm) differentiated the rat hippocampus-derived adult NSCs preferentially into oligodendrocytes while larger fibers (around 750 nm) differentiated the into the neuronal lineage in the presence of retinoic acid. The cells were able to spread in all directions on small diameter fibers, acquiring a glial-like morphology. On the opposite, in larger fibers the neurites were restricted to spread along a single fiber favoring the neuronal differentiation (Christopherson, Song et al. 2009).

Aligned fibers with diameters ranging from 500 to 700 nm were also suitable to induce the neuronal differentiation of olfactory ensheathing cells (Kueh, Li et al. 2012) and hESC-derived neurospheres (Kueh, Li et al. 2012; Wang, Ye et al. 2012).

Therefore, the fibrous mats with an aligned morphology and diameters around 500 nm were suitable substrates for NSCs proliferation as well as to induce the neuronal differentiation and to increase the neurite extension. However, the synthetic polymeric fibers were always covered with adhesion proteins such as laminin, which are required in the culture of NSCs, to evaluate the effect of the fibers topography on NSCs and exclude the effects of the chemical structure of the substrate.

Table 2.3 – Effects of the nanofibers alignment and diameter on the NSCs behavior.

Polymer/fiber characteristics	Stem cell	Additional factors	Stem cell fate	Reference
Alignment				
PCL and gelatin (aligned)	Neonatal mouse cerebellum C17.2 stem cells	N2 supplement	Cell proliferation and elongation; Neurite outgrowth parallel to the direction of the fiber alignment	(Ghasemi-Mobarakeh, Prabhakaran et al. 2008)
Collagen Type I (Aligned and randomly oriented)	Neonatal rats Spinal cord derived NSCs	EGF, bFGF, heparin	Faster expansion on aligned nanofibers; Activation of β1 integrin/MAPK pathway enhance cell proliferation	(Wang, Yao et al. 2011)
Collagen Type I (aligned and random orientation)	Rat spinal cord-derived NSCs	FBS	Nanofibers increased the proliferation rate, particularly on the aligned fibers, and inhibited apoptosis through changes in gene expression	(Zhou, Sui et al. 2013)
Poly(vinylidene) (PVDF) (different alignment degrees)	Monkey NSCs	Neuronal differentiation: N2 supplement, B27 and FGF2 Glial differentiation: FBS (without neuronal factors)	Superior growth and proliferation in non-aligned fibers as well as glial differentiation Differentiation into neuronal cells was superior in fibers with a middle degree of alignment but neuronal cells were guided along the fiber axis on highly-aligned fibers (difficulty of glial cells to migrate and interact with other cells)	(Lins, Wianny et al. 2016)
Diameter				
PLLA (aligned microfibers - 1500 nm and nanofibers – 300 nm)	Neonatal mouse cerebellum C17.2 stem cells	N-2 supplement	NSCs differentiated into neurons on nanofibers and neurite outgrowth along the fiber direction	(Yang, Murugan et al. 2005)
PLLA aligned fibers with different diameters (307 ± 47, 500 ± 53, 679 ± 72 and 917 ± 84)	Neonatal mouse cerebellum C17.2 cells	N2 supplement	The aligned fibers of 500 nm supported the adhesion and proliferation and neuronal differentiation of cells and increase the neurite outgrowth	(He, Liao et al. 2010)
Polyethersulfone (PES) fiber with different diameters (300, 750 and 1450 nm)	rat hippocampus-derived adult NSCs	Fibers coated with laminin; Retinoic acid	Fibers with 300 nm differentiated preferentially into oligodendrocytes while fibers with 750 nm differentiated into the neuronal lineage	(Christopherson, Song et al. 2009)
PCL (aligned and randomly oriented morphology; different diameters: 260, 480 and 930 nm)	Adult NSCs	Retinoic acid; FBS Fibers coated with laminin and polyornithine	Enhanced neuronal differentiation on aligned nanofibers with ; regulating the Wnt/β-catenin pathway in adult NSCs; neurites extend and elongate in the direction of the fiber axis	(Lim, Liu et al. 2010)

2.5.6.3.2 *Topography and functionalization*

Although the importance of the topography of the electrospun fibers on NSCs proliferation and differentiation, the functionalization of the fibers, adding biochemical cues, help to regulate the NSCs behavior (Table 2.4). Aligned PCL fibers aminolized and functionalized with BDNF, enhanced the proliferation of the NSCs and neuronal differentiation but not impaired the glial differentiation (Horne, Nisbet et al. 2009). Coating PLCL fibers with poly(norepinephrine) to attach collagen also increased the PC12 cells proliferation and their differentiation into neurons, with

superior extension and number of neurites (Taskin, Xu et al. 2015). The immobilization of RE-1 silencing transcriptional factor (REST) small interference RNA (siRNA) (gene delivery vector) on the PCL nanofibers surface via polydopamine coating, increased the NSCs differentiation into functional neurons while reduced their differentiation into astrocytes, when compared to the PCL film also immobilized with REST (Low, Rujitanaroj et al. 2013).

Similar to the electrospinning technique, the “spinneret based tunable engineered parameters” (STEP) technology (use a metal micropipette and without an electrical field) was used in the production of polystyrene nanofibers with aligned configuration (one layer) and crosshatch (double layer) configuration (Bakhru, Nain et al. 2011). The scaffolds were functionalized with poly-L-ornithine and laminin and NSCs were seeded on them. The cells presented a polarized morphology and follow the alignment of the fibers, differentiating mainly into neurons. However, cells were also seeded in a planar structure in close proximity to the cells on the fibers. The cells on the planar structure were also differentiated into the neuronal lineage, suggesting that a paracrine effect influenced the cells near to the ones on the fibers (Bakhru, Nain et al. 2011).

However, neurotrophic factors such as BDNF can also be encapsulated in the electrospun nanofibibers (from a copolymer of Ɛ-caprolactone and ethyl ethylene phosphate) (Low, Rujitanaroj et al. 2013). The controlled release of BDNF associated with the topographical cues of the scaffolds induced superior neuronal differentiation of mouse NSCs. The incorporation of molecules such as retinoic acid and purmorphamine on the gelatin outer shell, on fibers with a core-shell structure produced using co-axial electrospinning, enhanced the differentiation of NSCs into motor neurons and improved the neurite extension (Binan, Tendey et al. 2014).

The own polymer used to construct the fibrous scaffolds also influenced the cell behavior. The functional groups of collagen can interact with β1 integrin and activate MAPK signaling cascade on the neonatal rat spinal cord derived NSCs, enhancing the cell proliferation (Wang, Yao et al. 2011). Even without the aligned morphology, the fibrous scaffolds from chitosan were a better choice for the NSCs proliferation and neuronal differentiation when compared to fibers from either cellulose acetate or polyethersulfone (Du, Tan et al. 2014), reinforcing the importance to choose the appropriate polymer to produce the electrospun mats for NSCs interaction.

Therefore, the combinatorial effects of nanostructure of the scaffolds and the biochemical cues from the neurotrophic factors or other molecules are important in driving the NSPCs behavior. Even with that, additional factors must be added to the culture medium to promote the suitable cell maintenance (EGF, bFGF, FGF2) and to induce the neuronal (retinoic acid, N2 supplement) and the glial (FBS) differentiation.

Table 2.4 – Effects of the nanofibers functionalization on the NSCs behavior.

Polymer/fiber characteristics	Stem cell	Additional factors	Stem cell fate	Reference
Surface Functionalization				
PCL (3D non-woven scaffolds chemically modified with ethylamine – amine functionalization)	Adult rat brain-derived NSCs	FBS;	Increased the adhesion and spreading over all the scaffold NSCs differentiate primarily into oligodendrocytes in the presence of FBS	(Nisbet, Yu et al. 2008)
PCL (aligned vs random scaffolds aminolyzed and functionalized with BDNF)	Embryonic mice NSCs	EGF, FGF2	Enhance NSC proliferation; direct cell fate towards neuronal and oligodendrocyte specification	(Horne, Nisbet et al. 2009)
PCL nanofibers (immobilization with REST-siRNA)	Mice hippocampus-derived NSCs	N-2 supplement; B27; FGF2;	Improved the NSCs differentiation into functional neurons while reduced their differentiation into astrocytes	(Low, Rujitanaroj et al. 2013)
Polystyrene (highly aligned single and double layer crosshatch meshes – functionalized with poly-L-ornithine and laminin), STEP technology	Rat hippocampal NSCs	FGF2	Highly aligned fibers induced the neuronal NSCs differentiation and cellular polarization and elongation along the fiber alignment; NSCs on the fibers caused a paracrine signaling effect on near NSCs on planar surfaces, inducing their neuronal differentiation	(Bakhru, Nain et al. 2011)
Silica nanofibers (amino-functionalized with (3-aminoprpyl)trimethoxysilane)	Rat neural stem cells	N2 supplement, EGF, bFGF	Functionalized silica fibers improved the NSCs proliferation and neuronal maturation regarding PDL-coated flat substrates	(Chen, Hsieh et al. 2013)
Poly(lactic acid-*co*-caprolactone) (PLCL) (aligned and random orientation – coated with poly(norepinephrine) to attach collagen)	PC12 cells (derived from rat adrenal pheochromocytoma)	Attach collagen localize NGF from the culture medium	Cells proliferate and differentiate on the substrate and the alignment of neurites was verified on aligned topography with higher extension and neurites numbers	(Taskin, Xu et al. 2015)
Encapsulation of factors				
Copolymer of Ɛ-caprolactone and ethyl ethylene phosphate electrospun fibers	Mouse NSCs	Fibers loaded with BDNF and/or retinoic acid	Improved the differentiation of NSCs	(Low, Rujitanaroj et al. 2013)
PLLA (core) and gelatin (shell) (co-electrospun fibers)	Engineered neural stem-like cells	Gelatin shell loaded with retinoic acid and purmorphamine	Cells proliferate and differentiate into motor neurons; enhanced neurite outgrowth of the resulting neurons	(Binan, Tendey et al. 2014)
Polymer choice				
Chitosan, cellulose acetate and polyethersulfone electrospun fibers	PC12 cells and human NSC (from America Type Culture Collection)	B27, Leukemia inhibitory factor, fibers coated with collagen	Better NSCs proliferation ad neuronal differentiation in chitosan nanofibers	(Du, Tan et al. 2014)

2.5.6.3.3 *Conductivity*

Fibrous mats with conductive materials/polymers in their structure can provide electrical stimulation to NSCs (Table 2.5). The conducting polymer polyaniline was used to dope the electrospun nanofibers from PCL/gelatin blends (Ghasemi-Mobarakeh, Prabhakaran et al. 2009) or it was blended with PLLA and the resulting solutions were electrospun into fibrous substrates

(Prabhakaran, Ghasemi-Mobarakeh et al. 2011). In both cases, the presence of polyaniline on the scaffolds improved the proliferation and neuronal differentiation of NSCs and induced the neurite outgrowth under electrical stimulation. Electropun mats from polyaniline blended with poly[(L-lactide)-*co*-(Ɛ-caprolactone)] (PLCL) also provide better PC12 cell survival, differentiation and neurite extension compared to the PLCL fibers alone (Bhang, Jeong et al. 2012).

Another conducting polymer – polypyrrole – was deposited on electrospun PLGA nanofibers (Lee, Bashur et al. 2009) or polymerized on the surface of electrospun PLLA nanofibers (Zou, Qin et al. 2016), increasing the differentiation of PC12 cells and improving the neurite outgrowth along the fiber direction.

Electrospun nanofibers from conducting polymers such as piezoelectric polyvinylidene fluoride-trifluoroethylene (Lee, Collins et al. 2010) and poly(o-methoxyaniline) (Yeh, Dai et al. 2013), also induced the differentiation of NSCs into neurons and promoted the neurite extension. Although the apparent advantages of using conducting polymers as substrates for NSCs, the lack of degradability and toxicity issues are still a concern. The use of minimal amounts of conductive polymers and their combination with natural and/or synthetic biodegradable polymers is thus recommended. Furthermore, alterations in the structure of the conductive polymers to reduce the toxicity and maintain the electrical properties are another studied approach.

Table 2.5 - Effects of the nanofibers conductivity on the NSCs behavior.

Polymer/fiber characteristics	Stem cell	Additional factors	Stem cell fate	Reference
PCL/gelatin nanofibers doped with a polyaniline	NSCs	N2 supplement	Electrical stimulation improved the cell proliferation and the neurite outgrowth	(Ghasemi-Mobarakeh, Prabhakaran et al. 2009)
PLLA/polyaniline nanofibers	Rat nerve stem cells C17.2	N2 supplement	Electrical stimulation induced the neuronal differentiation and neurite outgrowth	(Prabhakaran, Ghasemi-Mobarakeh et al. 2011)
PLCL/polyaniline nanofibers	PC12 cells	N2 supplement	Electrical stimulation increase cell survival, differentiation and neurite extension	(Bhang, Jeong et al. 2012)
PLGA aligned or random nanofibers coated with polypyrrole	PC12 cells	NGF	Electrical stimulation increase the neurite length and more neurite formation, which was superior in aligned fibers	(Lee, Bashur et al. 2009)
PLLA aligned fibers coated with polypyrrole polymerized in the fibers	PC12 cells	NGF Substrates incubated with collagen type-I and laminin	With electrical stimulation longer neurite outgrowth and the neurites stretch along the fiber axis direction	(Zou, Qin et al. 2016)
Piezoelectric polyvinylidene fluoride-trifluoroethylene nanofibers	Human fetal brain-derived NSPCs	BDNF	Higher piezoelectricity induced superior neuronal differentition	(Lee, Collins et al. 2010)
Poly(o-methoxyaniline) nanofibers	NSCs from brains of rat embryos	EGF, bFGF, N2 supplement	Support the attachment, growth and differentiation of the cells (better that PDL coated glass substrates)	(Yeh, Dai et al. 2013)

2.6 References

Abbasi, N., S. M. Hashemi, et al. (2015). "Influence of oriented nanofibrous PCL scaffolds on quantitative gene expression during neural differentiation of mouse embryonic stem cells." Journal of Biomedical Materials Research Part A **104**(1): 155-164.

Akhavan, O. and E. Ghaderi (2013). "Differentiation of human neural stem cells into neural networks on graphene nanogrids." Journal of Materials Chemistry B **1**(45): 6291-6301.

Akhavan, O., E. Ghaderi, et al. (2015). "Near infrared laser stimulation of human neural stem cells into neurons on graphene nanomesh semiconductors." Colloids and Surfaces B: Biointerfaces **126**: 313-321.

Akhavan, O., E. Ghaderi, et al. (2016). "Rolled graphene oxide foams as three-dimensional scaffolds for growth of neural fibers using electrical stimulation of stem cells." Carbon **97**: 71-77.

Alvarez-Mejia, L., J. Morales, et al. (2015). "Functional recovery in spinal cord injured rats using polypyrrole/iodine implants and treadmill training." Journal of Materials Science: Materials in Medicine **26**(7): 1-11.

Alves-Sampaio, A., C. García-Rama, et al. (2016). "Biofunctionalized PEDOT-coated microfibers for the treatment of spinal cord injury." Biomaterials **89**: 98-113.

Anton, F. (1934). Process and apparatus for preparing artificial threads, Google Patents.

Arulmoli, J., H. J. Wright, et al. (2016). "Combination scaffolds of salmon fibrin, hyaluronic acid, and laminin for human neural stem cell and vascular tissue engineering." Acta biomaterialia **43**: 122-138.

Bagdi, K., K. Molná, et al. (2011). "Specific interactions, structure and properties in segmented polyurethane elastomers." eXPRESS Polym Lett **5**: 417.

Bai, S., W. Zhang, et al. (2014). "Silk nanofiber hydrogels with tunable modulus to regulate nerve stem cell fate." Journal of Materials Chemistry B **2**(38): 6590-6600.

Bakhru, S., A. S. Nain, et al. (2011). "Direct and cell signaling-based, geometry-induced neuronal differentiation of neural stem cells." Integrative Biology **3**(12): 1207-1214.

Banerjee, A., M. Arha, et al. (2009). "The influence of hydrogel modulus on the proliferation and differentiation of encapsulated neural stem cells." Biomaterials **30**(27): 4695-4699.

Béduer, A., C. Vieu, et al. (2012). "Engineering of adult human neural stem cells differentiation through surface micropatterning." Biomaterials **33**(2): 504-514.

Benson, M. D., M. I. Romero, et al. (2005). "Ephrin-B3 is a myelin-based inhibitor of neurite outgrowth." Proceedings of the national academy of sciences of the United States of America **102**(30): 10694-10699.

Bhang, S. H., S. I. Jeong, et al. (2012). "Electroactive Electrospun Polyaniline/Poly [(L-lactide)-co-(ε-caprolactone)] Fibers for Control of Neural Cell Function." Macromolecular bioscience **12**(3): 402-411.

Bhardwaj, N. and S. C. Kundu (2010). "Electrospinning: a fascinating fiber fabrication technique." Biotechnology Advances **28**(3): 325-347.

Binan, L., C. Tendey, et al. (2014). "Differentiation of neuronal stem cells into motor neurons using electrospun poly-l-lactic acid/gelatin scaffold." Biomaterials **35**(2): 664-674.

Blesch, A. and M. H. Tuszynski (2009). "Spinal cord injury: plasticity, regeneration and the challenge of translational drug development." Trends in neurosciences **32**(1): 41-47.

Bond, A. M., G.-l. Ming, et al. (2015). "Adult mammalian neural stem cells and neurogenesis: five decades later." Cell stem cell **17**(4): 385-395.

Bonner, J. F. and O. Steward (2015). "Repair of spinal cord injury with neuronal relays: From fetal grafts to neural stem cells." Brain research **1619**: 115-123.

Bozkurt, G., A. J. Mothe, et al. (2010). "Chitosan channels containing spinal cord-derived stem/progenitor cells for repair of subacute spinal cord injury in the rat." Neurosurgery **67**(6): 1733-1744.

Bradbury, E. J., L. D. Moon, et al. (2002). "Chondroitinase ABC promotes functional recovery after spinal cord injury." Nature **416**(6881): 636-640.

Brännvall, K., K. Bergman, et al. (2007). "Enhanced neuronal differentiation in a three-dimensional collagen-hyaluronan matrix." Journal of neuroscience research **85**(10): 2138-2146.

Braughler, J. M. and E. D. Hall (1989). "Central nervous systems trauma and stroke: I. Biochemical considerations for oxygen radical formation and lipid peroxidation." Free Radical Biology and Medicine **6**(3): 289-301.

Caprini, A., D. Silva, et al. (2013). "A Novel Bioactive Peptide: Assessing its Activity Over Murine Neural Stem Cells and its Potential for Neural Tissue Engineering." New biotechnology.

Carlberg, B., M. Z. Axell, et al. (2009). "Electrospun polyurethane scaffolds for proliferation and neuronal differentiation of human embryonic stem cells." Biomedical Materials **4**(4): 045004.

Casper, C. L., J. S. Stephens, et al. (2004). "Controlling surface morphology of electrospun polystyrene fibers: effect of humidity and molecular weight in the electrospinning process." Macromolecules **37**(2): 573-578.

Chan-Chan, L., R. Solis-Correa, et al. (2010). "Degradation studies on segmented polyurethanes prepared with HMDI, PCL and different chain extenders." Acta Biomaterialia **6**(6): 2035-2044.

Chan-Chan, L., C. Tkaczyk, et al. (2013). "Characterization and biocompatibility studies of new degradable poly (urea) urethanes prepared with arginine, glycine or aspartic acid as chain extenders." Journal of Materials Science: Materials in Medicine **24**(7): 1733-1744.

Chen, G., Y.-r. Hu, et al. (2010). "Functional recovery following traumatic spinal cord injury mediated by a unique polymer scaffold seeded with neural stem cells and Schwann cells." Chinese Medical Journal (English Edition) **123**(17): 2424.

Chen, W. and Y. W. Tong (2012). "PHBV microspheres as neural tissue engineering scaffold support neuronal cell growth and axon–dendrite polarization." Acta Biomaterialia **8**(2): 540-548.

Chen, W. S., P. H. Hsieh, et al. (2013). "Chemically modified electrospun silica nanofibers for promoting growth and differentiation of neural stem cells." Journal of Materials Chemistry B 9: 1205-1215.

Chen, Y.-W., S.-H. Chiou, et al. (2006). Using gelatin scaffold with coated basic fibroblast growth factor as a transfer system for transplantation of human neural stem cells. Transplantation proceedings, Elsevier **38**(5): 1616-1617.

Cheng, H., Y.-C. Huang, et al. (2007). "Laminin-incorporated nerve conduits made by plasma treatment for repairing spinal cord injury." Biochemical and biophysical research communications **357**(4): 938-944.

Cherry, J., A. Carlson, et al. (2012). "Oriented, Multimeric Biointerfaces of the L1 Cell Adhesion Molecule: An Approach to Enhance Neuronal and Neural Stem Cell Functions on 2-D and 3-D Polymer Substrates." Biointerphases **7**(1-4): 1-16.

Cholas, R. H., H.-P. Hsu, et al. (2012). "The reparative response to cross-linked collagen-based scaffolds in a rat spinal cord gap model." Biomaterials **33**(7): 2050-2059.

Chow, W. N., D. G. Simpson, et al. (2007). "Evaluating neuronal and glial growth on electrospun polarized matrices: bridging the gap in percussive spinal cord injuries." Neuron glia biology **3**(02): 119-126.

Christopherson, G. T., H. Song, et al. (2009). "The influence of fiber diameter of electrospun substrates on neural stem cell differentiation and proliferation." Biomaterials **30**(4): 556-564.

Colello, R. J., W. N. Chow, et al. (2016). "The incorporation of growth factor and chondroitinase ABC into an electrospun scaffold to promote axon regrowth following spinal cord injury." Journal of tissue engineering and regenerative medicine **10**(8): 656-668.

Colombo, G., M. Wirz, et al. (2001). "Driven gait orthosis for improvement of locomotor training in paraplegic patients." Spinal Cord **39**(5): 252-255.

Corey, J. M., C. C. Gertz, et al. (2008). "The design of electrospun PLLA nanofiber scaffolds compatible with serum-free growth of primary motor and sensory neurons." Acta biomaterialia **4**(4): 863-875.

Costa, L. M., J. E. Pereira, et al. (2013). "Rolipram promotes functional recovery after contusive thoracic spinal cord injury in rats." Behavioural brain research **243**: 66-73.

Cruz, G. J., R. Mondragón-Lozano, et al. (2012). "Plasma polypyrrole implants recover motor function in rats after spinal cord transection." Journal of Materials Science: Materials in Medicine **23**(10): 2583-2592.

De Vrieze, S., T. Van Camp, et al. (2009). "The effect of temperature and humidity on electrospinning." Journal of materials science **44**(5): 1357-1362.

Delgado-Rivera, R., S. L. Harris, et al. (2009). "Increased FGF-2 secretion and ability to support neurite outgrowth by astrocytes cultured on polyamide nanofibrillar matrices." Matrix Biology **28**(3): 137-147.

Dinan, B., N. Bhattarai, et al. "Characterization of Chitosan Based Hybrid Nanofiber Scaffolds for Tissue Engineering." Journal of Undergraduate Research in Bioengineering: 33-37.

Du, B. L., X. Zeng, et al. (2015). "Graft of the gelatin sponge scaffold containing genetically-modified neural stem cells promotes cell differentiation, axon regeneration, and functional recovery in rat with spinal cord transection." Journal of Biomedical Materials Research Part A **103**(4): 1533-1545.

Du, J., E. Tan, et al. (2014). "Comparative evaluation of chitosan, cellulose acetate, and polyethersulfone nanofiber scaffolds for neural differentiation." Carbohydrate polymers **99**: 483-490.

Dubendorf, P. (1999). "Spinal cord injury pathophysiology." Critical care nursing quarterly **22**(2): 31-35.

Duncan, I. and R. Hoffman (1997). "Schwann cell invasion of the central nervous system of the myelin mutants." Journal of anatomy **190**(1): 35-49.

Dusart, I. and M. Schwab (1994). "Secondary cell death and the inflammatory reaction after dorsal hemisection of the rat spinal cord." European Journal of Neuroscience **6**(5): 712-724.

Ellis-Behnke, R., Y. Liang, et al. (2009). "Forever young: how to control the elongation, differentiation, and proliferation of cells using nanotechnology." Cell transplantation **18**(9): 1047-1058.

Fabbro, A., A. Villari, et al. (2012). "Spinal cord explants use carbon nanotube interfaces to enhance neurite outgrowth and to fortify synaptic inputs." ACS nano **6**(3): 2041-2055.

Faden, A. I. (1990). "Opioid and nonopioid mechanisms may contribute to dynorphin's pathophysiological actions in spinal cord injury." Annals of neurology **27**(1): 67-74.

Fan, C., X. Li, et al. (2017). "A modified collagen scaffold facilitates endogenous neurogenesis for acute spinal cord injury repair." Acta Biomaterialia **15**(51): 304-316.

Fan, J., H. Zhang, et al. (2011). "Neural regrowth induced by PLGA nerve conduits and neurotrophin-3 in rats with complete spinal cord transection." Journal of Biomedical Materials Research Part B: Applied Biomaterials **97**(2): 271-277.

Fehlings, M., H. Nakashima, et al. (2016). "Rationale, design and critical end points for the Riluzole in Acute Spinal Cord Injury Study (RISCIS): a randomized, double-blinded, placebo-controlled parallel multi-center trial." Spinal Cord **54**(1): 8-15.

Fehlings, M. G., N. Theodore, et al. (2011). "A phase I/IIa clinical trial of a recombinant Rho protein antagonist in acute spinal cord injury." Journal of neurotrauma **28**(5): 787-796.

Fu, H.-L., Y. Hong, et al. (2014). "Collagenase-labile polyurethane urea synthesis and processing into hollow fiber membranes." Biomacromolecules **15**(8): 2924-2932.

Gao, M., H. Tao, et al. (2017). "Functionalized self-assembly polypeptide hydrogel scaffold applied in modulation of neural progenitor cell behavior." Journal of Bioactive and Compatible Polymers **32**(1): 45-60.

Geisel, N., J. Clasohm, et al. (2016). "Microstructured Multilevel Bacterial Cellulose Allows the Guided Growth of Neural Stem Cells." Small **12**(39): 5407-5413.

Gertz, C. C., M. K. Leach, et al. (2010). "Accelerated neuritogenesis and maturation of primary spinal motor neurons in response to nanofibers." Developmental Neurobiology **70**(8): 589-603.

Ghasemi-Mobarakeh, L., M. P. Prabhakaran, et al. (2008). "Electrospun poly(ε-caprolactone)/gelatin nanofibrous scaffolds for nerve tissue engineering." Biomaterials **29**(34): 4532-4539.

Ghasemi-Mobarakeh, L., M. P. Prabhakaran, et al. (2009). "Electrical stimulation of nerve cells using conductive nanofibrous scaffolds for nerve tissue engineering." Tissue Engineering Part A **15**(11): 3605-3619.

Ghosh, A., F. Haiss, et al. (2009). "Rewiring of hindlimb corticospinal neurons after spinal cord injury." Nature neuroscience **13**(1): 97-104.

Gjorevski, N. and C. M. Nelson (2009). "Bidirectional extracellular matrix signaling during tissue morphogenesis." Cytokine & growth factor reviews **20**(5): 459-465.

Goldsmith, H. S., A. Fonseca, et al. (2005). "Spinal cord separation: MRI evidence of healing after omentum–collagen reconstruction." Neurological research **27**(2): 115-123.

GrandPré, T., F. Nakamura, et al. (2000). "Identification of the Nogo inhibitor of axon regeneration as a Reticulon protein." Nature **403**(6768): 439-444.

Guelcher, S. A. (2008). "Biodegradable polyurethanes: synthesis and applications in regenerative medicine." Tissue Engineering Part B: Reviews **14**(1): 3-17.

Guo, J., H. Su, et al. (2007). "Reknitting the injured spinal cord by self-assembling peptide nanofiber scaffold." Nanomedicine: Nanotechnology, Biology and Medicine **3**(4): 311-321.

Hayes, K., A. Blight, et al. (1993). "Preclinical trial of 4-aminopyridine in patients with chronic spinal cord injury." Spinal Cord **31**(4): 216-224.

He, J., X.-M. Wang, et al. (2012). "Scaffolds for central nervous system tissue engineering." Frontiers of Materials Science **6**(1): 1-25.

He, L., S. Liao, et al. (2010). "Synergistic effects of electrospun PLLA fiber dimension and pattern on neonatal mouse cerebellum C17. 2 stem cells." Acta Biomaterialia **6**(8): 2960-2969.

Henriques, C., R. Vidinha, et al. (2009). "A systematic study of solution and processing parameters on nanofiber morphology using a new electrospinning apparatus." Journal of nanoscience and nanotechnology **9**(6): 3535-3545.

Horne, M. K., D. R. Nisbet, et al. (2009). "Three-dimensional nanofibrous scaffolds incorporating immobilized BDNF promote proliferation and differentiation of cortical neural stem cells." Stem cells and development **19**(6): 843-852.

Hsieh, F.-Y., H.-H. Lin, et al. (2015). "3D bioprinting of neural stem cell-laden thermoresponsive biodegradable polyurethane hydrogel and potential in central nervous system repair." Biomaterials **71**: 48-57.

Hulsebosch, C. E. (2002). "Recent advances in pathophysiology and treatment of spinal cord injury." Advances in physiology education **26**(4): 238-255.

Hurtado, A., J. M. Cregg, et al. (2011). "Robust CNS regeneration after complete spinal cord transection using aligned poly-l-lactic acid microfibers." Biomaterials **32**(26): 6068-6079.

Hyun, J. K. and H. W. Kim (2010). "Clinical and experimental advances in regeneration of spinal cord injury." Journal of tissue engineering **1**(1): 650857.

Imani, S., Z. Zagari, et al. (2016). "Functional Recovery of Carbon Nanotube/Nafion Nanocomposite in Rat Model of Spinal Cord Injury." Artificial cells, nanomedicine, and biotechnology **44**(1): 144-149.

Iwasaki, M., J. T. Wilcox, et al. (2014). "Synergistic effects of self-assembling peptide and neural stem/progenitor cells to promote tissue repair and forelimb functional recovery in cervical spinal cord injury." Biomaterials **35**(9): 2617-2629.

Iyer, N. R., T. S. Wilems, et al. (2017). "Stem cells for spinal cord injury: Strategies to inform differentiation and transplantation." Biotechnology and bioengineering **114**(2): 245-259.

Jain, A., Y. T. Kim, et al. (2006). "In situ gelling hydrogels for conformal repair of spinal cord defects, and local delivery of BDNF after spinal cord injury." Biomaterials **27**(3): 497-504.

James, N. D., J. Shea, et al. (2015). "Chondroitinase gene therapy improves upper limb function following cervical contusion injury." Experimental neurology **271**: 131-135.

Jan, E. and N. A. Kotov (2007). "Successful differentiation of mouse neural stem cells on layer-by-layer assembled single-walled carbon nanotube composite." Nano letters **7**(5): 1123-1128.

Kabu, S., Y. Gao, et al. (2015). "Drug delivery, cell-based therapies, and tissue engineering approaches for spinal cord injury." Journal of Controlled Release **219**: 141-154.

Kai, D., G. Jin, et al. (2013). "Electrospun synthetic and natural nanofibers for regenerative medicine and stem cells." Biotechnology Journal **8**(1): 59-72.

Kam, N. W. S., E. Jan, et al. (2008). "Electrical stimulation of neural stem cells mediated by humanized carbon nanotube composite made with extracellular matrix protein." Nano Letters **9**(1): 273-278.

Kaneko, A., A. Matsushita, et al. (2015). "A 3D nanofibrous hydrogel and collagen sponge scaffold promotes locomotor functional recovery, spinal repair, and neuronal regeneration after complete transection of the spinal cord in adult rats." Biomedical Materials **10**(1): 015008.

Keung, A. J., E. M. de Juan-Pardo, et al. (2011). "Rho GTPases mediate the mechanosensitive lineage commitment of neural stem cells." Stem Cells **29**(11): 1886-1897.

Khil, M. S., D. I. Cha, et al. (2003). "Electrospun nanofibrous polyurethane membrane as wound dressing." Journal of Biomedical Materials Research Part B: Applied Biomaterials **67**(2): 675-679.

Kidoaki, S., I. K. Kwon, et al. (2006). "Structural features and mechanical properties of in situ–bonded meshes of segmented polyurethane electrospun from mixed solvents." Journal of Biomedical Materials Research Part B: Applied Biomaterials **76**(1): 219-229.

King, V. R., A. Alovskaya, et al. (2010). "The use of injectable forms of fibrin and fibronectin to support axonal ingrowth after spinal cord injury." Biomaterials **31**(15): 4447-4456.

King, V. R., W. L. Huang, et al. (2006). "Omega-3 fatty acids improve recovery, whereas omega-6 fatty acids worsen outcome, after spinal cord injury in the adult rat." The Journal of neuroscience **26**(17): 4672-4680.

Koutsopoulos, S. and S. Zhang (2013). "Long-term three-dimensional neural tissue cultures in functionalized self-assembling peptide hydrogels, matrigel and collagen I." Acta biomaterialia **9**(2): 5162-5169.

Kubinová, Š., D. Horak, et al. (2011). "Highly superporous cholesterol-modified poly (2-hydroxyethyl methacrylate) scaffolds for spinal cord injury repair." Journal of Biomedical Materials Research Part A **99**(4): 618-629.

Kubinová, Š. and E. Syková (2012). "Biomaterials combined with cell therapy for treatment of spinal cord injury." Regenerative medicine **7**(2): 207-224.

Kueh, J. L.-L., D. Li, et al. (2012). "Directionality and bipolarity of olfactory ensheathing cells on electrospun nanofibers." Nanomedicine **7**(8): 1211-1224.

Kwon, B. K., E. Okon, et al. (2011). "A systematic review of non-invasive pharmacologic neuroprotective treatments for acute spinal cord injury." Journal of neurotrauma **28**(8): 1545-1588.

Lai, B.-Q., J.-M. Wang, et al. (2013). "The integration of NSC-derived and host neural networks after rat spinal cord transection." Biomaterials.

Lai, B.-Q., J.-M. Wang, et al. (2013). "Graft of a tissue-engineered neural scaffold serves as a promising strategy to restore myelination after rat spinal cord transection." Stem cells and development **23**(8): 910-921.

Lam, H. J., S. Patel, et al. (2010). "In vitro regulation of neural differentiation and axon growth by growth factors and bioactive nanofibers." Tissue Engineering Part A **16**(8): 2641-2648.

Lee, J. Y., C. A. Bashur, et al. (2009). "Polypyrrole-coated electrospun PLGA nanofibers for neural tissue applications." Biomaterials **30**(26): 4325-4335.

Lee, Y.-S., G. Collins, et al. (2010). Neural differentiation of human neural stem/progenitor cells on piezoelectric scaffolds. Bioengineering Conference, Proceedings of the 2010 IEEE 36th Annual Northeast, IEEE.

Lee, Y. B., S. Polio, et al. (2010). "Bio-printing of collagen and VEGF-releasing fibrin gel scaffolds for neural stem cell culture." Experimental neurology **223**(2): 645.

Leipzig, N. D. and M. S. Shoichet (2009). "The effect of substrate stiffness on adult neural stem cell behavior." Biomaterials **30**(36): 6867-6878.

Leipzig, N. D., R. G. Wylie, et al. (2011). "Differentiation of neural stem cells in three-dimensional growth factor-immobilized chitosan hydrogel scaffolds." Biomaterials **32**(1): 57-64.

Lewicka, M., O. Hermanson, et al. (2012). "Recombinant spider silk matrices for neural stem cell cultures." Biomaterials **33**(31): 7712-7717.

Li, G., D. Li, et al. (2013). "Alternating block polyurethanes based on PCL and PEG as potential nerve regeneration materials." Journal of Biomedical Materials Research Part A **102**(3): 685-697.

Li, H., A. Wijekoon, et al. (2013). "Encapsulated Neural Stem Cell Neuronal Differentiation in Fluorinated Methacrylamide Chitosan Hydrogels." Annals of biomedical engineering **42**(7): 1456-1469.

Li, N., Q. Zhang, et al. (2013). "Three-dimensional graphene foam as a biocompatible and conductive scaffold for neural stem cells." Scientific reports **3**: 1604.

Li, X., S. Liu, et al. (2016). "Training Neural Stem Cells on Functional Collagen Scaffolds for Severe Spinal Cord Injury Repair." Advanced Functional Materials **26**(32): 5835-5847.

Li, X., Z. Xiao, et al. (2013). "Promotion of neuronal differentiation of neural progenitor cells by using EGFR antibody functionalized collagen scaffolds for spinal cord injury repair." Biomaterials **34**(21): 5107-5116.

Liebscher, T., L. Schnell, et al. (2005). "Nogo-A antibody improves regeneration and locomotion of spinal cord–injured rats." Annals of neurology **58**(5): 706-719.

Liedmann, A., S. Frech, et al. (2012). "Differentiation of Human Neural Progenitor Cells in Functionalized Hydrogel Matrices." BioResearch Open Access **1**(1): 16-24.

Lim, S. H., X. Y. Liu, et al. (2010). "The effect of nanofiber-guided cell alignment on the preferential differentiation of neural stem cells." Biomaterials **31**(34): 9031-9039.

Lim, S. H. and H.-Q. Mao (2009). "Electrospun scaffolds for stem cell engineering." Advanced drug delivery reviews **61**(12): 1084-1096.

Lins, L. C., F. Wianny, et al. (2016). "Effect of polyvinylidene fluoride electrospun fiber orientation on neural stem cell differentiation." Journal of Biomedical Materials Research Part B: Applied Biomaterials **105**(8): 2376-2393.

Liu, T., J. D. Houle, et al. (2012). "Nanofibrous collagen nerve conduits for spinal cord repair." Tissue Engineering Part A **18**(9-10): 1057-1066.

Liu, T., J. Xu, et al. (2012). "Sustained release of neurotrophin-3 and chondroitinase ABC from electrospun collagen nanofiber scaffold for spinal cord injury repair." Journal of Biomedical Materials Research Part A **100**(1): 236-242.

Löw, K., M. Culbertson, et al. (2008). "Netrin-1 is a novel myelin-associated inhibitor to axon growth." The Journal of neuroscience **28**(5): 1099-1108.

Low, W. C., P.-O. Rujitanaroj, et al. (2013). "Nanofibrous scaffold-mediated REST knockdown to enhance neuronal differentiation of stem cells." Biomaterials **34**(14): 3581-3590.

Low, W. C., P.-O. Rujitanaroj, et al. (2013). "Nanofiber-mediated release of retinoic acid and brain-derived neurotrophic factor for enhanced neuronal differentiation of neural progenitor cells." Drug delivery and translational research **5**(2): 89-100.

Lu, P., G. Woodruff, et al. (2014). "Long-distance axonal growth from human induced pluripotent stem cells after spinal cord injury." Neuron **83**(4): 789-796.

Luo, C., M. Nangrejo, et al. (2010). "A novel method of selecting solvents for polymer electrospinning." Polymer **51**(7): 1654-1662.

Lutolf, M. and J. Hubbell (2005). "Synthetic biomaterials as instructive extracellular microenvironments for morphogenesis in tissue engineering." Nature biotechnology **23**(1): 47-55.

Ma, W., W. Fitzgerald, et al. (2004). "CNS stem and progenitor cell differentiation into functional neuronal circuits in three-dimensional collagen gels." Experimental neurology **190**(2): 276-288.

Ma, Z., Y. Hong, et al. (2011). "Biodegradable polyurethane ureas with variable polyester or polycarbonate soft segments: effects of crystallinity, molecular weight, and composition on mechanical properties." Biomacromolecules **12**(9): 3265-3274.

Madigan, N. N., S. McMahon, et al. (2009). "Current tissue engineering and novel therapeutic approaches to axonal regeneration following spinal cord injury using polymer scaffolds." Respiratory physiology & neurobiology **169**(2): 183-199.

Mahairaki, V., S. H. Lim, et al. (2010). "Nanofiber matrices promote the neuronal differentiation of human embryonic stem cell-derived neural precursors in vitro." Tissue Engineering Part A **17**(5-6): 855-863.

Mahoney, M. J. and K. S. Anseth (2006). "Three-dimensional growth and function of neural tissue in degradable polyethylene glycol hydrogels." Biomaterials **27**(10): 2265-2274.

Marcos-Fernández, A., G. A. Abraham, et al. (2006). "Synthesis and characterization of biodegradable non-toxic poly (ester-urethane-urea) s based on poly (ε-caprolactone) and amino acid derivatives." Polymer **47**(3): 785-798.

McDonald, J. W. and C. Sadowsky (2002). "Spinal-cord injury." The Lancet **359**(9304): 417-425.

McMurray, R. J., M. J. Dalby, et al. (2014). "Using biomaterials to study stem cell mechanotransduction, growth and differentiation." Journal of tissue engineering and regenerative medicine.

Meiners, S., I. Ahmed, et al. (2007). "Engineering electrospun nanofibrillar surfaces for spinal cord repair: a discussion." Polymer International **56**(11): 1340-1348.

Milbreta, U., L. H. Nguyen, et al. (2016). "Three-dimensional nanofiber hybrid scaffold directs and enhances axonal regeneration after spinal cord injury." ACS Biomaterials Science & Engineering **2**(8): 1319-1329.

Mohtaram, N. K., J. Ko, et al. (2014). "Electrospun biomaterial scaffolds with varied topographies for neuronal differentiation of human-induced pluripotent stem cells." Journal of Biomedical Materials Research Part A **103**(8): 2591-2601.

Moreau-Fauvarque, C., A. Kumanogoh, et al. (2003). "The transmembrane semaphorin Sema4D/CD100, an inhibitor of axonal growth, is expressed on oligodendrocytes and upregulated after CNS lesion." The Journal of neuroscience **23**(27): 9229-9239.

Mothe, A. J., I. Kulbatski, et al. (2008). "Adult spinal cord stem/progenitor cells transplanted as neurospheres preferentially differentiate into oligodendrocytes in the adult rat spinal cord." Cell Transplantation **17**(7): 735-751.

Mothe, A. J., R. Y. Tam, et al. (2013). "Repair of the injured spinal cord by transplantation of neural stem cells in a hyaluronan-based hydrogel." Biomaterials **34**(15): 3775-3783.

Mothe, A. J. and C. H. Tator (2013). "Review of transplantation of neural stem/progenitor cells for spinal cord injury." International Journal of Developmental Neuroscience **31**(7): 701-713.

Murugan, R. and S. Ramakrishna (2007). "Design strategies of tissue engineering scaffolds with controlled fiber orientation." Tissue engineering **13**(8): 1845-1866.

Nguyen, L. H., M. Gao, et al. (2017). "Three-dimensional aligned nanofibers-hydrogel scaffold for controlled non-viral drug/gene delivery to direct axon regeneration in spinal cord injury treatment." Scientific Reports **7** 42212.

Niederöst, B. P., D. R. Zimmermann, et al. (1999). "Bovine CNS myelin contains neurite growth-inhibitory activity associated with chondroitin sulfate proteoglycans." The Journal of neuroscience **19**(20): 8979-8989.

Nikulina, E., J. L. Tidwell, et al. (2004). "The phosphodiesterase inhibitor rolipram delivered after a spinal cord lesion promotes axonal regeneration and functional recovery." Proceedings of the National Academy of Sciences of the United States of America **101**(23): 8786-8790.

Nisbet, D., J. Forsythe, et al. (2009). "Review paper: a review of the cellular response on electrospun nanofibers for tissue engineering." Journal of biomaterials applications **24**(1): 7-29.

Nisbet, D., D. Moses, et al. (2009). "Enhancing neurite outgrowth from primary neurones and neural stem cells using thermoresponsive hydrogel scaffolds for the repair of spinal cord injury." Journal of Biomedical Materials Research Part A **89**(1): 24-35.

Nisbet, D., L. Yu, et al. (2008). "Characterization of neural stem cells on electrospun poly (ε-caprolactone) submicron scaffolds: evaluating their potential in neural tissue engineering." Journal of Biomaterials Science, Polymer Edition **19**(5): 623-634.

Nomura, H., C. H. Tator, et al. (2006). "Bioengineered strategies for spinal cord repair." Journal of neurotrauma **23**(3-4): 496-507.

Olayo, R., C. Ríos, et al. (2008). "Tissue spinal cord response in rats after implants of polypyrrole and polyethylene glycol obtained by plasma." Journal of Materials Science: Materials in Medicine **19**(2): 817-826.

Olson, H. E., G. E. Rooney, et al. (2009). "Neural Stem Cell–and Schwann Cell–Loaded Biodegradable Polymer Scaffolds Support Axonal Regeneration in the Transected Spinal Cord." Tissue Engineering Part A **15**(7): 1797-1805.

Oprea, S. (2010). "The effect of chain extenders structure on properties of new polyurethane elastomers." Polymer bulletin **65**(8): 753-766.

Ostrakhovitch, E., J. Byers, et al. (2012). "Directed differentiation of embryonic P19 cells and neural stem cells into neural lineage on conducting PEDOT-PEG and ITO glass substrates." Archives of Biochemistry and Biophysics **528**(1): 21-31.

Pan, L., Y. Ren, et al. (2009). "Viability and differentiation of neural precursors on hyaluronic acid hydrogel scaffold." Journal of neuroscience research **87**(14): 3207-3220.

Park, E., A. A. Velumian, et al. (2004). "The role of excitotoxicity in secondary mechanisms of spinal cord injury: a review with an emphasis on the implications for white matter degeneration." Journal of neurotrauma **21**(6): 754-774.

Park, H.-s., M.-S. Gong, et al. (2013). "Catalyst-free synthesis of high elongation degradable polyurethanes containing varying ratios of isosorbide and polycaprolactone: physical properties and biocompatibility." Journal of Materials Science: Materials in Medicine **24**(2): 281-294.

Patist, C. M., M. B. Mulder, et al. (2004). "Freeze-dried poly (D, L-lactic acid) macroporous guidance scaffolds impregnated with brain-derived neurotrophic factor in the transected adult rat thoracic spinal cord." Biomaterials **25**(9): 1569-1582.

Perales-Alcacio, J., J. Santa-Olalla Tapia, et al. (2013). "HUVEC biocompatibility and platelet activation of segmented polyurethanes prepared with either glutathione or its amino acids as chain extenders." Journal of Biomaterials Science, Polymer Edition **24**(14): 1601-1617.

Pertici, V., T. Trimaille, et al. (2014). "Repair of the injured spinal cord by implantation of a synthetic degradable block copolymer in rat." Biomaterials **35**(24): 6248-6258.

Pham, Q. P., U. Sharma, et al. (2006). "Electrospinning of polymeric nanofibers for tissue engineering applications: a review." Tissue engineering **12**(5): 1197-1211.

Piantino, J., J. Burdick, et al. (2006). "An injectable, biodegradable hydrogel for trophic factor delivery enhances axonal rewiring and improves performance after spinal cord injury." Experimental neurology **201**(2): 359-367.

Potter, W., R. E. Kalil, et al. (2008). "Biomimetic material systems for neural progenitor cell-based therapy." Frontiers in bioscience: a journal and virtual library **13**: 806.

Prabhakaran, M. P., L. Ghasemi-Mobarakeh, et al. (2011). "Electrospun conducting polymer nanofibers and electrical stimulation of nerve stem cells." Journal of bioscience and bioengineering **112**(5): 501-507.

Pritchard, C. D., J. R. Slotkin, et al. (2010). "Establishing a model spinal cord injury in the African green monkey for the preclinical evaluation of biodegradable polymer scaffolds seeded with human neural stem cells." Journal of neuroscience methods **188**(2): 258-269.

Purcell, E. K., Y. Naim, et al. (2012). "Combining Topographical and Genetic Cues to Promote Neuronal Fate Specification in Stem Cells." Biomacromolecules **13**(11): 3427-3438.

Puschmann, T. B., Y. de Pablo, et al. (2014). "A Novel Method for Three-Dimensional Culture of Central Nervous System Neurons." Tissue Engineering Part C: Methods **20**(6): 485-492.

Qi, L., N. Li, et al. (2013). "The effects of topographical patterns and sizes on neural stem cell behavior." PLoS ONE **8**(3): e59022.

Qu, J., D. Wang, et al. (2013). "Electrospun silk fibroin nanofibers in different diameters support neurite outgrowth and promote astrocyte migration." Journal of Biomedical Materials Research Part A **101**(9): 2267-2278.

Ragnarsson, K. (2007). "Functional electrical stimulation after spinal cord injury: current use, therapeutic effects and future directions." Spinal Cord **46**(4): 255-274.

Raineteau, O. and M. E. Schwab (2001). "Plasticity of motor systems after incomplete spinal cord injury." Nature Reviews Neuroscience **2**(4): 263-273.

Raspa, A., R. Pugliese, et al. (2016). "Recent therapeutic approaches for spinal cord injury." Biotechnology and bioengineering **113**(2): 253-259.

Ren, Y. J., Z. Y. Zhou, et al. (2009). "Preparation and characterization of fibroin/hyaluronic acid composite scaffold." International journal of biological macromolecules **44**(4): 372-378.

Rim, N. G., C. S. Shin, et al. (2013). "Current approaches to electrospun nanofibers for tissue engineering." Biomedical Materials **8**(1): 014102.

Ritfeld, G. J., B. M. Rauck, et al. (2014). "The effect of a polyurethane-based reverse thermal gel on bone marrow stromal cell transplant survival and spinal cord repair." Biomaterials **35**(6): 1924-1931.

Roman, J. A., T. L. Niedzielko, et al. (2011). "Single-walled carbon nanotubes chemically functionalized with polyethylene glycol promote tissue repair in a rat model of spinal cord injury." Journal of neurotrauma **28**(11): 2349-2362.

Romanyuk, N., T. Amemori, et al. (2015). "Beneficial effect of human induced pluripotent stem cell-derived neural precursors in spinal cord injury repair." Cell transplantation **24**(9): 1781-1797.

Rossignol, S. and A. Frigon (2011). "Recovery of locomotion after spinal cord injury: some facts and mechanisms." Annual review of neuroscience **34**: 413-440.

Ruschel, J., F. Hellal, et al. (2015). "Systemic administration of epothilone B promotes axon regeneration after spinal cord injury." Science **348**(6232): 347-352.

Sabelström, H., M. Stenudd, et al. (2014). "Neural stem cells in the adult spinal cord." Experimental neurology **260**: 44-49.

Sabelström, H., M. Stenudd, et al. (2013). "Resident neural stem cells restrict tissue damage and neuronal loss after spinal cord injury in mice." Science **342**(6158): 637-640.

Sadosky, A., B. Parsons, et al. (2016). "Pain relief and functional improvement in patients with neuropathic pain associated with spinal cord injury: an exploratory analysis of pregabalin clinical trials." Journal of Pain Research **9**: 405-416.

Saglam, A., A. Perets, et al. (2013). "Angioneural crosstalk in scaffolds with oriented microchannels for regenerative spinal cord injury repair." Journal of Molecular Neuroscience **49**(2): 334-346.

Samadikuchaksaraei, A. (2007). "An overview of tissue engineering approaches for management of spinal cord injuries." Journal of neuroengineering and rehabilitation **4**: 15.

Santerre, J., K. Woodhouse, et al. (2005). "Understanding the biodegradation of polyurethanes: from classical implants to tissue engineering materials." Biomaterials **26**(35): 7457-7470.

Schubert, M. A., M. J. Wiggins, et al. (1995). "Oxidative biodegradation mechanisms of biaxially strained poly (etherurethane urea) elastomers." Journal of biomedical materials research **29**(3): 337-347.

Shah, S., P. T. Yin, et al. (2014). "Guiding Stem Cell Differentiation into Oligodendrocytes Using Graphene-Nanofiber Hybrid Scaffolds." Advanced materials **26**(22): 3673-3680.

Shahriari, D., J. Y. Koffler, et al. (2017). "Hierarchically Ordered Porous and High Volume poly caprolactone (PCL) Microchannel Scaffolds Enhanced Axon Growth in Transected Spinal Cords." Tissue Engineering(ja).

Shinozaki, M., A. Iwanami, et al. (2016). "Combined treatment with chondroitinase ABC and treadmill rehabilitation for chronic severe spinal cord injury in adult rats." Neuroscience Research **113**: 37-47.

Sill, T. J. and H. A. von Recum (2008). "Electrospinning: applications in drug delivery and tissue engineering." Biomaterials **29**(13): 1989-2006.

Silva, G. A., C. Czeisler, et al. (2004). "Selective differentiation of neural progenitor cells by high-epitope density nanofibers." Science **303**(5662): 1352-1355.

Skarja, G. and K. Woodhouse (2001). "In vitro degradation and erosion of degradable, segmented polyurethanes containing an amino acid-based chain extender." Journal of Biomaterials Science, Polymer Edition **12**(8): 851-873.

Slotkin, J. R., C. D. Pritchard, et al. (2017). "Biodegradable scaffolds promote tissue remodeling and functional improvement in non-human primates with acute spinal cord injury." Biomaterials **123**: 63-76.

Smith-Thomas, L. C., J. Stevens, et al. (1995). "Increased axon regeneration in astrocytes grown in the presence of proteoglycan synthesis inhibitors." Journal of cell science **108**(3): 1307-1315.

Soderblom, C., X. Luo, et al. (2013). "Perivascular fibroblasts form the fibrotic scar after contusive spinal cord injury." The Journal of Neuroscience **33**(34): 13882-13887.

Solanki, A., S. T. D. Chueng, et al. (2013). "Axonal Alignment and Enhanced Neuronal Differentiation of Neural Stem Cells on Graphene-Nanoparticle Hybrid Structures." Advanced Materials **25**(38): 5477-5482.

Stokols, S. and M. H. Tuszynski (2006). "Freeze-dried agarose scaffolds with uniaxial channels stimulate and guide linear axonal growth following spinal cord injury." Biomaterials **27**(3): 443-451.

Straley, K. S., C. W. P. Foo, et al. (2010). "Biomaterial design strategies for the treatment of spinal cord injuries." Journal of neurotrauma **27**(1): 1-19.

Sun, Y., W. Li, et al. (2016). "Functional self-assembling peptide nanofiber hydrogels designed for nerve degeneration." ACS applied materials & interfaces **8**(3): 2348-2359.

Takami, T., M. Oudega, et al. (2002). "Methylprednisolone and interleukin-10 reduce gray matter damage in the contused Fischer rat thoracic spinal cord but do not improve functional outcome." Journal of neurotrauma **19**(5): 653-666.

Tang, S., X. Liao, et al. (2014). "The effects of controlled release of Neurotrophin-3 from PCLA scaffolds on the survival and neuronal differentiation of transplanted neural stem cells in a rat spinal cord injury model." PLoS ONE **9**(9): e107517.

Taskin, M. B., R. Xu, et al. (2015). "Poly (norepinephrine) as a functional bio-interface for neuronal differentiation on electrospun fibers." Physical Chemistry Chemical Physics **17**(14): 9446-9453.

Tatai, L., T. G. Moore, et al. (2007). "Thermoplastic biodegradable polyurethanes: The effect of chain extender structure on properties and *in-vitro* degradation." Biomaterials **28**(36): 5407-5417.

Tator, C. H. and M. G. Fehlings (1991). "Review of the secondary injury theory of acute spinal cord trauma with emphasis on vascular mechanisms." Journal of neurosurgery **75**(1): 15-26.

Tator, C. H., R. Hashimoto, et al. (2012). "Translational potential of preclinical trials of neuroprotection through pharmacotherapy for spinal cord injury." Journal of Neurosurgery: Spine **17**(Suppl1): 157-229.

Taylor, G. (1969). "Electrically driven jets." Proceedings of the Royal Society of London. A. Mathematical and Physical Sciences **313**(1515): 453-475.

Teng, Y. D., E. B. Lavik, et al. (2002). "Functional recovery following traumatic spinal cord injury mediated by a unique polymer scaffold seeded with neural stem cells." Proceedings of the National Academy of Sciences **99**(5): 3024-3029.

Teo, B. K. K., S. Ankam, et al. (2010). "Nanotopography/mechanical induction of stem-cell differentiation." Methods in cell biology **98**: 241-294.

Thomas, A. M., M. B. Kubilius, et al. (2013). "Channel density and porosity of degradable bridging scaffolds on axon growth after spinal injury." Biomaterials **34**(9): 2213-2220.

Tokiwa, Y., T. Ando, et al. (1990). "Biodegradation of synthetic polymers containing ester bonds." Polym. Mater. Sci. Eng **62**: 988-992.

Tsukamoto, A., N. Uchida, et al. (2013). "Clinical translation of human neural stem cells." Stem Cell Res Ther **4**(4): 102.

Tysseling-Mattiace, V. M., V. Sahni, et al. (2008). "Self-assembling nanofibers inhibit glial scar formation and promote axon elongation after spinal cord injury." The Journal of Neuroscience **28**(14): 3814-3823.

Uyar, T. and F. Besenbacher (2008). "Electrospinning of uniform polystyrene fibers: The effect of solvent conductivity." Polymer **49**(24): 5336-5343.

Viano, D. C., A. I. King, et al. (1989). "Injury biomechanics research: an essential element in the prevention of trauma." Journal of Biomechanics **22**(5): 403-417.

Vroemen, M., L. Aigner, et al. (2003). "Adult neural progenitor cell grafts survive after acute spinal cord injury and integrate along axonal pathways." European Journal of Neuroscience **18**(4): 743-751.

Wang, G., Q. Ao, et al. (2010). "The effect of topology of chitosan biomaterials on the differentiation and proliferation of neural stem cells." Acta Biomaterialia **6**(9): 3630-3639.

Wang, G., R. Labow, et al. (1997). "Biodegradation of a poly (ester) urea-urethane by cholesterol esterase: Isolation and identification of principal biodegradation products." Journal of biomedical materials research **36**(3): 407-417.

Wang, H., Y. Feng, et al. (2012). "Fabrication of PU/PEGMA crosslinked hybrid scaffolds by in situ UV photopolymerization favoring human endothelial cells growth for vascular tissue engineering." Journal of Materials Science: Materials in Medicine **23**(6): 1499-1510.

Wang, H. B., M. E. Mullins, et al. (2008). "Creation of highly aligned electrospun poly-L-lactic acid fibers for nerve regeneration applications." Journal of neural engineering **6**(1): 016001.

Wang, H. B., M. E. Mullins, et al. (2010). "Varying the diameter of aligned electrospun fibers alters neurite outgrowth and Schwann cell migration." Acta biomaterialia **6**(8): 2970-2978.

Wang, J., R. Ye, et al. (2012). "The effects of electrospun TSF nanofiber diameter and alignment on neuronal differentiation of human embryonic stem cells." Journal of Biomedical Materials Research Part A **100**(3): 632-645.

Wang, J., J. Zheng, et al. (2015). "FGL-functionalized self-assembling nanofiber hydrogel as a scaffold for spinal cord-derived neural stem cells." Materials Science and Engineering: C **46**: 140-147.

Wang, M., P. Zhai, et al. (2011). "Bioengineered scaffolds for spinal cord repair." Tissue Engineering Part B: Reviews **17**(3): 177-194.

Wang, Y., M. Yao, et al. (2011). "The promotion of neural progenitor cells proliferation by aligned and randomly oriented collagen nanofibers through β1 integrin/MAPK signaling pathway." Biomaterials **32**(28): 6737-6744.

Wang, Y., C. Zhou, et al. (2012). "Biodegradable parallel and porous HSPG/collagen scaffolds for the in vitro culture of NSCs for the spinal cord tissue engineering." Journal of Porous Materials **19**(2): 173-180.

Wang, Z., L. Yu, et al. (2011). "Preparation and rapid degradation of nontoxic biodegradable polyurethanes based on poly (lactic acid)-poly (ethylene glycol)-poly (lactic acid) and L-lysine diisocyanate." Polymer Chemistry **2**(3): 601-607.

Wannatong, L., A. Sirivat, et al. (2004). "Effects of solvents on electrospun polymeric fibers: preliminary study on polystyrene." Polymer International **53**(11): 1851-1859.

Weaver, C. L. and X. T. Cui (2015). "Directed neural stem cell differentiation with a functionalized graphene oxide nanocomposite." Advanced healthcare materials **4**(9): 1408-1416.

Willerth, S. M. and S. E. Sakiyama-Elbert (2007). "Approaches to neural tissue engineering using scaffolds for drug delivery." Advanced drug delivery reviews **59**(4): 325-338.

Winkler, T., H. Sharma, et al. (2002). "Topical application of dynorphin A (1–17) antiserum attenuates trauma induced alterations in spinal cord evoked potentials, microvascular permeability disturbances, edema formation and cell injury." Amino acids **23**(1-3): 273-281.

Wirz, M., D. H. Zemon, et al. (2005). "Effectiveness of automated locomotor training in patients with chronic incomplete spinal cord injury: a multicenter trial." Archives of physical medicine and rehabilitation **86**(4): 672-680.

Woerly, S., V. D. Doan, et al. (2004). "Prevention of gliotic scar formation by NeuroGel™ allows partial endogenous repair of transected cat spinal cord." Journal of neuroscience research **75**(2): 262-272.

Xie, J., W. Liu, et al. (2014). "Neurite outgrowth on electrospun nanofibers with uniaxial alignment: the effects of fiber density, surface coating, and supporting substrate." ACS nano **8**(2): 1878-1885.

Xie, J., M. R. MacEwan, et al. (2009). "Neurite outgrowth on nanofiber scaffolds with different orders, structures, and surface properties." ACS nano **3**(5): 1151-1159.

Xie, J., S. M. Willerth, et al. (2009). "The differentiation of embryonic stem cells seeded on electrospun nanofibers into neural lineages." Biomaterials **30**(3): 354-362.

Xiong, Y., Y. S. Zeng, et al. (2009). "Synaptic transmission of neural stem cells seeded in 3-dimensional PLGA scaffolds." Biomaterials **30**(22): 3711-3722.

Xu, C., F. Xu, et al. (2011). "Electrospinning of poly (ethylene-co-vinyl alcohol) nanofibres encapsulated with Ag nanoparticles for skin wound healing." Journal of Nanomaterials **2011**: 3.

Xu, X. Y., X. T. Li, et al. (2010). "The behaviour of neural stem cells on polyhydroxyalkanoate nanofiber scaffolds." Biomaterials **31**(14): 3967-3975.

Yang, F., R. Murugan, et al. (2004). "Fabrication of nano-structured porous PLLA scaffold intended for nerve tissue engineering." Biomaterials **25**(10): 1891-1900.

Yang, F., R. Murugan, et al. (2005). "Electrospinning of nano/micro scale poly (L-lactic acid) aligned fibers and their potential in neural tissue engineering." Biomaterials **26**(15): 2603-2610.

Yang, K., H. Jung, et al. (2014). "Multiscale, hierarchically patterned topography for directing human neural stem cells into functional neurons." ACS nano **8**(8): 7809-7822.

Yang, K., K. Jung, et al. (2013). "Nanotopographical manipulation of focal adhesion formation for enhanced differentiation of human neural stem cells." ACS applied materials & interfaces **5**(21): 10529-10540.

Yang, K., J. Lee, et al. (2016). "Graphene oxide hierarchical patterns for the derivation of electrophysiologically functional neuron-like cells from human neural stem cells." ACS Applied Materials & Interfaces **8**(28): 17763-17774.

Yang, K., E. Park, et al. (2015). "Biodegradable nanotopography combined with neurotrophic signals enhances contact guidance and neuronal differentiation of human neural stem cells." Macromolecular bioscience **15**(10): 1348-1356.

Yang, Z., H. Duan, et al. (2010). "The effect of the dosage of NT-3/chitosan carriers on the proliferation and differentiation of neural stem cells." Biomaterials **31**(18): 4846-4854.

Yang, Z., L. Mo, et al. (2010). "Effects of chitosan/collagen substrates on the behavior of rat neural stem cells." Science China Life Sciences **53**(2): 215-222.

Yao, S., X. Liu, et al. (2016). "Co-effects of matrix low elasticity and aligned topography on stem cell neurogenic differentiation and rapid neurite outgrowth." Nanoscale **8**(19): 10252-10265.

Ye, J., Y. Qin, et al. (2016). "Using primate neural stem cells cultured in self-assembling peptide nanofiber scaffolds to repair injured spinal cords in rats." Spinal cord **54**: 933-941.

Yeh, L.-C., C.-F. Dai, et al. (2013). "Neat poly (ortho-methoxyaniline) electrospun nanofibers for neural stem cell differentiation." Journal of Materials Chemistry B **1**(40): 5469-5477.

Yim, E. and M. P. Sheetz (2012). "Force-dependent cell signaling in stem cell differentiation." Stem Cell Res Ther **3**(5): 41.

Yin, Y., P. Huang, et al. (2014). "Collagen nanofibers facilitated presynaptic maturation in differentiated neurons from spinal-cord-derived neural stem cells through MAPK/ERK1/2-Synapsin I signaling pathway." Biomacromolecules **15**(7): 2449-2460.

Yiu, G. and Z. He (2006). "Glial inhibition of CNS axon regeneration." Nature Reviews Neuroscience **7**(8): 617-627.

Yoshii, S., S. Ito, et al. (2009). "Functional restoration of rabbit spinal cord using collagen-filament scaffold." Journal of tissue engineering and regenerative medicine **3**(1): 19-25.

Zahir, T., H. Nomura, et al. (2008). "Bioengineering neural stem/progenitor cell-coated tubes for spinal cord injury repair." Cell transplantation **17**(3): 245-254.

Zandén, C., N. H. Erkenstam, et al. (2014). "Stem cell responses to plasma surface modified electrospun polyurethane scaffolds." Nanomedicine: Nanotechnology, Biology and Medicine **10**(5): 949-958.

Zander, N. E., J. A. Orlicki, et al. (2012). "Quantification of Protein Incorporated into Electrospun Polycaprolactone Tissue Engineering Scaffolds." ACS applied materials & interfaces **4**(4): 2074-2081.

Zawadzka, M., L. E. Rivers, et al. (2010). "CNS-resident glial progenitor/stem cells produce Schwann cells as well as oligodendrocytes during repair of CNS demyelination." Cell Stem Cell **6**(6): 578-590.

Zhang, C., X. Wen, et al. (2008). "Synthesis and characterization of biodegradable elastomeric polyurethane scaffolds fabricated by the inkjet technique." Biomaterials **29**(28): 3781-3791.

Zhang, C., N. Zhang, et al. (2006). "Improving the elasticity and cytophilicity of biodegradable polyurethane by changing chain extender." Journal of Biomedical Materials Research Part B: Applied Biomaterials **79**(2): 335-344.

Zhang, Q., S. Yan, et al. (2016). "Multichannel silk protein/laminin grafts for spinal cord injury repair." Journal of Biomedical Materials Research Part A **104**(12): 3045-3057.

Zhang, Z., S. Yao, et al. (2017). "Effect of hierarchically aligned fibrin hydrogel in regeneration of spinal cord injury demonstrated by tractography: A pilot study." Scientific Reports **7**: 40017.

Zhao, C., A. Tan, et al. (2012). "Nanomaterial scaffolds for stem cell proliferation and differentiation in tissue engineering." Biotechnology Advances.

Zhong, Y. and R. V. Bellamkonda (2008). "Biomaterials for the central nervous system." Journal of the Royal Society Interface **5**(26): 957-975.

Zhou, J., F. Sui, et al. (2013). "Novel nanometer scaffolds regulate the biological behaviors of neural stem cells." Neural Regeneration Research **8**(16): 1455.

Zhu, Y., N. Uezono, et al. (2017). "Neural stem cell therapy aiming at better functional recovery after spinal cord injury." Developmental Dynamics **247**(1): 75-84.

Zhu, Y., A. Wang, et al. (2010). "Nanofibrous patches for spinal cord regeneration." Advanced Functional Materials **20**(9): 1433-1440.

Zimmermann, D. R. and M. T. Dours-Zimmermann (2008). "Extracellular matrix of the central nervous system: from neglect to challenge." Histochemistry and cell biology **130**(4): 635-653.

Zou, Y., J. Qin, et al. (2016). "Fabrication of Aligned Conducting PPy-PLLA Fiber Films and Their Electrically Controlled Guidance and Orientation for Neurites." ACS applied materials & interfaces **8**(20): 12576-12582.

Zou, Z., T. Liu, et al. (2014). "Biocompatibility of functionalized designer self-assembling nanofiber scaffolds containing FRM motif for neural stem cells." Journal of Biomedical Materials Research Part A **102**(5): 1286-1293.

Zustiak, S. P., S. Pubill, et al. (2013). "Hydrolytically degradable poly (ethylene glycol) hydrogel scaffolds as a cell delivery vehicle: Characterization of PC12 cell response." Biotechnology progress **29**(5): 1255-1264.

Zweckberger, K., C. S. Ahuja, et al. (2016). "Self-assembling peptides optimize the post-traumatic milieu and synergistically enhance the effects of neural stem cell therapy after cervical spinal cord injury." Acta Biomaterialia 42: 77-89.

Chapter 3

Electrospun biodegradable chitosan based-poly(urethane urea) scaffolds for soft tissue engineering

3. Electrospun biodegradable chitosan based-poly(urethane urea) scaffolds for soft tissue engineering

3.1 Introduction

Tissue engineering has been researching and developing new therapeutic approaches for the treatment and/or replacement of damaged tissues and organs. In these approaches, engineered scaffolds are employed aiming at creating an appropriate environment to support endogenous cell regrowth and possibly cell transplantation from exogenous sources. Scaffold properties, such as chemical composition, architecture and mechanical properties, should be tailored in order to promote tissue regeneration. A tissue engineering scaffold should be biocompatible, biodegradable without releasing toxic products, and integrate well with the host tissues without inducing an exacerbated foreign body reaction. These properties are mainly determined by the choice of the scaffold raw material. Regarding the structure, the scaffold should have porosity that allows the infiltration of cells and a rapid vascularization essential for tissue regeneration. An appropriate degradation rate is also essential and should be in tune with the rate of new tissue formation (Liu and Cao 2007).

Since their discovery in 1937 by Otto Bayer, polyurethanes (PUs) have been produced with distinct properties: coatings/adhesives, elastomers and flexible or rigid foams. PUs are segmented polymers composed of hard and soft segments. Soft segments (SS) are derived from a polyol (usually a polyether or a polyester), while hard segments (HS) are derived from a diisocyanate and chain extenders (Guelcher 2008). Due to the thermodynamic incompatibility between the segments, they segregate into separate phases of soft and hard segment domains (Oprea 2010). The soft segment is derived from the polyol and the hard segment is derived from the polyisocyanate and the chain extender. The hard segments are organized in discrete domains by hydrogen bonds and van der Walls interactions in the soft segment. Different types of hydrogen bonds can be formed in the PU structure. They are established between the proton donators - urethane and urea N-H groups and urethane and urea C=O groups - and the proton acceptors - ester/ether carbonyl or oxygen groups.

PUs have been widely used in industry, from the machinery to the medical field. In medical field, they were used for long-term devices such as heart valves, aortic grafts, dialysis membranes, indwelling catheters, intra-aortic balloons, mammary implants due to PUs biocompatibility and durability (Zdrahala and Zdrahala 1999). However, PUs that can degrade *in vivo* have recently been synthetized as biomaterials for tissue engineering purposes.

PU properties depend on its composition and structure: they can be controlled through the choice of precursor constituents and adjustment of synthesis properties. Biodegradable PUs, designed to undergo hydrolytic and enzymatic degradation, have been developed for tissue engineering (Guelcher 2008). Amorphous soft segments, labile functional groups and enzyme recognizable moieties increase the degradation rate of PUs. In order to avoid toxicity issues

related with decomposition products, lysine-derived or aliphatic polyisocyanates are preferred (Guan, Fujimoto et al. 2005; Hafeman, Zienkiewicz et al. 2011). Natural polymers such as chitosan (CS) (Barikani, Honarkar et al. 2009) and gelatin (Lee, Kwon et al. 2014) or aminoacids such as glycine, arginine and aspartic acid (Skarja and Woodhouse 2000; Chan-Chan, Tkaczyk et al. 2013) can be used as chain extenders to introduce in PU structure biological cues improving cell adhesion.

Scaffold's properties depend on the material and production technique used, which determines the scaffold architecture and also influences the physico-chemical properties. The electrospinning technique allows the production of small diameter (typically ranging from hundreds of nanometers to a few micrometers) fibers (Henriques, Vidinha et al. 2009). In a typical set-up, a polymeric solution is forced through a metallic capillary, to which a high voltage is applied, and flies towards a collector. During the flight, the viscous jet is stretched by the electrostatic repulsion, due to the charge it carries, while the solvent evaporates. Randomly oriented solid fibers are collected as a non-woven structure with high porosity and interconnected pores, which resemble the extracellular matrix of connective tissue. Fibers with preferential orientation can also be designed using a rotator mandrel rotating at high speed. Those fibers mimic the extracellular matrix of anisotropic tissues, guiding the regeneration of different tissues.

Electrospun scaffolds have been produced from many polymers, including PUs. Han et al synthetized a PU based on policaprolactone-diol (PCL-diol), L-lysine diisocyanate and L-lysine ethyl ester (chain extender) and obtained from it a tubular electrospun scaffold to substitute blood vessels (Han, Cao et al. 2011; Bergmeister, Seyidova et al. 2015). The scaffold revealed adequate mechanical properties for its purpose and the ability to support adhesion and proliferation of human umbilical vein endothelial cells. PUs mats have been studied as scaffolds to support the differentiation of stem cells for cardiac (Guan, Wang et al. 2011; Parrag, Zandstra et al. 2012), ligament (Bashur, Shaffer et al. 2009) tendon (Cardwell, Dahlgren et al. 2012) vision (Wu, Du et al. 2012) annulus fibrosus (Liu, Zhu et al. 2015) and neural (Carlberg, Axell et al. 2009) regeneration. To improve the biocompatibility of the electrospun scaffolds, blends of PUs with natural polymers such as gelatin (Kim, Heo et al. 2009; Vatankhah, Prabhakaran et al. 2014; Jamadi, Ghasemi-Mobarakeh et al. 2016) and collagen (Chen, Qiu et al. 2009; Jia, Prabhakaran et al. 2014), were studied.

CS is widely used in biomedical applications due to its attractive biological properties (biocompatibility, biodegradability and antimicrobial, antioxidant and hemostatic properties) (Dash, Chiellini et al. 2011). Therefore, CS has been introduced in PU elastomers to improve the biocompatibility/biodegradability of PUs (Usman, Zia et al. 2016). Films were produced from these CS based PUs (Barikani, Honarkar et al. 2009; Barikani, Honarkar et al. 2010; Zia, Anjum et al. 2014) but, to the best of our knowledge, they have never been electrospun. In this chapter, we describe the synthesis and characterization of PUs extended with CS and the production and characterization of electrospun mats, with random and aligned orientation, from the synthetized PUs. First, three different PUs based on PCL-diol and isophorone diisocyanate (IPDI) were synthetized using dimethylol proprionic acid (DMPA) and/or CS as chain extenders. The chemical

structure and the extent of microphase separation were evaluated using proton nuclear magnetic resonance (^{1}H NMR) and Fourier transform infrared spectroscopy (FTIR, deconvolution of the C=O and N-H stretching bands), respectively. Thermal characterization was evaluated using differential scanning calorimetry (DSC) and thermogravimetric analysis (TGA).

Secondly, electrospun fibrous mats from the synthetized PUs were produced using the electrospinning technique. Films were also produced for comparison purposes. Techniques such as X-ray diffraction (XRD) analysis, X-ray photoelectron spectroscopy (XPS), water contact angle (WCA) measurements were used to characterize the films and mats. Mechanical and degradation properties were also evaluated as well as the viability of Caucasian foetal foreskin fibroblasts (HFFF2) cells on the films and mats.

Thirdly, electrospun mats were produced with random and aligned morphology and characterized according to their morphology, mechanical properties and the viability of HFFF2 cells on the mats.

3.2 Materials and methods

3.2.1 Depolimerization of chitosan and determination of molecular weight

Commercial CS has high molecular weight that make it insoluble in organic solvents and, as consequence, its use as a chain extender in PUs synthesis is limited. CS was depolymerized by oxidative destruction of the β-D-glucoside bonds using sodium nitrite ($NaNO_2$) as the oxidant agent according to (Huang, Khor et al. 2004; Loh, Schneider et al. 2010). Briefly, 1 % (w/v) chitosan (*Mw*=500 kDa determined by GPC – gel permeation chromatography – and a degree of deacetylation, *DD* = 75.5%, determined by NMR), from Cognis S, was dissolved in 2% (v/v) acetic acid glacial (from Panreac) and reacted with $NaNO_2$ (from Sigma-Aldrich) in a proportion of CS:$NaNO_2$ of 20:1 during 1h at 800 rpm. To recover the obtained depolymerized CS, NaOH (4M, from EKA) was added drop-wise in order to the solution reach a basic pH. Further, the polymer was centrifuged and washed with distilled water. At the end, the recovered polymer was frozen and lyophilized during 24h. The obtained CS powder was dried is an oven at 60 ºC for 7 days and dissolved in dimethyl sulfoxide (DMSO, Merck) 72 h before the PUs synthesis.

Intrinsic viscometry was measured using the Ubbelohde AVS 400 (from Schott Gerate) in order to determine the molecular weight (M_w) of the depolymerized chitosan. The solvent system 0.2M acetic acid/0.1M sodium acetate (from Scharlau) was chosen, the temperature was set to 30 ºC, and the CS concentrations were ranged from 5 to 25 mg/mL.

The deacetylation degree, %DD, was investigated by analyzing the FTIR spectra using the Baxter et al. (1992) equation (Baxter, Dillon et al. 1992): $\%\, DD = 100 - (A_{1655}/A_{3450}) \times 115$ where, A_{1655} and A_{3450} are the absorptions at 1655 cm^{-1} and 3450 cm^{-1}, respectively.

3.2.2 Synthesis of Polyurethane extended with chitosan

The following materials were used for the synthesis of the polyurethanes (PUs): polycaprolactone-diol (PCL-diol, M_n = 2000), dimethylol propionic acid (DMPA, 99%), N-methylpyrrolidone (NMP, 99%) and sodium bisulfite ($NaHSO_3$, M_w=104.06) from Acros Organics; isophorone diisocyanate (IPDI) from Huls, triethylamine (TEA) from Fluka, isopropanol from LabChem, dimethyl sulfoxide (DMSO, dried over molecular sieves) from Merck and depolymerized CS (section 3.2.1).

The syntheses were carried out following the procedures presented by Barikani et al. (Barikani, Honarkar et al. 2010) with slight modifications. Three different polyurethanes were synthesized via a prepolymer route using DMPA and CS as chain extenders, either alone or in combination. The prepolymer was derived from PCL and IPDI. According to the chain extenders employed the polymers are designed as PU-DMPA, PU-DMPA/CS and PU-CS.

PU-DMPA/CS synthesis was conducted as follows. PCL-diol (20 g) was dried under vacuum at 90ºC during 24 h and put in a 500 cm^3 four-necked reactor equipped with a mechanical stirrer, a heating oil bath, a condenser, a dropping funnel and a nitrogen inlet and outlet. The temperature of the bath was set at 60 ºC. IPDI (8.95 g) was added drop wise to the reactor and the temperature of the bath was raised to 90 ºC. The reaction took place during 4 h to achieve the NCO terminated pre-polymer. Then DMPA (1.34 g), previously dried at 90 ºC under vacuum for 24 h and dissolved in NMP, was introduced in the reactor. After 1 h, the temperature of the bath was decreased to 65 ºC and TEA (1.01 g) was added, keeping the mixture under stirring for 30 min, in order to neutralize the carboxyl groups of DMPA. Then, CS (1.14 g), previously dried at 60 ºC during 7 days and dissolved in DMSO (100 mL), was added and reacted during 1 h. To end the reaction, $NaHSO_3$ (2.08 g) was added to the mixture and stirring proceeded at a higher speed for 30 min. Finally, cold distilled water was added dropwise at reduced speed leading to the precipitation of the polymer. The polymer was thoroughly washed with distilled water, immersed in isopropanol during 48 h and vacuum dried until constant weight.

PU-DMPA and PU-CS were synthetized in similar way but skipping the addition of CS and DMPA, respectively, and using twice the amount of chain extender (DMPA or CS) used in the PU-DMPA/CS synthesis. TEA was not used in PU-CS.

3.2.3 Characterization of synthesized polyurethanes

3.2.3.1 Fourier Transform Infrared spectroscopy

To analyze chemical bonds, IR spectra of PUs and raw material used in their synthesis were recorded with a FT-IR Nicolet 6700 spectrometer, from Thermo Electron Corporation, in ATR (attenuated total reflectance) mode with a resolution of 4 cm^{-1}. Both N-H and C=O stretching bands of PUs IR spectra were fitted with Gaussian profile and constant background using the Fityk 0.9.8 program to evaluate PU hydrogen bonds and consequently, PU microphase segregation.

3.2.3.2 Nuclear Magnetic Resonance

^{1}H NMR spectra were recorded using a BrukerAvance III 400 MHz spectrometer in order to investigate PUs' chemical structure. The analyzed samples were dissolved in DMSO-d_6 (99.96 atom %, Sigma-Aldrich) and chemical shifts (δ) were registered in ppm using tetramethylsilane (TMS) as standard.

3.2.3.3 Thermal analysis

Thermogravimetric analysis (TGA) and differential scanning calorimetry (DSC) were used to quantify the thermal degradation of the synthetized PUs and to determine their phase transitions, respectively. Measurements were performed with a NETZSCH TGA-DSC-STA 449F3 Jupiter equipment, using an aluminum crucible, under nitrogen atmosphere. Data collection and analysis were performed with the control software Proteus.

For the TGA spectra acquisition, the sample mass was recorded during a heating cycle from room temperature up to 500 ºC. In DSC, the samples were scanned from room temperature to 250 ºC. In both measurements, the heating rate of the samples was 10 ºC/min.

3.2.4 Electrospinning and film casting

In order to optimize the experimental electrospinning processing conditions, different solvents (N,N-dimethylformamide (DMF), tetrahydrofuran (THF), chloroform and dimethylacetamide (DMAc, from Sigma-Aldrich), all from Carlo Erba unless otherwise identified), solvent proportions (30:70, 50:50 and 70:30), polymeric concentrations (15, 20 and 25 wt%), and electrospinning set-up parameters were evaluated for PU-DMPA/CS.

In order to prepare fibrous mats, the PUs were dissolved in a solvent system comprising 50 wt % DMF and 50 wt % THF by magnetic stirring overnight.

Solutions for electrospinning were prepared with polymer concentrations of 40%, 20% and 13% in weight for PU-DMPA, PU-DMPA/CS, and PU-CS, respectively. Each solution was loaded on a 5 mL syringe with 21G stainless steel blunt needle (internal diameter of 0.508 mm) attached. A syringe pump (SyringePump NE-300) was used to control the flow rate that was set to 1.0 mL/h. A voltage ranging from 13 to 16 kV was applied to the needle by a high-voltage power supply (Power Supply – iseg T1CP300 304p). An aluminum plate, grounded and kept at a distance of 20 cm from the needle tip was used to collect fibers without preferred orientation. Aligned fibers were obtained using a rotatory mandrel (constructed in Tissue Engineering Group of the FCT-UNL, with a mandrel diameter of 8 cm) rotating at high speed (4000 rpm). In order to facilitate the detachment of the fiber mats to be used in mechanical tests, the collector/rotatory drum was covered with a paper foil. Samples for cell culture were deposited on 12 mm diameter coverslips, fixed to the collector. The optimized electrospinning set-up parameters for each PU solution are summarized in Table 3.1.

Films were prepared from 20 wt% PUs solutions dissolved in 50:50 THF:DMF by solvent casting. A calibrated Gardner knife (Braive Instruments) moving at 1.25 mm/s was used to spread

out the solution. The films were allowed to dry at ambient conditions and then were put under vacuum in a desiccator to evaporate the solvents.

Table 3.1– Electrospinning set-up parameters used in the production of fibrous mats from synthesized PUs.

PUs	Electrospinning				
	Concentration (wt.%)	*Solvents (50:50)*	*Voltage (kV)*	*Flow rate (mL/h)*	*Distance (cm)*
PU-DMPA	40	THF:DMF	15	1.0	20
PU-DMPA/CS	20	THF:DMF	16	1.0	20
PU-CS	13	THF:DMF	13	1.0	20

3.2.5 Physico-chemical characterization of fibrous mats and films

3.2.5.1 Scanning Electron Microscopy (SEM)

The morphology of the electrospun fibers was observed using a Zeiss Auriga Crossbeam electron microscope operating in high vacuum at 5 kV. All samples were sputter coated with a mixture of gold/palladium (60:40) before observation. Fiber diameter was measured by image analysis using ImageJ software (National Institutes of Health, USA) (Schneider, Rasband et al. 2012). At least 100 fibers were analyzed per sample. The results are expressed as the average ± experimental standard deviation.

The degree of fiber alignment was evaluated using the Fast Fourier Transform (FFT), as previously described by (Ayres, Bowlin et al. 2006). Briefly, the FFT function converts the information in the image of the “real” space into the “frequency” space, resulting in an output image with grayscale pixels. The pattern presented by the pixels reflect the degree of alignment of the original image. To get the FFT frequency distribution, the radial summation of the pixel intensities for each degree between 0º and 360º is performed in a circular projection on the originated FFT image. The FFT analysis was performed using SEM images converted to 8-bit grayscale TIF format and cropped to 1024 × 1024 pixels. Afterwards, images were processed with the oval profile plug-in (authored by William O’Connnell) in the ImageJ software. The angular distribution of the fibers was also determined by direct measurement of the angle in the ImageJ software.

3.2.5.2 Porosity

The porosity of the matrices were determined based on the Archimedes’ Principle with a specific gravity bottle according to the formula:

$$\text{Porosity (\%)} = \frac{(W_2 - W_3 - W_s)/\rho}{(W_1 - W_3)/\rho} \times 100$$

w_1- specific gravity bottle weight filled with water

w_2- specific gravity bottle weight with water and scaffold

w_3- specific gravity bottle weight after removal of water-saturated matrix from W2

w_s- scaffold weight

ρ-density of water

(w_1 - w_3)/ρ – total volume of the scaffold including pores

(w_2 - w_3 - w_s)/ρ – pore volume of the scaffold

3.2.5.3 Mechanical characterization

PUs fiber mats and films were subjected to uniaxial tensile tests with an equipment from Reometric Scientific using the Minimat Firmware version 3.1 software. Samples with an initial gauge length of 10 mm were strained using a 20 N load cell and a crosshead speed of 2 mm/s at room temperature. At least 10 samples of 10 × 30 mm^2 from three different electrospun depositions or cast films were used. Aligned mats were stretched in the direction of the fiber alignment. Samples thickness was measured with a digital micrometer (Mitutoyo Corporation, Japan). The strain was calculated dividing the variations in grip length by the initial grip separation. The stress was calculated dividing the measured force by the cross-section area of the specie. A stress-strain curve was recorded and the Young modulus was determined from the slope of the linear region of the stress-strain curve.

Hysteresis tests were also performed on the PUs fibrous mats, 10 cycle hysteresis behavior was evaluated by stretching the samples to 80% elongation with a crosshead speed of 10 mm/min and afterwards, immediately retract them at the same crosshead speed. The tests were conducted at room temperature and at least three samples from each mat were tested.

3.2.5.4 X-Ray Diffraction (XRD)

XRD experiments were conducted to get information about the crystalline structure of PUs after processing into fibers and films. XRD was performed using a PANalytical X'Pert PRO X-ray diffractometer, operating with Cu-Kα radiation (λ = 1.54060 Å) in the range 5°<2θ<40° with a 0.1º step. The diffractograms were fitted with a sum of pseudo-Voigt functions (products of Gaussian and Lorentzian peaks), assuming a background fitted to a quadratic polynomial, using the software Igor Pro from Wavemetrics.

The crystalline degree, $w_{c,x}$, was calculated using the equation: $w_{c,x} = I_c/(I_c + I_a)$ where I_c is the area of the diffraction peaks resulting from the crystalline reflections and I_a is the area of the peaks resulting from amorphous reflections (Ferreira, Gomes et al. 2014).

The crystallite size, τ, was calculated using the Scherrer equation (Monshi, Foroughi et al. 2012): $\tau = 0.89\lambda/\beta cos\theta$ where $\lambda = 0.154\ nm$ is the wavelength of the Cu-Kα radiation, β is the full width at half maximum (FWHM) of the diffraction peak and θ is the diffraction angle.

3.2.5.5 X-ray Photoelectron Spectroscopy (XPS) Analysis

In order to analyze chemically the surface of fiber and films, XPS spectra were obtained using an X-ray spectrometer (XSAM800 - KRATOS) operated in the fixed analyser transmission (FAT) mode, with a pass energy of 20 eV, a power of 120 W (10 mA and 12 kV), the non-monochromatised Mg Kα X-radiation (hv=1253.7 eV), at room temperature, and a pressure in the sample chamber in the range of 10^{-7} Pa. Spectra were collected at two take-off angles, 0º and

60º. No flood gun was used. The charge accumulation was corrected taking as a reference the lowest binding energy C 1s component set at 285 eV. The curve fitting, with pseudo-Voigt profiles and Shirley background was carried out using the freeware XPSPeak 4.1. Peaks within the same region were constrained to identical full width at half maximum and identical Gaussian/Lorentzian ratio except the peak at higher binding energy in the C 1s region. For quantification purposes, the sensitivity factors from the Vision 2 software for Windows, Version 2.2.9 (for data acquisition and processing) were used: C 1s: 0.318; O 1s: 0.736 and N 1s: 0.505.

3.2.5.6 **Wettability**

The wettability of fiber mats and films was assessed by static WCA measurements at room temperature and 98% humidity, employing a contact angle goniometer (model OCA15, DataPhysics Instruments GmbH, Filderstadt, Germany), using the sessile drop method. Water drops with 5 µL were generated with an electronic micrometric syringe and carefully deposited on the samples and the contact angle value acquired within the following 5 min (the shape of the drops was stable during that period). The information collected was analyzed using the SCA15 software. The results are expressed as the average ± experimental standard deviation of at least five measurements recorded in different regions of the samples.

3.2.5.7 **Degradation tests**

Hydrolytic and enzymatic degradation of all PU fiber mats and films was evaluated from mass loss measurements. For the hydrolytic degradation studies, the degradation medium was a phosphate buffer saline (PBS, pH 7.4 ± 0.2) solution with 0.04 % w/v sodium azide (Merck, to prevent contamination by gram negative bacteria). Samples were followed over a period of 60 days. An esterase – lipase PS “Amano” from Amano Enzyme Inc. – was used in the enzymatic degradation studies. The enzyme solution was prepared at a concentration of 10 U/mL, in accordance with (Labow, Meek et al. 1999), adding 0.04 % w/v sodium azide. The enzymatic solution was replaced every other day to maintain a constant enzymatic activity. The degradation was evaluated over a period of 40 days.

Six samples with ~20 mg were used for each condition studied. Their initial mass (W_i) was measured (with a resolution of 0.1 mg) before immersing in 5 mL of the degradation media and incubated at 37 ºC. Weakly, the samples were taken out of the degradation medium, washed by immersion in distilled water during 1 h and dried in an incubator at 37 ºC for 24 h before the measurement of their remaining mass (W_k). Results of degradation tests are presented as the average of the relative remaining mass expressed in percentage ($100 \times W_k / W_i$) ± experimental standard deviation.

At the end of the experiment, degraded samples were analyzed using FTIR spectroscopy.

3.2.5.8 **Cell culture experiments**

Cell culture

Human fetal foreskin fibroblasts (HFFF2 cell line, obtained from ECACC, UK) were cultured in Dulbecco’s modified Eagle’s medium (DMEM, catalog #D5030, Sigma-Aldrich),

supplemented with GlutaMAX (#35050-038), 10% v/v fetal bovine serum (FBS, #10270106), 100 units/mL of penicillin, 100 µg/mL streptomycin (#15140122) and 2.50 µg/mL amphotericin B (#15290018) all from Life Technologies.

Indirect cytotoxicity test

To evaluate if films and electrospun fiber mats produced from the synthetized PUs could present cytotoxicity, the extract method was used in accordance with the International Standard ISO 10993-5. To prepare the extracts, samples from electrospun mats and films were cut, weighted, sterilized under UV light (254 nm) during 30 min on each side, and put inside a centrifuge tube with culture medium without FBS (1 mL of culture medium per 15 mg of sample). These tubes were placed inside an incubator at 37 ºC, under orbital shaking, for 48 h. Meanwhile, HFFF2 cells were seeded in DMEM at a density of 20×10^3 cells/cm^2 in a 96 well plate and were incubated at 37 ºC in a 5% CO_2 humidified atmosphere incubator (Sanyo MCO-19AIC(UV)) during 24 h. After this period, the cell culture medium was replaced either by the extracts or by their dilutions (dilution factors 3/2 and 3), supplemented with 10% FBS. Negative (viable cells) and positive (cells in a cytotoxic environment) controls were established by culturing cells with complete medium and complete medium with 10% DMSO, respectively. After 48 h in contact with the extracts, a calorimetric viability assay was performed, as described below.

Cellular adhesion and proliferation

In order to determine the adhesion and proliferation of cells when seeded on the materials, electrospun mats deposited on coverslips with 12 mm diameter and films cut with a 12 mm circle punch were used as samples for cell culture. Before cell seeding, the samples were sterilized (as previously described), washed three times with PBS and soaked in complete culture medium. HFFF2 cells were seeded, at a density of 10×10^3 cells/cm^2, over a 0.5 cm^2 area on each sample held by home-made Teflon inserts, which were placed in a 24-well tissue culture plate (Sarstedt, Germany). Cell controls were set by seeding cells at the same density directly over the surface of the tissue culture plate (TCP) wells for viability assays, and on glass coverslips for fluorescence imaging. After seeding, cells were incubated in the CO_2 incubator. Cell adhesion and proliferation was evaluated using the resazurin viability assay. The assay was performed 24 h after cell seeding (day 1 of culture) to estimate cell adhesion, and then on days 3, 5, 8 and 10 of culture to assess cell proliferation.

Resazurin viability assay

Cell viability was assayed using a resazurin (Alfa Aesar) solution (0.2 mg/mL in PBS) as cell viability indicator (Gomes, Rodrigues et al. 2017). Viable cells reduce resazurin (with an absorption peak at 600 nm) to resofurin (with an adsorption peak at 570 nm). For the assay, all media were replaced by complete medium supplemented with 10 % of the resazurin solution. This medium was also dispensed in wells without cells to be used as reference. Five replicas were used for each experimental condition. After 3 h of incubation in the CO_2 incubator, medium

absorbance was measured at 570 nm with a reference wavelength of 600 nm (BioTek ELX 80UV microplate reader). The corrected absorbance (obtained by subtracting the absorbance measured at 600 nm from the one measured at 570 nm and subtracting the medium control) is proportional to cell viability. The combined standard uncertainty was calculated by propagation of uncertainties.

Cell imaging

After 5 days of culture, cells growing in different substrates and control cells seeded on glass coverslips were fixed with 3.7% w/v paraformaldehyde, permeabilized with Triton X-100 (0.5% in PBS) and stained with 4',6-Diamidino-2-Phenylindole, Dilactate – DAPI (300 nM in PBS, from Molecular Probes™, ThermoFisher Scientific, Inc.) and Acti-stain™ 555 Fluorescent Phalloidin (100 nM in PBS, from # PHDH1 - Cytoskeleton, Inc.) to observe nuclei and actin cytoskeleton, respectively. All samples were mounted on glass coverslips with fresh PBS and imaged with an epi-fluorescent microscope Nikon Ti-S.

3.3 Results and Discussion

3.3.1 Depolymerization of Chitosan

High molecular weight commercial CS is insoluble in organic solvents and, consequently, its use as a chain extender in PU synthesis is limited. CS was depolymerized by oxidation, which destroyed the β-D-glucoside bonds using $NaNO_2$ as the oxidant agent according to the method of Loh et al. (2010) (Loh, Schneider et al. 2010). The proportion of oxidant agent $NaNO_2$ to CS was settled to be 1:20.

The molecular weight of the depolymerized CS was determined using viscosimetric measurements. In order to do that, an Ubbelohde viscosimeter was used to measure the elution time of CS solutions with different concentrations dissolved in the aqueous solution of 0.2 M CH_3COOH/0.1 M CH_3COONa, as well as the aqueous solution itself, at 30 ºC. The intrinsic viscosity of CS was determined to be 0.41 dl/g. Then, the Mark-Houwink equation $[\eta] = KM_v^{\alpha}$, where [η] is the intrinsic viscosity, M_v is the viscosimetric molecular weight and K and α are constants dependent on the solution (solute-solvent system) and temperature, was used to determine the molecular weight of CS. The parameters of the equation were determined based on the work of Kasaai (2007) (Kasaai 2007). The parameters were determined to be $K=2.16\times10^{-5}$ g/dL and α=0.969, Therefore, the resulting depolymerized CS has a viscosimetric molecular weight of 26 kDa.

FTIR spectrum of the original and the depolymerized CS was recorded to evaluate structural changes during the depolymerization process (Figure 3.1). There was no significant alterations in the absorption spectra of CS, indicating that the depolymerization process only cleave the 1,4-β-D-glucoside bonds resulting in CS with lower the molecular weight but similar structure. The deacetylation degree of CS was determined according to Baxter method (Baxter,

Dillon et al. 1992), from the ratio between the absorption bands of 3358 cm^{-1} and 1650 cm^{-1}. These bands are assigned to N-H extension vibration and C=O stretching of N-acetyl group, respectively. The resulting deacetylation degree was 76.1 % for the original and 75.4 % for the depolymerized CS. The values were similar to the deacetylation degree of the original CS determined by NMR (75.5 %), indicating that the depolymerization process using $NaNO_2$ did not significantly affect the CS deacetylation degree.

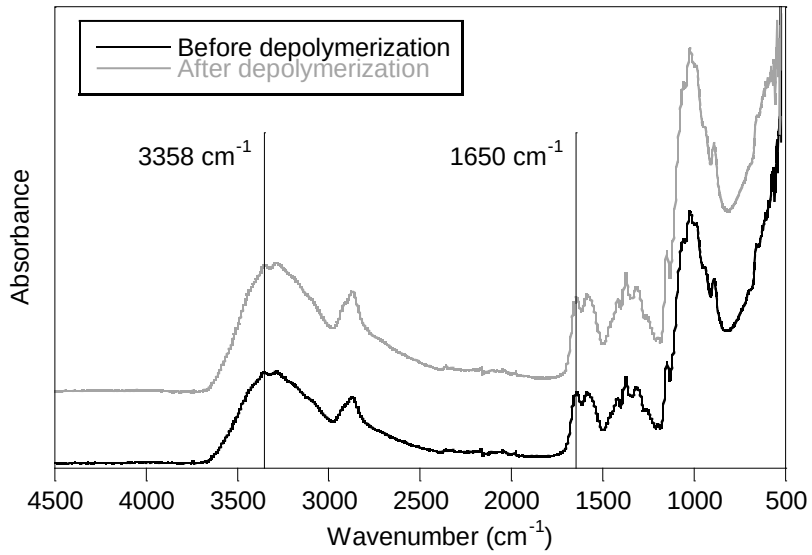

Figure 3.1 – IR spectra of CS before and after depolymerization. The deacetylation degree was determined from the 3358 and 1650 cm^{-1} bands.

3.3.2 Polyurethanes Characterization

Three PUs were obtained using DMPA and/or CS as chain extenders. PUs were synthetized using two step batch procedure. In the first step, PCL-diol react with IPDI to form urethane bonds, resulting in the –NCO terminated pre-polymer. The reaction proceed by adding either DMPA and/or chitosan. The reaction with CS may result in either urethane or urea bonds formed by reacting –NCO with either hydroxyl or amine groups, respectively, leading to the elongation of the PU chains. The chemical structure of such polymers were previously analyzed (Barikani, Honarkar et al. 2010) and is schematically represented in Figure 3.2. Chemical structure of PUs were confirmed by ^1H NMR and FTIR analysis.

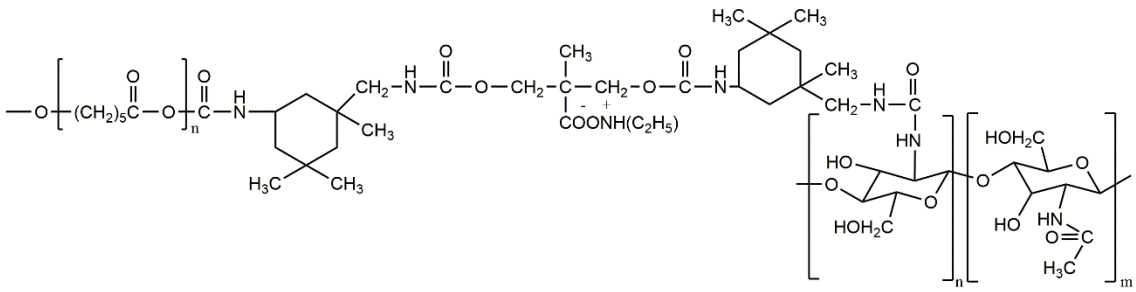

Figure 3.2 – Chemical structure of PU-DMPA/CS showing the urea bond between IPDI and the amine group of CS.

3.3.2.1 Chemical characterization

The chemical structure of PCL-diol and IPDI was confirmed using the ^{1}H NMR spectroscopy (Figure 3.3). The CH_2 signals from –O(*CH_2*)$_5$– of PCL-diol are allocated at the triplets 3.97 (1), 2.25 (4), 1.51 (2+2') and 1.28 (3) ppm. The –*CH_2*-O– is presented at 3.58 ppm (1'+6) (Rodriguez, Luo et al. 2011; Li, Li et al. 2014). The characteristic bands of IPDI are according to (Zhang, Cheng et al. 2003; Prabhakar, Chattopadhyay et al. 2005). The CH_3 group is present at 0.90 to 1.30 ppm (1, 2 and 3). Bands at 1.40 -1.90 ppm identify the CH_2 groups (4, 5, and 6). Peaks of *CH_2*=NCO *cis* and *trans* isomers are detected at 3.12 ppm and 3.40 ppm, respectively. The 3.80 ppm peak is due to the *CH*-NCO. It was not possible to acquire the ^{1}H NMR spectrum of CS due to their poor solubility in DMSO.

The ^{1}H NMR spectra shown in Figure 3.4 provide information that confirms the synthesis of PUs. Methyl groups of IPDI and DMPA are observed at 0.80–0.98 ppm. The 1.30 ppm peak is due to the central methylene (–CH_2*CH_2*CH_2–) groups of PCL. Other CH_2 groups of PCL and triethylamine ethyl (CH_3*CH_2*–) groups (in PUs with DMPA) are presented at 1.48–1.59 ppm (Zia, Barikani et al. 2008). In the PU-CS spectrum, the 1.55 – 1.59 ppm band was less intense due to the absence of triethylamine protons (Daemi, Barikani et al. 2013). The peaks at 2.26 – 2.29 ppm identify the methylene protons of PCL-diol (*CH_2*O– and *CH_2*CO–) and of CS (–OH*CH_2*). A slight signal displacement to lower chemical shifts is observed in PU-CS due to the contribution of CS methylene protons, thereby confirming the involvement of CS in the final PU structure. Peaks of –CHOH groups in CS and PCL CH_2 groups attached to the urethane oxygen atom (Zhang, He et al. 2017) are detected at 3.89 – 3.91 ppm. The peak for methylene group of either CS or DMPA bounded to the urethane oxygen atom (–*CH_2*OCONH) and the –COO*CH_2*– protons in PCL-diol are located at 3.97 – 4.01 ppm. Due to CS, the chemical shift of this band is displaced to lower values in PU-CS spectrum. Weak peaks at 6.82–7.18 ppm position are attributed to urethane NH (–*NH*COO–) groups and to NH groups of CS (Barikani, Honarkar et al. 2009).

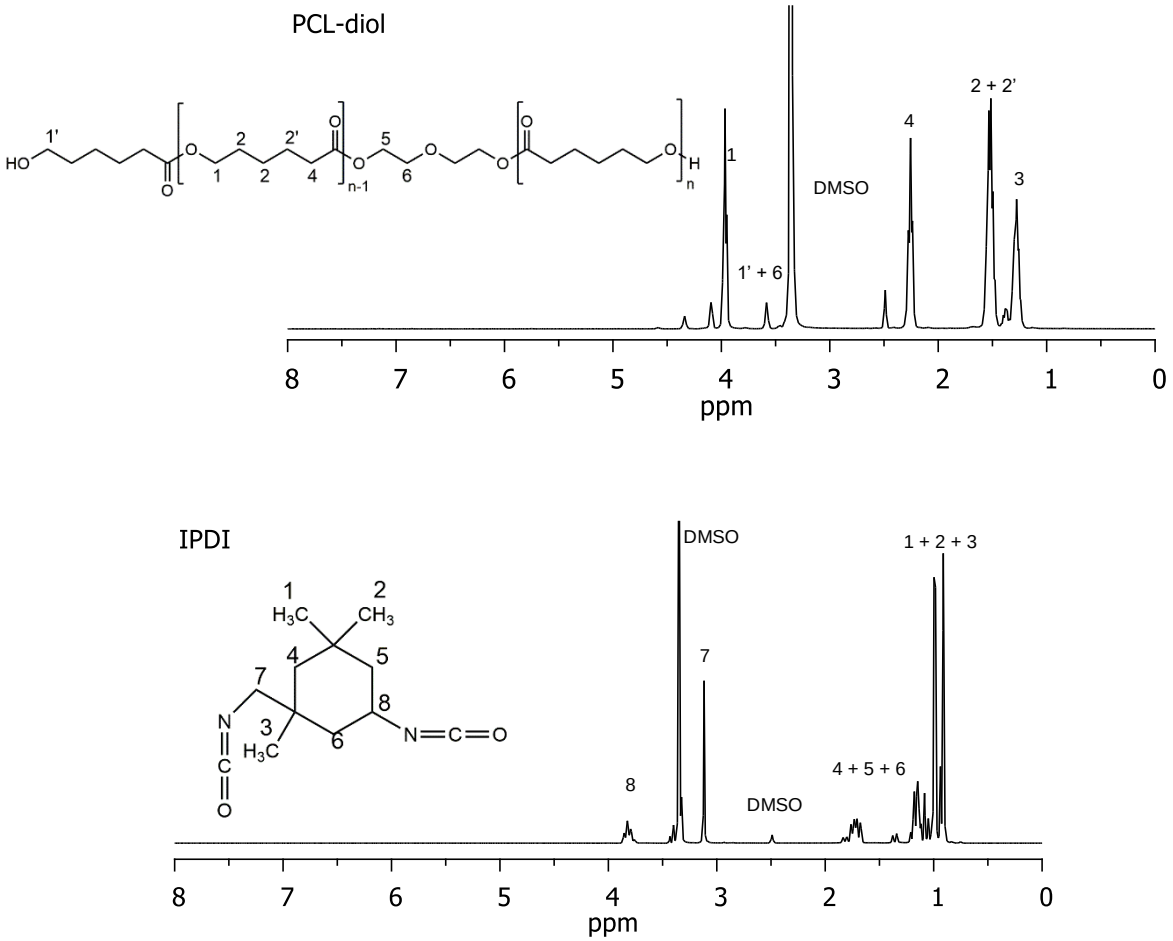

Figure 3.3 – ^{1}H NMR spectra of PCL-diol and IPDI used in the chemical synthesis of PUs.

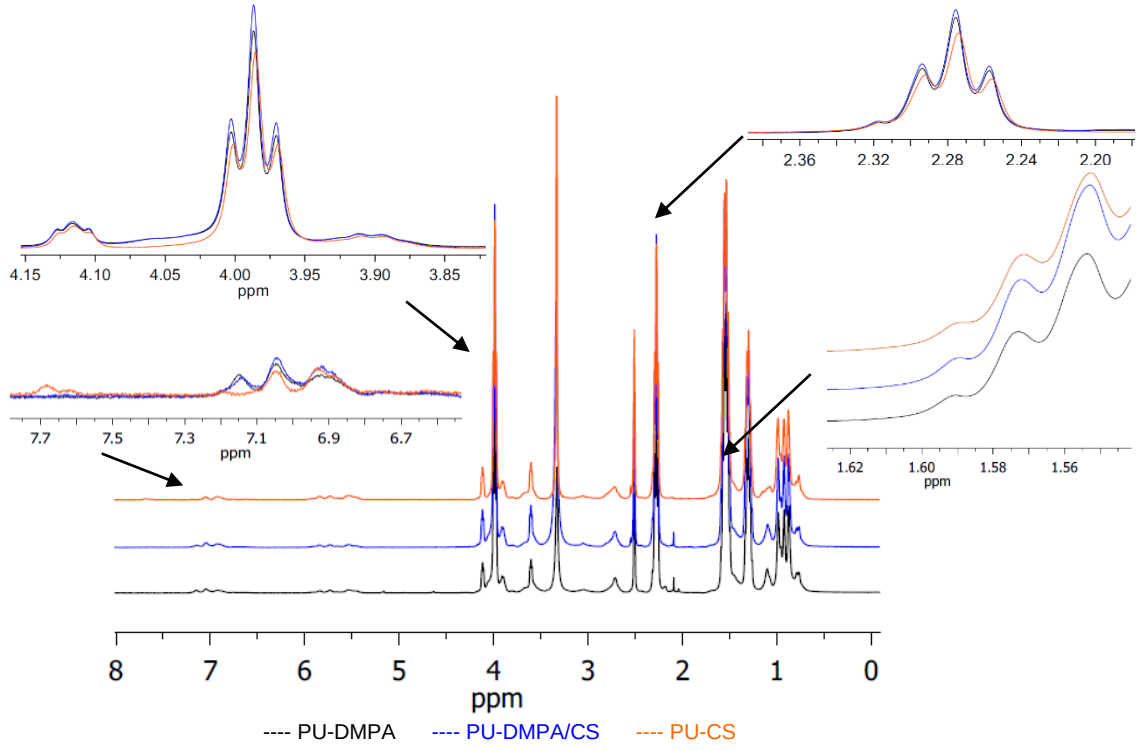

Figure 3.4 – ^{1}H NMR spectra of the synthetized PUs.

PU-DMPA/CS synthesis steps were monitored using FTIR spectroscopy (Figure 3.5). In PCL-diol IR spectrum, it is observed a peak at 1720 cm^{-1} corresponding to the weak C=O stretching vibration due to the presence of $–C(O)OCH_2-$ ester bonds in the repeated units of the PCL-diol. The wave number 3437 cm^{-1} is assigned to the hydroxyl band (Jeong, Kang et al. 2003), which is absent in the PU-DMPA/CS spectrum, indicating that all hydroxyl groups reacted with the isocyanate groups to form the PU.

The NCO groups of the IPDI are detected in the range 2270-2285 cm^{-1}. The absence of this band in the PU-DMPA/CS spectrum indicate the absence of –NCO free groups in the final product. Isocyanate groups are still present on the pre-polymer spectrum, which are available to react with the chain extenders. When the first chain extender (DMPA) is reacted with the pre-polymer, the NCO band of the disocyanate decrease. Thus, it was formed urethane bonds between the NCO terminal groups of the pre-polymer and the OH groups of DMPA.

The CS spectrum presents a band at 3352 cm^{-1}, which is assigned to the N-H extension vibration of the polysaccharide moieties (Brugnerotto, Lizardi et al. 2001). At 1657 cm^{-1} is identified a peak that belongs to amide I band, resulting from the C=O stretching of *N*-acetyl group of chitosan (Anitha, Divya Rani et al. 2009). At 1571 cm^{-1} was observed the peak corresponding to the NH_3^+ deformation in the chitosan (Delair 2011).

FTIR spectra of the synthesized PUs are shown in Figure 3.6. These spectra reveal bands that were associated with urethane and urea linkages formation (Barikani, Honarkar et al. 2009; Barikani, Honarkar et al. 2010). The wave number range 1800 – 1600 cm^{-1} is assigned to the stretching vibration of carbonyls present in ester, acetyl, urethane and urea groups. According to the literature (Garrett, Xu et al. 2003; Yilgor, Yilgor et al. 2006; Shi, Zhan et al. 2008), free urethane carbonyls have an absorption peak in the 1733 – 1724 cm^{-1} range whereas H-bonded urethane carbonyls peak at 1715 – 1695 cm^{-1}. The non-H bonded urea C=O are located between 1700 cm^{-1} and 1670 cm^{-1} and the urea C=O groups that form hydrogen bonds peaks in the range 1666 – 1635 cm^{-1}. The higher intensity of the peak at 1637 cm^{-1} for PU-CS suggests the presence of more H-bonded urea C=O groups due to the higher CS content.

FTIR spectra also show other characteristic absorption bands at 3365 cm^{-1} (N-H stretching vibration), 2947 and 2865 cm^{-1} (C-H symmetric and asymmetric stretching vibrations of CH_2 groups, respectively), 1544 cm^{-1} (amide II, N-H bending and C-N stretching), 1460 cm^{-1} (CH_2 bending vibration), 1360 cm^{-1} (C-H bending vibration), 1302 cm^{-1} (CH_2 wagging), 1238 – 1100 cm^{-1} (C-O-C stretching) and 1038 cm^{-1} (C-O stretching).

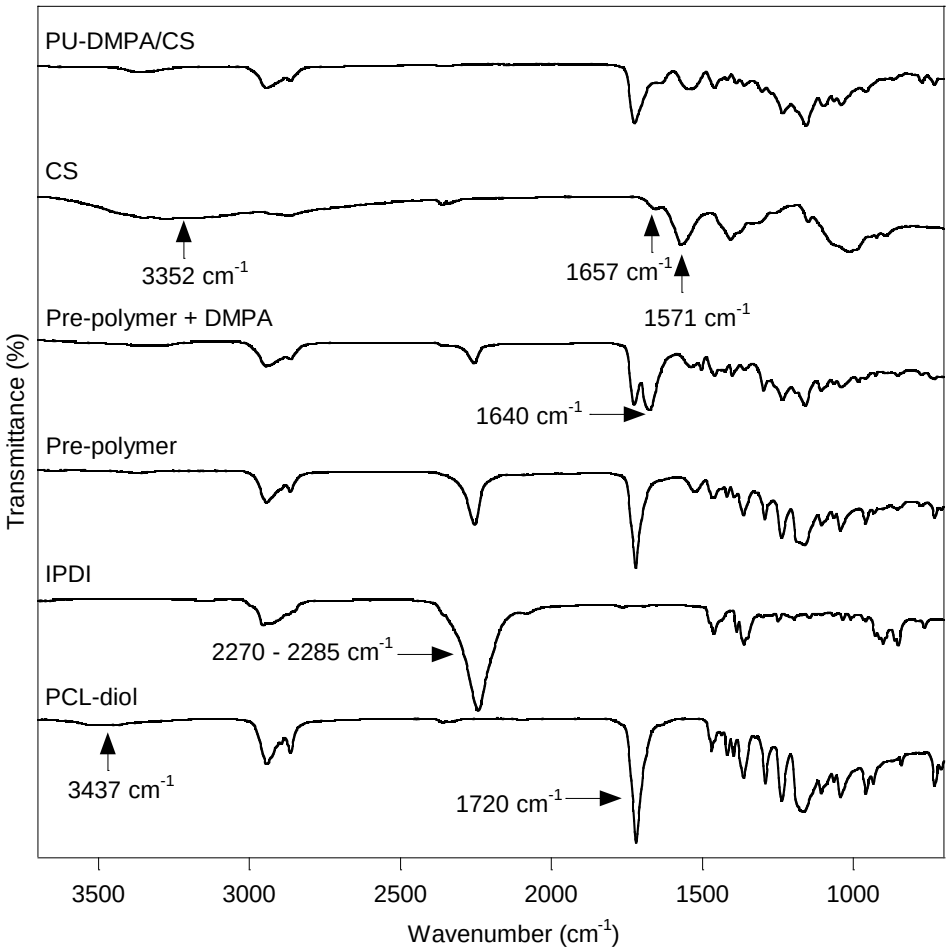

Figure 3.5– FTIR spectra of the precursors and the intermediate pre-polymer to reach the PU-DMPA/CS.

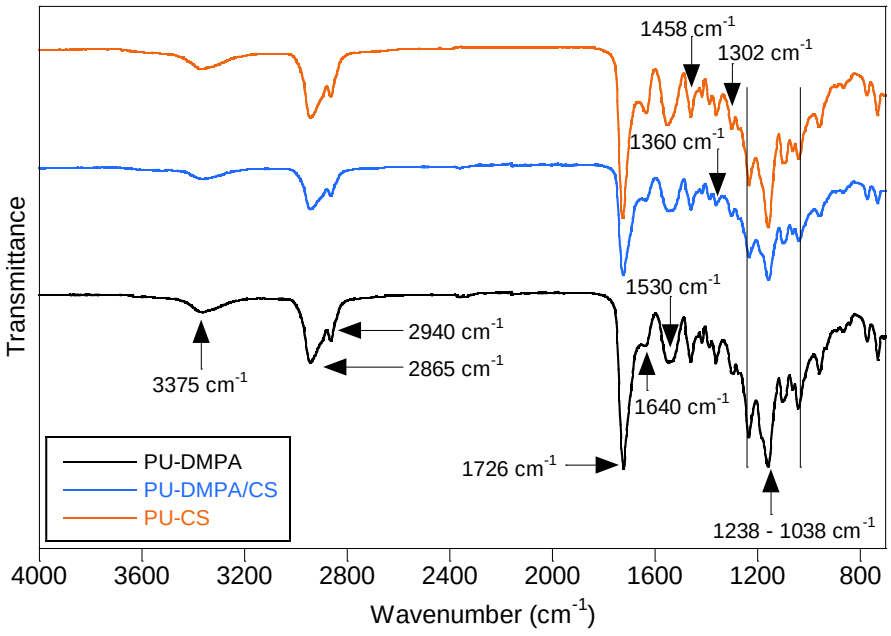

Figure 3.6– FTIR spectra of the synthetized PUs.

Deconvolution of the C=O and NH stretching bands

The extent of microphase separation is dependent on the hydrogen bonds established during the PU synthesis. The hydrogen bonds can be established between the hydrogen atom of the NH in the urethane and urea linkage (donator proton) and the carbonyl urethane, carbonyl urea and oxygen atom of ester linkage (acceptor group). Hydrogen bonds established between the same segments conducted to superior phase segregation. FTIR is used to evaluate the extent of hydrogen bonds and, consequently, the extent of microphase separation.

Two stretching bands are sensitive to hydrogen bonding: N-H band at 3300 – 3450 cm^{-1} region and C=O band at 1600 – 1800 cm^{-1}. These bands were fitted with a sum of Gaussian functions using the software Fityk. First, the second derivative of each region was determined to extract the number of relative minima of the function, which corresponded to the number of Gaussian bands used in the fitting procedure. The second derivative of the carboxylic region of the PU-CS sample is represented in Figure 3.7, as an example.

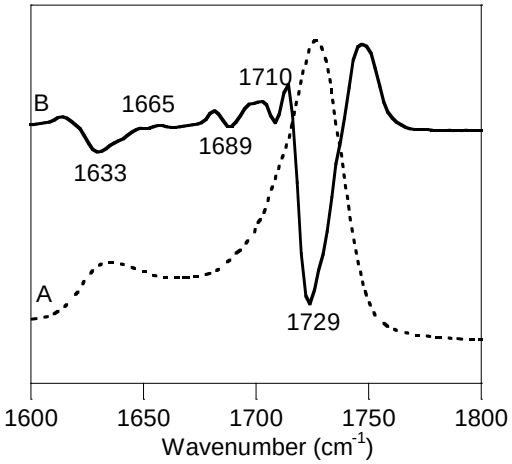

Figure 3.7 – Carboxyl region (1600 – 1800 cm^{-1}) of PU-CS IR spectrum: Absorbance spectrum (A); second-derivative spectrum (B).

For the C=O stretching region, the original data, the fitting and the Gaussian curves of PU with different CS quantities are presented in Figure 3.8. In Table 2.1 is presented the wavenumber (cm^{-1}) and the relative areas of the Gaussian curves, as well as the percentage of hydrogen bonds.

Five distinct bands were identified in the carbonyl stretching band. The free C=O urethane group was identified at 1720 – 1730 cm^{-1}, while the hydrogen bonded urethane groups were detected at 1710 cm^{-1}. Bands at 1690 – 1700 cm^{-1}, 1660 – 1680 cm^{-1} and 1635 - 1645 cm^{-1} were ascribed to free, disordered hydrogen bonded and ordered hydrogen bonded urea carbonyl, respectively (Queiroz, de Pinho et al. 2003; Chattopadhyay, Sreedhar et al. 2006; Yilgor, Yilgor et al. 2006; Pereira and Oréfice 2011). As the urea carbonyl group can interact with two NH groups, bidentate hydrogen bonds can be formed, which are stronger and induce better hard domain cohesion than single hydrogen bonds (He, Zhang et al. 2014). Thus, it was distinguished between order and disordered hydrogen bonded urea carbonyl.

The percentage of free urethane carbonyl groups decrease while the hydrogen bonded groups increase in PUs with CS (PU-DMPA/CS and PU-CS) when compared to PU-DMPA. The increment in the CS content on the PU structure cause a decrease in ordered (12.7 to 10.3 %) and an increase in disordered (2.48 to 16.1 %) hydrogen carbonyl urea bonds. The presence of CS molecules with three functional groups can form a three dimensional structure, acting as a reinforcing filler to drive microphase segregation (Ahmad, Khan et al. 2014). However, high CS content can increase the hard segment branching, causing the disruption of the hydrogen bonds and consequently, deteriorate the microphase separation (Sheth, Wilkes et al. 2005).

The shift of urea carbonyl band from 1641 cm^{-1} in PU-DMPA to 1637 cm^{-1} in PU-CS can be due to the presence of soft segments dissolved in the hard segments, which prevented the ordering of carbonyl hydrogen bonds. Consequently, the polyester oxygen compete with urea carbonyls for the NH groups, resulting in a mixing state. Therefore, in PU-CS the CS disrupt the hard segment order, preventing phase segregation. In PU-DMPA/CS the presence of DMPA prevent CS branching, resulting in the organized structure that better phase segregate. However, the phase segregation is still superior in PU-CS when compared to PU-DMPA, where urea groups are absent and the urethane carbonyl groups are less prone to hydrogen bond.

Table 3.2 – Wavenumber (v) and relative area (A) of the 5 components of the C=O stretching band and the percentage of carbonyl hydrogen bonded.

C=O	***v*** **(cm^{-1})**	***A*** **(%)**	***v*** **(cm^{-1})**	***A*** **(%)**	***v*** **(cm^{-1})**	***A*** **(%)**	***v*** **(cm^{-1})**	***A*** **(%)**	***v*** **(cm^{-1})**	***A*** **(%)**	**% C=O H-bonded**
PU-DMPA	1726	52.6	1706	3.97	1689	13.4	1667	2,48	1641	12.7	33.99
PU-DMPA/CS	1729	38.5	1710	33.9	1689	8.75	1669	8.49	1639	10.3	52.71
PU-CS	1729	45.9	1711	23.7	1690	4.02	1668	16.1	1637	10.3	50.13

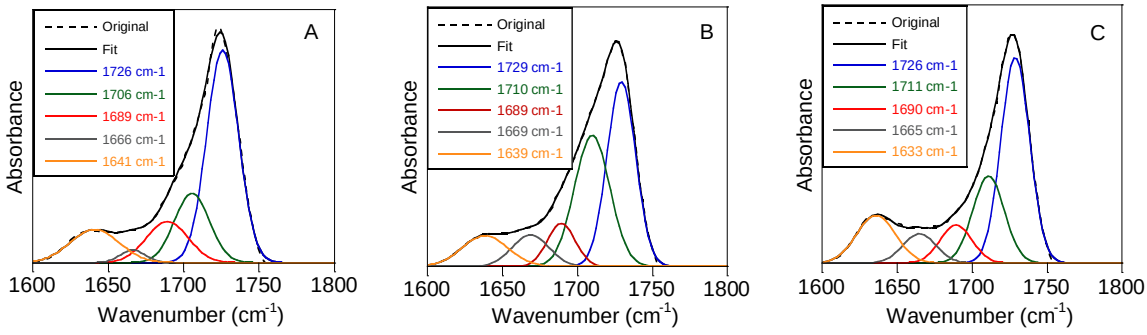

Figure 3.8– ATR-FTIR spectra in the carbonyl group stretching and the deconvoluted curves of (A) PU-DMPA, (B) PU-DMPA/CS and (C) PU-CS.

In Figure 3.9 is shown the original curve, the fitting and the Gaussian curves of the N-H stretching region of the synthetized PUs. Additional information relative to the wavenumber (cm^{-1}) and the areas of the Gaussian curves, as well as the percentage of N-H hydrogen bonded is presented in Table 3.3. The N-H stretching region in 3300 – 3400 cm^{-1} can be resolved into four

bands. The band at 3270 – 3280 cm^{-1} identify the hydrogen bonds established between the N-H and the ester of the SS. The bands at 3309 – 3315 cm^{-1} and at 3368 – 3373 cm^{-1} are ascribed to hydrogen bonds in the ordered and disordered state in the HS, respectively (He, Zhang et al. 2014; Shokrolahi and Yeganeh 2014) (Skarja and Woodhouse 2000). The N-H free groups are detected at 3450 cm^{-1}. The N-H groups can establish hydrogen bonds with either the carbonyl group of the hard segment or the ester group of the soft segment, remaining few N-H free groups (Park, Lim et al. 2011). A slight decrease of N-H free groups was observed in PUs with CS when compared to the PU-DMPA, similar to what was verified in the carbonyl stretching region.

In PU-CS, the area of the band corresponding to disorder hydrogen bonds is higher and the area of the band from ordered hydrogen bonds is smaller when compared to other PUs. In PU-CS, the wavenumbers of both ordered and disordered hydrogen bonds bands were shifted to lower values when compared to other PUs, indicating the superior strength of both types of hydrogen bonds.

Table 3.3 – Wavenumber (v) and relative area (A) of the 3 components of the N-H stretching band and the percentage of amine hydrogen bonded.

N-H	***v*** **(cm^{-1})**	***A*** **(%)**	***N*** **(cm^{-1})**	***A*** **(%)**	***v*** **(cm^{-1})**	***A*** **(%)**	***v*** **(cm^{-1})**	***A*** **(%)**	**% N-H H-bonded**
PU-DMPA	3276	21.9	3315	17.9	3373	56.7	3443	3.46	96.5
PU-DMPA/CS	3277	13.3	3315	19.0	3373	76.9	3458	1.56	97.8
PU-CS	3271	12.9	3309	8.71	3368	65.4	3455	2.28	98.4

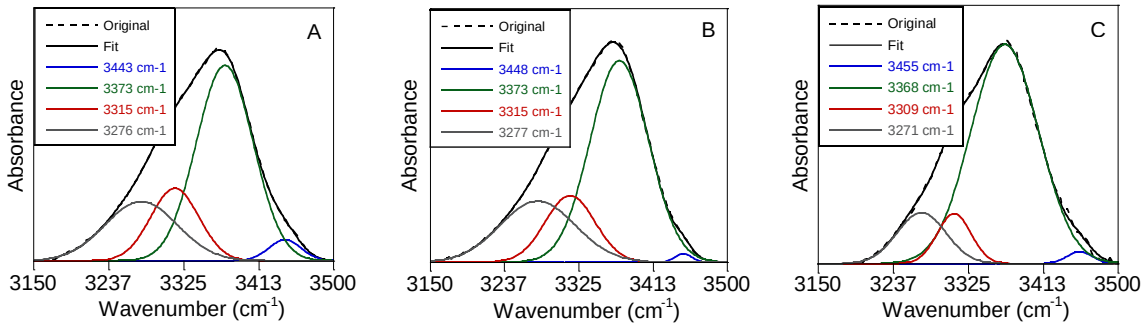

Figure 3.9– ATR-FTIR spectra in the amine group stretching and the deconvoluted curves of(A) PU-DMPA, (B) PU-DMPA/CS and (C) PU-CS.

Two forms of hydrogen bonds can be established with the N-H groups. The interaction between the urethane/urea groups in the hard domains, which drives phase separation, and the hydrogen bonds between the urea/urethane groups and the oxygen atoms of the esters in the SS. The last type of hydrogen bond occurred between the SS and the HS, leading to phase mixing between both segments. In the C=O region, a decrease in the intensity of the C=O free band accompanied by an increase in hydrogen bonded band in PUs with CS, indicate better phase segregation, particularly in PU-DMPA/CS. In the N-H region, the decrease of the area of the band corresponding to the hydrogen bonds established between SS and HS (3270 cm^{-1}) in PUs with

CS, also confirmed a better phase segregation in these PUs. However, the disordered hydrogen bonds in HS was superior in PUs with CS than in PU-DMPA.

3.3.2.2 **Thermal analysis**

TGA curves of PCL-diol, CS and synthetized PUs and their corresponding derivative plots (DTG curves) are shown in Figure 3.10. CS shows thermal mass losses at 100 ºC due to the loss of the entrapped water molecules and at 262 ºC due to the removal of volatile products from thermal and oxidative decomposition (Neto, Giacometti et al. 2005). At 500 ºC, CS remains with 42.2 % of their weight.

Thermal degradation of PUs occurs between 250 and 480 ºC, al lower temperatures in hard segments and then in soft segments (Chattopadhyay and Webster 2009), with almost no mass remaining above 500 ºC. PCL-diol soft segments have a maximum degradation at 415 ºC (T_{soft}) in PU-DMPA and at 412 ºC in PU-DMPA/CS and PU-CS (Table 3.4). At lower temperatures, the decomposition of urethane and urea linkages takes place, and a series of reactions may proceed simultaneously, including the dissociation to isocyanate and alcohol, the formation of primary amine and ofelin and the formation of secondary amine and carbon dioxide (Rueda-Larraz, d'Arlas et al. 2009). In the last stage, hard phase degradations are observed at 258 ºC (T_{hard}) in PU-DMPA, at 288 ºC and 382ºC in PU-DMPA/CS and at 314 ºC in PU-CS (Table 3.4). As the CS content in the PU backbone increases, the hard phase thermal degradation shifts to higher temperatures.

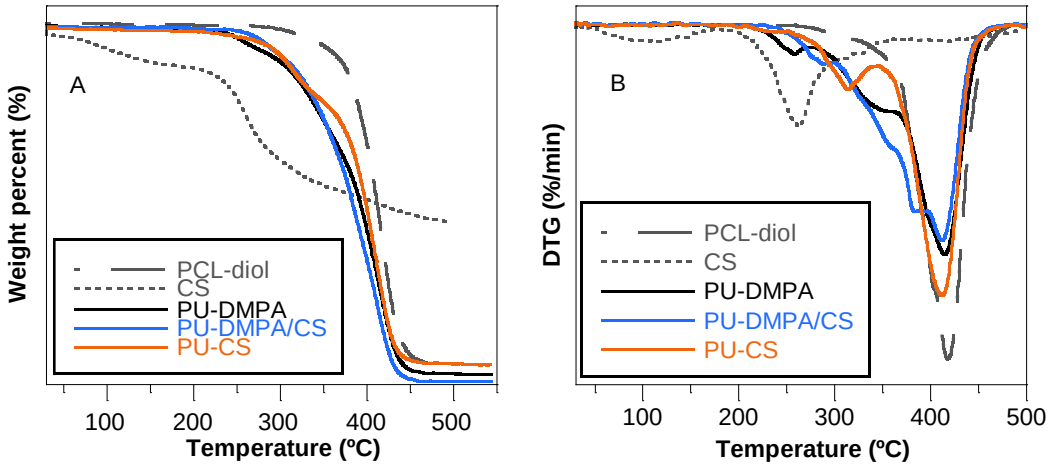

Figure 3.10 – Mass losses (A) and the corresponding derivatives (B) vs. temperature of PCL-diol, CS, PU-DMPA, PU-DMPA/CS and PU-CS.

The DSC curves for CS, PCL-diol and synthetized PUs are shown in Figure 3.11. The CS present an endothermic event around 100 ºC resulting from the evaporation of water molecules entrapped in CS. The glass transition temperature (*Tg*) of CS, which depends on the deacetylation degree, molecular weight and crystallinity of CS, should appear as a small baseline step in the DSC curve but water evaporation and degradation are likely to prevent its observation (Kittur, Prashanth et al. 2002). No CS melting peak is observed before the onset of thermal degradation.

PCL has a negative *Tg* (out of our measurements temperature range) and melts at a temperature (*Tm*) of 61.3 ºC, confirming its crystallinity.

All PUs present an endothermic melting peak at a temperature slightly above the PCL-diol melting temperature (Table 3.4). This result reveals that phase separation enables soft segment crystallization in these PUs (Furukawa, Mitsui et al. 2005; Oniki, Suzuki et al. 2013). No melting transitions are observed at higher temperatures suggesting the lack of HS order. This may be due to the use of an asymmetric isocyanate (Tatai, Moore et al. 2007) and to the absence of a melting transition in CS.

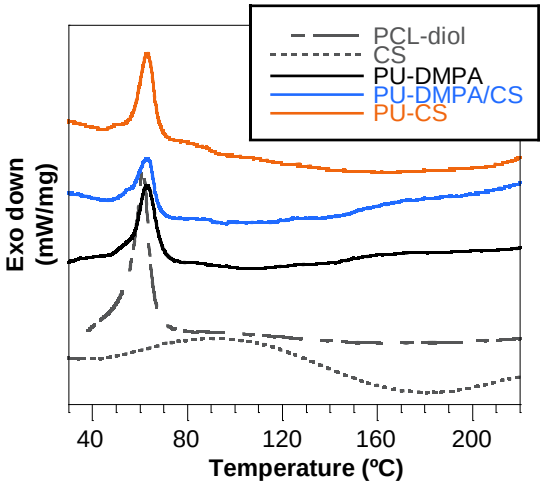

Figure 3.11 – DSC curves of PCL-diol, CS and PUs with an increasing CS content substituting DMPA as chain extender.

Table 3.4– Thermal analysis data of the synthetized polyurethanes: from TGA, degradation temperatures of hard and soft segments (T_{hard} and T_{soft}) and, from DSC, melting temperature (T_m) and enthalpy of fusion (ΔH_m) of the soft segment

Polyurethane	**TGA**		**DSC**	
	T_{hard} (ºC)	T_{soft} (ºC)	T_m (ºC)	ΔH_m (J/g)
PU-DMPA	258	415	63.2	34.9
PU-DMPA/CS	288, 382	412	63.1	24.0
PU-CS	314	412	63.3	32.1
PCL-diol	-	418	61.3	73.2
CS	262	-	-	-

3.3.3 Optimization of the electrospinning process

Electrospinning technique was used to produce fiber mats from the synthetized PUs. In order to obtain a fibrous scaffold without defects several solution concentrations and solvent mixtures were tested and the set-up parameters (flow rate, voltage and distance between the needle and the collector) were adjusted.

Electrospinning conditions were first optimized for the PU-DMPA/CS. Then, solutions from PU-CS and PU-DMPA were prepared using the same solvent system, adjusting the set-up parameters. All the scaffolds were prepared with the same solvent system for fiber characteristics comparison, in particular the comparison of mechanical properties that are highly dependent of the solvents used in fibers production.

The choice of the solvents used for polymer dissolution widely affect the resulting fibers. The solvent must dissolve properly the synthetized PUs and also guarantee suitable electrospinnability (must have appropriate boiling point, conductivity and dipole-moment). PUs are soluble in polar solvents, the principal solvent used for PUs dissolution is the 1,1,1,3,3,3-hexafluoro-2-propanol (HFP) (Bashur, Shaffer et al. 2009; Caracciolo, Thomas et al. 2009; Shah, Manthe et al. 2009; Amoroso, D'Amore et al. 2011). HFP is a very aggressive and toxic solvent that is able to break the inter-urea hydrogen bonds and to promote the appropriate dissolution of PUs. However, other less toxic organic polar solvents were used in the dissolution of PUs to get solutions suitable for electrospinning such as DMF (Hu, Wang et al. 2011), DMAc (Tan, Hu et al. 2015), DMSO, THF (Mondal 2014), chloroform (Riboldi, Sadr et al. 2008) and dichloromethane (Han, Cao et al. 2011).

DMF and DMAc are dipolar aprotic solvents, which have high boiling points, dielectric constants and dipole moments due to the presence of carbonyl groups that act as electronegative acceptors. Solutions with these solvents have low viscosity, rendering thin and regular fibers when electropun (Pattamaprom, Hongrojjanawiwat et al. 2006). However, the resulting fibers cannot dry before reach the collector and fuse with each other due to the high boiling point of these solvents (Veleirinho, Rei et al. 2008). On the other hand, solvents such as THF, chloroform and dichloromethane have low boiling points and dielectric constants. Solutions with these solvents have high viscosity and surface tension (Lee, Kim et al. 2002). Usually, when these solutions were electrospun, the resulting fibers have large and irregular diameters. Due to the high viscosity and low boiling point, the jet can dry and block the needle tip, preventing the electrospinning process.

PUs fibers without defects are usually produced using a mixture of two solvents: one with high boiling point and dielectric constant and other with low boiling point and dielectric constant (Wang, Burugapalli et al. 2013; Mondal 2014; Trinca, Abraham et al. 2015). In this work, binary mixtures of solvents such as: Chloroform:DMAc, Chloroform:DMF, THF:DMAc and THF:DMF at 50:50 proportion were used to dissolve the synthetized PUs for electrospinning. Solutions from THF:DMF solvent mixture were the ones that when electrospun render fibrous mats without defects and with uniform fiber diameters (Figure 3.12B). Therefore, other THF:DMF proportions were evaluated to dissolve and electrospun PUs. PUs dissolved in 30:70 THF:DMF solvents rendered less viscous solutions due to the high amount of DMF. Fibers produced from this solution did not dry before reaching the collector; resulting in a bounded fiber network (Figure 3.12A). On the opposite, PUs solutions with 70:30 THF:DMF have superior viscosity and when electrospun rendered fibrous mats with less uniform fiber diameters (Figure 3.12C) due to the fast THF evaporation before the fibers reach the collector.

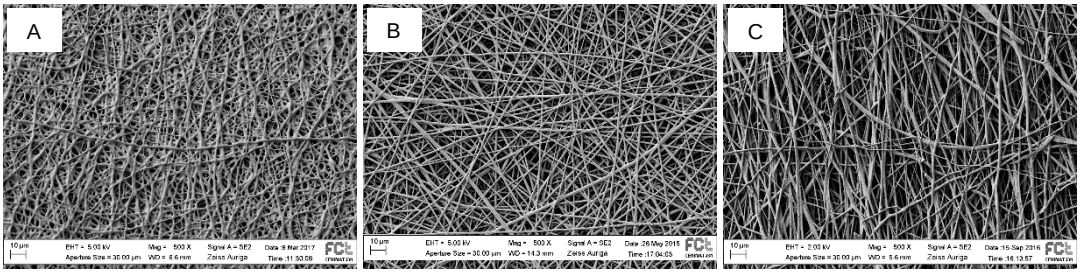

Figure 3.12 – SEM images of the electrospun fibers produced from 20% PU-DMPA/CS solution with THF:DMF at different ratios, using the setup parameters 16 kV, 1.0mL/h and 20cm. (A) 30:70; (B) 50:50 and (C) 70:30. Scale bar 10 µm.

After the choice of the solvent, the concentration of the solution was optimized. It is important to establish the critical solution concentration to produce fibrous mats without beads, i.e., the concentration required for polymer chain entanglement (Chen, Huang et al. 2010). This value depends on the characteristics intrinsic to the polymer, mainly the molecular weight. Higher polymer concentrations are required for polymers with low molecular weight. Three PUs concentrations were tested: 15, 20 and 25 wt%. Fibers with beaded morphology were observed using the 15 wt% solution (Figure 3.13A), indicating that this concentration is not enough to produce polymer chain entanglement. The applied electrical field and surface tension break the polymer chains into fragments before reaching the collector. Increasing the solution concentration to 20 wt% was enough to produce fibers with uniform diameters and without defects (Figure 3.13B). Solutions with 25 wt% concentration (Figure 3.13C) clogged at the needle tip due to their superior viscosity, which result in irregular fibers with large diameters.

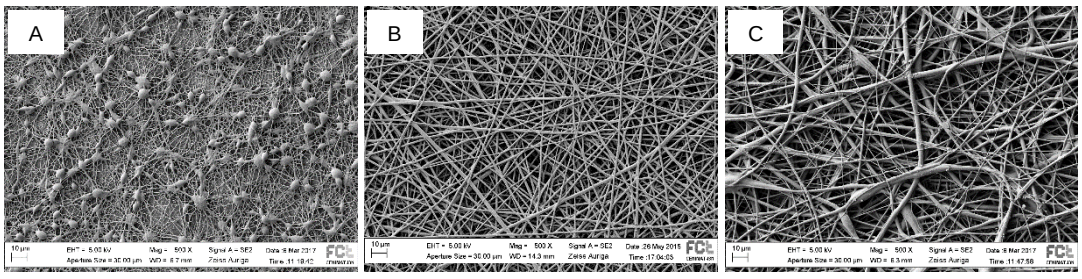

Figure 3.13– SEM images of the electrospun fibers produced from PU-DMPA/CS solution at different concentrations with 50:50 THF:DMF solvent system, using the setup parameters16 kV, 1.0mL/h and 20cm. (A) 15 wt%; (B) 20 wt% and (C) 25 wt%. Scale bar 10 µm.

The electrospinning set-up parameters (voltage, distance between the needle tip to the collector and flow rate) were adjusted to get uniform fibers and a stable electrospinning process over long periods. Small variations of the set-up parameters did not influence significantly the fiber diameter and morphology but influence the stability of the electrospun process over time. Therefore, in order to deposit fibers over a long period of time in order to create a matrix with considerable thickness for further manipulation and characterization, the parameters were settled

as 20 cm for the distance between the needle tip and the collector, 16 kV for the applied voltage and 1.0 mL/h for the flow rate.

The solutions of PU-CS and PU-DMPA were also electrospinnable using the 50:50 THF:DMF solvent binary mixture. The 13 wt% PU-CS solution concentration was used to produce fibers without defects and with uniform diameter, similar to the PU-DMPA/CS fibers. The electrospinning setup parameters were defined as 20 cm distance from the needle tip to collector, 13 kV applied voltage and 1.0 mL/h flow rate. The PU-CS has larger chain length when compared to other PUs, allowing the solution to be electrospun at lower concentrations.

To electrospun PU-DMPA, a solution of 40 wt% concentration was required and set-up parameters were defined at 20 cm distance from the needle tip to collector, 15 kV applied voltage and 1.0 mL/h flow rate. Such high concentration was required to achieve the viscosity that allows the solution to be successfully electrospun, suggesting a small polymer chain length (Zhang, Miao et al. 2004).

Mats from the synthetized PUs were obtained using the defined parameters and further tests were performed to access their properties. For comparison purposes, thin films were also produced from each PU. In the following, Films and fiber Mats are identified by preceding the PU designation by F_ and M_, respectively.

3.3.4 Characterization of the electrospun nanofibers

3.3.4.1 Morphology

SEM images of the electrospun fiber mat are shown in Figure 3.14, together with their respective fiber diameter histograms. PU-DMPA/CS and PU-CS exhibit a regular shape with an average diameter of (873 ± 313) nm and (1066 ± 304) nm, respectively. In the PU-DMPA mats, fibers with a mean diameter of (1620 ± 523) nm form a network of irregular fused fibers. This is a consequence of the incomplete solvent evaporation (which depends not only on the solvent evaporation rate but also on the interactions between the solvent and the polymer) during the flight of the polymeric jet towards the collector.

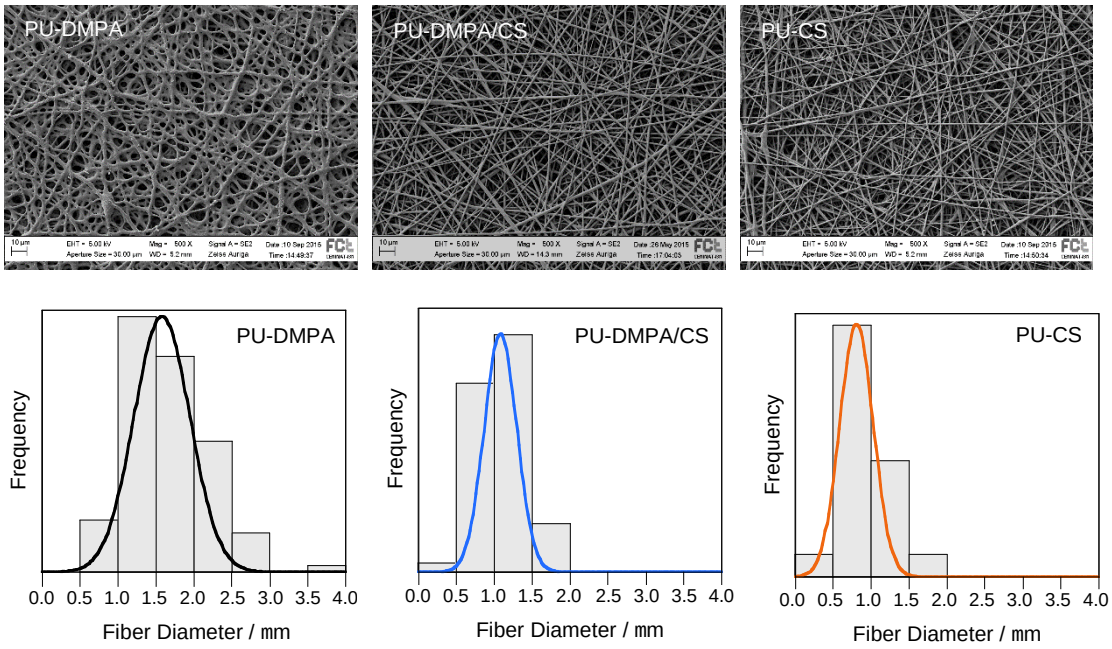

Figure 3.14 – SEM images of electrospun fibrous matrices produced from PU-DMPA, PU-DMPA/CS and PU-CS and their respective fiber diameter histograms. Scale bar: 10 µm.

The porosity of the fibrous mats was determined using the Archimedes method. The porosity of the PU-DMPA, PU-DMPA/CS and PU-CS fibrous mats is 74±4, 73±4 and 46±5%, respectively. SEM images depicted in Figure 3.14 are well correlated with the porosity values. PU-DMPA/CS and PU-CS mats with a regular morphology have superior porosity when compared to PU-DMPA mats. The porosity is dependent on the fiber diameter (Wang, Burugapalli et al. 2013), mats with superior fiber diameter exhibit higher pore size and pore volume. Although PU-DMPA mats have superior fiber diameter, they were less porous than other mats due to their fused morphology.

3.3.4.2 **Mechanical properties**

Typical stress-strain curves for films and mats are represented in Figure 3.15. All samples showed high strains at break due to the soft segment.

Films exhibit stress-strain curves typical of thermoplastic elastomers, with an initial linear region (elastic behavior extending up to about 30% strain) followed by a plastic deformation with strain hardening at higher elongations due to strain induced crystallization of soft segments, characteristic of a higher degree of phase separation (Ahmad, Khan et al. 2014).

The slopes of the linear regions of the films' stress-strain curves are (2.5 ± 0.4) MPa for PU-DMPA, (6.3 ± 0.9) MPa for PU-DMPA/CS and (6.4 ± 0.5) MPa for PU-CS (Table 3.5), showing that the Young's modulus is higher for films produced from PUs containing CS as chain extender. However, the Young's modulus does not differ between the PU-DMPA/CS film and the PU-CS film. The increase in Young's modulus with the presence of CS can be related to the increase in hydrogen bonding between hard segments that, acting as physical crosslinks, results in a more rigid structure (Delpech and Coutinho 2000; Garrett, Runt et al. 2000; Saralegi, Rueda et al. 2013)

and to the enhancement of the hard domains cohesion due to the presence of urea bonds (absent in PU-DMPA).

The Young's modulus obtained for the fiber mats increases with CS content in the PU structure: (0.82±0.04) MPa for PU-DMPA, (1.54 ± 0.30) MPa for PU-DMPA/CS and (3.25 ± 0.31) MPa for PU-CS (Table 3.5). Comparing these results with the films' Young's modulus we can conclude how processing impacts the mechanical properties – the Young's modulus is lower for the fiber mat's than for the corresponding films. The mechanical properties depend on the structure and porosity of the fibrous mats. The fibrous mats is a porous structure that possess bonded and non-bonded structures among fibers. At low strain, the non-bonded (physically crossed) structures are responsible for the energy dissipation due to their easily slippage, while bonded structures resist to the applied load. At higher strains, both the breaking of the bonded structures on the fibers and the slippage are a source of dissipation energy (Lee, Lee et al. 2005).

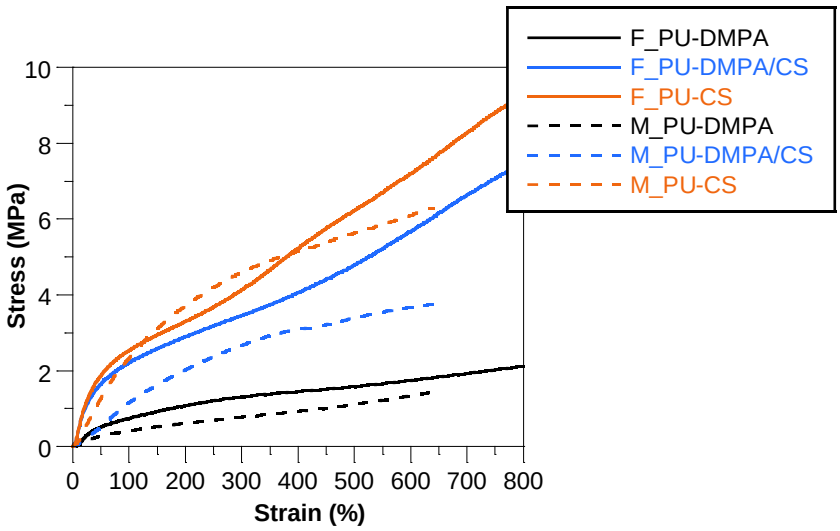

Figure 3.15– Tensile response curves of the electrospun nanofibrous matrices produced from PU-DMPA, PUU-DMPA/CS and PU-CS.

The hysteresis behavior of the PUs fibrous mats were evaluated. The PUs mats were subjected to 10 cycles of hysteresis by stretching the samples up to 80% elongation with a rate of 80% per minute and then reversing the crosshead direction at the same rate. The hysteresis curves are shown in Figure 3.16 as well as the hysteresis values (in %), which were obtained from the average of at least three independent tests.

The hysteresis percentage of the first hysteresis loop is (63.0 ± 0.9) % for PU-DMPA, (77.0 ± 1.3) % for PU-DMPA/CS and (53.3 ± 4.1) %.for PU-CS. PU-CS fibrous mats exhibited the lowest percentage of hysteresis, due to their superior structural organization, higher molecular weight of the hard segment (only CS) and also the phase segregation of hard and soft segments on this polymer (Ertem, Yilgor et al. 2012). The first cycle has the highest hysteresis value due to superior fibers structural disruption with strain. Then, the others cycles are smaller and turn to a constant

value because deformation is maintained in the same range resulting in slightly alterations in the fibers morphology (Tang, Macosko et al. 2014). This hysteresis behavior is characteristic of thermoplastic PUs elastomers.

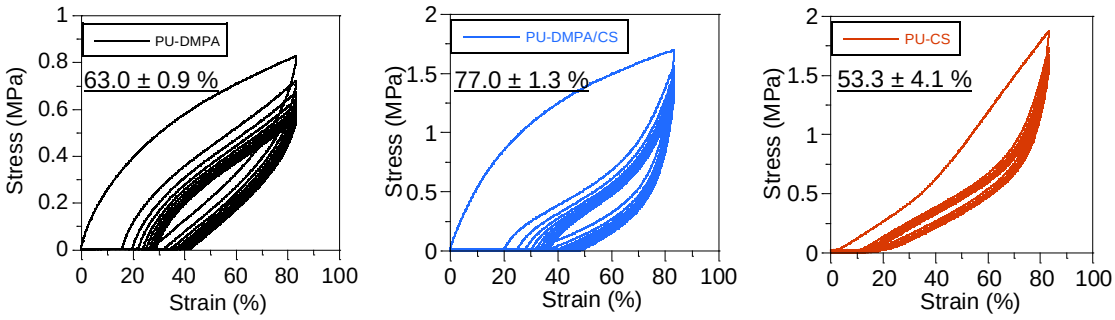

Figure 3.16– Hysteresis loops after 10 cycles stretching and recovering of electrospun fibrous mats.

3.3.4.3 Crystallinity analysis

In Figure 3.17 is shown the XRD patterns for CS, PCL-diol and PU films and fibrous mats. The fitting of the PUs diffractograms was performed by a sum of Voigt functions. As an example, Figure 3.18 shows the fitting of the PU-DMPA/CS fibrous mats. CS exhibited two crystalline reflections at 2θ = 10.5º and 19.7º, and a small shoulder at 21.9º. The two reflections were from the (020) and (110) planes of chitin, respectively, which are characteristic of the semi-crystalline structure of CS (Zhang, Xue et al. 2005). PCL-diol presented three strong reflections peaks at 2θ = 21.4º, 22.0º and 23.7º, which corresponded to the (110), (111) and (200) planes of the crystal structure. Other small peaks at 2θ = 15.7º and 24.5º appear due to the diffraction by the (102) and (201) planes (Ferreira, Gomes et al. 2014).

In all difractograms were observed peaks at around 2θ = 19º, 21º and 24º are noticeable. The broad peak at 2θ = 19º is related to the amorphous/irregular phase of PUs, resulting from the hard segments. They interact very fast with each other due to their strong interactions, and their disposition in the PU structure becomes amorphous without time to organize in a stable disposition (Zia, Bhatti et al. 2009; Zhang, Jiang et al. 2011). The two sharp diffraction peaks at 21º and 24º arise from the diffraction at, respectively, (110) and (200) diffraction planes of the PCL (Alishiri, Shojaei et al. 2014). These sharp peaks indicate the ability of soft segments to crystallize in the PUs' structure due to phase separation. PCL crystallized regardless of the hard segment; therefore, the polymers phase separated at some extent.

Regarding the films, the one made of PU-DMPA/CS exhibited the highest crystalline degree (Table 3.5). Its higher crystallinity, when compared to the PU-DMPA film, , may be related with a higher phase segregation resulting from more and stronger hydrogen bonds due to the presence of CS in the PU structure, including those involving the urea linkages, and, possibly, between the ionic groups of DMPA and the CS amine group (Momtaz, Barikani et al. 2015). In the PU-CS film, the crystalline diffraction peaks of soft segment are almost absent. CS, as the unique chain extender, is responsible for stronger hydrogen bonding, resulting in the formation of a rigid network that restricts the free mobility characteristic of the soft segment, decreasing the

crystallinity of the final PU (Lin, Wei et al. 2014). For the PUs containing CS, the relative value of the crystalline peak intensity is higher in the diffractograms of the fibrous mats than in the films. This difference shows that the technique used to process the solutions influences the reorganization of the PU molecules. During electrospinning, the polymeric jet is subject to strain resulting from the repulsive electrical interactions between its charged elements. Meanwhile, solvent evaporates from the thin polymeric jet. Due to a rapid solvent evaporation, electrospinning may compromise the rearrangement of the semi-crystalline structure observed in a cast film (Shah, Manthe et al. 2009; Ribeiro, Sencadas et al. 2016). However, with the appropriate solution concentrations and applied voltages, the crystalline degree can be higher in the electrospun fibers than in the films due to the molecular chain orientation along the fiber axis caused by the stretching forces exerted on the polymeric solutions (Kongkhlang, Tashiro et al. 2008; Ero-Phillips, Jenkins et al. 2012). This phenomenon seems to be dominant when electrospinning the CS containing PUs.

For films, crystallite size, calculated from the FWHM of the (110) diffraction peak, is approximately equal for PU-DMPA and PU-DMPA/CS, slightly higher for the latter, in line with its higher crystalline degree. PU-CS films exhibit the smallest crystallite size, which is not surprising given its nearly zero crystalline degree. For fibers, crystallite size is similar for all PUs, somewhat smaller for the PU-DMPA mats that also possess the smallest crystalline degree. For PU-DMPA/CS and PU-CS, crystallite size is nearly the same in spite of their very different crystalline degree, suggesting that the higher crystalline degree of PU-DMPA/CS is due to a higher abundance of crystalline regions.

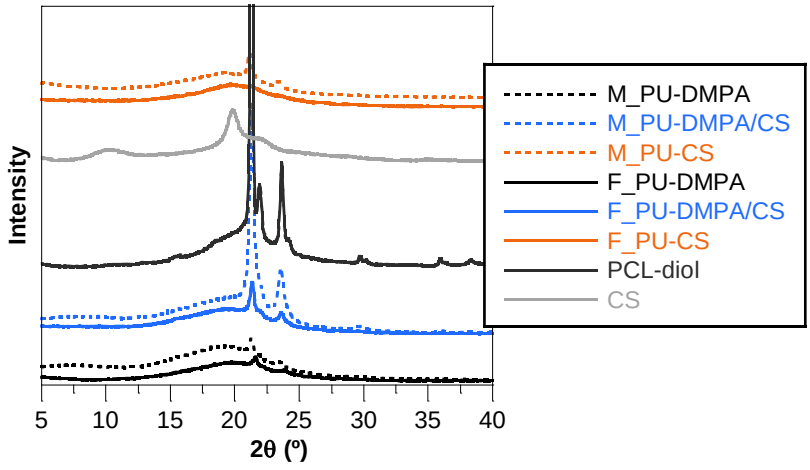

Figure 3.17 – X-Ray diffractograms of PCL-diol, CS, and films and fiber mats from PU-DMPA, PU-DMPA/CS and PU-CS.

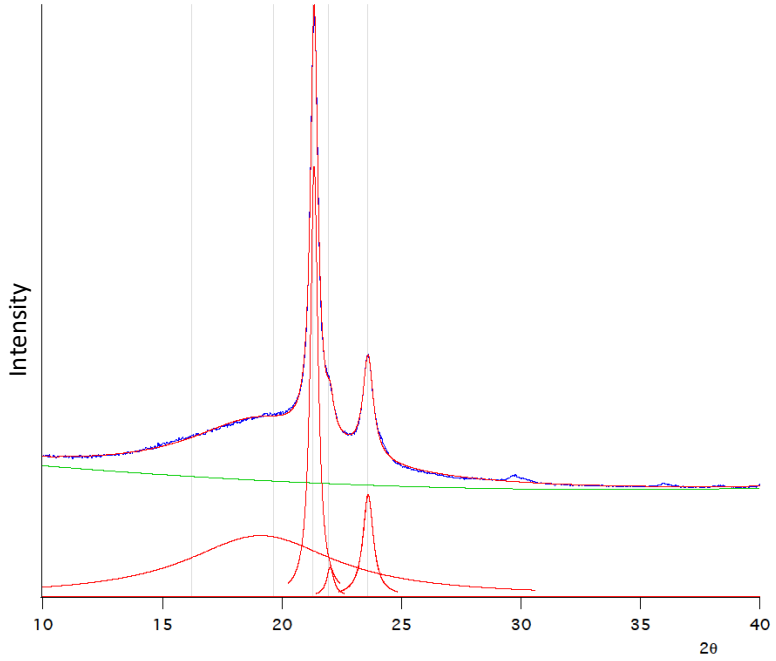

Figure 3.18– Fitting of the characteristic peaks of the PU-DMPA/CS fibrous mat diffractogram with Voigt functions (red) and a cubic background (green).

Table 3.5– Results from XRD and tensile tests of films and fibrous mats. Crystalline degree, ($w_{c,x}$), full with at half maximum of the highest intensity crystalline diffraction peak, (FWHW), crystallite size, (τ_c), Young's modulus, (Y), strain at break (ε_r), and tensile stress at 600% strain (σ_{600}).

Films/Fibrous Mats	***XRD***			***Mechanical tests***		
	Crystallinity $w_{c,x}$ (%)	FWHW (º)	Crystallite size τ_c (nm)	Young Modulus Y (MPa)	Elongation at break ε_r (%)	Tensile stress at 600% σ_{600} (MPa)
F_PU-DMPA	3.60 ± 0.17	0.379	21.1	2.5 ± 0.4	>600	1.9 ± 0.3
F_PU-DMPA/CS	11.7 ± 0.2	0.347	23.1	6.3 ± 0.9	>600	6.3 ± 0.5
F_PU-CS)	0.83 ± 0.02	0.616	13.0	6.4 ± 0.5	>600	7.6 ± 0.6
M_PU-DMPA	4.89 ± 0.03	0.432	18.5	0.82 ± 0.04	>600	1.2 ± 0.1
M_PU-DMPA/CS	31.5 ± 0.3	0.380	21.0	1.5 ± 0.3	>600	3.5 ± 0.2
M_PU-CS	7.79 ± 0.14	0.363	22.0	3.3 ± 0.3	>600	5.3 ± 0.3

3.3.4.4 **XPS analysis**

N, C and O atomic percentages at the PUs films' and fiber mats' surface were determined by XPS. For all samples, measurements were acquired at two take-off angles – 0° and 60° – in order to investigate the differences between the uppermost surface and the bulk in a layer ~10

nm thick. For both take-off angles, the C 1s region in the spectra, located at 285-290 eV, was fitted with four component peaks (Table 3.6). The peak at the lowest binding energy was used as reference peak for charge accumulation correction and set at 285 eV. It is assigned to C sp^3 in C-C/C-H. The second peak, centered at (285.8 ± 0.2) eV was assigned to carbon in C-N and to α-carbons in ester (or carboxylic) and amide groups (Beamson 1992). The third one was centered at (286.8 ± 0.2) eV and was assigned to carbon singly bound to oxygen (Beamson 1992). Finally, the fourth peak, centered at (289.2 ± 0.2) eV is assignable to carbons from amide (from chitosan), ester (from DMPA), urethane and even unreacted isocyanate groups (Beamson 1992). The N 1s region was fitted with a single peak at (399.8 ± 0.1) eV indicative of amide and/or PU nitrogen (N-C(O)-O). The existence of a component corresponding to a positive nitrogen due to protonation or involvement in hydrogen bonding is just suspected and no corresponding peak was fitted. The O 1s was resolved in two component peaks at (532 ± 0.3) eV assigned to carbonyl oxygen in X-C=O groups (X being one or two nitrogen and/or an oxygen), and at (533.5 ± 0.2) eV corresponding to oxygen singly bound to carbon in ester or urethane groups. The first peak may also correspond to oxygen in alcohol groups (Beamson 1992). Figure 2.1 shows the C 1s, N 1s, and O 1s spectra and the respective fitted components for PU-CS films and fiber mats at a 0º take-off angle.

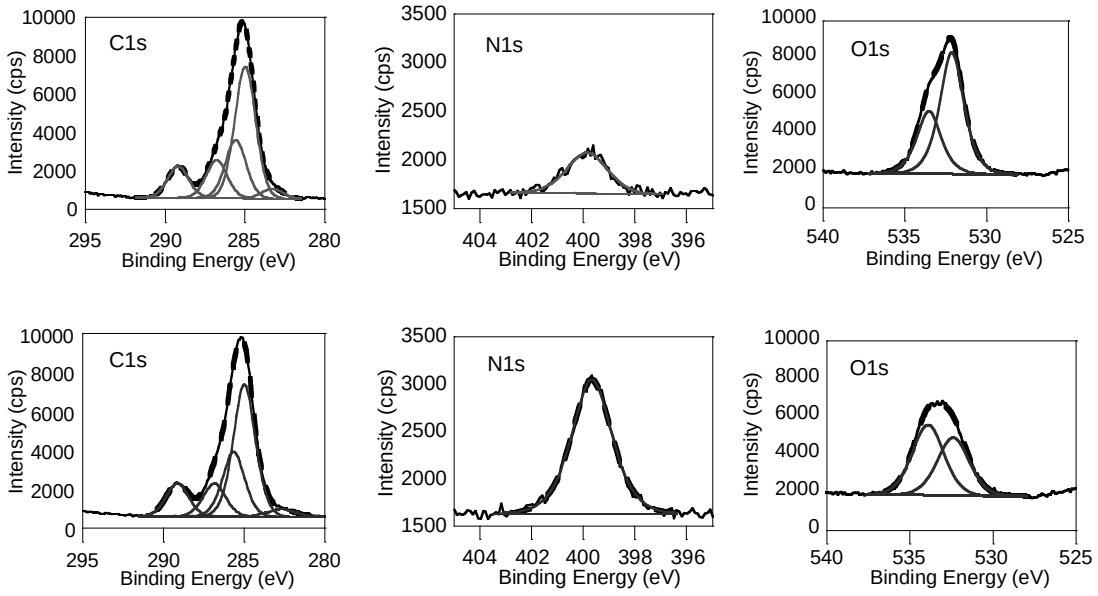

Figure 3.19 – The C1s, N1s and O1s XPS spectra and the respective fitted peaks for PU-CS films (top line) and fibrous mats (botoom line) at 0º take-off angle. The small peak fitted at ~283 eV in the C 1s regions is a component due to the sample holder.

Quantitatively, Table 3.6 gathers, for the take-off angle 0º, the XPS atomic percentages as well as a few XPS atomic ratios. The first clear result is that the amount of nitrogen at the surface is much lower for films than for fiber mats as observed through the ratios of the amount of nitrogen to total carbon (N/C), and especially through the N /(C 1s4) since the component C 1s4 cannot

come from any contamination. Whereas in fiber mats, that ratio is around 0.5, increasing slightly but monotonically with the replacement of DMPA by CS, in the films, that ratio, in the absence of CS, is 0.17 and its variation with the CS content is far from monotonic. This is indicative that some added chitosan is present in the superficial 10 nm. But, basically, the largest contributor to the nitrogen detected at the surface is the isocyanate.

Table 3.6 – XPS atomic percentage composition of different PU films and fibers surfaces.

		Fiber mats			Films		
		PU-DMPA	PU-DMPA/CS	PU-CS	PU-DMPA	PU-DMPA/CS	PU-CS
C 1s	C 1s1: C-C, C-H	35.2	41.9	36.5	45.6	47.3	36.3
	C 1s2: C-N, C-H (vib)	17.9	11.6	17.8	9.0	8.4	16.0
	C 1s3: C-O	9.3	8.5	9.1	8.0	8.7	10.4
	C 1s4: N-C=O, O-C=O, Urethane, -N=C=O	9.5	9.4	9.0	9.1	8.2	8.7
O 1s	O 1s1: C=O	11.6	11.5	9.9	16.5	16.2	17.7
	O 1s2: C-O	11.7	12.0	12.1	10.5	8.9	9.1
N 1s	amide, urethane, cyanate	4.8	5.1	5.6	1.3	2.3	1.7
Atomic ratios	O1s1/O1s2	1.0	1.0	0.8	1.6	1.8	1.9
	C 1s4/O1s1	0.8	0.8	0.9	0.6	0.5	0.5
	C 1s4/O1s2	0.8	0.8	0.7	0.9	0.9	1.0
	N / C 1s4	0.52	0.60	0.61	0.17	0.27	0.16
	N/C	0.067	0.071	0.077	0.019	0.032	0.024
	O/C	0.32	0.33	0.30	0.38	0.35	0.37

Another striking difference between mats and films, concerns the two oxygen components: in mats they have similar areas that are similar to the one of carbon in urethane, ester, amide groups (C 1s4 component). This is compatible with the C 1s4 being mainly composed of groups where the number of C=O and O-C bonds are the same. This means that at the surface of the fiber mats the segments with ester and urethane groups are dominant, the urethane being half of the total ones at the surface (the percentage of N 1s, mainly from urethanes, is approximately half the percentage of C 1s4). With the replacement of DMPA by CS, the slight increase of the nitrogen amount may mean that the surface incorporates some CS. In the films, however, the O 1s lower binding energy component, is much larger than the O 1s2 component (see O 1s1 / O

1s2 ratio in table 3), the ratio C 1s4 / O 1s2 keeping a value around 1. Moreover, in films both components show an average increase of 0.4 eV in the position binding energy. These results combined with the fact that the amount of nitrogen is low, are compatible with the O 1s1 component, contrarily to the mats case, not being just attributable to O=C in the groups assigned to C 1s4 component. They should also contain C-O-C or C-OH groups where the oxygen, despite being singly bound to carbon, may have a lower binding energy and superpose to the oxygen in a carbonyl group.

Differences between the two take-off angles were not significant indicating that, within the analysed depth in XPS (~10 nm), the chemical composition is homogeneous. Usually, differences between the take-off angles are related with phase segregation behavior. However, the absence of significant differences between the angles is not necessarily related with the absence of phase segregation. As investigated before by Queiroz et al., the undetected differences between the take-off angles could be explained by a segregation yielding a superficial layer thicker than the XPS characteristic analysis depth (Queiroz, do Rego et al. 2006). Therefore, the results for phase segregation for films are constant and extended to a layer of at least 10 nm thickness.

As mentioned above, ester groups from PCL segment are predominant at the films' surface, while ester and urethane are present in similar concentrations at the fiber's surface. A possible reason for this difference is the attraction towards the surface of groups with a higher polarity by the surface charge carried by the polymeric jet during electrospinning.

3.3.4.5 **Wettability**

In Figure 3.20 is shown the results of WCA measurements performed on fiber mats and films, as well as the representative image of the water drop on the substrates surface.

For films, the WCA was higher for PU-DMPA (103 ± 2 º) samples, indicating the hydrophobicity of this films' surface. This hydrophobic character is not surprising, as PCL is PUs' main component. When DMPA is replaced by CS as chain extender, the WCA is reduced to (76 º ± 2 º) in the case of PU-DMPA/CS and to (91 º ± 5 º) in the case of PU-CS.

This shows that replacement of DMPA by CS in the PU structure reduces the film's hydrophobicity, which is in agreement with the XPS indication that some added chitosan is present at the surface. Zhu et al. reported that the incorporation of macromolecules (such as CS) in the PUs structure reduce the hydrophobicity of the final PU (Zhu, Gao et al. 2004). However, in another study, Barikani and co-workers, who incorporated CS in the PU backbone and produced films from aqueous PU dispersions, verified that the increment of CS on the final PU structure increase the hydrophobicity of the film surface (Barikani, Honarkar et al. 2010), but the values obtained are lower than ours. These diffeences may be due to differences between the methods to produce the films.

In the fibrous mats, the WCA increases slightly with the increment of CS in the PUs structure: (124 º ± 5 º), (139 º ± 2 º) and (153 º ± 4 º) for PU-DMPA, PU-DMPA/CS and PU-CS mats, respectively. All the values are superior to the ones of the corresponding films. The WCA can be influenced by the surface chemistry, roughness and fiber diameter of the fibrous mats.

According to the surface chemistry analyzed by XPS, the fibers' surface present urethane groups in contrast to the films surface, which present mainly PCL. This fact alone should result in more hydrophilic fiber mats than films, contrary to what was observed. However, the higher surface roughness and porosity of the fibers lead to the entrapment of air bubbles at the water-material interface, leaving less contact area for water, contributing to an increase in WCA on mats (Tijing, Park et al. 2013). Among the mats, the higher fiber diameters contribute to inferior WCA values (Tijing, Park et al. 2013), which can explain the lower WCA for PU-DMPA fibers that have the larger fiber diameter.

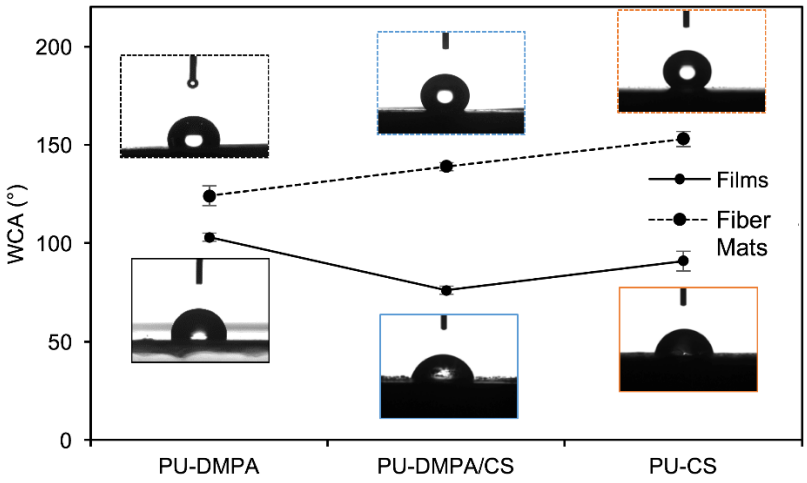

Figure 3.20– Water contact angle values for the PUs films and mats and the respective water drop images.

3.3.4.6 Hydrolytic and enzymatic degradation

In Figure 3.21 is shown the degradation profile of PU films and fibers immersed in both PBS (Figure 3.21A) and lipase solution (Figure 3.21B).

In PBS, films and fibrous mats made of PU-DMPA/CS and PU-CS barely lose weight during 60 days. Those of PU-DMPA show two distinct degradation stages: in the first month they barely lose weight and then, a sharp weight loss is observed, a characteristic signature of bulk erosion process.

Lipase cleave preferentially the ester bonds of the PCL soft segment in the PU structure, resulting in α-hydroxyacids degradation products and urethane and urea fragments (Tokiwa, Ando et al. 1990; He and Chu 2013). In comparison with PBS, the degradation of the PUs films and mats was accelerated in lipase solution, and the mass loss profiles are typical of surface erosion process. After 40 days, PU-CS samples exhibit the smallest weight loss.

Physico-chemical properties, such as crystallinity, hydrophilicity and water absorption are correlated with hydrolytic degradation. Hydrophilic samples tend to have superior degradation rates while the higher ordered structure of samples with higher crystallinity tend to slower down the degradation process (Umare and Chandure 2008). The degradation rate of the samples decrease with the increment of the CS content in the PU structure. A slower degradation rate is

indicative of a higher molar mass resulting from the multi-functionality of CS molecule that is capable of reacting with multiple isocyanate groups leading to a crosslinked PU.

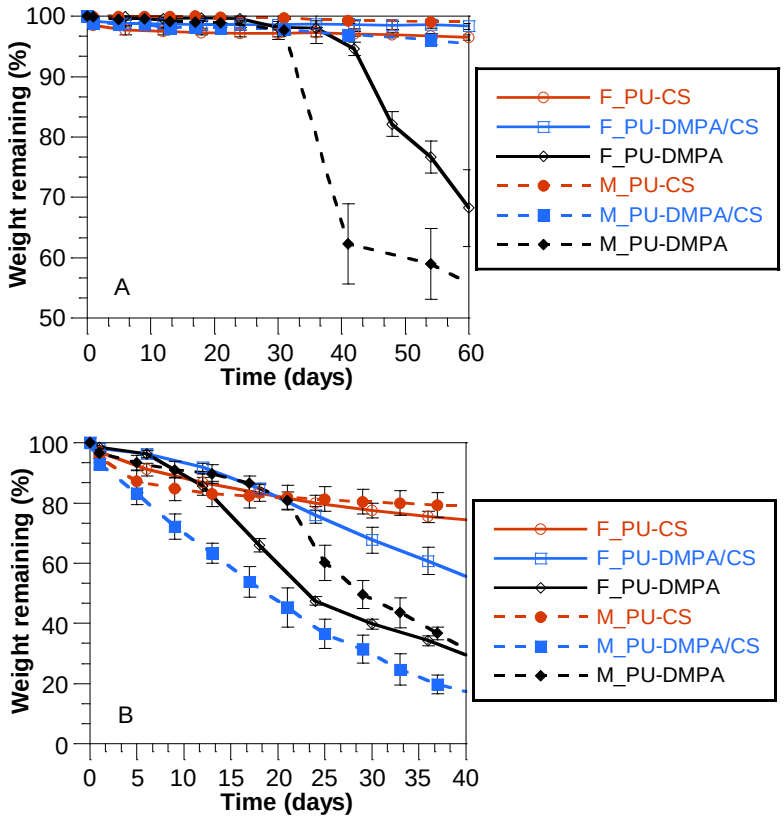

Figure 3.21 – Hydrolitic degradation of PU films (F_) and fibrous mats (M_) produced from the synthetized PUs immersed in PBS (A) and in lipase solution (B).

After the degradation assays, the PU samples were dried and analyzed using FTIR to identify their remaining structure. PBS and lipase cleave the ester linkages in PUs, which can be detected by variations in bands between 1038 and 1238 cm^{-1} assigned to the PCL C-O-C bond (Figure 3.22). The C-O stretching vibration of alcohol and carboxylic acids increase in the degraded samples when compared to the original samples, indicating that carboxylic acids were formed from the degradation of the esters in PCL (Guelcher, Srinivasan et al. 2008). The simultaneous increase in the intensity of the C=O group (1722 cm^{-1}) and the slight decrease in the intensity of the bonded carboxyl group (1640 cm^{-1}) indicates that some urethane and urea bonds were disrupted, leaving free carboxyl groups. These differences were barely detected in PU-CS samples that have a slow degradation rate during the period of study.

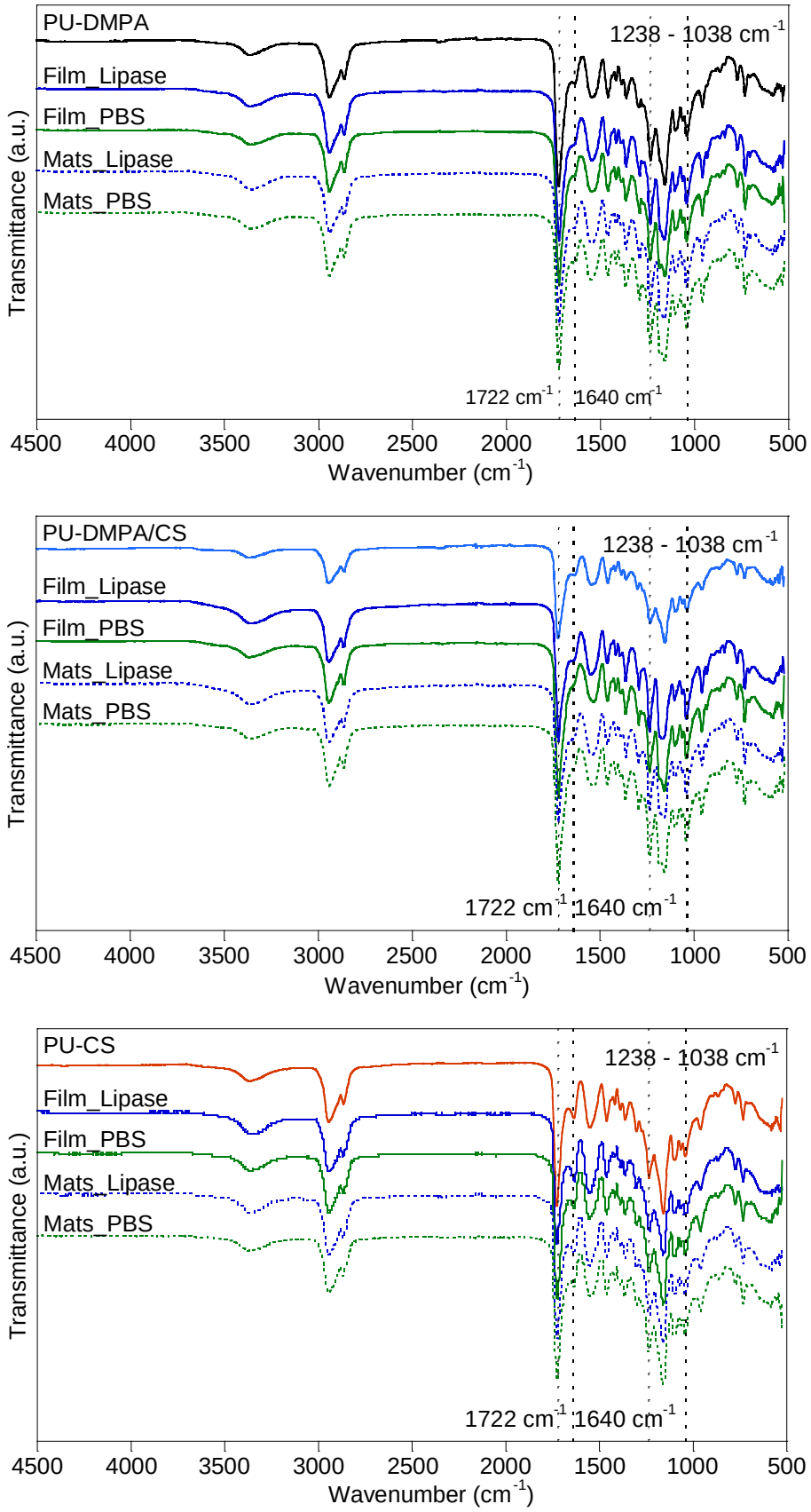

Figure 3.22 – FTIR spectra of PU-DMPA, PU-DMPA/CS and PU-CS films and fibrous mats after degradation in PBS and in lipase solution.

3.3.4.7 **Cellular assays**

Toxicity

The potential cytotoxic effects of films and electrospun mats, obtained from the synthesized PUs, were evaluated using the extract method and a culture of HFFF2 cells. Results of the colorimetric resazurin assay, performed with cells in contact with the extracts, are shown in Figure 3.23. Viability values are normalized to the negative control (C-, cells in complete culture medium) and are all superior to 94%, indicating the absence of cytotoxicity. On the opposite, the positive control (C+, cells seeded with 10% DMSO) viability is very low, which confirms the test's sensitivity to cell viability. Cells in contact with the pure extracts during 48h were visualized using the optical microcospe before to perform the resazurin test (Figure 3.24). The cells cultured with PU pure extract are stretched over all the well, established contact points with each other similar to the cells in the C-. On the opposite, a few cells were observed in C+, confirming that most of the cells die in the presence of DMSO.

These data indicate that neither the synthetized PUs nor their processing leads to the leaching of soluble cytotoxic compounds from the films and fiber matrices. Therefore, they can be considered for applications in tissue engineering.

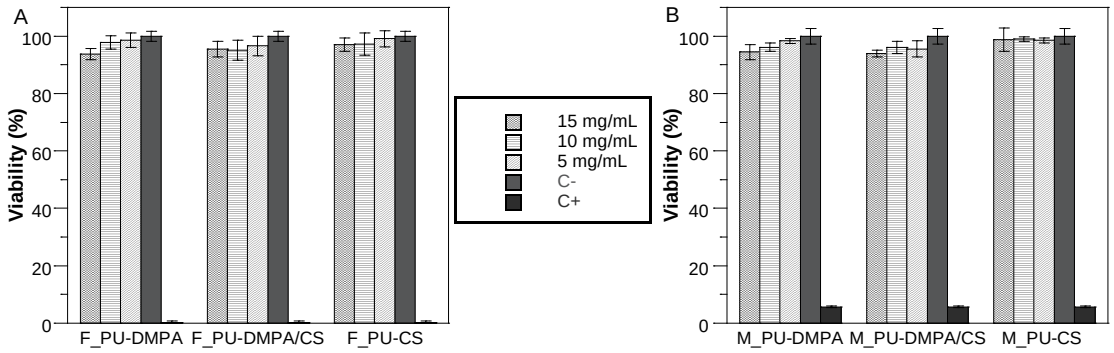

Figure 3.23– Results of HFFF2 cells' viability, obtained in a cytotoxicity assessment of PU-DMPA, PU-DMPA/CS and PU-CS (A) films and (B) electrospun mats. For each material extracts were obtained by placing a 15 mg sample in 1 mL of DMEM (15 mg/mL) and by diluting this extract by the factors 3/2 (10 mg/mL) and 3 (5 mg/mL).

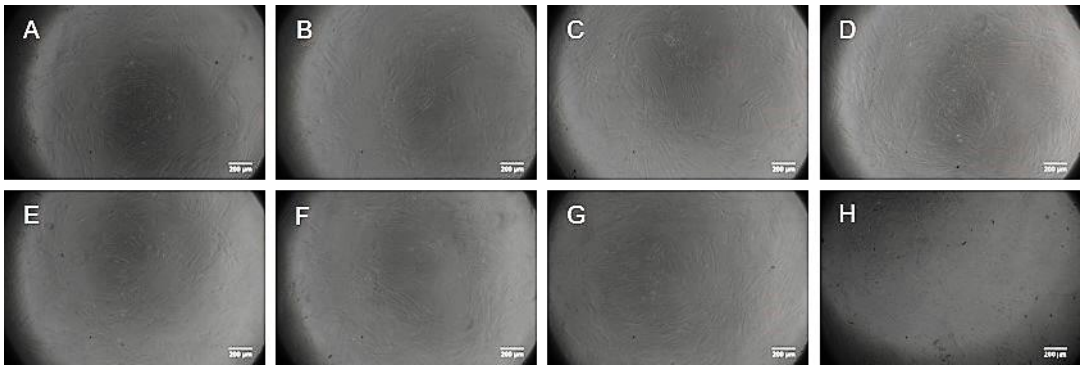

Figure 3.24– Optical microscope images of the HFFF2 cells seeded in 96 well plate in contact with pure extracts of PU- DMPA (A), PU-DMPA/CS (B) and PU-CS (C) films, negative control (live cells) (D), PU-

DMPA (E), PU-DMPA/CS (F) and PU-CS (G) fiber mats, and positive control (dead cells) (H). Scale bar: 200 µm.

Cellular adhesion and proliferation

Viability of HFFF2 cells seeded over the surface of PU films, fibrous mats and TCP wells (cell controls, CC) was assessed using the resazurin colorimetric assay. The test was performed after 24 h (day 1) to evaluate the cell adhesion and the on subsequent days up to 10 days in culture to evaluate the cell proliferation. Figure 3.25 shows the results.

The adhesion ratio, calculated as the quotient between the average for each experimental condition and the average viability of cell controls, is reported in Table 3.7. The cell adhesion to all mats was similar to the CC without statistically significant difference. However, cell adhesion to all films was significantly lower (around 50%) when compared to the CC. For all PUs, the difference between cell adhesion to films and electrospun fiber mats is also statistically significant.

Following day 1, cell population scarcely increases in films and fiber mats produced from PU-DMPA. The incorporation of CS in the PU structure increases cell proliferation, with fibrous mats presenting higher cellular proliferation when compared with the corresponding films.

Fibrous scaffolds produced by electrospinning are suitable substrates for cell adhesion and proliferation due to their fibrillar structure similar to the ECM, their high surface area to volume ratio and 3D porous architecture that allow the exchange of nutrients and toxic products conferring the cells with an appropriate environment for their metabolism (see review: (Cui, Zhou et al. 2016)). Therefore, a better performance of the fiber mats compared to films was expected.

Other factors such as surface composition, hydrophobicity, surface roughness and degree of microphase separation in PUs influence the cell behavior. Concerning surface composition, fibrous mats revealed a higher content of N which increases when DMPA is replaced by CS. The N may favor the interaction with the negatively charged cell surface membrane, which may contribute to the observed differences between films and fiber mats cell adhesion and to the higher proliferation ratio in samples made of PUs containing CS. Moderate hydrophilicity is required to allow the adsorption of proteins (from culture medium and released from the cells) retaining their native conformation (Wilson, Clegg et al. 2005). Although all PU fiber mats with CS are hydrophobic substrates, they support the adhesion and proliferation of the fibroblasts at a level comparable to the control. PUs containing CS, which have a higher phase segregation, exhibit superior cell adhesion and proliferation, consistent with previous reports (Hsu, Chen et al. 2007; Dicesare, Fox et al. 2012).

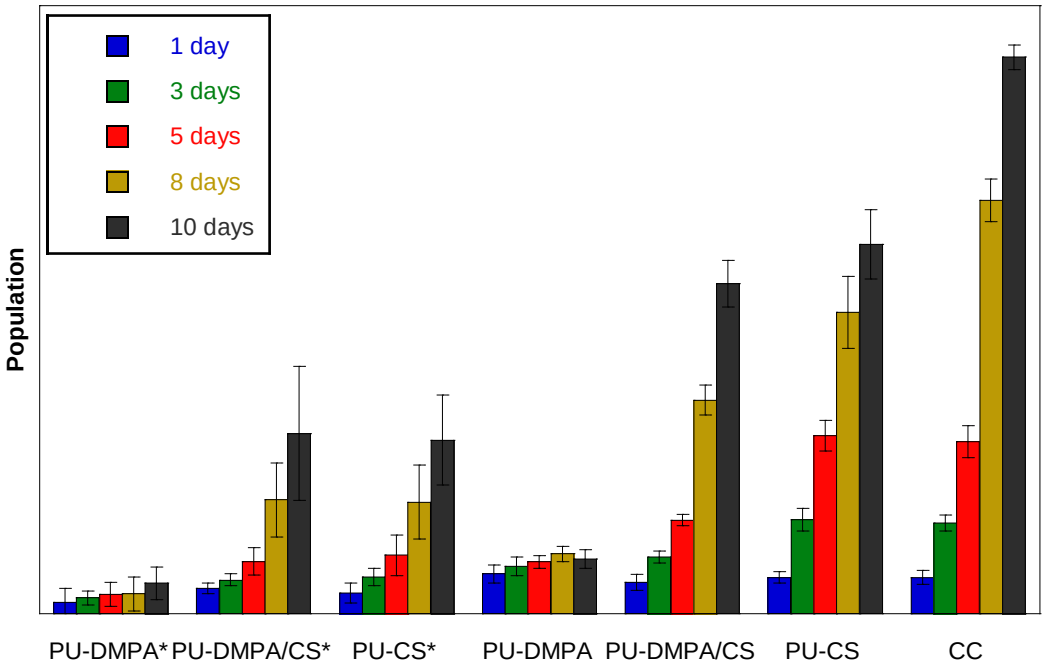

Figure 3.25 – HFFF2 cell population. Cells were seeded on PU-DMPA, PU-DMPA/CS and PU-CS films (*), fibrous mats and TCP wells (CC) and assayed with resazurin on days 1, 3, 5, 8 and 10 of culture. Error bars represent the mean ± standard deviation of n=5 samples.

Table 3.7– Adhesion ratio of HFFF2 cells to films (F_) and fiber mats (M_) produced from PU-DMPA, PU-DMPA/CS and PU-CS and results of the Student's t –test for the probability parameter p regarding the statistical significance of the difference between adhesion ratios (Y=Yes, p<0.05; N=No, p>0.05). Adhesion ratio uncertainty is the combined standard uncertainty.

	Adhesion ratio / %	F_PU-DMPA	F_PU-DMPA/CS	F_PU-CS	M_ PU-DMPA	M_ PU-DMPA/CS	M_ PU-CS	Cell control
F_PU-DMPA	47 ± 8	-	N	N	Y	Y	Y	Y
F_PU-DMPA/CS	65 ± 8	0.0645	-	N	Y	Y	Y	Y
F_PU- CS	52 ± 7	0.5064	0.0901	-	Y	Y	Y	Y
M_ PU-DMPA	84 ± 8	0.0027	0.0220	0.0013	-	N	Y	N
M_ PU-DMPA/CS	91 ± 10	0.0024	0.0194	0.0032	0.4795	-	N	N
M_ PU- CS	104 ± 10	0.0003	0.0013	0.0003	0.0417	0.2089	-	N
Cell control	100 ± 9	0.0003	0.0006	<0.0001	0.0516	0.3378	0.5981	-

After 5 days in culture, fluorescent images of cells are shown in Figure 3.26. Differences in cell morphology are noticeable in cells grown on the different materials and on different substrates (films and fiber mats) of the same PU.

The higher projected cell area observed on the PU-CS substrates, is related to the presence of CS in the PU, which increases their affinity with cells. On films, cells are less spread than on fiber mats and on glass coverslip. On fiber mats, cells display a more elongated morphology. On the glass surface, cells protruded over all directions with noticeable stress fiber

formation. Fibroblast shape is regulated by focal adhesions: with these transmembrane proteins (integrins, which in turn link to the binding domains of the ECM proteins) to the cell cytoskeleton (Zamir and Geiger 2001). Although small diameter fibers (less than 1 µm) may limit size, number and location of focal adhesions, restraining cell spreading on fibers (Badami, Kreke et al. 2006), the number of integrin binding domains may be greater in fiber mats than in films due to the higher adsorption of proteins on their high surface area. This may explain the slightly higher cell proliferation observed on PU-DMPA/CS and PU-CS fibers than on films.

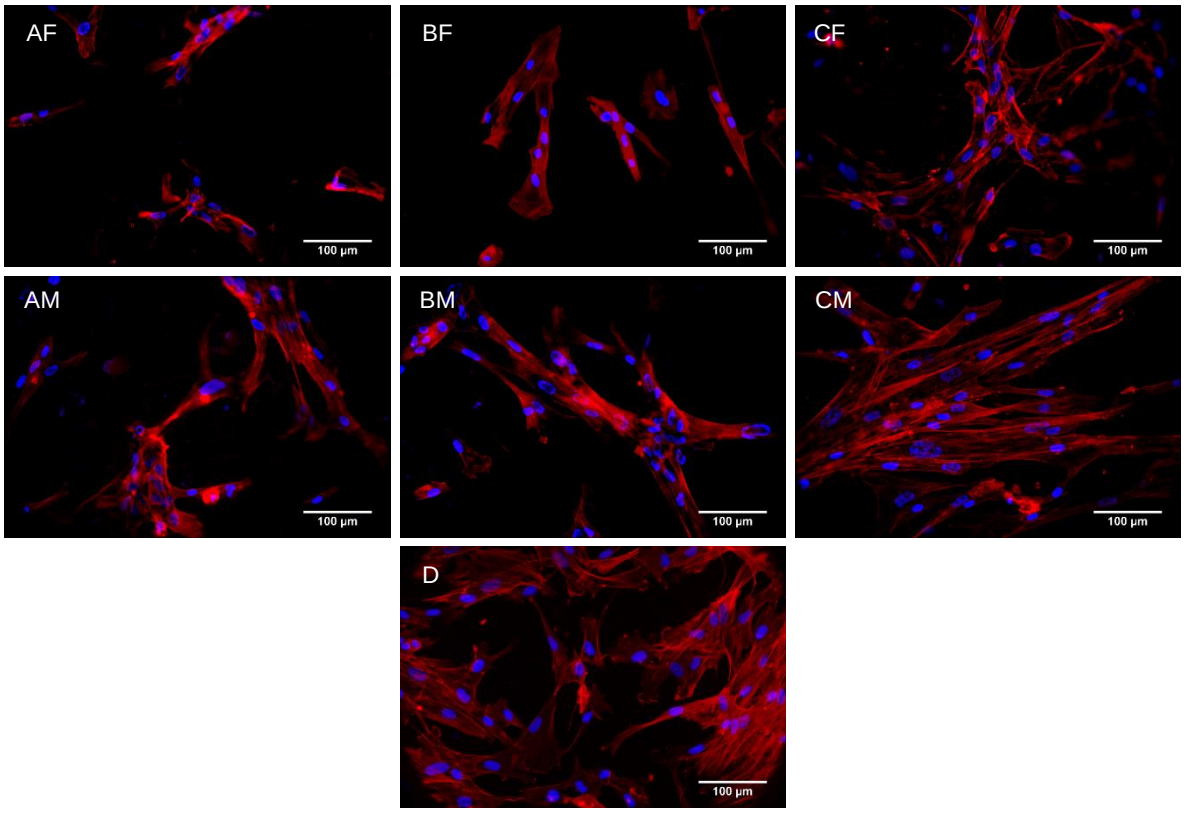

Figure 3.26– Fluorescent images of the cells stained with phalloidin (red) and DAPI (blue) growing on PU-DMPA (AF) films and (AM) fibrous mats, PU-DMPA/CS (BF) films and (BM) fibrous mats, PU-CS (CF) films and (CM) fibrous mats and (D) glass coverslip, after 5 days in culture.

3.3.5 Aligned vs. random electrospun mats

Aligned electrospun fibrous mats can mimic the extracellular matrix of anisotropic tissues. These mats have been preferred for cardiac and neural tissue engineering applications, inducing cell orientation that guide the formation of an oriented ECM.

3.3.5.1 Mats morphology

In order to produce fiber mats from the synthetized PUs, a solvent mixture with 50 wt% THF and 50 wt% DMF and a polymer concentration of 40 wt%, 20 wt% and 13 wt% for PU-DMPA, PU-DMPA/CS and PU-CS, respectively, were used. To get the aligned fibrous mats, a rotatory

mandrel rotating at high speed was used instead of the flat collector. In the following, Random and Aligned fibrous mats are identified by preceding the PU designation by R_ and A_, respectively.

SEM images of the electrospun fibers with either random or aligned morphology are shown in Figure 3.27 and Figure 3.28, respectively. The diagrams with the fiber diameter distribution are also represented. Random and aligned PU-DMPA/CS and PU-CS fibers exhibit a regular shape with smooth surface morphology. In random and aligned PU-DMPA mats, fibers were fused with each other. Fibers in aligned PU-DMPA and PU-DMPA/CS mats have an average diameter of (1121 ± 604) nm and (777 ± 294) nm, respectively, which is smaller than the diameter of random fibers counterparts: (1620 ± 523) nm for PU-DMPA and (1066 ± 304) nm for PU-DMPA/CS. For PU-CS mats, the fiber diameter of fibers in random mats was (873±313) nm, which is similar to the fiber diameter of fibers in aligned mats (878 ± 352) nm. As the fibers are stretched while the mandrel rotates at high speed, it is expected that the fibers in the aligned mats have inferior diameter than the fibers in the random mats (Lee and Deng 2012).

The alignment degree of the fibers in the mats was studied by the analysis of the SEM images on ImageJ software, using the preferred angle plugin with the FFT and the oval projection method. A direct measurement of the angle of the fibers with the horizontal (0º) was taken to get the fiber angular distribution. Both the FFT intensity graph as well as the angular distribution histogram of the fibers in random and aligned mats are represented in Figure 3.27 and Figure 3.28, respectively. From the histogram of the angular distribution, the randomly oriented fibers from all PUs have the fibers distributed equally in all directions while the aligned fibers have the angular distribution centered at 90º. Aligned mats of PU-DMPA, PU-DMPA/CS and PU-CS have 88, 79, and 97% of their fibers in the 60º-120º range, respectively. The alignment degree can be inferred from the analysis of the shape and weight of the peaks at the FFT intensity graph (Figure 3.27 and Figure 3.28, column 3). Small intense multiple peaks are indicative of fibers with less order in the mats while fewer intense peaks are indicative of highly ordered fibers in the mats (Ayres, Bowlin et al. 2006). Therefore, the FFT intensity graph of the fibers in the aligned mats, which have fewer and intense peaks, corroborate the higher order of the fibers on the aligned fibrous mats. Amongst the aligned mats, PU-CS mats exhibited superior alignment degree.

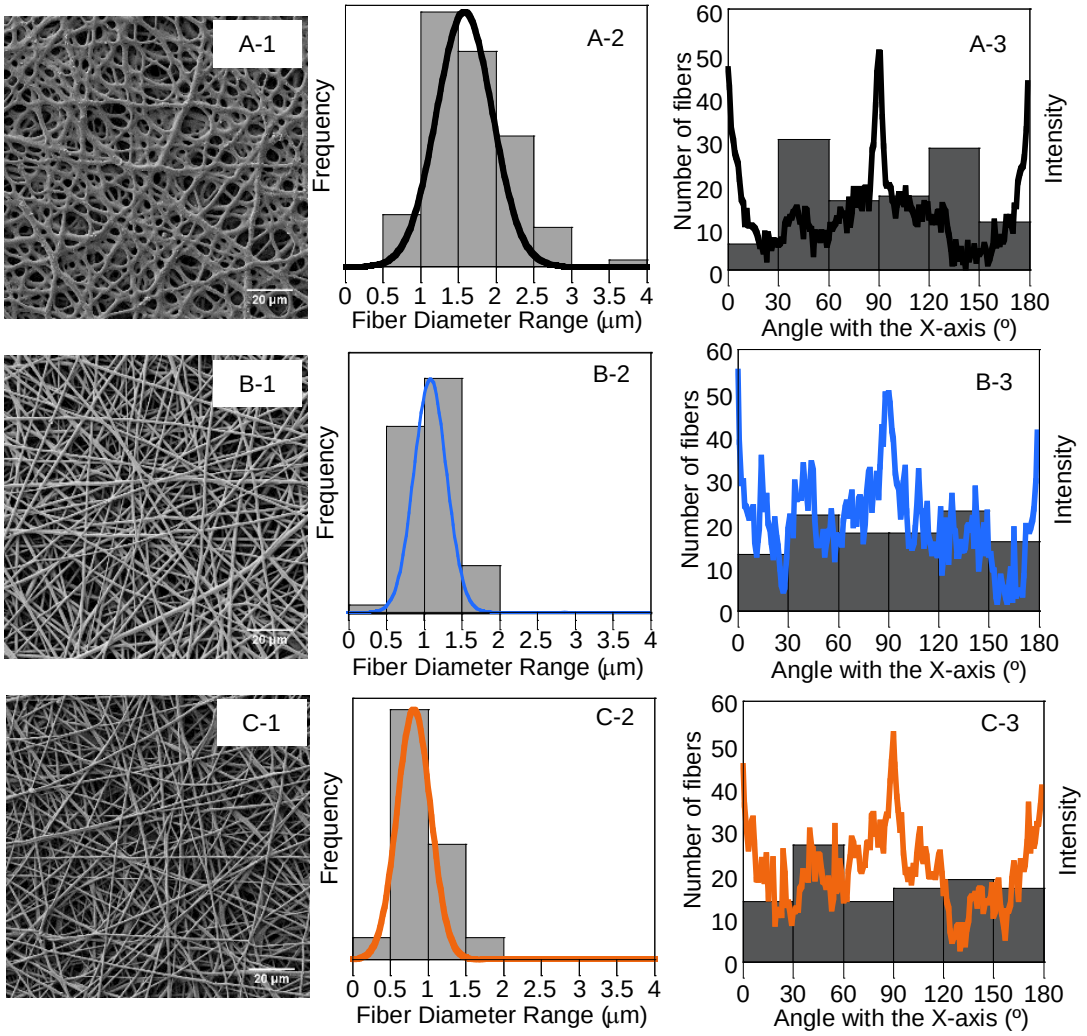

Figure 3.27 – SEM images of randomly oriented electrospun fibrous mats (column 1) from PU-DMPA (A), PU-DMPA/CS (B) and PU-CS (C), and the respective histograms of the fiber diameter (column 2) and the angular distribution (column 3). Scale bar: 20 μm.

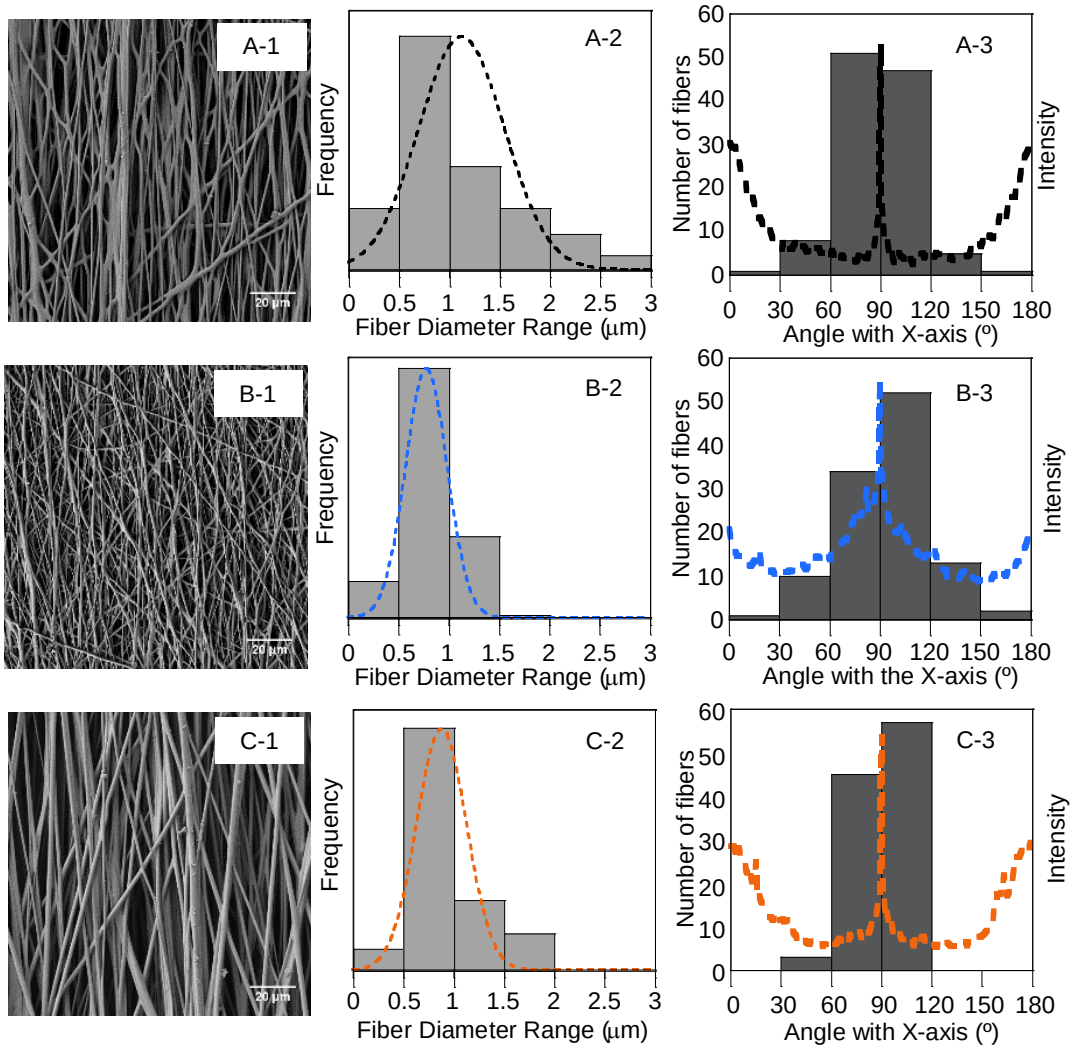

Figure 3.28– SEM images of aligned electrospun fibrous matrices (column 1) from PU-DMPA (A), PU-DMPA/CS (B) and PU-CS (C), and the respective histograms of the diameter (column 2) and the angular distribution (column 3). Scale bar: 20 μm.

3.3.5.2 **Mechanical properties**

In Figure 3.29 is presented the typical stress-strain curves of the aligned and random fibrous mats. The Young's modulus, obtained from the slope of the linear region of the mats' stress-strain curves are (0.82 ± 0.04) MPa, (1.54 ± 0.30) MPa and (3.25 ± 0.31) MPa for PU-DMPA, PU-DMPA/CS and PU-CS random mats, respectively. The Young's modulus obtained for aligned mats are superior to the ones obtained for random mats: (15 ± 1) MPa for PU-DMPA, (27 ± 3) MPa for PU-DMPA/CS and (38 ± 2) MPa for PU-CS aligned mats. According to the elongation at break, aligned mats exhibited smaller values than randomly mats that have elongations at break superior to 600 %. The elongation at break of the aligned fibers are (91 ± 9) %, (116 ± 8) % and (107 ± 9) % for PU-DMPA, PU-DMPA/CS and PU-CS, respectively.

The behavior of the electrospun mats under stress was previously described by Lee et al. The fibers first slippage over each other and oriented on the direction of the stretching. Then, the load is assured by the inter-fiber interactions and contact bonding points on the fibers. Finally,

each individual fiber started to break until no load can be handled (Lee, Lee et al. 2005). In aligned mats, the mechanical load was applied parallel to the fiber alignment and the fibers are stretched in the fiber direction. Therefore, fibrous mats with aligned fibers are under stress being unable to withstand higher deformations but handling superior loads. On the opposite, fibers in random mats aligned first on the stress direction supporting higher elongations but with reduced loads (Yao, Bastiaansen et al. 2014).

Snapshots were taken at the end of the mechanical tensile stress-strain test for aligned and random mats. As an example, the snapshot of PU-CS random and aligned mats after the test is represented in Figure 3.29. It is observed that the random mats withstand superior deformations and the width of the sample is reduced while the mat is stretched. In the aligned mats, the fibers start to break at early deformations.

For all mats, regardless the fiber orientation, the Young's modulus increase with the increment of CS content on the PU structure, which can be related to the increase in hydrogen bonding between hard segments with the increment of CS content in PU backbone, resulting in a more rigid structures.

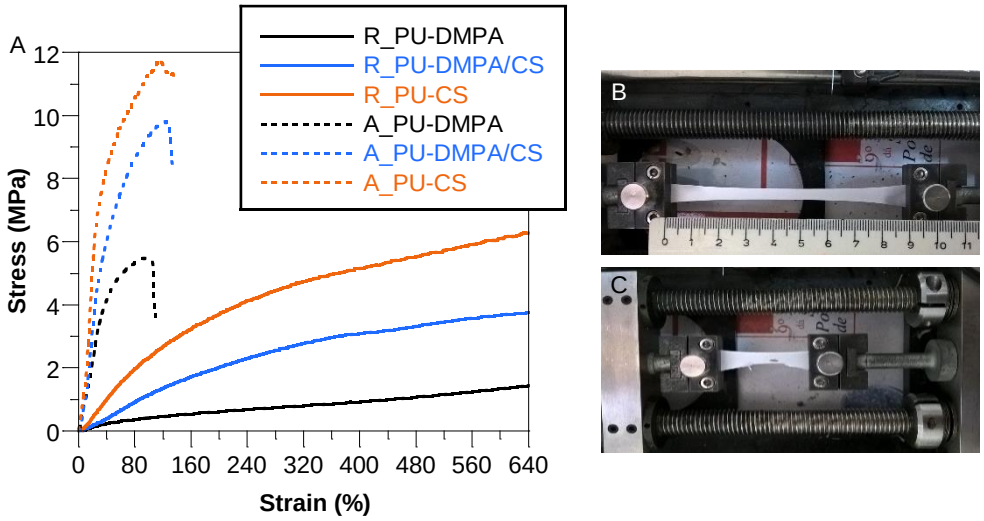

Figure 3.29– Stress-strain curves of the electrospun random and aligned fibrous matrices produced from PU-DMPA, PU-DMPA/CS and PU-CS (A). The representative snapshot of one PU-CS random (B) and aligned (C) mat at the end of the tensile test.

3.3.5.3 **Wettability**

The WCA values of the random and aligned mats and the respective sessile drop image are represented in Figure 3.30. The WCA values are (124 ± 5) º, (139 ± 2) º and (153 ± 4) º for PU-DMPA, PU-DMPA/CS and PU-CS random mats, respectively. The WCA values of the aligned mats are slightly inferior to the WCA of the corresponding random mats: (116 ± 2) º for PU-DMPA, (124 ± 1) º for PU-DMPA/CS and (122 ± 2) º for PU-CS. All the fibrous mats are hydrophobic with WCA superior to 90 º.

The morphology of the fibrous mats (alignment degree, fiber diameter and porosity) affect the WCA (Cui, Li et al. 2008). Aligned mats have porosities and pore shapes different from the

random mats, which influence the water drop when it contact the substrate (Kim, Hwang et al. 2016). Aligned mats with elongated pores increase the water drop-material interface compared to the pores of random mats. Regardless the fiber alignment, the hydrophobicity is superior in CS containing PU mats.

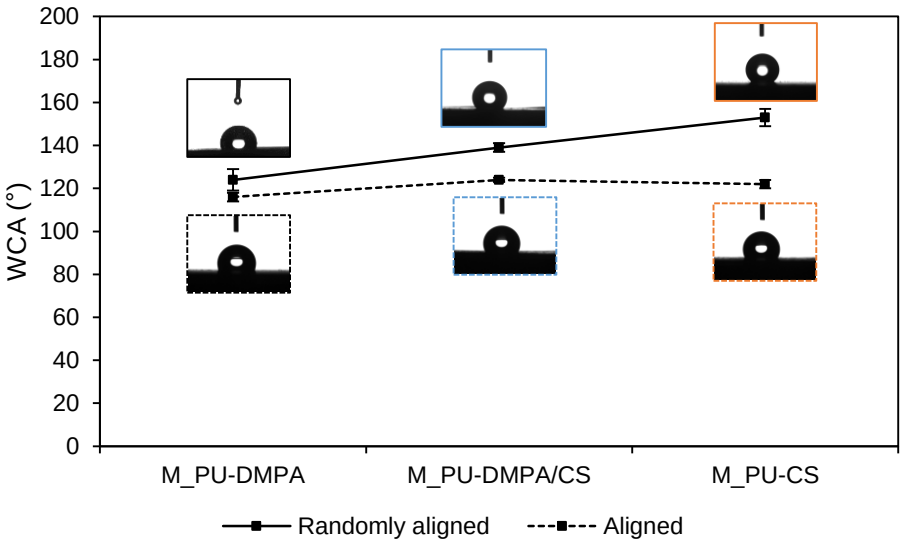

Figure 3.30– Water contact angle values of the PU-DMPA, PU-DMPA/CS and PU-CS electrospun fibrous mats with random and aligned morphology after 1 min recording time.

3.3.5.4 **Cellular assays**

To evaluate the viability of the HFFF2 cells seeded on PU random and aligned fibrous mats, a resazurin colorimetric assay was performed at 1, 3, 5, 8 and 10 days after seeding to quantify the cellular adhesion at day 1 and proliferation on the following days.

In Figure 3.31 is shown the results of the cell population over time on the mats and TCP wells (cell control, CC). In comparison to CC, cell adhesion to all fiber mats has no statistically significant difference, except to PU-DMPA/CS aligned mats in which cell adhesion is slightly lower. The difference between cell adhesion to PU-DMPA/CS aligned mats and PU-CS random and aligned mats and PU-DMPA random mats is also statistically significant. On the following days, cell population scarcely increased in PU-DMPA random mats but, and although inferior to other mats, cell population increase in PU-DMPA aligned mats. The proliferation rate increase with the increment of the CS content in the PU structure, apart from the cell morphology. Random mats support superior HFFF2 cells proliferation than aligned mats of PUs containing CS.

Aligned fibrous substrates better resemble the flat controls and cells establish stronger contact points with them, being more favorable substrates for cell adhesion and proliferation than random mats (Chang, Fujita et al. 2013; Zandén, Erkenstam et al. 2014). However, cells on aligned fibers can follow the direction of the fibers instead of cross over the fibers, reducing the cell-cell contact and consequently cell proliferation (Bashur, Shaffer et al. 2009).

HFFF2 cells were fixed and then stained with phalloidin (F-actin filaments) and DAPI (nucleus) after 5 days in culture on aligned and random mats and on the glass coverslip. Representative pictures are shown in Figure 3.32. Due to the high fluorescent background,

images from cells on PU-DMPA/CS random mats were manipulated using the Image J software to extract the nuclei and to remove the background. In the PU-DMPA and PU-DMPA/CS aligned mats the nuclei were not detected even using the Image J software. The organization of the cell cytoskeleton on the mats is different from the control. On the control, cells are well spread, while the cells on the mats have inferior projected area. On the aligned mats, the cells elongated the actin fibers parallel to the direction of the fiber alignment. The nuclei are also elongated on the fiber direction. It was also clearly noticed the superior cell number and the establishment of cell-cell contacts, forming a network structure on PU-CS random mats. These observations are in agreement with the resazurin assay, where PU-CS random mats have a superior proliferation rate at day 5 when compared to other mats.

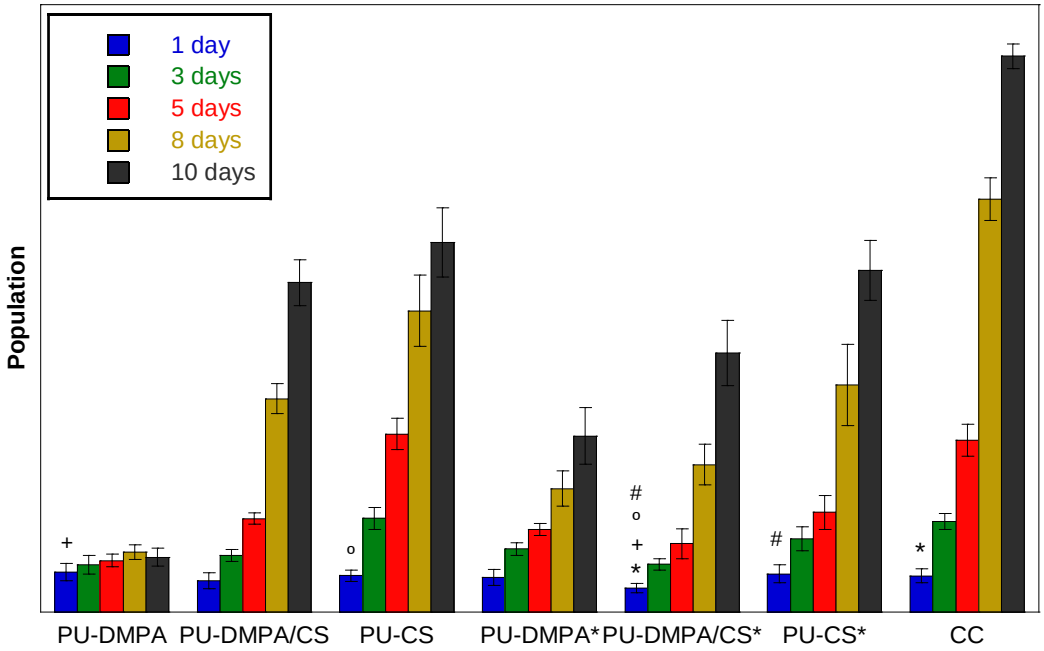

Figure 3.31 – Viability assay of HFFF2 cells seeded on PU-DMPA, PU-DMPA/CS and PU-CS random and aligned (*) mats and TCP wells (CC), after 1, 3, 5, 8 and 10 days in culture (mean ± standard deviation, n=5). Symbols indicate statistical significance (p>0.05).

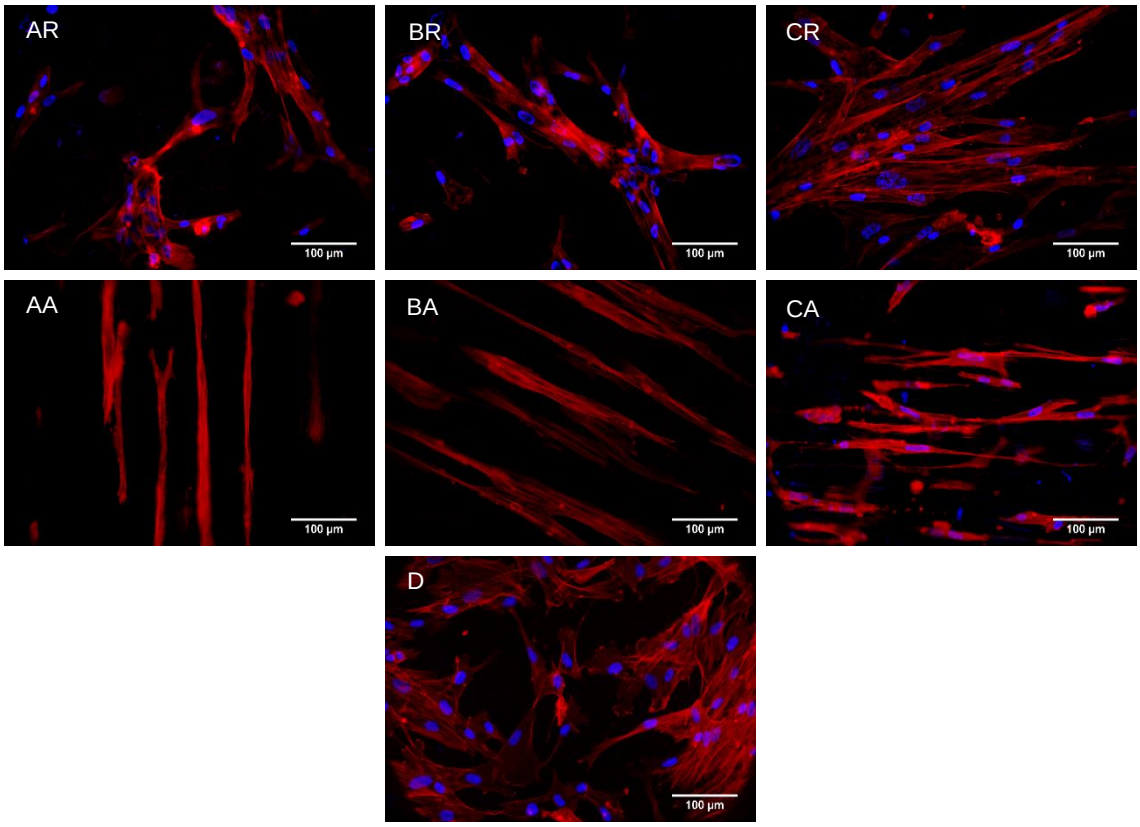

Figure 3.32 - Fluorescent images of phalloidin (red) and cell nuclei (DAPI, blue) stained HFFF2 cells seeded on electrospun nanofibrous mats of PU-DMPA random (AR) and aligned (AA) morphology, PU-DMPA/CS random (BR) and aligned (BA) morphology, PU-CS random (CR) and aligned (CA) morphology and cell control (D) at day 5 of culture.

3.4 Conclusions

In this chapter, PUs extended with DMPA and/or CS were synthetized and used to produced electrospun fiber mats and cast films.

In comparison with the corresponding films, fiber mats have more urethane and urea groups at the surface, are more hydrophobic, have a lower Young's modulus and a higher crystallinity degree. Films and fibers suffered bulk erosion in PBS and surface erosion in lipase. The fibrous structure, as well as the presence of CS, were essential to support the adhesion and proliferation of HFFF2 cells.

In comparison to the corresponding random mats, the aligned mats have superior Young modulus in the direction of the alignment and inferior elongation at break, are less hydrophobic and support reduced proliferation rates of HFFF2 cells. However, the aligned mats aligned the HFFF2 cells in the direction of the fiber alignment. In conclusion, the fiber mats obtained from PUs extended with CS exhibited physical, chemical and biological properties suitable for soft tissue engineering purposes.

3.5 References

Ahmad, N., M. Khan, et al. (2014). "The influence of cross-linking/chain extension structures on mechanical properties of htpb-based polyurethane elastomers." Arabian Journal for Science and Engineering **39**(1): 43-51.

Alishiri, M., A. Shojaei, et al. (2014). "Synthesis and characterization of biodegradable acrylated polyurethane based on poly (ε-caprolactone) and 1, 6-hexamethylene diisocyanate." Materials Science and Engineering: C **42**: 763-773.

Amoroso, N. J., A. D'Amore, et al. (2011). "Elastomeric electrospun polyurethane scaffolds: the interrelationship between fabrication conditions, fiber topology, and mechanical properties." Advanced Materials **23**(1): 106-111.

Anitha, A., V. Divya Rani, et al. (2009). "Synthesis, characterization, cytotoxicity and antibacterial studies of chitosan, *O*-carboxymethyl and *N,O*-carboxymethyl chitosan nanoparticles." Carbohydrate Polymers **78**(4): 672-677.

Ayres, C., G. L. Bowlin, et al. (2006). "Modulation of anisotropy in electrospun tissue-engineering scaffolds: analysis of fiber alignment by the fast Fourier transform." Biomaterials **27**(32): 5524-5534.

Badami, A. S., M. R. Kreke, et al. (2006). "Effect of fiber diameter on spreading, proliferation, and differentiation of osteoblastic cells on electrospun poly (lactic acid) substrates." Biomaterials **27**(4): 596-606.

Barikani, M., H. Honarkar, et al. (2009). "Synthesis and characterization of polyurethane elastomers based on chitosan and poly (ε-caprolactone)." Journal of Applied Polymer Science **112**(5): 3157-3165.

Barikani, M., H. Honarkar, et al. (2010). "Synthesis and characterization of chitosan-based polyurethane elastomer dispersions." Monatshefte für Chemie-Chemical Monthly **141**(6): 653-659.

Bashur, C. A., R. D. Shaffer, et al. (2009). "Effect of fiber diameter and alignment of electrospun polyurethane meshes on mesenchymal progenitor cells." Tissue Engineering Part A **15**(9): 2435-2445.

Baxter, A., M. Dillon, et al. (1992). "Improved method for ir determination of the degree of N-acetylation of chitosan." International journal of biological macromolecules **14**(3): 166-169.

Beamson, G., & Briggs, D. (1992). "High Resolution XPS of Organic Polymers: The Scienta ESCA300 Database.", Chichester: John Wiley & Sons, Ltd.

Bergmeister, H., N. Seyidova, et al. (2015). "Biodegradable, thermoplastic polyurethane grafts for small diameter vascular replacements." Acta biomaterialia **11**: 104-113.

Brugnerotto, J., J. Lizardi, et al. (2001). "An infrared investigation in relation with chitin and chitosan characterization." Polymer **42**(8): 3569-3580.

Caracciolo, P. C., V. Thomas, et al. (2009). "Electrospinning of novel biodegradable poly (ester urethane) s and poly (ester urethane urea) s for soft tissue-engineering applications." Journal of Materials Science: Materials in Medicine **20**(10): 2129-2137.

Cardwell, R. D., L. A. Dahlgren, et al. (2012). "Electrospun fibre diameter, not alignment, affects mesenchymal stem cell differentiation into the tendon/ligament lineage." Journal of tissue engineering and regenerative medicine **8**(12): 937–945.

Carlberg, B., M. Z. Axell, et al. (2009). "Electrospun polyurethane scaffolds for proliferation and neuronal differentiation of human embryonic stem cells." Biomedical Materials **4**(4): 045004.

Chan-Chan, L., C. Tkaczyk, et al. (2013). "Characterization and biocompatibility studies of new degradable poly (urea) urethanes prepared with arginine, glycine or aspartic acid as chain extenders." Journal of Materials Science: Materials in Medicine: 1-12.

Chang, J.-C., S. Fujita, et al. (2013). "Cell orientation and regulation of cell–cell communication in human mesenchymal stem cells on different patterns of electrospun fibers." Biomedical Materials **8**(5): 055002.

Chattopadhyay, D., B. Sreedhar, et al. (2006). "Influence of varying hard segments on the properties of chemically crosslinked moisture-cured polyurethane-urea." Journal of Polymer Science Part B: Polymer Physics **44**(1): 102-118.

Chattopadhyay, D. and D. C. Webster (2009). "Thermal stability and flame retardancy of polyurethanes." Progress in Polymer Science **34**(10): 1068-1133.

Chen, R., C. Huang, et al. (2010). "Preparation and characterization of coaxial electrospun thermoplastic polyurethane/collagen compound nanofibers for tissue engineering applications." Colloids and Surfaces B: Biointerfaces **79**(2): 315-325.

Chen, R., L. Qiu, et al. (2009). "Electrospinning thermoplastic polyurethane-contained collagen nanofibers for tissue-engineering applications." Journal of Biomaterials Science, Polymer Edition **20**(11): 1513-1536.

Cui, W., X. Li, et al. (2008). "Degradation patterns and surface wettability of electrospun fibrous mats." Polymer Degradation and Stability **93**(3): 731-738.

Cui, W., Y. Zhou, et al. (2016). "Electrospun nanofibrous materials for tissue engineering and drug delivery." Science and Technology of Advanced Materials **11**(1): 014108.

Daemi, H., M. Barikani, et al. (2013). "Compatible compositions based on aqueous polyurethane dispersions and sodium alginate." Carbohydrate polymers **92**(1): 490-496.

Dash, M., F. Chiellini, et al. (2011). "Chitosan—A versatile semi-synthetic polymer in biomedical applications." Progress in polymer science **36**(8): 981-1014.

Delair, T. (2011). "Colloidal polyelectrolyte complexes of chitosan and dextran sulfate towards versatile nanocarriers of bioactive molecules." European Journal of Pharmaceutics and Biopharmaceutics **78**(1): 10-18.

Delpech, M. C. and F. M. Coutinho (2000). "Waterborne anionic polyurethanes and poly (urethane-urea) s: influence of the chain extender on mechanical and adhesive properties." Polymer testing **19**(8): 939-952.

Dicesare, P., W. M. Fox, et al. (2012). "Cell–material interactions on biphasic polyurethane matrix." Journal of Biomedical Materials Research Part A **101**(8): 2151-2163.

Ero-Phillips, O., M. Jenkins, et al. (2012). "Tailoring crystallinity of electrospun plla fibres by control of electrospinning parameters." Polymers **4**(3): 1331-1348.

Ertem, S. P., E. Yilgor, et al. (2012). "Effect of soft segment molecular weight on tensile properties of poly (propylene oxide) based polyurethaneureas." Polymer **53**(21): 4614-4622.

Ferreira, J. L., S. Gomes, et al. (2014). "Electrospinning polycaprolactone dissolved in glacial acetic acid: Fiber production, nonwoven characterization, and In Vitro evaluation." Journal of Applied Polymer Science **131**(22): 41068.

Furukawa, M., Y. Mitsui, et al. (2005). "Microphase-separated structure and mechanical properties of novel polyurethane elastomers prepared with ether based diisocyanate." Polymer **46**(24): 10817-10822.

Garrett, J., J. Runt, et al. (2000). "Microphase separation of segmented poly (urethane urea) block copolymers." Macromolecules **33**(17): 6353-6359.

Garrett, J. T., R. Xu, et al. (2003). "Phase separation of diamine chain-extended poly (urethane) copolymers: FTIR spectroscopy and phase transitions." Polymer **44**(9): 2711-2719.

Gomes, S., G. Rodrigues, et al. (2017). "Evaluation of nanofibrous scaffolds obtained from blends of chitosan, gelatin and polycaprolactone for skin tissue engineering." International Journal of Biological Macromolecules **102**: 1174-1185.

Guan, J., K. L. Fujimoto, et al. (2005). "Preparation and characterization of highly porous, biodegradable polyurethane scaffolds for soft tissue applications." Biomaterials **26**(18): 3961-3971.

Guan, J., F. Wang, et al. (2011). "The stimulation of the cardiac differentiation of mesenchymal stem cells in tissue constructs that mimic myocardium structure and biomechanics." Biomaterials **32**(24): 5568-5580.

Guelcher, S. A. (2008). "Biodegradable polyurethanes: synthesis and applications in regenerative medicine." Tissue Engineering Part B: Reviews **14**(1): 3-17.

Guelcher, S. A., A. Srinivasan, et al. (2008). "Synthesis, mechanical properties, biocompatibility, and biodegradation of polyurethane networks from lysine polyisocyanates." Biomaterials **29**(12): 1762-1775.

Hafeman, A. E., K. J. Zienkiewicz, et al. (2011). "Characterization of the degradation mechanisms of lysine-derived aliphatic poly (ester urethane) scaffolds." Biomaterials **32**(2): 419-429.

Han, J., R. W. Cao, et al. (2011). "Electrospinning and biocompatibility evaluation of biodegradable polyurethanes based on L-lysine diisocyanate and L-lysine chain extender." Journal of Biomedical Materials Research Part A **96**(4): 705-714.

He, M. and C.-C. Chu (2013). "A new family of functional biodegradable arginine-based polyester urea urethanes: Synthesis, chracterization and biodegradation." Polymer **54**(16): 4112-4125.

He, Y., X. Zhang, et al. (2014). "The role of diisocyanate structure on microphase separation of solution polymerized polyureas." Polymer **55**(3): 906-913.

Henriques, C., R. Vidinha, et al. (2009). "A systematic study of solution and processing parameters on nanofiber morphology using a new electrospinning apparatus." Journal of nanoscience and nanotechnology **9**(6): 3535-3545.

Hsu, S., C. Chen, et al. (2007). "Cell migration on nanophase-separated poly (carbonate urethane) s." Journal of Medical and Biological Engineering **27**(1): 15-21.

Hu, J., X. Wang, et al. (2011). "One-step Electro-spinning/netting Technique for Controllably Preparing Polyurethane Nano-fiber/net." Macromolecular rapid communications **32**(21): 1729-1734.

Huang, M., E. Khor, et al. (2004). "Uptake and cytotoxicity of chitosan molecules and nanoparticles: effects of molecular weight and degree of deacetylation." Pharmaceutical research **21**(2): 344-353.

Jamadi, E. S., L. Ghasemi-Mobarakeh, et al. (2016). "Synthesis of polyester urethane urea and fabrication of elastomeric nanofibrous scaffolds for myocardial regeneration." Materials Science and Engineering: C **63**: 106-116.

Jeong, J. H., H. S. Kang, et al. (2003). "Polymer micelle-like aggregates of novel amphiphilic biodegradable poly (asparagine) grafted with poly (caprolactone)." Polymer **44**(3): 583-591.

Jia, L., M. P. Prabhakaran, et al. (2014). "Guiding the orientation of smooth muscle cells on random and aligned polyurethane/collagen nanofibers." Journal of biomaterials applications **29**(3): 364-377

Kasaai, M. R. (2007). "Calculation of Mark–Houwink–Sakurada (MHS) equation viscometric constants for chitosan in any solvent–temperature system using experimental reported viscometric constants data." Carbohydrate Polymers **68**(3): 477-488.

Kim, J. I., T. I. Hwang, et al. (2016). "A Controlled Design of Aligned and Random Nanofibers for 3D Bi-functionalized Nerve Conduits Fabricated via a Novel Electrospinning Set-up." Scientific reports **6**: 23761.

Kim, S. E., D. N. Heo, et al. (2009). "Electrospun gelatin/polyurethane blended nanofibers for wound healing." Biomedical Materials **4**(4): 044106.

Kittur, F., K. H. Prashanth, et al. (2002). "Characterization of chitin, chitosan and their carboxymethyl derivatives by differential scanning calorimetry." Carbohydrate polymers **49**(2): 185-193.

Kongkhlang, T., K. Tashiro, et al. (2008). "Electrospinning as a new technique to control the crystal morphology and molecular orientation of polyoxymethylene nanofibers." Journal of the American Chemical Society **130**(46): 15460-15466.

Labow, R. S., E. Meek, et al. (1999). "The biodegradation of poly (urethane) s by the esterolytic activity of serine proteases and oxidative enzyme systems." Journal of Biomaterials Science, Polymer Edition **10**(7): 699-713.

Lee, J. and Y. Deng (2012). "Increased mechanical properties of aligned and isotropic electrospun PVA nanofiber webs by cellulose nanowhisker reinforcement." Macromolecular research **20**(1): 76-83.

Lee, K., B. Lee, et al. (2005). "Stress-strain behavior of the electrospun thermoplastic polyurethane elastomer fiber mats." Macromolecular Research **13**(5): 441-445.

Lee, K. H., H. Y. Kim, et al. (2002). "Influence of a mixing solvent with tetrahydrofuran and N, N-dimethylformamide on electrospun poly (vinyl chloride) nonwoven mats." Journal of Polymer Science Part B: Polymer Physics **40**(19): 2259-2268.

Lee, T., S. Kwon, et al. (2014). "Biodegradable sol–gel coatings of waterborne polyurethane/gelatin chemical hybrids." Progress in Organic Coatings **77**(6): 1111-1116.

Li, G., D. Li, et al. (2014). "Alternating block polyurethanes based on PCL and PEG as potential nerve regeneration materials." Journal of Biomedical Materials Research Part A **102**(3): 685-697.

Lin, N., S. Wei, et al. (2014). "Green bionanocomposites from high-elasticity “soft” polyurethane and high-crystallinity “rigid” chitin nanocrystals with controlled surface acetylation." RSC Advances **4**(90): 49098-49107.

Liu, C., C. Zhu, et al. (2015). "The effect of the fibre orientation of electrospun scaffolds on the matrix production of rabbit annulus fibrosus-derived stem cells." Bone research **3**: 15012.

Liu, W. and Y. Cao (2007). "Application of scaffold materials in tissue reconstruction in immunocompetent mammals: our experience and future requirements." Biomaterials **28**(34): 5078-5086.

Loh, J. W., J. Schneider, et al. (2010). "Spinning disc processing technology: Potential for large-scale manufacture of chitosan nanoparticles." Journal of pharmaceutical sciences **99**(10): 4326-4336.

Momtaz, M., M. Barikani, et al. (2015). "Effect of ionic group content on thermal and structural properties of polycaprolactone-based shape memory polyurethane ionomers." Iranian Polymer Journal **24**(6): 505-513.

Mondal, S. (2014). "Influence of solvents properties on morphology of electrospun polyurethane nanofiber mats." Polymers for Advanced Technologies **25**(2): 179-183.

Monshi, A., M. R. Foroughi, et al. (2012). "Modified Scherrer equation to estimate more accurately nano-crystallite size using XRD." World Journal of Nano Science and Engineering **2**(3): 154-160.

Neto, C. d. T., J. Giacometti, et al. (2005). "Thermal analysis of chitosan based networks." Carbohydrate Polymers **62**(2): 97-103.

Oniki, Y., K. Suzuki, et al. (2013). "Molecular design of environmentally benign segmented polyurethane (urea) s: effect of the hard segment component on the molecular aggregation states and biodegradation behavior." Polymer Chemistry **4**(13): 3735-3743.

Oprea, S. (2010). "The effect of chain extenders structure on properties of new polyurethane elastomers." Polymer bulletin **65**(8): 753-766.

Park, K., W. H. Lim, et al. (2011). "Effect of molecular shape of diisocyanate units on the microscopic/macroscopic phase separation structure of polyurethanes." Journal of Polymer Science Part B: Polymer Physics **49**(12): 890-897.

Parrag, I. C., P. W. Zandstra, et al. (2012). "Fiber alignment and coculture with fibroblasts improves the differentiated phenotype of murine embryonic stem cell-derived cardiomyocytes for cardiac tissue engineering." Biotechnology and bioengineering **109**(3): 813-822.

Pattamaprom, C., W. Hongrojjanawiwat, et al. (2006). "The influence of solvent properties and functionality on the electrospinnability of polystyrene nanofibers." Macromolecular materials and engineering **291**(7): 840-847.

Pereira, I. M. and R. L. Oréfice (2011). "Study of the morphology exhibited by linear segmented polyurethanes." Macromolecular Symposia, Wiley Online Library **299-300**(1): 190-198.

Prabhakar, A., D. Chattopadhyay, et al. (2005). "Structural investigations of polypropylene glycol (PPG) and isophorone diisocyanate (IPDI)-based polyurethane prepolymer by 1D and 2D NMR spectroscopy." Journal of Polymer Science Part A: Polymer Chemistry **43**(6): 1196-1209.

Queiroz, D. P., M. N. de Pinho, et al. (2003). "ATR-FTIR studies of poly (propylene oxide)/polybutadiene bi-soft segment urethane/urea membranes." Macromolecules **36**(11): 4195-4200.

Queiroz, D. P., A. B. do Rego, et al. (2006). "Bi-soft segment polyurethane membranes: Surface studies by X-ray photoelectron spectroscopy." Journal of membrane science **281**(1): 239-244.

Ribeiro, C., V. Sencadas, et al. (2016). "Tailoring the morphology and crystallinity of poly (L-lactide acid) electrospun membranes." Science and Technology of Advanced Materials **12** (1): 015001.

Riboldi, S., N. Sadr, et al. (2008). "Skeletal myogenesis on highly orientated microfibrous polyesterurethane scaffolds." Journal of Biomedical Materials Research Part A **84**(4): 1094-1101.

Rodriguez, E. D., X. Luo, et al. (2011). "Linear/network poly (ε-caprolactone) blends exhibiting shape memory assisted self-healing (SMASH)." ACS applied materials & interfaces **3**(2): 152-161.

Rueda-Larraz, L., B. F. d'Arlas, et al. (2009). "Synthesis and microstructure–mechanical property relationships of segmented polyurethanes based on a PCL–PTHF–PCL block copolymer as soft segment." European Polymer Journal **45**(7): 2096-2109.

Saralegi, A., L. Rueda, et al. (2013). "Thermoplastic polyurethanes from renewable resources: effect of soft segment chemical structure and molecular weight on morphology and final properties." Polymer International **62**(1): 106-115.

Schneider, C. A., W. S. Rasband, et al. (2012). "NIH Image to ImageJ: 25 years of image analysis." Nature methods **9**(7): 671-675.

Shah, P. N., R. L. Manthe, et al. (2009). "Electrospinning of L-tyrosine polyurethanes for potential biomedical applications." Polymer **50**(10): 2281-2289.

Sheth, J. P., G. L. Wilkes, et al. (2005). "Probing the hard segment phase connectivity and percolation in model segmented poly (urethane urea) copolymers." Macromolecules **38**(13): 5681-5685.

Shi, Y., X. Zhan, et al. (2008). "Quantitative IR characterization of urea groups in waterborne polyurethanes." Journal of Polymer Science Part A: Polymer Chemistry **46**(7): 2433-2444.

Shokrolahi, F. and H. Yeganeh (2014). "Soft segment composition and its influence on phase-separated morphology of PCL/PEG-based poly (urethane urea) s." Iranian Polymer Journal **23**(7): 505-512.

Skarja, G. and K. Woodhouse (2000). "Structure-property relationships of degradable polyurethane elastomers containing an amino acid-based chain extender." Journal of Applied Polymer Science **75**(12): 1522-1534.

Tan, L., J. Hu, et al. (2015). "Design of bilayered nanofibrous mats for wound dressing using an electrospinning technique." Materials Letters **156**: 46-49.

Tang, D., C. W. Macosko, et al. (2014). "Thermoplastic polyurethane elastomers from bio-based poly (δ-decalactone) diols." Polymer Chemistry **5**(9): 3231-3237.

Tatai, L., T. G. Moore, et al. (2007). "Thermoplastic biodegradable polyurethanes: The effect of chain extender structure on properties and *in-vitro* degradation." Biomaterials **28**(36): 5407-5417.

Tijing, L. D., C.-H. Park, et al. (2013). "Characterization and mechanical performance comparison of multiwalled carbon nanotube/polyurethane composites fabricated by electrospinning and solution casting." Composites Part B: Engineering **44**(1): 613-619.

Tokiwa, Y., T. Ando, et al. (1990). "Biodegradation of synthetic polymers containing ester bonds." Polymeric Materials: Science and Engineering Division **62**: 988-992.

Trinca, R. B., G. A. Abraham, et al. (2015). "Electrospun nanofibrous scaffolds of segmented polyurethanes based on PEG, PLLA and PTMC blocks: Physico-chemical properties and morphology." Materials Science and Engineering: C **56**: 511-517.

Umare, S. S. and A. S. Chandure (2008). "Synthesis, characterization and biodegradation studies of poly (ester urethane) s." Chemical Engineering Journal **142**(1): 65-77.

Usman, A., K. M. Zia, et al. (2016). "Chitin and chitosan based polyurethanes: A review of recent advances and prospective biomedical applications." International journal of biological macromolecules **86**: 630-645.

Vatankhah, E., M. P. Prabhakaran, et al. (2014). "Phenotypic modulation of smooth muscle cells by chemical and mechanical cues of electrospun Tecophilic/gelatin nanofibers." ACS applied materials & interfaces **6**(6): 4089-4101.

Veleirinho, B., M. F. Rei, et al. (2008). "Solvent and concentration effects on the properties of electrospun poly (ethylene terephthalate) nanofiber mats." Journal of Polymer Science Part B: Polymer Physics **46**(5): 460-471.

Wang, N., K. Burugapalli, et al. (2013). "Tailored fibro-porous structure of electrospun polyurethane membranes, their size-dependent properties and trans-membrane glucose diffusion." Journal of membrane science **427**: 207-217.

Wilson, C. J., R. E. Clegg, et al. (2005). "Mediation of biomaterial-cell interactions by adsorbed proteins: a review." Tissue engineering **11**(1-2): 1-18.

Wu, J., Y. Du, et al. (2012). "The engineering of organized human corneal tissue through the spatial guidance of corneal stromal stem cells." Biomaterials **33**(5): 1343-1352.

Yao, J., C. W. Bastiaansen, et al. (2014). "High strength and high modulus electrospun nanofibers." Fibers **2**(2): 158-186.

Yilgor, I., E. Yilgor, et al. (2006). "FTIR investigation of the influence of diisocyanate symmetry on the morphology development in model segmented polyurethanes." Polymer **47**(11): 4105-4114.

Zamir, E. and B. Geiger (2001). "Molecular complexity and dynamics of cell-matrix adhesions." Journal of cell science **114**(20): 3583-3590.

Zandén, C., N. H. Erkenstam, et al. (2014). "Stem cell responses to plasma surface modified electrospun polyurethane scaffolds." Nanomedicine: Nanotechnology, Biology and Medicine **10**(5): 949-958.

Zdrahala, R. J. and I. J. Zdrahala (1999). "Biomedical applications of polyurethanes: a review of past promises, present realities, and a vibrant future." Journal of biomaterials applications **14**(1): 67-90.

Zhang, S., L. Cheng, et al. (2003). "NMR studies of water-borne polyurethanes." Journal of applied polymer science **90**(1): 257-260.

Zhang, S., J. Jiang, et al. (2011). "Facile synthesis of waterborne UV-curable polyurethane/silica nanocomposites and morphology, physical properties of its nanostructured films." Progress in Organic Coatings **70**(1): 1-8.

Zhang, S., W. Miao, et al. (2004). "Reaction study of water-borne polyurethanes based on isophorone diisocyanate, dimethylol propionic acid, and poly (hexane neopentyl adipate glycol)." Journal of applied polymer science **92**(1): 161-164.

Zhang, Y., W. He, et al. (2017). "Gemini quaternary ammonium salt waterborne biodegradable polyurethanes with antibacterial and biocompatible properties." Materials Chemistry Frontiers **1**(2): 361-368.

Zhang, Y., C. Xue, et al. (2005). "Determination of the degree of deacetylation of chitin and chitosan by X-ray powder diffraction." Carbohydrate research **340**(11): 1914-1917.

Zhu, Y., C. Gao, et al. (2004). "Endothelium regeneration on luminal surface of polyurethane vascular scaffold modified with diamine and covalently grafted with gelatin." Biomaterials **25**(3): 423-430.

Zia, K. M., S. Anjum, et al. (2014). "Synthesis and molecular characterization of chitosan based polyurethane elastomers using aromatic diisocyanate." International journal of biological macromolecules **66**: 26-32.

Zia, K. M., M. Barikani, et al. (2008). "Molecular engineering of chitin based polyurethane elastomers." Carbohydrate Polymers **74**(2): 149-158.

Zia, K. M., I. A. Bhatti, et al. (2009). "XRD studies of polyurethane elastomers based on chitin/1, 4-butane diol blends." Carbohydrate Polymers **76**(2): 183-187.

Chapter 4

A new biodegradable gelatin based poly(ester urethane urea): synthesis, characterization and electrospun scaffolds for soft tissue engineering

4. A new biodegradable gelatin based-poly(ester urethane urea): synthesis, characterization and electrospun scaffolds for soft tissue engineering

4.1 Introduction

Polyurethanes (PU) have been used as biomaterials due to their adjustable physic-chemical and biological properties. They are produced by the reaction of a polyol, a polyisocyanate and a chain extender, to form segmented copolymers composed of soft and hard segments that phase segregate due to the thermodynamic incompatibility between them (Oprea 2010).

To synthetize biocompatible and biodegradable PU for tissue engineering scaffolds, PU constituents and their ratio are varied (Tatai, Moore et al. 2007; Li, Li et al. 2013). Usually, polyesters, such as polycaprolactone, are used as soft segment since ester groups are susceptible to hydrolysis. To avoid toxic degradation products aliphatic or lysine-derived isocyanates are preferred (Guan, Fujimoto et al. 2005; Hafeman, Zienkiewicz et al. 2011).The chain extender is the most variable component and can be chosen to control the degradation rate and to introduce biological motifs for cell interaction. . Amino acids, such as aspartic acid (Chan-Chan, Tkaczyk et al. 2013), phenylalanine (Skarja and Woodhouse 2000), arginine (He and Chu 2013), tyrosine (Sarkar, Yang et al. 2008), glutamic acid, cysteine and glycine (Perales-Alcacio, Santa-Olalla Tapia et al. 2013), small peptide sequences, such as glycine-leucine (Parrag and Woodhouse 2010), glycine-alanine-glycine-alanine (Liu, Xu et al. 2010), and phenylalanine-lysine ethyl ester-phenylalanine (Wang, Zheng et al. 2014), and even natural polymers such as chitosan (Barikani, Honarkar et al. 2009) have been used as chain extenders. Of these, PU extended with phenylalanine (Rockwood, Woodhouse et al. 2007; Rockwood, Akins et al. 2008), tyrosine (Shah, Manthe et al. 2009) and glycine-leucine (Parrag and Woodhouse 2010) were processed by electrospinning (Henriques, Vidinha et al. 2009) and rendered fibrous mats with potential applications in tissue engineering.

Gelatin is a natural polymer derived, by hydrolysis, from collagen. It has been widely used in tissue engineering because it is biocompatible, biodegradable and have the motifs for cell adhesion and proliferation (Kang, Tabata et al. 1999). Literature reports the fabrication of PU-based scaffolds incorporating gelatin. There are studies that synthetized PUs modified with gelatin. Sarkar et al (Sarkar, Chourasia et al. 2006) claimed the synthesis of a polyester urethane, based on polyethylene lactate ester diol and gelatin. In their procedure, a prepolyurethane solution was mixed to gelatin solution and glutaraldehyde. A gas foaming method was used to produce sheets from the polymeric solution. In another study (Kucińska-Lipka, Gubańska et al. 2013), foams of gelatin modified polyether urethanes, synthesized using two different chain extenders were prepared. Lee et al (Lee, Kwon et al. 2014) used a vinyl modified gelatin and a PCL-diol based prepolymer, which was end capped to form acrylate termini, to obtain crosslinked waterborne/gelatin films. Solutions from blends of PUs and gelatin were also used to produce

electrospun fibrous mats for soft tissue engineering scaffolds (Kim, Heo et al. 2009; Vatankhah, Prabhakaran et al. 2014; Jamadi, Ghasemi-Mobarakeh et al. 2016). However, the solubility of gelatin in water requires the crosslinking of these scaffolds. Chemical crosslinkers such as glutaraldehyde, genipin and carbodiimide are highly toxic and there are concerns about possible cytotoxic effects of their free reactive groups (Amadori, Torricelli et al. 2015).

In this chapter, PUs based on polycaprolactone-diol (PCL-diol) and gelatin in different Gel/PCL-diol weight proportions – 5%, 7.5% and 10% – were synthesized. These polymers will be designed by PU-Gel-5, PU-Gel-7.5 and PU-Gel10, respectively. In the synthesis, the –NCO terminated pre-polymer, resulting from the reaction between PCL-diol and isophorone diisocyanate (IPDI), was reacted with gelatin without the use of any other chain extender. To the best of our knowledge, there are no reports on the synthesis of such a polyester poly(urethane urea) incorporating gelatin in the polymer backbone as the only chain extender The PU, obtained as solid precipitates, were characterized chemically by proton nuclear magnetic resonance (^{1}H NMR) and Fourier transform infrared spectroscopy (FTIR) and thermally by thermogravimetric analysis (TGA) and differential scanning calorimetry (DSC). Electrospun fibrous mats with random and aligned morphology and solvent cast films, produced from a solution of PU-Gel-5 dissolved in a mixture of N,N-dimethylformamide (DMF) and tetrahydrophuran (THF) were characterized according to the mechanical properties, crystallinity, wettability and degradation profile. Films and fibrous mats ability to support cell adhesion and proliferation was also tested.

4.2 Materials and methods

4.2.1 Synthesis of PU-Gel

The following materials were used in the PU-Gel synthesis: polycaprolactone-diol (PCL-diol, M_n = 2000) and Sodium bisulfite ($NaHSO_3$, Mw=104.06) from Acros Organics; Isophorone diisocyanate (IPDI) from Huls, isopropanol from LabChem, dimethyl sulfoxide (DMSO, dried over molecular sieves) from Merck and cold water fish skin gelatin (M_w= 60 kg/mol) from Sigma-Aldrich (#G7041).

The synthesis were conducted as follows: PCL-diol (20 g) was dried under vacuum at 90 ºC during 24 h and added to a 500 cm^3 four-necked reactor equipped with a mechanical stirrer, a heating oil bath, a condenser, a dropping funnel and a nitrogen inlet and outlet. The reactor was immersed in an oil bath whose temperature was set at 60 ºC. IPDI (8.95 g) was added dropwise to the reactor and the temperature of the bath was raised to 90 ºC. The reaction took place during 4 h to achieve the NCO terminated pre-polymer. The temperature of the reactor was then lowered to 50 ºC and gelatin (1.0, 1.5 or 2.0 g), previously dried at 60 ºC during 7 days and dissolved in DMSO, was added and the reaction proceed for 1 h. To end up the reaction, $NaHSO_3$ (2.08 g) was added and the mixture was stirred for 30 min at high speed (800 rpm). After lowering the temperature to 30 ºC, cold distilled water was added dropwise keeping the mixture at a reduced stirring speed (180 rpm) to precipitate the polymer. The polymer was thoroughly washed with

distilled water, immersed in isopropanol during 48 h and vacuum dried until constant weight. The polymer synthesis route is outlined in Figure 4.1.

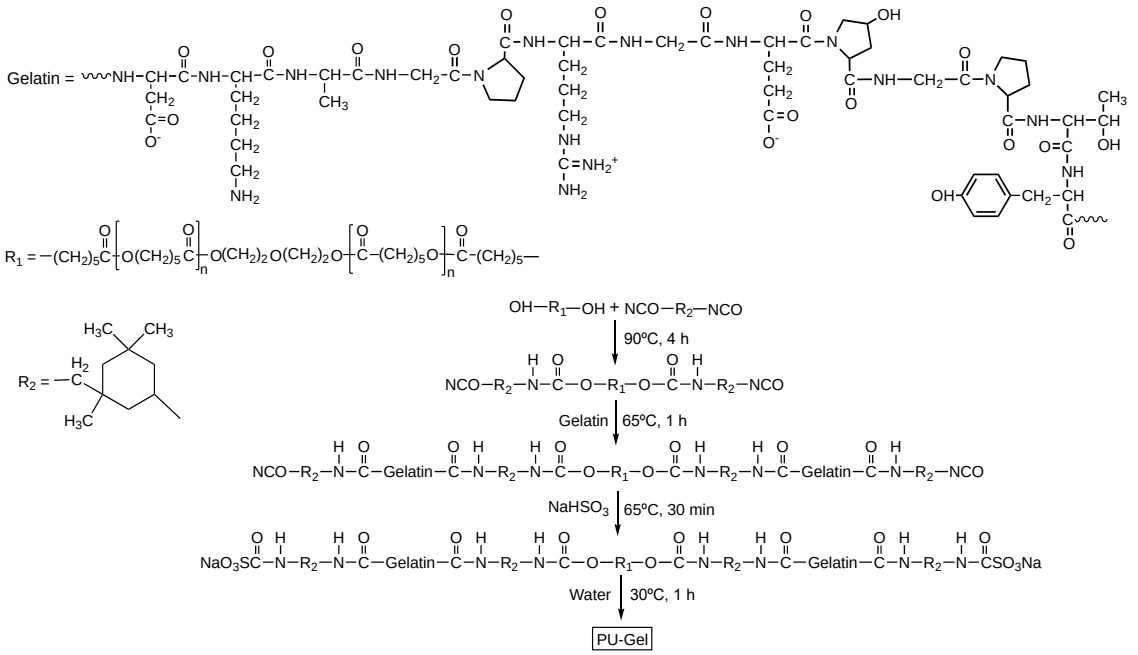

Figure 4.1– Synthesis route of polyurethane based gelatin.

4.2.2 Characterization of PU-Gel

Chemical characterization of PU-Gel was performed using Fourier Transform Infrared Spectroscopy (FTIR) and nuclear magnetic resonance (^{1}H NMR) analysis as described previously (section 3.2.3). Briefly, a FT-IR Nicolet 6700 spectrometer, from Thermo Electron Corporation, in ATR (attenuated total reflectance) mode operating with a resolution of 4 cm^{-1} was used to record IR spectra. N-H and C=O IR stretching bands were fitted with Gaussian profile and constant background using the Fityk 0.9.8 program to evaluate PU hydrogen bonds. The ^{1}H NMR PU-Gel spectra were recorded in DMSO-d_6 (99.96% atm, Sigma-Aldrich) solution using a BrukerAvance III 400 MHz spectrometer. Chemical shifts (δ) are registered in ppm and tetramethylsilane (TMS) was used as the standard.

Thermogravimetric analysis (TGA) and differential scanning calorimetry (DSC) were used to evaluate PUs thermal properties as described preciously (section 3.2.3). Briefly, data were recorded using a TGA-DSC-STA 449F3 Jupiter equipment under nitrogen atmosphere operating from room temperature up to 500ºC in the case of TGA and 250ºC in the case DSC at a rate of 10ºC/min. The collected data were analyzed with the control software NETZSCH Proteus.

4.2.3 Electrospinning and film casting

In order to optimize the experimental processing conditions, several solvent mixtures and electrospinning parameters were studied. All PU-Gel were dissolved in a solvent systems comprising 50% N,N-dimethylformamide (DMF) and 50% tetrahydrofuran (THF). The PU-Gel-10 was also dissolved in 1,1,1,3,3,3-Hexafluor-2-propanol (HFP, from Sigma-Aldrich). The PU-Gel-

5 was also dissolved in other solvent systems at 50:50 proportion: DMF:Chloroform, dimethylacetamide (DMAc):Chloroform and DMAc:THF, all solvents from Carlo Erba. Solutions were prepared at 18 wt% and dissolved under magnetic stirring overnight.

For electrospinning, the solutions were loaded on a 5 mL syringe with a 21G stainless steel blunt needle (internal diameter of 0.508 mm). A syringe pump (SyringePump NE-300) was used to set the flow rate to 1.0 mL/h. A high-voltage power supply (Power Supply – iseg T1CP300 304p) was used to apply 18 kV to the needle, while the aluminum plate, at a distance of 20 cm from the needle tip, was kept grounded to collect the fibers. In order to facilitate the detachment of the fiber mats to be used in physico-chemical characterization, the collector was covered with a paper foil. Samples for cell culture were deposited on 12 mm diameter glass coverslips, fixed to the collector. A rotatory mandrel, with 8 cm diameter, covered with paper foil and rotating at high rotation speed (4000 rpm) was also used to collect mats with aligned morphology.

To prepare the films, a calibrated Gardner knife from Braive Instruments was used to spread out the solutions at a constant speed of 1.25 mm/s. After drying at ambient conditions, the films were put under vacuum in a desiccator to complete solvent extraction.

4.2.4 Characterization of PU-Gel electrospun fibers

4.2.4.1 Scanning electron microscopy

The morphology, diameter and degree of alignment of the electrospun fibers were determined by SEM using a Zeiss Auriga Crossbeam electron microscope. Before observation, the samples were sputter coated with a mixture of gold/palladium (60/40). The fiber diameter was measured by image analysis using ImageJ software (National Institutes of Health, USA) and measurements of at least 100 fibers per sample were taken. The result is expressed as the average ± experimental standard deviation. The alignment degree of the mats was determined using the Fast Fourier Transform (FFT) analysis, developed by (Ayres, Bowlin et al. 2006), as described previously (section 3.2.5).

4.2.4.2 Mechanical tests

PU-Gel films and fiber mats were subjected to uniaxial tensile tests using a tensile test machine from Rheometric Scientific (Minimat Firmware version 3.1) with a 20 N load cell. Samples of 10 × 10 mm^2 were pulled at a rate of 2 mm/min at ambient conditions. Aligned mats were stretched in the direction of the fiber alignment. At least 10 samples from three different electrospun depositions or cast films were used. The Young's modulus was determined from the slope of the linear region of the stress-strain curve and expressed as the average ± experimental standard deviation.

Hysteresis tests were also performed: 10 cycle hysteresis behavior was evaluated by stretching the samples to 80% elongation with a crosshead speed of 10 mm/min and afterwards,

immediately retract them at the same crosshead speed. The tests were conducted at room temperature and at least three samples from each mat were tested.

4.2.4.3 X-ray diffraction analysis

The crystalline structure of PU-Gel films and fibrous mats was analyzed by XRD with a PANalytical X'Pert PRO X-ray diffractometer, using CuKα radiation (λ = 1.54060 Å) in the range 5°<2θ<40° with a 0.1º step. The diffractograms were fitted with a sum of pseudo-Voigt functions, assuming a background fitted to a second degree polynomial. The crystalline degree, $w_{c,x}$, and crystallite size, τ, were calculated using the equations described in section 3.2.5.4.

4.2.4.4 Water contact angle

The wettability of PU-Gel films and fibrous mats was assessed by static WCA measurements at room temperature and 98% humidity, using a contact angle goniometer (OCA15, DataPhysics Instruments GmbH, Filderstadt, Germany). Water drops with 5 µL were generated with an electronic micrometric syringe and carefully deposited on the samples surface and contact angle value was acquired within the following 5 min (the shape of the drops was stable in that period). The collected information was analyzed using the SCA v.4.3.12 and v.4.3.16 software. The results are expressed as the average ± standard deviation of at least five measurements recorded in different regions of the sample.

4.2.4.5 Degradation assays

Hydrolytic and enzymatic degradation of PU-Gel films and fiber mats were evaluated, over a period of 37 days, from mass loss measurements as described in section 3.2.5.7 using different degradation media. For the hydrolytic degradation studies, the degradation medium was a phosphate buffer saline (PBS, pH 7.4 ± 0.2). Enzymatic degradation studies were performed using lipase (activity: 27 U/mg from Amano Enzyme Inc.) prepared at a concentration of 10 U/mL, in accordance with (Labow, Meek et al. 1999) and trypsin (activity: 256 U/mg from Amresco) prepared at a concentration of 104 U/mL, as reported by (Mandalari, Faulks et al. 2008). All solutions were supplemented with 0.04 % w/v sodium azide (Merck, to prevent contamination by gram-negative bacteria). Enzymatic solutions were replaced every other day to maintain a constant enzymatic activities.

4.2.4.6 Cell culture experiments

In vitro studies were performed using human fetal foreskin fibroblasts (HFFF2 cell line, obtained from ECACC, UK) cultured in Dulbecco's modified Eagle's medium (DMEM, catalog #D5030, Sigma-Aldrich), supplemented with GlutaMAX (#35050-038), 10% v/v fetal bovine serum (FBS, #10270106), 100 units/mL of penicillin, 100 µg/mL streptomycin (#15140122) and 2.50 µg/mL amphotericin B (#15290018) all from Life Technologies. Cells were incubated at 37 ºC in a 5% CO_2 humidified atmosphere incubator (Sanyo MCO-19AIC(UV)).

Cell viability was assayed using the colorimetric resazurin assay described in detail in section 3.2.5.8.

Indirect cytotoxicity test

PU-Gel films and fibrous mats were checked for cytotoxicity using the extract method in accordance with the International Standard ISO 10993-5. To get the extracts, samples were cut, weighted, sterilized under 254 nm UV light during 30 min on each side, immersed in culture medium without FBS (1 mL of medium per 15 mg of sample) and incubated at 37 ºC in orbital agitation during 48 h. HFFF2 cells were seeded at a density of 20×10^3 cells/cm^2 and incubated at 37 ºC in a 5% CO_2 humidified atmosphere during 24 h. After this period, the medium was replaced with the pure extracts and their dilutions (dilution factors 3/2 and 3) supplemented with 10% FBS. Negative (viable cells) and positive (cells in a cytotoxic environment) controls were established by culturing cells with complete medium and complete medium with 10% DMSO, respectively. After 48 h in contact with the extracts, the resazurin viability assay was performed.

Cell adhesion and proliferation

Electrospun fibers deposited on coverslips were sterilized (as previously describes), washed three times with PBS and soaked in complete culture medium. HFFF2 cells were seeded at a density of 10×10^3 cells/cm^2, over a 0.5 cm^2 area on each sample held by home-made Teflon inserts, which were placed in a 24-well tissue culture plate (Sarstedt, Germany). Cell controls were set by seeding cells at the same density over the surface of the tissue culture plate (TCP) wells for viability assays, and on glass coverslips for fluorescence imaging. Cells were incubated at 37 ºC in a 5% CO_2 humidified atmosphere. The viability was accessed after 1, 3, 5, 7, 9, and 11 days using the resazurin assay to access cell adhesion and proliferation. After 5 days of culture, the cytoskeleton and nucleus of cells growing in fibrous mats and coverslips were stained with Acti-stain™ 555 Fluorescent Phalloidin (from Cytoskeleton, Inc.) and 4',6-Diamidino-2-Phenylindole, Dilactate – DAPI (from Molecular Probes™, ThermoFisher Scientific, Inc.), as described in section 3.2.5.8.

4.3 Results and discussion

4.3.1 PU-Gel Characterization

PU-Gel was synthetized using a two steps procedure. In the first step pre-polymer is formed by reacting hydroxyl (-OH) groups of PCL-diol with -NCO groups of IPDI, establishing urethane bonds. In the second step, -OH and amine ($-NH_2$) groups of gelatin react with the pre-polymer –NCO, resulting in the formation of new urethane and urea bonds, respectively.

4.3.1.1 Chemical characterization

The ^{1}H NMR spectra of PCL, IPDI, gelatin and PU-Gel 1.0 g are represented in Figure 4.2. In the PU-Gel-5 spectrum, the peaks between 0.75 and 1.20 ppm are due to methyl groups of IPDI (Zhang, Cheng et al. 2003) and of gelatin aminoacids (Hu, Li et al. 2011); the peak with the smallest chemical shift derives from amino acids with side chains with terminal methyl groups

(alanine, valine, leucine and isoleucine). Methylene groups of PCL (–OC*H*$_2$C*H*$_2$C*H*$_2$CH$_2$C*H*$_2$COO–) are observed at 3.95-3.98, 1.47-1.57, 1.24-1.32 and 2.24-2.27 ppm, respectively (Zia, Barikani et al. 2008). Resonances from methylene linked to urea N (NHCONH–*CH*$_2$) are present at 2.73 ppm (Li, Kong et al. 2015). The peak at 3.12 ppm in IPDI spectrum, assigned to the methylene protons next to –NCO (Zhang, Cheng et al. 2003), does not appear in PU-Gel-5, indicating that urethane/urea bonds were formed. CH_2 groups attached to the urethane oxygen atom (–*CH*$_2$OCONH) are detected at 3.89 – 3.91 ppm (Zhang, He et al. 2017). Peaks in the region 5.68-5.86 ppm are assigned to the urea NH (–*NH*CO*NH*–) (Zhang, Cheng et al. 2003; Li, Zhao et al. 2014; Li, Kong et al. 2015). These peaks are observed in the PU-Gel-5 spectrum, confirming the presence of the urea group and demonstrating that gelatin bonds to the pre-polymer, incorporating the polymer structure. Weak peaks at 6.82–7.24 ppm position are ascribed to urethane NH (–*NH*COO–) (Zhang, Cheng et al. 2003).

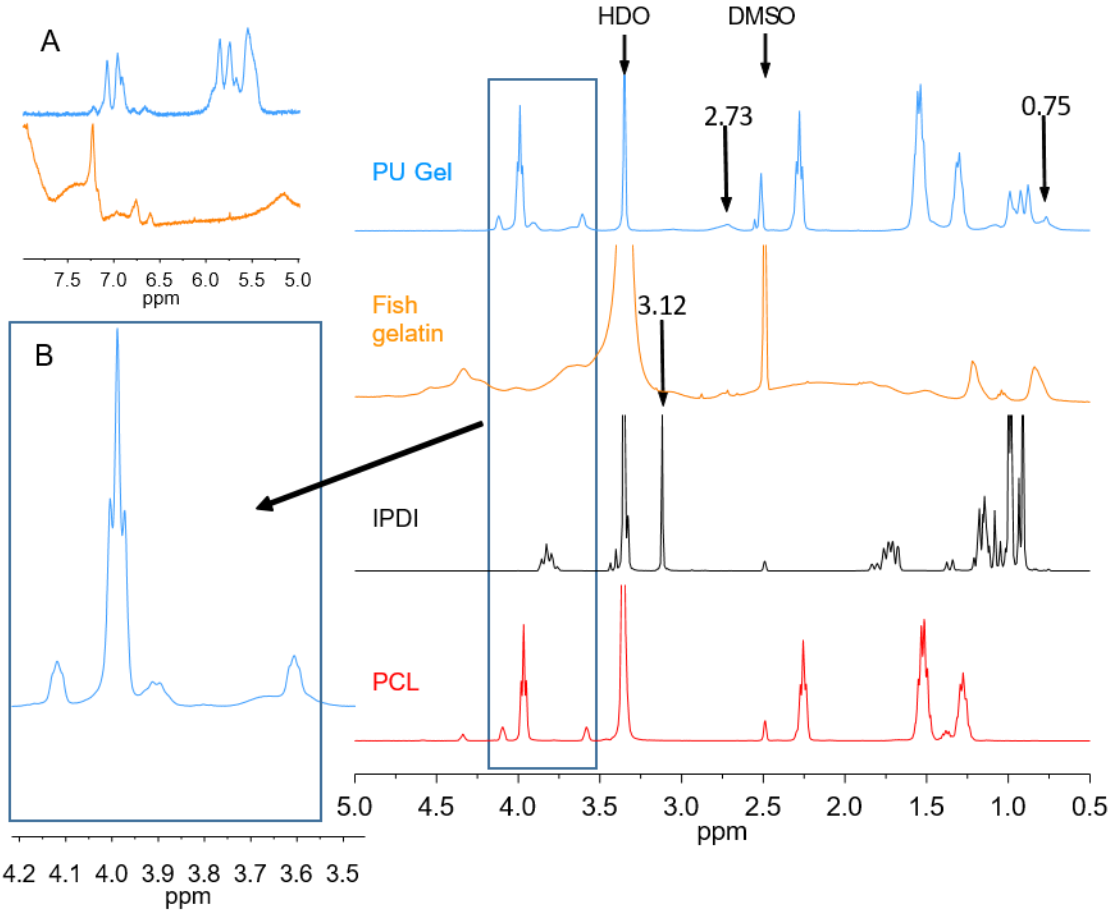

Figure 4.2– ^{1}H NMR spectra of PU-Gel 1.0 g and its precursors in the range between 0.5 ppm to 5.0 ppm. For chemical shifts higher than 5.0 ppm, PCL and IPDI spectra didn´t reveal any peak. Spectra of fish gelatin and PU-Gel 1.0g between 5.0 ppm and 8.0 ppm (A). Spectra of PU-Gel 1.0g in the range 3.65 – 4.20 ppm (B).

Figure 4.3 presents the FTIR spectra of PU-Gel 1.0g, PU-Gel 1.5g and PU-Gel 2.0g, as well as the spectra of their precursors: PCL, IPDI and fish gelatin, and the intermediate pre-polymer.

In comparison with the pre polymer, the spectra of all PU-Gel reveal the increase in the intensity of the band at 3360 cm^{-1} (N-H stretching), the extinction of the IPDI peak at 2260 cm^{-1} (out of phase -N=C=O stretch) and the appearance of a new peak at 1640 cm^{-1} (C=O stretching), which increases with the amount of gelatin added to the pre-polymer. The peak at 1640 cm^{-1} is characteristic of the gelatin amide I band but it may also be due to H-bonded urea C=O groups (Garrett, Xu et al. 2003; Yilgor, Yilgor et al. 2006; Shi, Zhan et al. 2008). At around 1540 cm^{-1} and 1236 cm^{-1} are the bands due to the urea N-H deformation and C-N stretching, respectively, which overlap with the amide II and amide III bands of gelatin. All these changes can be related to the formation of new urea/urethane bonds (Li, Kong et al. 2015) due to incorporation of gelatin in the PU-Gel structure.

The C-H symmetric and asymmetric vibrations from CH_2 groups are identified at 2940 and 2865 cm^{-1}, respectively. The carbonyl stretching vibration of PCL-diol and urethane bonds are detected around 1725 cm^{-1}.

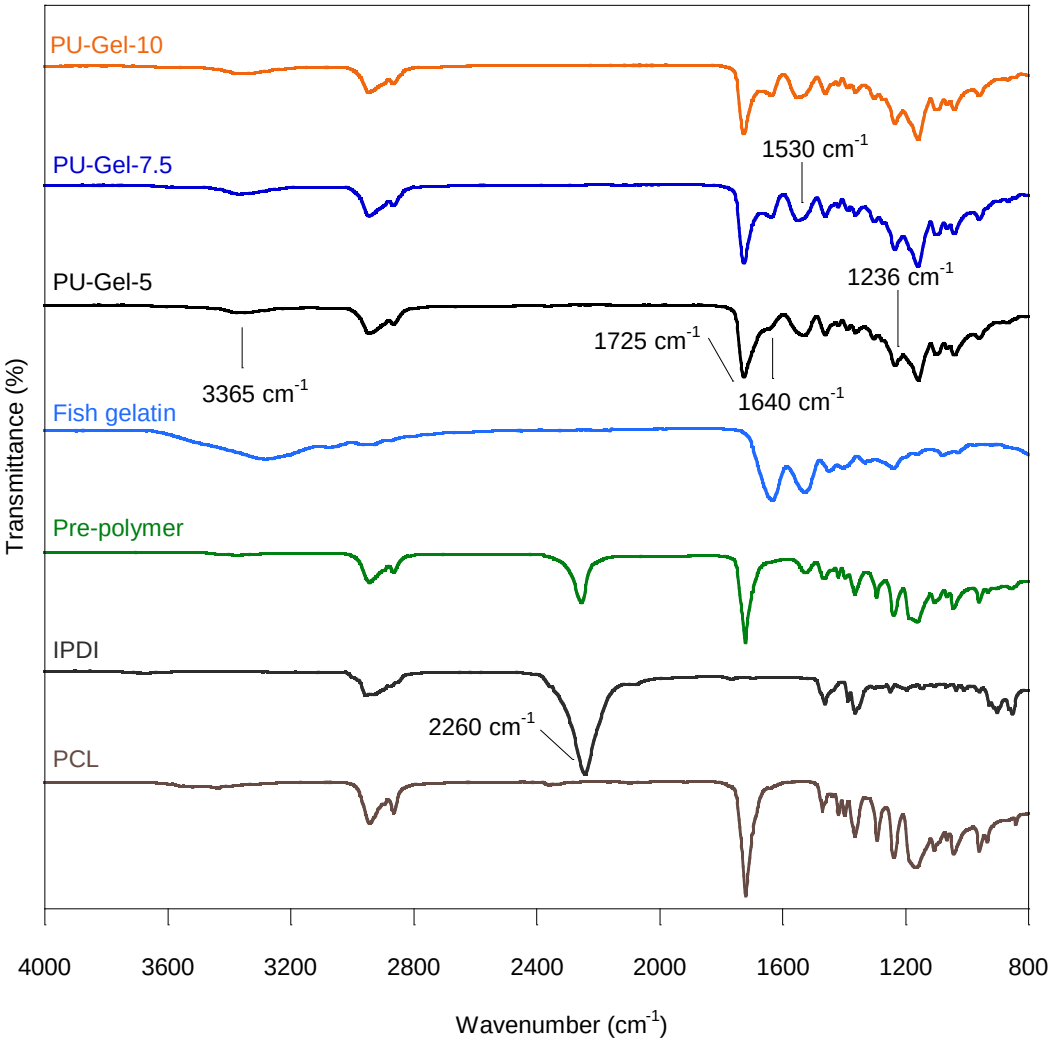

Figure 4.3– FTIR spectra of PUs synthetized with different amounts of gelatin and their constituents.

Deconvolution of N-H and C=O bands

The extent of microphase separation depends on the hydrogen bonding established in PUs, which can be studied by the analysis of the amine (3300 – 3450 cm^{-1}) and carboxyl (1600 – 1800 cm^{-1}) stretching regions of the PUs FTIR spectra. These regions were fitted with a sum of Gaussian functions using the software Fityk.

The original data, the fitting and the Gaussian curves for each PU-Gel carboxylic region are presented in Figure 4.4. In Table 4.1 is presented the wavenumber (cm^{-1}), the relative areas of Gaussian curves and the percentage of hydrogen bonds. Five Gaussian curves fit the carboxyl region of PUs. At 1720 – 1730 cm^{-1} is detected the free C=O urethane groups and at 1705 – 1710 cm^{-1} is observed the hydrogen bonded C=O urethane groups. The free, disordered and ordered hydrogen bonded C=O urea groups were observed at 1690 – 1700 cm^{-1}, 1660 – 1680 cm^{-1} and 1635 - 1645 cm^{-1}, respectively.

Regarding this band, the free C=O urethane groups increase while the hydrogen bond C=O urethane groups decrease with the increment of gelatin in the PU backbone. The PU-Gel-5 has higher percentage of hydrogen bonds, with a superior degree of microphase segregation. The microphase separation is prevented in PU-Gel-7.5 and PU-Gel10. Increasing the gelatin content in PU backbone, destroy the formed hydrogen bonds and destabilize the phase segregation. This behavior was observed when chain extenders with more than two functional groups were used in the PU synthesis (Sheth, Wilkes et al. 2005; Ahmad, Khan et al. 2014).

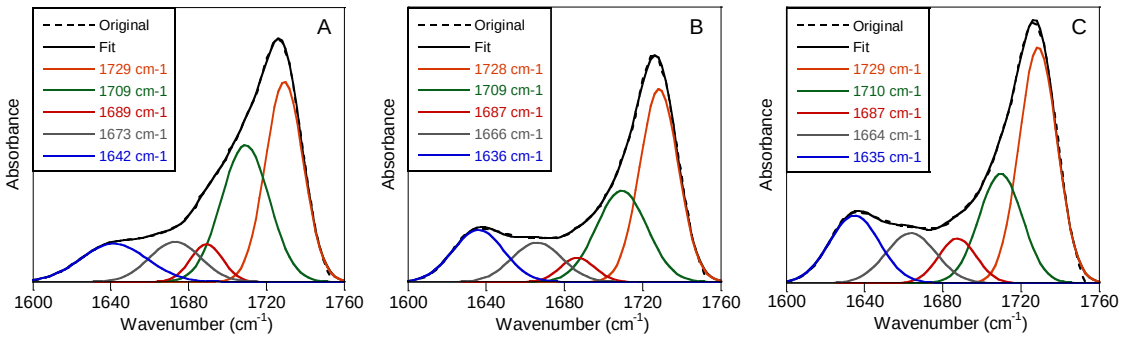

Figure 4.4– C=O stretching band analysis for PU-Gel with different gelatin contents: (A) 5%; (B) 7.5%; (C) 10%.

Table 4.1– Wavenumber (v) and relative area (A) of the 5 components of the C=O stretching band and the percentage of carbonyl hydrogen bonded.

C=O	***v*** **(cm^{-1})**	***A*** **(%)**	***v*** **(cm^{-1})**	***A*** **(%)**	***v*** **(cm^{-1})**	***A*** **(%)**	***v*** **(cm^{-1})**	***A*** **(%)**	***v*** **(cm^{-1})**	***A*** **(%)**	**% of C=O H-bonded**
5%	1729	38.0	1709	32.9	1689	6.10	1673	10.3	1641	12.7	55.9
7.5%	1728	42.5	1709	26.4	1686	4.74	1666	11.3	1636	15.1	52.8
10%	1729	42.1	1710	22.3	1687	7.88	1664	11.8	1635	15.9	50.0

For the amine region, the original data, the fitting and the Gaussian curves for PU-Gel are represented in Figure 4.5. The wavenumber (cm^{-1}), the relative Gaussian areas and the percentage of hydrogen bonds in the amine region are detailed in Table 2.1. The amine region is fitted with four distinct bands, which are from: the amine hydrogen bonded to oxygen polyester SS at 3270 – 3280 cm^{-1}, the order hydrogen bonds in HS at 3309 – 3315 cm^{-1}, the disorder hydrogen bond in HS at 3368 – 3373 cm^{-1} and the free amines at 3450 cm^{-1}.

From the analysis of the amine stretching region, it was observed that PU-Gel-5 has lower free amine groups and superior hydrogen bonded amine groups. For all PUs, the hydrogen bonds in the hard segment are mostly disordered due to the higher functionality of gelatin that prevent the HS to pack efficiently. PU-Gel-5 has the lowest percentage of hydrogen bonds established between the HS and the SS (24.0 %), indicating that the remaining hydrogen bonds are mainly established between HS, which contribute to superior phase segregation.

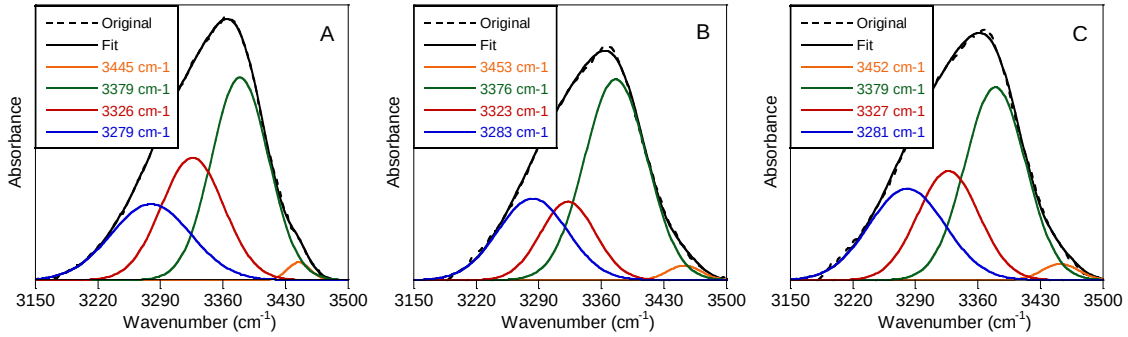

Figure 4.5 – N-H stretching band analysis for PU-Gel with different gelatin contents: (A) 5%; (B) 7.5%; (C) 10%.

Table 4.2– Frequency (v) and relative area (A) of the 4 components of the N-H stretching band and the percentage of amine hydrogen bonded.

N-H	***v*** **(cm^{-1})**	***A*** **(%)**	***v*** **(cm^{-1})**	***A*** **(%)**	***v*** **(cm^{-1})**	***A*** **(%)**	***v*** **(cm^{-1})**	***A*** **(%)**	**% of N-H h-bonded**
5%	3279	24.0	3326	30.3	3379	45.7	3445	2.57	98.4
7.5%	3283	25.2	3323	19.0	3376	55.9	3453	2.14	97.9
10%	3281	27.4	3327	26.4	3379	46.3	3452	2.32	97.7

4.3.1.2 **Thermal characterization**

In Figure 4.6 is shown the DSC thermograms of PU extended with different amounts of gelatin, as well as those of PCL and fish gelatin.

PCL displays a melting peak at a temperature (*Tm*) of 61.3 ºC, confirming its crystallinity, while in fish gelatin a broad endothermic peak around 100 ºC is mainly related with water evaporation. The absence of a melting transition peak in fish gelatin is due to its essentially denatured amorphous structure (absence of helix-coil transitions) (Chuaynukul, Prodpran et al. 2014).

In all PU-Gel thermograms, an endothermic melting peak appears around 50 ºC – 60ºC due to the melting of the soft segment phase (PCL). As can be seen in Table 4.3, in the case of PU-Gel-5, this peak occurs at about the PCL melting temperature but, as the gelatin content in the PU backbone increases, it shifts to lower temperatures (51.3 ºC for PU-Gel7.5 and 51.8 ºC for PU-Gel-10). Values of the melting enthalpy (ΔH_m) and degree of crystallinity (X_c) of the soft segment were calculated and are also presented in Table 4.3. A decrease of the melting enthalpy with the increase of gelatin content is also observed. This denotes a decrease of the soft segment crystallinity degree. The reduction can be explained by the extent of crosslinking between gelatin and the pre-polymer, which gives rise to a rigid 3D structure preventing microphase separation (Zou, Chen et al. 2015). Thus, the increment of gelatin in the PU backbone results in a phase mixed structure. No melting transitions are observed at higher temperatures, indicating the lack of hard segment order (Tatai, Moore et al. 2007).

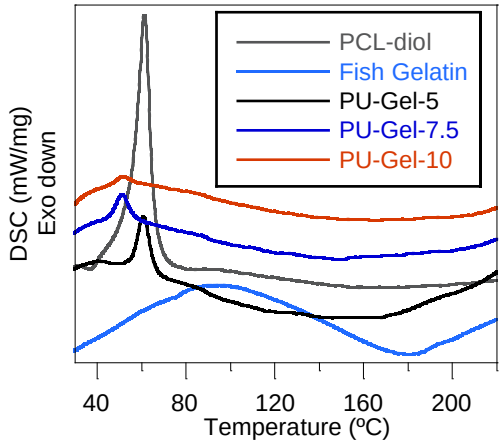

Figure 4.6– DSC thermograms of PUs synthesized with different amounts of gelatin.

Table 4.3– Thermal analysis data of PU-Gel. From DSC: Melting temperature (T_m), melting enthalpy (ΔH_m) and crystallinity (X_c) of the soft segment. From TGA: degradation temperatures of the two observed stages (T_1 and T_2) and corresponding weight losses (Δw_1 and Δw_2).

Polyurethanes	*DSC*			TGA			
	T_m (ºC)	ΔH_f (J/g)	X_c (%)	T_{hard} (ºC)*	Δw_1 (wt%)	T_{soft} (ºC)*	Δw_2 (wt%)
PU-Gel-10	51.8	2.54	1.86	342	13.5	415	62.0
PU-Gel-7.5	51.3	7.85	5.77	338	13.8	413	63.0
PU-Gel-5	60.9	11.7	8.57	334	13.9	409	60.1

TGA curves of fish gelatin, PCL and three PU-Gel, and their corresponding derivative plots (DTG) are presented in Figure 4.7A and Figure 4.7B, respectively.

Fish gelatin shows a first stage of mass loss up to 200 ºC due to the evaporation of absorbed and bounded water molecules (about 88% of the mass remains at the end of this stage), and a second degradation stage between 200 ºC and 400 ºC associated with protein degradation

(Barreto, Pires et al. 2003; Benbettaïeb, Karbowiak et al. 2016). At 500 ºC around 30% of gelatin mass remains. In PCL-diol a single degradation stage is observed at 418 ºC.

Thermal degradation of PU-Gel occurred in two stages: a first stage at a temperature, T_1, around 340 ºC, and a second one at a temperature, T_2, around 410 ºC (Table 4.3). The first degradation stage is related to the hard segment degradation (urea and urethane linkages are broken), while the second one is related to the soft segment degradation (Chattopadhyay and Webster 2009). The decomposition temperature of each stage as well as the corresponding weight loss, Δw_1 and Δw_2, are reported in Table 4.3. Weight loss was nearly total at the end of the assay (500 ºC).

The thermal degradation profiles were very similar for all the PU-Gel, although the increase in gelatin content lead to a small increase in the degradation temperatures. This result can be explained by the increasing number of urethane/urea groups in polymer backbone, which by establishing strong hydrogen bonds increase the resistance to thermal degradation (Tang, Macosko et al. 2014).

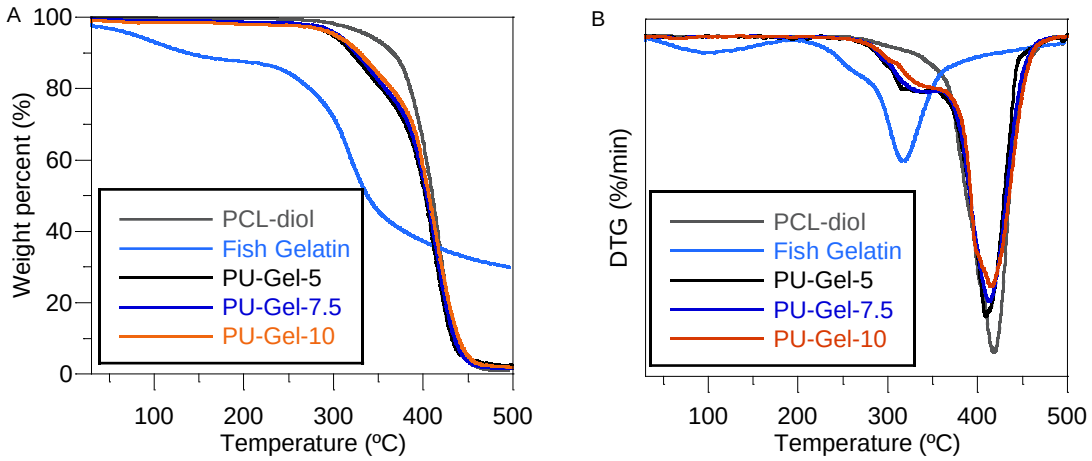

Figure 4.7 – Thermal analysis of PU-Gel synthesized with different amounts of gelatin: (A) thermogravimetric analysis spectra; (B) Derivative weight loss curves.

4.3.2 Characterization of fiber mats

4.3.2.1 Optimization process and fibers morphology

For electrospinning, all PU-Gel were dissolved in 18 wt% solutions dissolved in different solvent mixtures in order to produce fiber mats.

PU-Gel-10 was dissolved in a solvent mixture with 50:50 THF:DMF. However, its dissolution was not complete and consequently, during the electrospinning process, some fibers were formed but at the same time undissolved polymer projections were thrown to the collector, destroying the few existing fibers (Figure 4.8B). Due to the capacity to break inter-urea bonds, 1,1,1,3,3,3-hexafluoro-2-propanol (HFP), which is an aggressive and toxic solvent, have been widely used to dissolve PUs. However, this solvent did not completely dissolve PU-Gel-10. Electrospun this solution, resulted in irregular diameter fibers that contain lots of projections

(Figure 4.9A). As HFP did not improve the PU-Gel-10 solubility, it was not used to dissolve other PU-Gel due to their toxicity and high cost.

PU-Gel-7.5 solution, prepared from 50:50 THF:DMF mixture, was electrospinnable but the resulting fibers had a beaded morphology because the dissolution of the polymer was still incomplete (Figure 4.8C). Even after adjusting the solution concentration and the electrospinning set-up parameters, the resulting fibers were not free of defects.

When the solution of PU-Gel-5 prepared using a 50:50 THF:DMF mixture was electrospun, the resulting fibers were produced without defects and with an uniform diameter (Figure 4.8D).

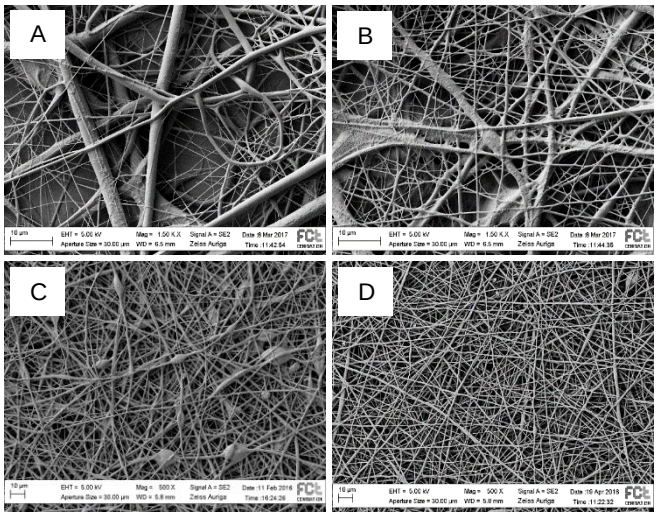

Figure 4.8 – SEM images of the fibrous mats produced from (A) PU-Gel-10 dissolved in HFP, (B) PU-Gel-10 dissolved in 50:50 THF:DMF, (C) PU-Gel-7.5 dissolved in 50:50 THF:DMF and (D PU-Gel-5 dissolved in 50:50 THF:DMF.

Other solvent mixtures were tested in order to improve the PU-Gel-5 fibers quality. Those include: Chloroform:DMF, THF:DMAc and Chloroform:DMAc in a 50:50 proportion. Replacing the DMF by DMAc, resulted in a fiber mat similar to the one produced using THF:DMF but the fiber's diameter is more irregular (Figure 4.9B). Although both DMAc and DMF have high boiling points and dielectric constants responsible to decrease the viscosity of the solutions, the electrospinning process was more stable when DMF was used as solvent. When THF was replaced by chloroform using either DMF or DMAc, projections were thrown to the collector during the electrospinning process (Figure 4.9C and Figure 4.9D). Solutions with chloroform have higher viscosity and surface tension than solutions with THF due to the inferior boiling point and dielectric constant. During the electrospinning, solutions with chloroform clogged in the needle tip, causing the interruption of the jet and resulting in mats with defects.

The binary solvent mixture of 50:50 THF:DMF is the one used to produce fibrous mats without defects. Solutions of PU-Gel-5 were prepared with this solvents at 18% w/w concentration and electrospun at 1.0 mL/h flow rate, 18 kV applied voltage and 20 cm distance from the needle tip to the collector. The resulting mats have a mean fiber diameter of (705 ± 309) nm.

When high gelatin content is used in PUs, an increase in gelatin chemical crosslink, and consequently, polymer gelation may occur, which prevent the complete polymer dissolution and deteriorate the eletrospinning process. Therefore, only the PU-Gel-5 mats were characterized and are denominated simply PU-Gel from now on. The PU-Gel solution used to electrospun fiber mats was also used to produce casted films for comparison purposes. Films an fiber mats are identified by preceding PU-Gel by F_ and M_, respectively.

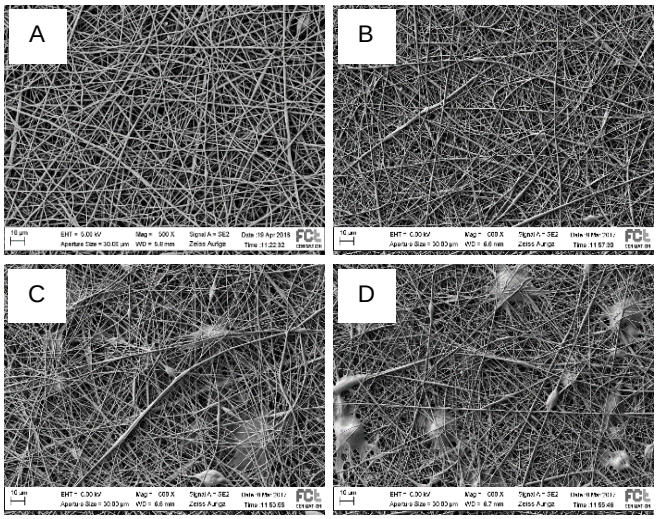

Figure 4.9 – SEM images of the fibrous mats produced from PU-Gel-5 dissolved in (A) 50:50 THF:DMF, (B) 50:50 THF:DMAc, (C) 50:50 Chloroform:DMF and (D) 50:50 Chloroform:DMAc.

4.3.2.2 **Mechanical properties**

Figure 4.10A shows a typical stress-strain curve for films and fiber mats. Films have the stress-strain curves typical of thermoplastic elastomers, with an initial (up to about 30% strain) linear region typical of an elastomer followed by a plastic deformation with strain hardening at higher elongations due to strain induced crystallization of soft segments (Ahmad, Khan et al. 2014). The stress-strain curves of fiber mats have the initial linear region; however, the strain hardening at higher elongations is absent. In fibrous mats, the lower density of the electrospun samples, when compared to films, the initial reorientation of most fibers in the pulling direction and the degree of molecular orientation in this direction are responsible for the differences in stress-strain curves of mats and films (Pedicini and Farris 2003).

Young's modulus of PU-Gel films is (8.2 ± 0.5) MPa, which is superior to the Young's modulus of fiber mats (1.9 ± 0.3) MPa (Table 4.4). The elongation at break of PU-Gel films and fiber mats was superior to 600%. Its exact value was not determined because the slippage of the samples on the grips before rupture. Clearly, the polymer processing impacts the mechanical properties. As expected, fiber mats have inferior Young's modulus than the films due to their porous structure, different from the compact structure of the films, which determines a smaller effective sample's material transverse area being stretched.

The hysteresis behavior of the PU-Gel films and fibrous mats was evaluated by subjecting the samples to 10 cycles of hysteresis. In Figure 4.10B is shown the hysteresis loops and the percentage of the first hysteresis loop. The first hysteresis loop is the one with superior hysteresis percentage, which is reduced in the following loops until reach a constant value. This is the typical behavior of a thermoplastic elastomer. Films have (53 ± 4) % hysteresis, which is superior to the hysteresis in fibrous mats - (30 ± 6) %. This result is expected because when the fibers are stretched up to 80 % they did not break, only slippage in order to align in the stretching direction. Therefore, the fibers can elongate with reduced permanent deformation.

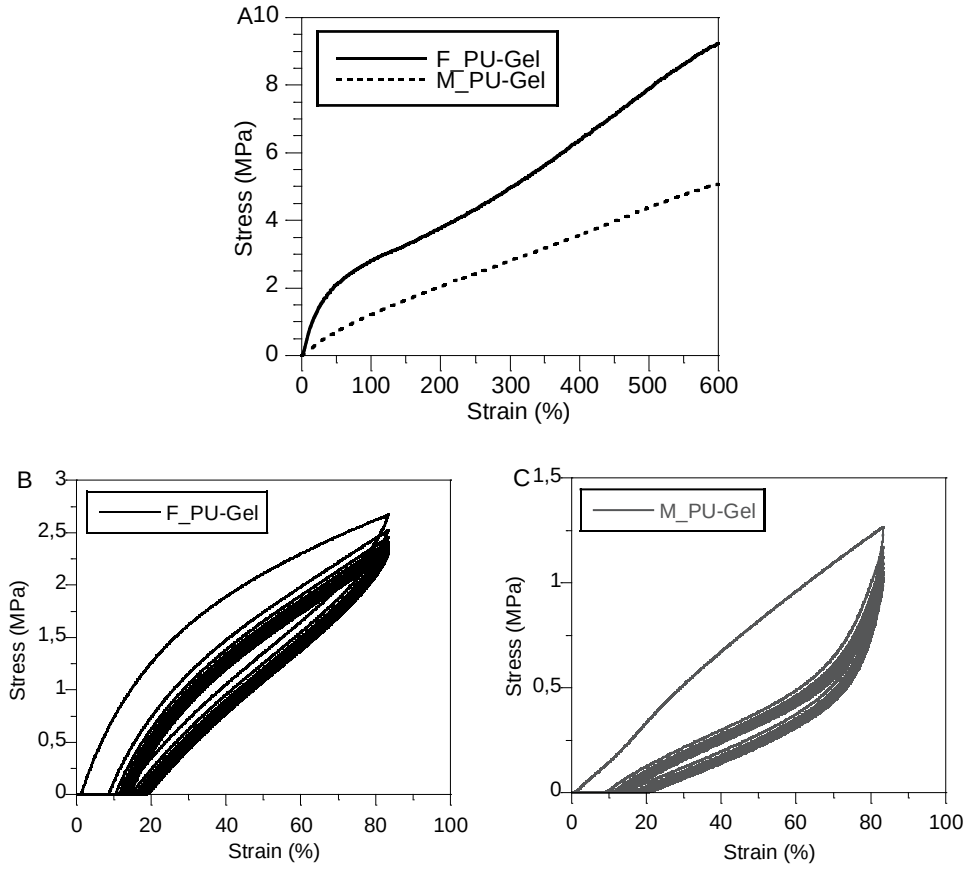

Figure 4.10 – Typical stress-strain curves of PU-Gel films (F_PU-Gel) and fiber mats (M_PU-Gel) (A) and the respective hysteresis loops (B and C) after 10 cycles stretching and recovery.

4.3.2.3 **XRD analysis**

XRD patterns for the PCL, gelatin and PU-Gel films and fibrous mats are presented in Figure 4.11A. The fitting of the PU-Gel diffractogram was performed by a sum of Voigt functions. As an example, in Figure 4.11B is shown the fitting of PU-Gel mats. The fitting was also performed in the diffractograms of the films. XRD diffractogram of PCL have three main peaks at 2θ = 21.4º, 22.0º and 23.7º, which corresponded to the (110), (111) and (200) planes of the crystal structure, respectively. Other small peaks at 2θ = 15.7º and 24.5º appear due to the diffraction by the (102) and (201) planes (Ferreira, Gomes et al. 2014). The gelatin showed one wide crystalline reflection

at 2θ = 20.9º from the triple-helical crystalline structure of collagen renatured in gelatin (Jalaja, Naskar et al. 2015).

PU-Gel diffractograms display one wide diffraction peak at 2θ = 19º associated with the amorphous contributions and two small diffraction peaks at 2θ = 21º and 23º from the diffraction at (110) and (200) crystallographic planes of PCL, respectively. In PU-Gel the diffraction peaks of PCL are almost absent due to the formation of a rigid network that restricts the organization of soft segments, decreasing the crystallinity. These results were similar to the ones obtained by Sarkar et al. (Sarkar, Chourasia et al. 2006) who produced a gelatin based PU using polyethylene lactate ester diol as soft segment and 2,4-toluene diisocyanate. The intensity of crystalline peaks is superior in the diffractograms of fibrous mats than in the films. Crystallite size, calculated from the FWHM of the (110) diffraction peak (Table 4.4), is also higher for the PU-Gel mats, in line with its higher crystalline degree. Therefore, the reorganization of the PU molecules is affected by the processing technique. The stretching forces exerted on the polymeric solutions during the electrospinning process, can induce the molecular chain orientation along the fiber length (Kongkhlang, Tashiro et al. 2008; Ero-Phillips, Jenkins et al. 2012).

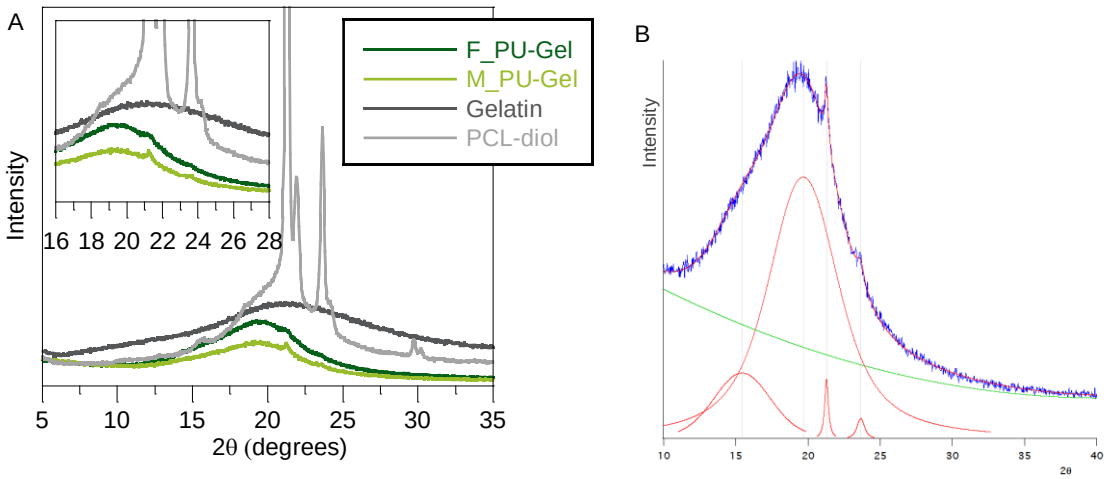

Figure 4.11 – X-ray diffractograms of PU-Gel film and fibrous mat (A). (B) X-ray diffractogram of PU-Gel fibrous mat (blue), the fitting of their characteristic peaks with Voigt functions (red) and a quadratic background (green).

Table 4.4 – Results from XRD and tensile tests of PU-Gel films and fibrous mats. Crystalline degree ($w_{c,x}$), full width at half maximum of the highest intensity crystalline diffraction peak (*FWHW*), crystallite size (t_c), Young modulus (Y), elongation at break (ε_r) and tensile stress at 600% strain (σ_{600}).

Films/Fibrous Mats	***XRD***			***Mechanical tests***		
	$w_{c,x}$ (%)	*FWHW* (º)	t_c (nm)	Y (MPa)	ε_r (%)	σ_{600} (MPa)
F_PU-Gel	0.77 ± 0.06	0.101	79.0	8.2 ± 0.5	>600	9.9 ± 0.6
M_PU-Gel	1.96 ± 0.12	0.0003	>100	1.9 ± 0.3	>600	5.3 ± 0.3

4.3.2.4 **Wettability**

The contact angle measurements on PU-Gel films and mats, as well as the images of the water drop in contact with the film and mat surface is represented in Figure 4.12. The WCA of the fiber mats and films is (145 ± 3) º and (108 ± 3) º, respectively, indicating the hydrophobicity (WCA > 90º) of the sample's' surface. The presence of gelatin in PUs should reduce the hydrophobicity of the samples. Kim et al. (Kim, Heo et al. 2009) produced fibrous mats from blends of hydrophilic gelatin and hydrophobic PU, which have inferior WCA when compared to mats produced using just PU. However, in our work the presence of gelatin is not the determinant factor affecting the WCA values. The high WCA obtained for PU-Gel samples is probably related to the extensive crosslink that occurred when the gelatin was incorporated into the PU backbone, preventing the wetting and spreading of the liquid molecules over the films and mats. Similar results were observed for films obtained from isocyanate-terminated PU grafted onto chitosan molecules (Lee, Kwon et al. 2014; Mahanta, Mittal et al. 2015), where WCA increases with increment of CS ceosslinking density.

The surface of the fiber mats, different from the films, influence the WCA measurements. The higher surface roughness and porosity of the fibers can lead to the entrapment of air bubbles at the water-fiber interface, leaving less contact area for water, which may be responsible for the superior WCA values observed in the fibrous mats (Tijing, Park et al. 2013).

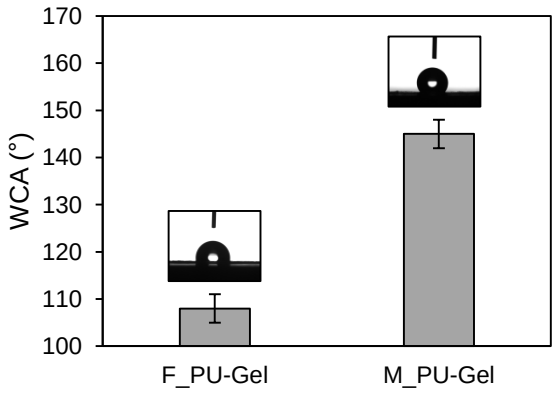

Figure 4.12 – Water contact angle values of the PU-Gel films and electrospun fibrous mats and the respective water drop images.

4.3.2.5 **Degradation profile**

Figure 4.13A and Figure 4.13B shows the degradation profile of PU-Gel films and fibrous mats, respectively, when immersed in PBS, lipase and trypsin solution. In PBS solution, PU-Gel films and fibrous mats barely lose weight during 37 days.

Lipase is an esterase that catalyzes the hydrolysis of the PCL soft segment ester linkages, resulting in α-hydroxyacids degradation products and urethane and urea fragments (Tokiwa, Ando et al. 1990; He and Chu 2013). In lipase solution, the films degraded at a constant rate during 37 days, losing (7.2 ± 0.5) % of their initial weight. On the opposite, mats lost 15% of their weight in the first two weeks and only 3.5% of their weight in the following 3 weeks. The

structural arrangement of the samples influence their degradation mechanism. Mats with a porous structure can facilitate the diffusion of the enzyme inside the PU structure, accelerating the degradation mechanism.

PU-Gel samples degradation was also evaluated in trypsin degrading solution. Trypsin is an enzyme that hydrolyses proteins, cleaving peptide chains at the carboxyl site of lysine or arginine aminoacids. Gelatin is derived from the hydrolysis of collagen, maintaining nearly the same chemical composition. Therefore, trypsin was found to be an effective enzyme for gelatin degradation (Giménez, Moreno et al. 2013). The degradation profile of the PU-Gel films and fibrous mats in trypsin is similar to the one in PBS, denoting that the trypsin solution had no effect on the degradation process of PU-Gel substrates. The low quantity of gelatin in the PU backbone and their crosslinking can make their degradation imperceptible.

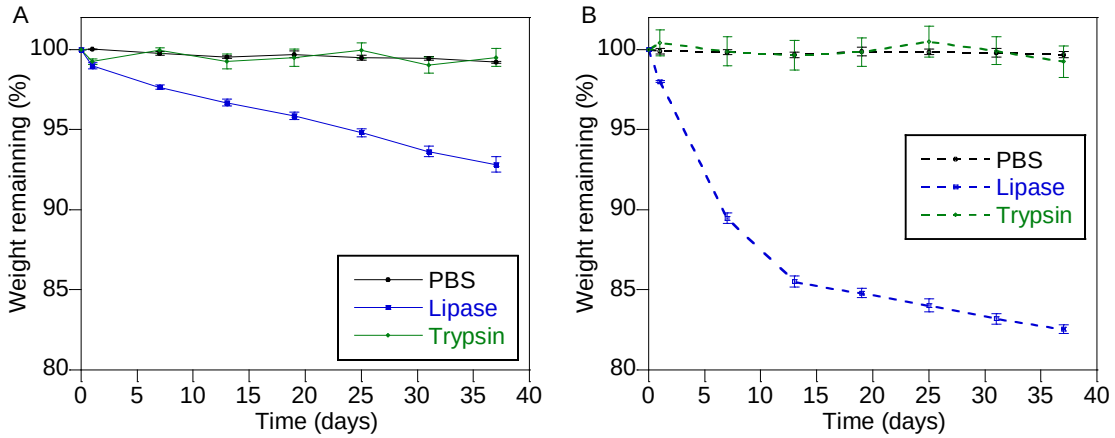

Figure 4.13 – Degradation profile of the PU-Gel films (A) and fibrous mats (B) in PBS, lipase and trypsin.

4.3.2.6 **Viability of HFFF2 cells**

Cytotoxicity

Extract method was used to evaluate possible cytotoxic effect of PU-Gel films and mats. Results of the colorimetric resazurin assay, performed with HFFF2 cells in contact with extracts, are shown in in Figure 4.14. Viability values are normalized to the negative control (viable cells, C-) and are all superior to 93.5 %, indicating the absence of toxicity for PU-Gel samples. On the opposite, the positive control (C+) viability is very low, which confirms the test's reliability. The cells are also observed in the optical microscope and a representative image of the cells in contact with the pure extract during 48 h is represented in Figure 4.15. The cells presented a regular stretched morphology like the ones in the control wells. On the opposite, few cells are observed in the positive control and presented a round morphology. The absence of cytotoxic leachable products from the PU-Gel fibers, indicates that PU-Gel fibrous mats can be considered for applications in tissue engineering.

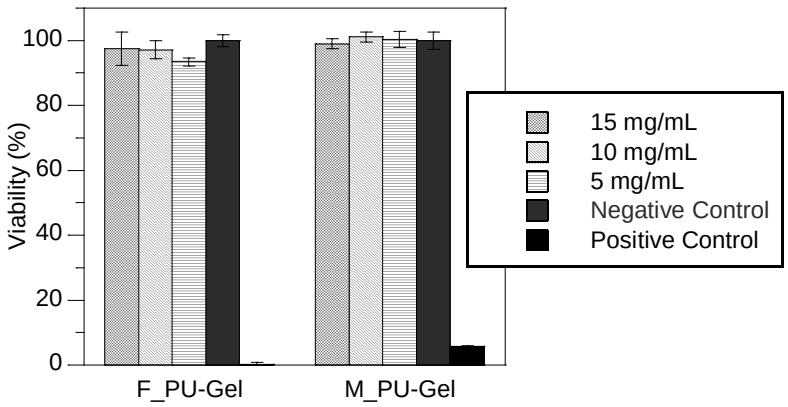

Figure 4.14 – Cytotoxicity assessment of HFFF2 cells cultured with extracts from PU-Gel films and mats at concentrations of 15, 10, and 5 mg/mL. Positive and negative controls have culture medium with and without 10% DMSO, respectively.

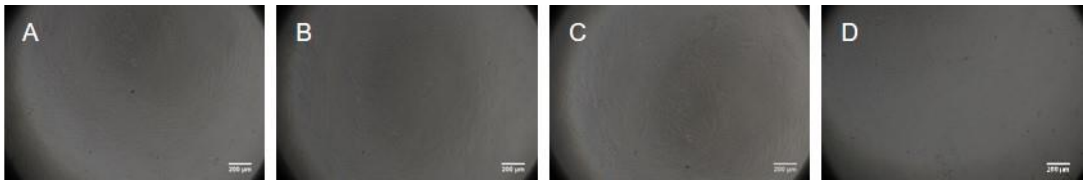

Figure 4.15 – Optical microscope images of the HFFF2 cells seeded in 96 well plate in contact with pure extracts of PU- Gel films (A) and fiber mats (B), negative control (live cells) (C) and positive control (dead cells) (D). Scale bar: 200 µm.

Adhesion and proliferation assay

Figure 4.16A displays the viability of HFF2 cells seeded on PU-Gel films, PU-Gel fibrous mats and TCP wells (cell control, CC), which was accessed using the resazurin test. Cell adhesion was evaluated 24 h after cell seeding (day 1) and cell proliferation was evaluated on subsequent days up to 11 days in culture.

On the first day, and in comparison to CC, cell adhesion on fibrous mats is significantly inferior while cell adhesion on films has no statistically difference. Following day 1, the cells on fibrous mats increase their proliferation over time but never reach the CC population. However, cells on films grow similar to CC up to day 5, and then cell population remains constant until the end of the assay. Fibrous mats are suitable substrates for cell adhesion and proliferation due to their fibrillar structure similar to the ECM, their high surface area and their 3D structure that allow the exchange of nutrients and toxic products conferring the cells with the appropriate environment and maintain their metabolism (Cui, Zhou et al. 2016).

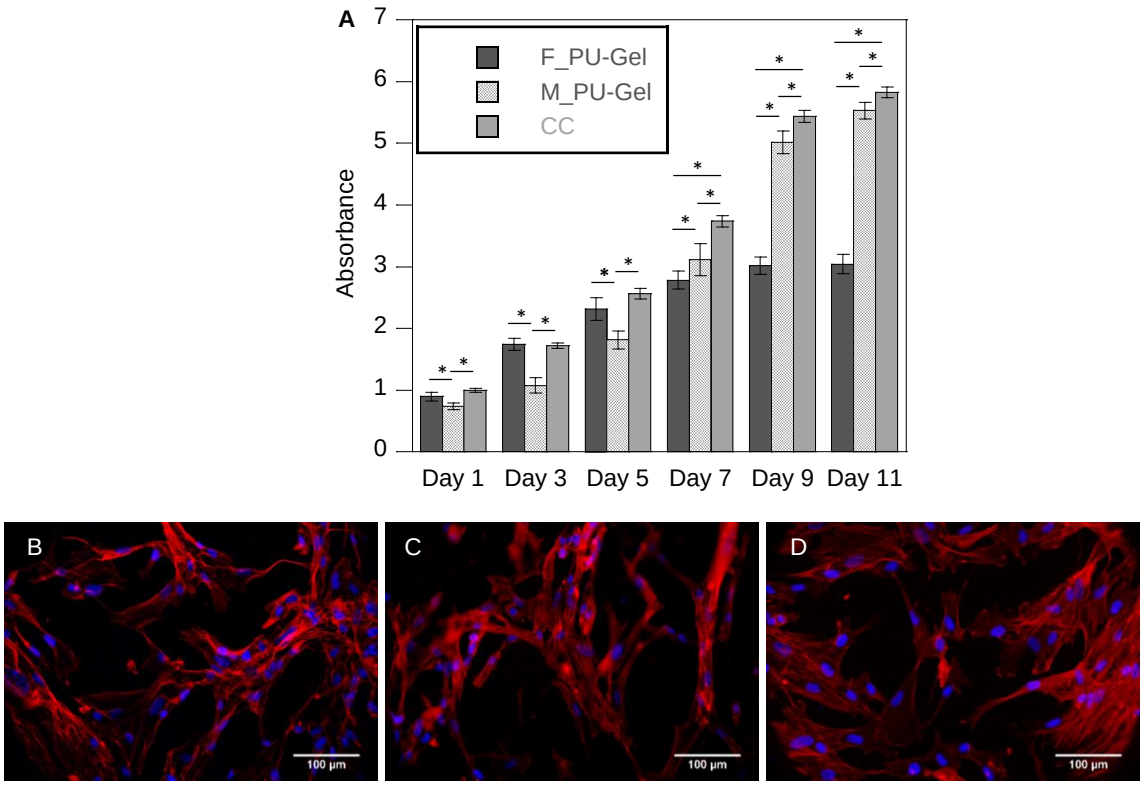

Figure 4.16 – (A) Proliferation of HFFF2 cells seeded on the PU-Gel films and fiber mats after 1, 3, 5, 7, 9 and 11 days of culture (mean ± standard deviation, n=5). Significance: *p<0.05. Fluorescent images of phalloidin (red) and DAPI (blue) stained HFFF2 cells seeded on (B) PU-Gel films, (C) PU-Gel fibrous mats and (D) glass coverslips, after 5 days in culture. Scale bar: 100 µm.

Fluorescent images of cells after 5 days in culture on films, fibrous mats and glass coverslips are shown in Figure 4.16. The higher projected cell area is observed on the flat substrates where cells protruded over all directions with noticeable stress fiber formation. On the mats, the cells exhibited longer and thin filaments with inferior projected area. PU-Gel fibers, with an average diameter of 705 nm, can limit the size of the focal adhesions and limit cell spreading. Similar results were reported by Bashur et al. (Bashur, Dahlgren et al. 2006). In his work, fibroblasts grown on PLLA mats with diameters similar to the ones of the PU-Gel mats, have reduced cell area. The limitation in cell spreading on the mats can explain the inferior adhesion and proliferation of the fibroblasts in the initial days, where they are adapting to the new environment.

4.3.3 Random vs Aligned fibrous mats

4.3.3.1 Fibrous mats morpholgy

PU-Gel solutions at 18 wt% concentration in 50:50 THF:DMF solvents was electrospun to create non-woven fibrous structures. Random mats were collected in a flat collector while aligned mats were collected in a rotatory mandrel. In Figure 4.17 is shown the SEM images of the PU-Gel fibrous mats with random and aligned fibers as well as the fiber diameter distributions. Both fibrous mats were produced without defects. In random mats, the fibers have an average

diameter of (705 ± 309) nm while aligned mats have superior average diameter, (816±416) nm. The alignment degree was obtained by analyzing the SEM images on ImageJ software using the preferred angle plugin with the Fast Fourier Transform (FFT) and the oval projection method. The direct measurement of the angle of the fibers with the horizontal (0º) was performed to get the fiber angular distribution. Both the FFT intensity graph as well as the angular distribution histogram are represented in Figure 4.17C and Figure 4.17F, respectively. From the fiber angular distribution analysis, in the aligned mats 96% of the fibers are within the range of 60º to 120º with respect to the 90º. On the opposite, in random mats the fibers were deposited in all directions without any preferential orientation. From the analysis of the shape and weight of the peaks at the FFT intensity graph in aligned mats, few and high intense peaks were observed. Thus, confirming ordered fibers in the mats (Ayres, Bowlin et al. 2006). On the opposite, FFT intensity graph of random mats shows multiple peaks with small intensities, indicating fibers with poor order in the mats.

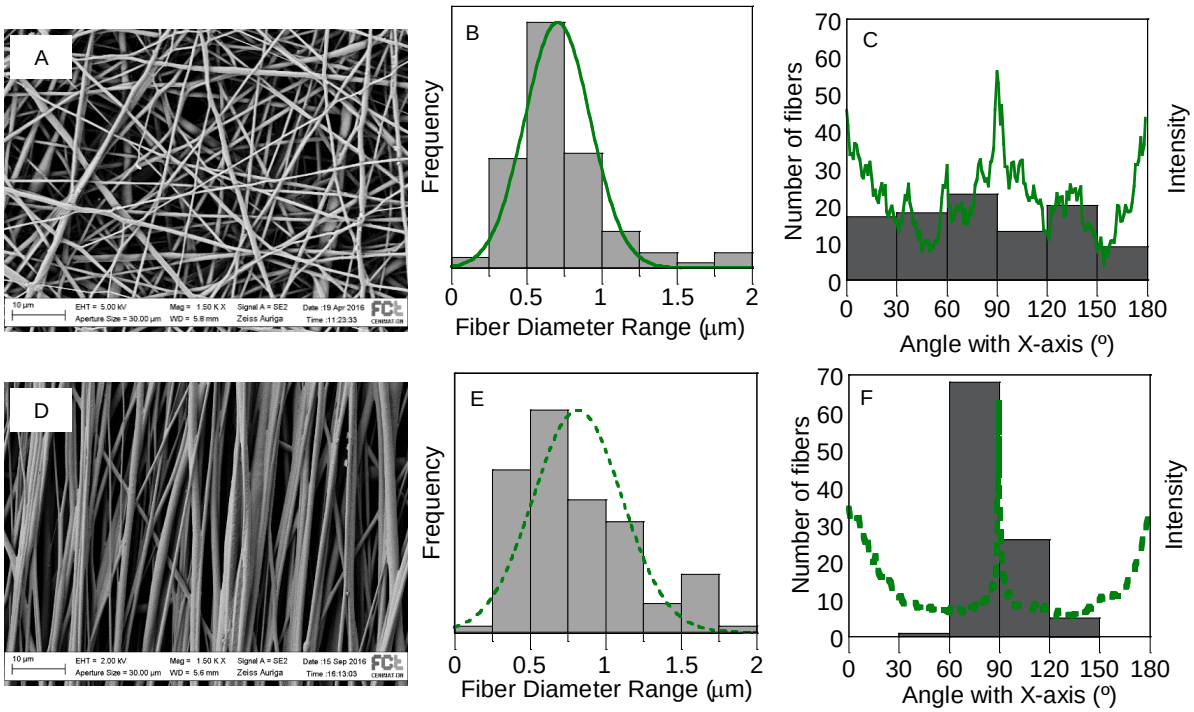

Figure 4.17 – SEM images of random (A) and aligned (D) PU-Gel fibrous mats, and the respective histograms of the fiber diameter distribution (B and E) and the angle distribution (C and F).

4.3.3.2 **Mechanical properties**

In Figure 4.18 is shown the representative stress-strain curves of aligned and random PU-Gel mats. The Young's modulus of the random mats is (5.19 ± 0.08) MPa, which is inferior to the one of the aligned mats that is (17 ± 2) MPa. On the opposite, random mats can withstand a maximum elongation at break of (713 ± 13) %, which is superior to the elongation at break of aligned mats that is (419 ± 25) %. Aligned fibers can withstand superior loads but with inferior elongations (Yao, Bastiaansen et al. 2014). In the aligned fibers, as the mechanical load is applied in the direction of the fiber alignment, the aligned fibers are already stretched. Thus, aligned mats

did not organize in the stretching direction as the randomly oriented fibers do, resulting in inferior elongations.

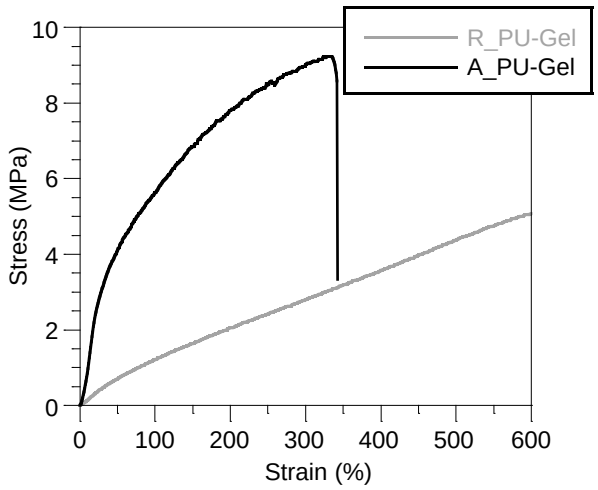

Figure 4.18 – Stress-strain curves of the random (R_) and aligned (A_) PU-Gel fibrous mats.

4.3.3.3 **Wettability**

Figure 4.19 displays the WCA values of the random and aligned PU-Gel mats and the respective sessile drop picture in contact with the substrate. The WCA values for the PU-Gel fibrous mats in random and aligned morphology are (145 ± 3) º and (143 ± 3) º, respectively. Both mats are hydrophobic and their WCA values very similar. The WCA depends on the morphology of the fibrous mats such as, the alignment degree, the fiber diameter and the porosity and pore size. Inferior WCA has been reported in fibrous mats with aligned morphology (Kim, Hwang et al. 2016) and in mats with superior pore size and diameter (Cui, Li et al. 2008). In PU-Gel mats, the alignment degree did not affect the WCA measurements. Probably, other factors such as the surface chemistry have superior influence in the WCA measurements.

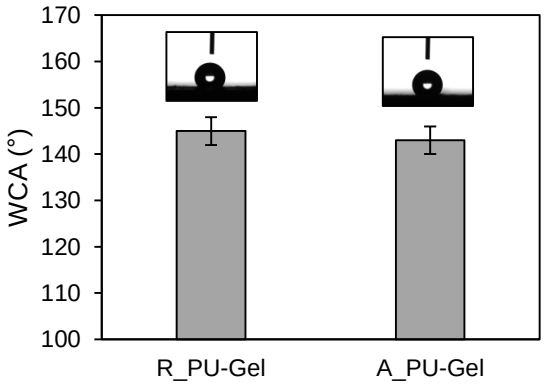

Figure 4.19 – Water contact angle values of random and aligned PU-Gel mats.

4.3.3.4 **Cellular assays**

The biocompatibility of the HFFF2 cells seeded on random and aligned PU-Gel mats was evaluated using the rezasurin calorimetric assay over 11 days. Figure 4.20A shows the results of

cell population over time for the random and aligned PU-Gel mats as well as for the tissue culture plate (TCP) wells (cell control,CC). In comparison to CC, cell adhesion (evaluated after 24 h of cell seeding) to aligned mats has no statistically significant difference while adhesion to random mats is slightly inferior. On the following days, cell population remains inferior in random mats when compared to aligned mats and CC, which has similar cell population values on the following days.

Other studies reported better proliferation of mesenchymal stem cells (Chang, Fujita et al. 2013; Zandén, Erkenstam et al. 2014) and neural stem cells (Kim, Hwang et al. 2016), on fibrous mats with aligned morphology. One explanation for that is the similarity of the aligned fibrous substrate with the flat controls, which provide more contact points for cell adhesion and proliferation. However, in a study of Jamadi et al. (Jamadi, Ghasemi-Mobarakeh et al. 2016) the proliferation of cardiomyocytes was reduced on the aligned fibrous mats of PUs blended with gelatin. For 3T3 cell line, no differences in cell adhesion and proliferation on random and aligned PCL and gelatin composite electrospun mats were observed (Fee, Surianarayanan et al. 2016). Although the direct comparison of the studies is difficult to perform due to the different cell types and different materials, all the studies agreed that the anisotropic mats are good to cellular guidance.

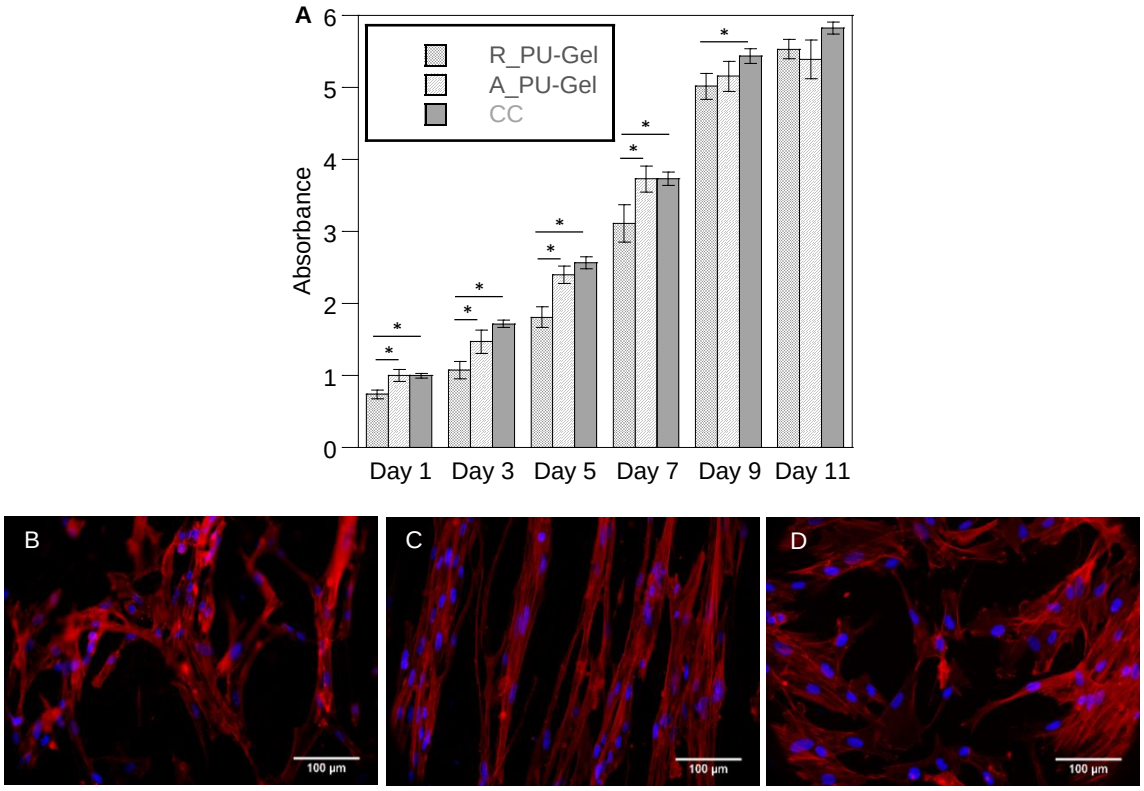

Figure 4.20 – Proliferation assay of HFFF2 cells seeded on the electrospun PU-Gel fibrous mats with random and aligned morphology every other day during 11 days of culture (mean ± standard deviation, *n=5*) (A) Significance: **p*<0.05. Fluorescent images of phalloidin (red) and DAPI (blue) stained HFFF2 cells in the (B) random PU-Gel mats, (C) aligned PU-Gel mats and (D) glass coverslips, after 5 days in culture. Scale bar: 100 µm.

Fluorescent images of cells after 5 days in culture on different substrates is shown in Figure 4.20B, C and D. On the control, cells are well spread with high projected area. On the opposite, cells stretched and elongated on the mats. On the aligned mats, the cell's cytoskeleton followed the fiber alignment as well as the cell's nuclei. In addition, the cells grew on bundles that can establish cell-cell contacts between them.

4.4 Conclusion

In this chapter it was described the synthesis and characterization of gelatin based PUs and their processing into fibrous mats using the electrospinnig technique.

PUs based on PCL-diol and gelatin in different Gel/PCL-diol weight proportions (5%, 7.5% and 10%) were synthesized. However, only the PU-Gel with inferior gelatin content (5%) rendered fibrous mats with uniform fiber diameter and without defects, when electrospun. Fibrous mats have a lower Young's modulus and a higher crystallinity, are more hydrophobic and degrade faster in lipase solution when compared to the corresponding films. The fibrous structure support the adhesion and proliferation of HFFF2 cells.

Aligned mats produced using a rotating mandrel have superior Young's modulus and reduced elongation at break in the direction of fiber alignment, and support superior adhesion and proliferation of HFFF2 cells when compared to the random mats. In addition, aligned mats guide cell in the direction of fiber's alignment. Thus, PU-Gel mats can offer mechanical and chemical support as well as guidance cues for fibroblasts, which is an indicator of their suitable application in soft tissue engineering.

4.5 References

Ahmad, N., M. Khan, et al. (2014). "The influence of cross-linking/chain extension structures on mechanical properties of htpb-based polyurethane elastomers." Arabian Journal for Science and Engineering **39**(1): 43-51.

Amadori, S., P. Torricelli, et al. (2015). "Effect of sterilization and crosslinking on gelatin films." Journal of Materials Science: Materials in Medicine **26**(2): 1-9.

Ayres, C., G. L. Bowlin, et al. (2006). "Modulation of anisotropy in electrospun tissue-engineering scaffolds: analysis of fiber alignment by the fast Fourier transform." Biomaterials **27**(32): 5524-5534.

Barikani, M., H. Honarkar, et al. (2009). "Synthesis and characterization of polyurethane elastomers based on chitosan and poly (ε-caprolactone)." Journal of Applied Polymer Science **112**(5): 3157-3165.

Barreto, P., A. Pires, et al. (2003). "Thermal degradation of edible films based on milk proteins and gelatin in inert atmosphere." Polymer Degradation and Stability **79**(1): 147-152.

Bashur, C. A., L. A. Dahlgren, et al. (2006). "Effect of fiber diameter and orientation on fibroblast morphology and proliferation on electrospun poly (D, L-lactic-co-glycolic acid) meshes." Biomaterials **27**(33): 5681-5688.

Benbettaïeb, N., T. Karbowiak, et al. (2016). "Impact of electron beam irradiation on fish gelatin film properties." Food chemistry **195**: 11-18.

Chan-Chan, L., C. Tkaczyk, et al. (2013). "Characterization and biocompatibility studies of new degradable poly (urea) urethanes prepared with arginine, glycine or aspartic acid as chain extenders." Journal of Materials Science: Materials in Medicine **24**(7): 1733-1744.

Chang, J.-C., S. Fujita, et al. (2013). "Cell orientation and regulation of cell–cell communication in human mesenchymal stem cells on different patterns of electrospun fibers." Biomedical Materials **8**(5): 055002.

Chattopadhyay, D. and D. C. Webster (2009). "Thermal stability and flame retardancy of polyurethanes." Progress in Polymer Science **34**(10): 1068-1133.

Chuaynukul, K., T. Prodpran, et al. (2014). "Preparation, thermal properties and characteristics of gelatin molding compound resin." Research Journal of Chemical & Environmental Sciences **2**(4): 01-09.

Cui, W., X. Li, et al. (2008). "Degradation patterns and surface wettability of electrospun fibrous mats." Polymer Degradation and Stability **93**(3): 731-738.

Cui, W., Y. Zhou, et al. (2016). "Electrospun nanofibrous materials for tissue engineering and drug delivery." Science and Technology of Advanced Materials **11**(1): 014108.

Ero-Phillips, O., M. Jenkins, et al. (2012). "Tailoring crystallinity of electrospun plla fibres by control of electrospinning parameters." Polymers **4**(3): 1331-1348.

Fee, T., S. Surianarayanan, et al. (2016). "Nanofiber Alignment Regulates NIH3T3 Cell Orientation and Cytoskeletal Gene Expression on Electrospun PCL+ Gelatin Nanofibers." PLoS ONE **11**(5): e0154806.

Ferreira, J. L., S. Gomes, et al. (2014). "Electrospinning polycaprolactone dissolved in glacial acetic acid: Fiber production, nonwoven characterization, and In Vitro evaluation." Journal of Applied Polymer Science **131**(22): 41068.

Garrett, J. T., R. Xu, et al. (2003). "Phase separation of diamine chain-extended poly (urethane) copolymers: FTIR spectroscopy and phase transitions." Polymer **44**(9): 2711-2719.

Giménez, B., S. Moreno, et al. (2013). "Antioxidant properties of green tea extract incorporated to fish gelatin films after simulated gastrointestinal enzymatic digestion." LWT-Food Science and Technology **53**(2): 445-451.

Guan, J., K. L. Fujimoto, et al. (2005). "Preparation and characterization of highly porous, biodegradable polyurethane scaffolds for soft tissue applications." Biomaterials **26**(18): 3961-3971.

Hafeman, A. E., K. J. Zienkiewicz, et al. (2011). "Characterization of the degradation mechanisms of lysine-derived aliphatic poly (ester urethane) scaffolds." Biomaterials **32**(2): 419-429.

He, M. and C.-C. Chu (2013). "A new family of functional biodegradable arginine-based polyester urea urethanes: Synthesis, chracterization and biodegradation." Polymer **54**(16): 4112-4125.

Henriques, C., R. Vidinha, et al. (2009). "A systematic study of solution and processing parameters on nanofiber morphology using a new electrospinning apparatus." Journal of nanoscience and nanotechnology **9**(6): 3535-3545.

Hu, X., D. Li, et al. (2011). "Biological hydrogel synthesized from hyaluronic acid, gelatin and chondroitin sulfate by click chemistry." Acta biomaterialia **7**(4): 1618-1626.

Jalaja, K., D. Naskar, et al. (2015). "Fabrication of cationized gelatin nanofibers by electrospinning for tissue regeneration." Rsc Advances **5**(109): 89521-89530.

Jamadi, E. S., L. Ghasemi-Mobarakeh, et al. (2016). "Synthesis of polyester urethane urea and fabrication of elastomeric nanofibrous scaffolds for myocardial regeneration." Materials Science and Engineering: C **63**: 106-116.

Kang, H.-W., Y. Tabata, et al. (1999). "Fabrication of porous gelatin scaffolds for tissue engineering." Biomaterials **20**(14): 1339-1344.

Kim, J. I., T. I. Hwang, et al. (2016). "A Controlled Design of Aligned and Random Nanofibers for 3D Bi-functionalized Nerve Conduits Fabricated via a Novel Electrospinning Set-up." Scientific reports **6**.

Kim, S. E., D. N. Heo, et al. (2009). "Electrospun gelatin/polyurethane blended nanofibers for wound healing." Biomedical Materials **4**(4): 044106.

Kongkhlang, T., K. Tashiro, et al. (2008). "Electrospinning as a new technique to control the crystal morphology and molecular orientation of polyoxymethylene nanofibers." Journal of the American Chemical Society **130**(46): 15460-15466.

Kucińska-Lipka, J., I. Gubańska, et al. (2013). "Gelatin-modified polyurethanes for soft tissue scaffold." The Scientific World Journal **2013**: 450132.

Labow, R. S., E. Meek, et al. (1999). "The biodegradation of poly (urethane) s by the esterolytic activity of serine proteases and oxidative enzyme systems." Journal of Biomaterials Science, Polymer Edition **10**(7): 699-713.

Lee, T., S. Kwon, et al. (2014). "Biodegradable sol–gel coatings of waterborne polyurethane/gelatin chemical hybrids." Progress in Organic Coatings **77**(6): 1111-1116.

Li, G., D. Li, et al. (2013). "Alternating block polyurethanes based on PCL and PEG as potential nerve regeneration materials." Journal of Biomedical Materials Research Part A **102**(3): 685-697.

Li, S., X. Kong, et al. (2015). "Preparation of uniform poly (urea–siloxane) microspheres through precipitation polymerization." RSC Advances **5**(110): 90313-90320.

Li, S., J. Zhao, et al. (2014). "Synthesis and characterization of aliphatic segmented poly (ether amide urethane) s through a non-isocyanate route." RSC Advances **4**(45): 23720-23729.

Liu, H., W. Xu, et al. (2010). "Silk-inspired polyurethane containing GlyAlaGlyAla tetrapeptide. I. Synthesis and primary structure." Journal of applied polymer science **117**(1): 235-242.

Mahanta, A. K., V. Mittal, et al. (2015). "Polyurethane-grafted chitosan as new biomaterials for controlled drug delivery." Macromolecules **48**(8): 2654-2666.

Mandalari, G., R. M. Faulks, et al. (2008). "Release of protein, lipid, and vitamin E from almond seeds during digestion." Journal of Agricultural and Food Chemistry **56**(9): 3409-3416.

Oprea, S. (2010). "The effect of chain extenders structure on properties of new polyurethane elastomers." Polymer bulletin **65**(8): 753-766.

Parrag, I. C. and K. A. Woodhouse (2010). "Development of biodegradable polyurethane scaffolds using amino acid and dipeptide-based chain extenders for soft tissue engineering." Journal of Biomaterials Science, Polymer Edition **21**(6-7): 843-862.

Pedicini, A. and R. J. Farris (2003). "Mechanical behavior of electrospun polyurethane." Polymer **44**(22): 6857-6862.

Perales-Alcacio, J., J. Santa-Olalla Tapia, et al. (2013). "HUVEC biocompatibility and platelet activation of segmented polyurethanes prepared with either glutathione or its amino acids as chain extenders." Journal of Biomaterials Science, Polymer Edition **24**(14): 1601-1617.

Rockwood, D. N., R. E. Akins, et al. (2008). "Culture on electrospun polyurethane scaffolds decreases atrial natriuretic peptide expression by cardiomyocytes in vitro." Biomaterials **29**(36): 4783-4791.

Rockwood, D. N., K. A. Woodhouse, et al. (2007). "Characterization of biodegradable polyurethane microfibers for tissue engineering." Journal of Biomaterials Science, Polymer Edition **18**(6): 743-758.

Sarkar, D., J. C. Yang, et al. (2008). "Structure-property relationship of L-tyrosine-based polyurethanes for biomaterial applications." Journal of Applied Polymer Science **108**(4): 2345-2355.

Sarkar, S., A. Chourasia, et al. (2006). "Synthesis and characterization of gelatin based polyester urethane scaffold." Bulletin of Materials Science **29**(5): 475-484.

Shah, P. N., R. L. Manthe, et al. (2009). "Electrospinning of L-tyrosine polyurethanes for potential biomedical applications." Polymer **50**(10): 2281-2289.

Sheth, J. P., G. L. Wilkes, et al. (2005). "Probing the hard segment phase connectivity and percolation in model segmented poly (urethane urea) copolymers." Macromolecules **38**(13): 5681-5685.

Shi, Y., X. Zhan, et al. (2008). "Quantitative IR characterization of urea groups in waterborne polyurethanes." Journal of Polymer Science Part A: Polymer Chemistry **46**(7): 2433-2444.

Skarja, G. and K. Woodhouse (2000). "Structure-property relationships of degradable polyurethane elastomers containing an amino acid-based chain extender." Journal of Applied Polymer Science **75**(12): 1522-1534.

Tang, D., C. W. Macosko, et al. (2014). "Thermoplastic polyurethane elastomers from bio-based poly (δ-decalactone) diols." Polymer Chemistry **5**(9): 3231-3237.

Tatai, L., T. G. Moore, et al. (2007). "Thermoplastic biodegradable polyurethanes: The effect of chain extender structure on properties and *in-vitro* degradation." Biomaterials **28**(36): 5407-5417.

Tijing, L. D., C.-H. Park, et al. (2013). "Characterization and mechanical performance comparison of multiwalled carbon nanotube/polyurethane composites fabricated by electrospinning and solution casting." Composites Part B: Engineering **44**(1): 613-619.

Tokiwa, Y., T. Ando, et al. (1990). "Biodegradation of synthetic polymers containing ester bonds." Polym. Mater. Sci. Eng **62**: 988-992.

Vatankhah, E., M. P. Prabhakaran, et al. (2014). "Phenotypic modulation of smooth muscle cells by chemical and mechanical cues of electrospun Tecophilic/gelatin nanofibers." ACS applied materials & interfaces **6**(6): 4089-4101.

Wang, F., Z. Zheng, et al. (2014). "Trypsin-inspired poly (urea-urethane) s containing phenylalanine-lysine ethyl ester-phenylalanine units." Polymer Degradation and Stability **100**: 86-92.

Yao, J., C. W. Bastiaansen, et al. (2014). "High strength and high modulus electrospun nanofibers." Fibers **2**(2): 158-186.

Yilgor, I., E. Yilgor, et al. (2006). "FTIR investigation of the influence of diisocyanate symmetry on the morphology development in model segmented polyurethanes." Polymer **47**(11): 4105-4114.

Zandén, C., N. H. Erkenstam, et al. (2014). "Stem cell responses to plasma surface modified electrospun polyurethane scaffolds." Nanomedicine: Nanotechnology, Biology and Medicine **10**(5): 949-958.

Zhang, S., L. Cheng, et al. (2003). "NMR studies of water-borne polyurethanes." Journal of applied polymer science **90**(1): 257-260.

Zhang, Y., W. He, et al. (2017). "Gemini quaternary ammonium salt waterborne biodegradable polyurethanes with antibacterial and biocompatible properties." Materials Chemistry Frontiers **1**(2): 361-368.

Zia, K. M., M. Barikani, et al. (2008). "Molecular engineering of chitin based polyurethane elastomers." Carbohydrate Polymers **74**(2): 149-158.

Zou, J., Y. Chen, et al. (2015). "Effect of hard segments on the thermal and mechanical properties of water blown semi-rigid polyurethane foams." Journal of Polymer Research **22**(6): 1-10.

Chapter 5

Biocompatibility evaluation of electrospun mats from chitosan or gelatin based poly(urethane urea)

5. Biocompatibility evaluation of electrospun mats from chitosan or gelatin based poly(urethane urea)

5.1 Introduction

Stem cells from adult or embryonic origin as well as the induced pluripotent stem cells have the ability to proliferate indefinitely and to differentiate into different lineages, replacing the damaged or dead cells in adults (Watt and Driskell 2010). Therefore, stem cells arise as valuable cell sources for regenerative medicine. While embryonic stem cells are pluripotent cells differentiating into any of the three germ layers, the somatic stem cells are able to self-renewal and differentiate into all the cells of the originating organ. The progress on adult stem cells has been faster and less problematic than on embryonic stem cells due to the absence of ethical issues and lower risk of *in vivo* teratoma formation (Trounson and McDonald 2015).

Though the widespread study of the stem cells, their application in regenerative medicine is still limited. One of the problems that stem cell transplantation is facing is their low survival rate due to the inhospitable environment inside the lesions/injuries. Further, the differentiation of survivors' stem cells was uncontrolled in the hostile site. One reason for that is the absence of a physical substrate to support and control the stem cell behavior (Watt and Huck 2013; Zweckberger, Ahuja et al. 2016). In the body, the stem cells are located into specific microenvironments, called niches, which are responsible for the regulation of stem cell behavior (Scadden 2006). The niche has in their constitution the stem cells, supporting cells, soluble biomolecules and the extracellular matrix (ECM). The ECM is much more than the physical support of the stem cells, it provides cues to control the stem cell behavior, influencing their fate (Watt and Huck 2013). Therefore, supporting scaffolds that provide topographical and biological cues are required to increase the stem cell survival and to regulate their functions.

Scaffolds produced by the electrospinning technique are meshes of sub-micrometric fibers that resemble the ECM. Characteristics such as fiber diameter and alignment degree can be easily controlled to regulate the stem cell behavior (Christopherson, Song et al. 2009). Such structures support the adhesion, proliferation, growth and differentiation of cells due to the high surface to volume ratio of the fibers, providing higher contact points for cell attachment as well as allowing the exchange of nutrients and waste products essential for cell survival, see recent review (Jiang, Carbone et al. 2015).

Polyurethanes (PUs) are segmented polymers constituted by a polyol, an isocyanate and a chain extender (a low molecular weight diol or diamine). They are widely used in several applications in the medical field due to their high stability and suitability for long-term applications (Zdrahala and Zdrahala 1999). Much attention has been devoted to the PUs during the last years as polymers with tunable physico-chemical properties obtained by changing their constituents. Therefore, PUs can be synthetized to be biocompatible, biodegradable and with mechanical properties adjustable for different tissue engineering applications. In order to do that, natural polymers such as chitosan (Barikani, Honarkar et al. 2009) and gelatin (Lee, Kwon et al. 2014) or

aminoacids such as glycine, arginine and aspartic acid (Skarja and Woodhouse 2000; Chan-Chan, Tkaczyk et al. 2013) have been incorporated in the PU structure as chain extenders.

PUs can be dissolved in organic solvents to be processed by the electrospinning, rendering fibrous substrates for stem cell support. However, PUs extended with natural polymers have not been processed with the electrospinning technique. Usually, the PUs were blended with natural polymers and electrospun to render fibrous mats with motifs for cell adhesion. Examples of these polymers are collagen (Jia, Prabhakaran et al. 2014), ethyl cellulose (Chen, Liao et al. 2015), gelatin (Vatankhah, Prabhakaran et al. 2014), and mixtures of collagen and chitosan (Huang, Chen et al. 2011) or collagen and elastin (Wong, Liu et al. 2013). Furthermore, the electrospun PU mats were usually coated with adhesion proteins such as poly-D-lysine (Puschmann, de Pablo et al. 2014) to promote neuronal cells adhesion and fibronectin, to provide a better environment for mesenchymal stem cells (MSCs) (Bashur, Shaffer et al. 2009; Cardwell, Dahlgren et al. 2012).

In this chapter was produced sub-micrometric fibrous scaffolds with random and aligned morphology, through the electrospinning technique, from PU extended with either chitosan (PU-CS) or gelatin (PU-Gel). Chitosan and gelatin are biocompatible and biodegradable natural polymers widely used in tissue engineering and their incorporation in the PU structure provide better cellular adhesion, as previously described. The resulting mats were characterized according to the morphology, mechanical properties and wettability. The biocompatibility of the polymeric fibers was evaluated using the 3T3 cell line (fibroblasts) and two types of stem cells: human MSCs and human neural stem cells (NSCs). The mats were not coated with adhesion proteins in order to monitor the influence of the physical and chemical properties of the mats to the cells.

5.2 Materials and methods

5.2.1 Materials

PU-CS and PU-Gel were synthetized as described in chapter 3 and 4, respectively. The PUs have in their constitution polycaprolactone-diol (PCL-diol, Mn=2000, Acros Organics) as soft segment, isophorone diisocyanate (IPDI, Huls) and chitosan (Mw=26kDa – depolimerization with $NaNO_2$, Cognis S) or gelatin (from cold water fish skin, Sigma-Aldrich) as chain extenders, resulting in PU-CS and PU-Gel, respectively. N,N-Dimethylformamide (DMF) and Tetrahydrophuran (THF) were purchased from Carlo Erba and used as received.

For 3T3 cultivation, Dulbecco's modified Eagle's medium (DMEM/F12; Gibco, Thermo Fisher Scientific; Waltham, MAA, USA), fetal bovine serum (InvivoGen; San Diego, CA, USA), trypsin/ethylenediaminetetraacetic acid (EDTA) solution (Life Technologies; Prague, Czech Republic), gentamicin (Sandoz - Novartis company) and resazurin (Sigma-Aldrich) were used.

For MSCs cultivation, alpha-minimum essential medium (MEM; EastPort; Prague, Czech Republic), platelet lysate (PL; IKEM; Prague, Czech Republic), trypsin/ethylenediaminetetraacetic acid (EDTA) solution (Life Technologies; Prague, Czech Republic), gentamicin (Sandoz - Novartis company) and resazurin (Sigma-Aldrich) were used.

For SPC-01 (a neural stem cell line derived from human fetal spinal cord tissue) cultivation the following reagents were used: Dulbecco's modified Eagle's medium (DMEM/F12; Gibco, Thermo Fisher Scientific; Waltham, MAA, USA), human serum albumin (Baxter Healthcare; Norfolk, UK), L-glutamine, human apo-transferrin, putrescine dichloride, human recombinant insulin, progesterone, sodium selenite, 4-hydroxytamoxifen (OHT), laminin (Sigma-Aldrich), human epidermal growth factor (EGF), human fibroblast growth factor (bFGF; PeproTech; London, UK), primocin (InvivoGen; San Diego, CA, USA), TrypZean (Lonza; Basel, Switzerland) and WST-1 [2-(2-methoxy-4-nitrophenyl)-3-(4-nitrophenyl)-5-(2,4-disulfophenyl)-2H-tetrazolium, monosodium salt] from Roche (Mannheim, Germany).

Chemiblocker, Triton X-100, goat serum, Alexa-Fluor 568 phalloidin, GAM Alexa-Fluor 594, 4, 6-diamidino-2-phenylindole dihydrochloride (DAPI), mouse antineurofilament 70 kDa (clone DA2) antibody (Merck Millipore; Prague, Czech Republic), mouse antihuman MAP2 antibody (Chemicon, Merck Millipore, Prague, Czech Republic) and Aqua Popy/Mount (Polysciences, Inc.; Prague, Czech Republic) were used for fluorescent staining.

5.2.2 Characterization of polyurethanes

5.2.2.1 Fourier Transform Infrared Spectroscopy

Fourier transform infrared spectroscopy (FTIR) was used to identify the structure of the PUs. IR spectra were recorded with a spectrometer FT-IR Nicolet 6700, from Thermo Electron Corporation, in ATR (attenuated total reflectance) mode with a resolution of 4 cm^{-1}.

5.2.3 Production of fibrous mats

PU-CS at 18% (w/w) and PU-Gel at 13% (w/w) were dissolved in DMF:THF 50:50 (w/w) under magnetic stir overnight. The prepared solutions were fed on a 5 mL plastic syringe connected to a 21G stainless steel blunt needle (internal diameter of 0.508 nm) using a syringe pump (SyringePump NE-300) programmed with a flow rate of 1.0 mL/h. A high voltage of 13 kV and 15 kV was applied to the needle, for the PU-CS and PU-Gel solutions, respectively, with a high voltage power supply (Power Supply – iseg T1CP300º340p), while an aluminum plate, at a distance of 20 cm from the needle tip, was kept grounded to collect the fibers. Aligned fibers were collected with the same conditions using the cylinder mandrel rotating at high speed (4000 rpm). Fibers were deposited in paper foil that was used to cover the collector. For cell culture, the mats were bonded in 12 mm glass coverslips with the spinning solutions and were sterilized by ultraviolet (UV) radiation during 20 min on each side. Afterwards, the coverslips were truly washed with autoclaved distilled water during 3 days. Samples were transferred to Teflon inserts, mounted into 24-well tissue culture plates and washed three times with PBS.

5.2.4 Characterization of fibrous mats

5.2.4.1 Morphology of electrospun nanofibers

The morphology of electrospun fibers was evaluated using the Zeiss Auriga Crossbeam electron microscope operating at high vacuum. Before observation, the samples were sputter coated with a mixture of gold/palladium (60/40). The diameter of the fibers was analyzed using

the ImageJ software (National Institutes of Health, Bethesda, MD, USA), analyzing at least 100 fibers. The result is expressed as the average ± experimental deviation. The fiber alignment of the produced fibrous mats was characterized by the Fast Fourier Transform (FFT), as previously described by (Ayres, Bowlin et al. 2006). Briefly, the FFT function converts the information in the image of the "real" space into the "frequency" space, resulting in an output image with grayscale pixels. The pattern presented by the pixels reflect the degree of alignment of the original image. To get the FFT frequency distribution, the radial summation of the pixel intensities for each degree between 0º and 360º is performed in a circular projection on the originated FFT image. The FFT analysis was performed using SEM images converted to 8-bit grayscale TIF format and cropped to 1024 × 1024 pixels. Afterwards, images were processed with the oval profile plug-in (authored by William O'Connnell) in the ImageJ software. The angular distribution of the fibers was also determined by direct measurement in the ImageJ software.

5.2.4.2 Mechanical properties

Random and aligned PU-CS and PU-Gel fiber mats were subjected to uniaxial tensile tests using a tensile test machine from Reometric Scientific (Minimat Firmware version 3.1) with a 20 N load cell. The samples with an initial gauge length of 10 mm and 10 mm width were stretched at a crosshead speed of 2 mm/min at ambient conditions. Aligned mats were pulled in the fiber direction. At least 10 samples from three different electrospun depositions were used. For wet testing, the mats were immersed in distilled water during 48 h and then, before start the tensile test, with the sample on the grips, drops of water were added to the samples. The Young modulus was determined from the slope of the linear region of the stress-strain curve.

5.2.4.3 Water contact angle

The wettability of the mats was assessed by static WCA measurements at room temperature and 98% humidity, using the OCA15 contact angle measuring instrument (DataPhysics Instruments GmbH, Filderstadt, Germany). Water drops with 5 µL were generated with an electronic micrometric syringe and carefully deposited on the samples surface. The contact angle value was acquired at the moment of the drop deposition and during the next 5 min (the shape of the drops was stable in that period). The collected information was analyzed using the SCA v.4.3.12 and v.4.3.16 software. The results are expressed as the average ± experimental standard deviation of at least five measurements recorded in different regions of the sample.

5.2.5 Cell culture experiments

5.2.5.1 3T3 fibroblasts

3T3 fibroblasts cell line were plated in a density of 1×10^4 cells, in DMEM supplemented with 10% FBS and 0.25 % gentamicin, on the fibrous mats assembled in Teflon inserts and incubated in a humidified atmosphere with 5% CO2 at 37 °C during 1 week. The proliferation of the 3T3 cells on the mats were determined using resazurin assay. At time points of 1, 3 and 7 days, culture medium was removed from the wells and replaced with fresh culture medium

supplemented with 10% (v/v) resazurin solution and incubated for 3 hours at 37 °C, 5% CO_2. The wells without cells were used as background control as well as the electrospun meshes without cells. Following incubation, the medium was read on the microplate reader Tecan Genios in fluorescence mode using excitation 535 nm and emission 590 nm. The results are expressed as the mean ± standard deviation of the experiments in triplicate. The wells were refilled with fresh culture medium and placed in incubator to continue the proliferation assay.

5.2.5.2 Human umbilical cord – mesenchymal stem cells

Mesenchymal stem cells (MSCs) were isolated from human umbilical cord tissue as previously described (Macková, Plichta et al. 2016). Extracted cells were plated on culture flasks containing α- MEM with 5 % thrombocyte lysate and 0.25 % gentamicin. Cells were cultivated in a humidified atmosphere with 5% CO2 at 37 °C and the medium was changed twice a week. After reaching the near-confluency, cells were harvested by a trypsin/EDTA solution. Cells in the fourth passage were used for the experiments with the fibrous mats.

5.2.5.3 MSCs culture on fibrous mats

To evaluate the cell density and area, a suspension of 1×10^4 MSCs in MEM with and without PL were transferred to each well with the fibrous mats in the Teflon inserts and incubated at 37 °C in a humidified 5% CO_2 atmosphere during 4 h. Afterwards, the cells were fixed with 4% paraformaldehyde in PBS for 15 min and stained with phalloidin and DAPI. The cell density was determined by counting the nuclei of at least 5 randomly chosen fields scanned using the ZEISS AXIO Observer D1 microscope with 20× objective and analyzed with the ImageJ software. The cell area was accessed by scanning 5 non-covered regions with at least 30 cells using the fluorescent microscope ZEISS AXIO Observer D1 microscope with 20× objective. The growth area of each individual cell was determined with the ImageJ software.

The proliferation of MSCs on electrospun PU nanofibrous meshes and on control (glass coverslip coated with 0.1% gelatin) were determined using the resazurin assay. Here, a suspension of 5×10^3 MSCs in MEM were added per well. At time points of 1, 3, 7 and 10 days, culture medium was removed from the wells and replaced with fresh culture medium supplemented with 10% (v/v) resazurin solution and incubated for 3 hours at 37 °C, 5% CO_2. The wells without cells were used as background control as well as the electrospun meshes without cells. Following incubation, the medium was read on the microplate reader Tecan Genios in fluorescence mode using excitation 535 nm and emission 590 nm. The results are expressed as the mean ± standard deviation of the experiments in triplicate. The wells were refilled with fresh culture medium and placed in incubator to continue the proliferation assay.

5.2.5.4 Human fetal neural stem cells

The human fetal neural stem cell line SPC-01_GFP-3 was generated from 8-week-old human fetal spinal cord (Pollock, Stroemer et al. 2006). It is a conditionally immortalized cell line through retroviral vectors containing the gene c-Myc fused to a mutated form of the estrogen

receptor, activated by the presence of 4-hydroxy tamoxifen (4-OHT). The 4-OHT regulated the telomerase activity, allowing the indefinitely stable cell expansion. Without 4-OHT, the cells differentiate.

Cells were cultured on laminin-coated tissue culture flasks in DMEM-F12 supplemented with 0.03% human serum albumin, 100 µg/mL human apo-transferrin, 5 µg/mL human recombinant insulin, 16.2 µg/mL putrescine dihydrochloride, 60 ng/mL progesterone, 2×10^{-3} M L-glutamine, 40 ng/mL sodium selenite, 20 ng/mL human EGF, 10ng/mL human bFGF, 100×10^{-9} M OHT, and 100 µg/mL primocin, which was changed thrice a week. When the cells reach confluence, they are passage using 0.25% TrypZean for 2 min at 37 °C followed by 0.25 mg/ml soybean trypsin inhibitor.

5.2.5.5 NSCs culture on fibrous mats

A suspension of 1.5×10^4 cells was seeded on each Teflon insert with the fibrous mats in the complete medium and the culture was monitored during 21 days. Glass coverslips coated with laminin were also mounted into the Teflon inserts and used as control. The immunofluorescent staining for the neurofilaments protein NF70 and MAP2 was performed to evaluate the differentiation of cells after 14 and 21 days in culture and phalloidin was used to stain cells after 7 and 14 days to analyze the cell growth.

Proliferation of the cells on the mats was evaluated using the WST-1 chromometry assay. After 1, 7 and 14 days the culture medium was removed and replaced with fresh culture medium with 10% WST reagent and incubated at 37 °C for 3 hours to convert the tetrazolium salts into formazan. Afterwards, 100 µL of processed medium was transferred from each well to a 96-well plate and the absorbance was read at 450 nm in the Sunrise Tecan microplate reader.

5.2.5.6 Fluorescent staining

The fluorescent staining of the cytoskeleton and the nucleus of cells growing in different fibrous substrates was performed with phalloidin and DAPI, respectively. Cells on culture were fixed with 4% w/v paraformaldehyde for 15 min at room temperature followed by washing 3× with PBS (pH 7.4). Cells were permeabilized with 0.5% v/v Triton X-100 and washed with PBS. Afterwards, cells were stained with phalloidin (1:400) in 0.1% v/v Triton X-100 during 2 h at 4 ºC. Then, cells were stained with DAPI (1:1000) for 3 min at room temperature followed by triple washing with PBS. The samples were mounted in glass coverslips with Aqua Poly/Mount and visualized and analyzed on inverted fluorescence microscope (Zeiss – Axio Oberver D1) with 20× objective.

The immunoflueroscent staining of NSCs for MAP2 and NF70 was performed to evaluate the growth and morphology of the cells as well as neuronal differentiation. In order to do that, the cells on the substrates were washed with PBS and fixed with 4 % paraformaldehyde in PBS, washed three times with PBS and treated with goat serum (10 %). Thereafter, the coverslips were incubated with primary antibody anti-MAP2 (1:1000), anti-NF70 (1:200) diluted in PBS containing 10% goat serum and 0.1% Triton X-100, followed by incubation in secondary goat-antimouse

IgG-Alexa Fluor 594 (1:300). The nuclei was stained with DAPI (1:1000). The samples were scanned using a LSM 510 DUO laser scanning confocal microscope (Zeiss).

5.2.5.7 **Statistical analysis**

The one-way ANOVA test followed by the post hoc HSD test were performed on SigmaStat software to determine the statically significant differences ($p < 0.05$). The results are presented as mean ± standard deviation.

5.3 Results and discussion

5.3.1 PU-CS and PU-Gel characterization

PU-CS and PU-Gel were synthetized as previously described in chapter 3 and 4, respectively. FTIR spectra of the synthetized PU-CS and PU-Gel are shown in Figure 5.1. Two spectral regions are related to the PU formation: the wavenumber range 1800 – 1600 cm^{-1}, which is assigned to the stretching vibration of carbonyls present in ester, acetyl, urethane and urea group; and the wavenumber range 3300 – 3400 cm^{-1}, which is assigned to the stretching vibration of amines present in urethane and urea group.

FTIR spectra also show other characteristic absorption bands at 2947 and 2865 cm^{-1} (C-H symmetric and asymmetric stretching vibrations of CH_2 groups, respectively), 1544 cm^{-1} (amide II, N-H bending and C-N stretching), 1460 cm^{-1} (CH_2 bending vibration), 1360 cm^{-1} (C-H bending vibration), 1302 cm^{-1} (CH_2 wagging), 1238 – 1100 cm^{-1} (C-O-C stretching) and 1038 cm^{-1} (C-O stretching).

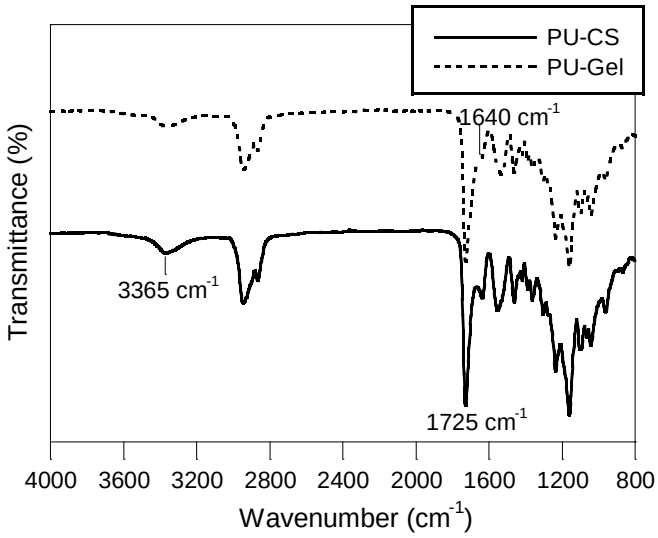

Figure 5.1 – FTIR spectra of PU synthetized with gelatin or chitosan as chain extenders.

5.3.2 Fibrous mats characterization

5.3.2.1 Fibrous mats morphology

PU-CS and PU-Gel fibrous mats with random and aligned morphology were produced using electrospinning. SEM images of the fibrous mats together with their respective fiber diameter distributions are presented in Figure 5.2. In all mats, the fibers have a regular shape without defects. For random mats, the average fiber diameter is (873 ± 313) nm for PU-CS and (705 ± 309) nm for PU-Gel, while for aligned fibers, the average fiber diameter is (961 ± 418) nm and (816 ± 416) nm for PU-CS and PU-Gel, respectively. Although without significance, the fiber's diameter was slightly inferior for random mats and for PU-Gel mats when compared to PU-CS mats.

The alignment degree of the fibers was analyzed using the fiber's angular distribution and the FFT analysis (Figure 5.2). Fiber's angular distribution were obtained from direct measurements of the angle of the fibers with the horizontal (0°) on the SEM images, using the imageJ software. On the aligned mats, which have the angular distribution centered at 90º, 97 % of PU-CS fibers are within the 60° - 120° range while 96 % of PU-Gel fibers are in the same range. Random PU-Gel and PU-CS mats have the fibers distributed equally in all directions. From the FFT intensity values (shape and weight of the peaks) is possible to infer the fibers alignment degree. Fewer intense peaks are indicative of ordered fibers on the mats while, multiple peaks with small intensities indicated fibers without order on the mats (Ayres, Bowlin et al. 2006). One intense peak is observed in aligned PU-CS and PU-Gel mats and multiple peaks with small intensities are detected in random PU-CS and PU-Gel mats. Although without significance, PU-CS mats have superior alignment degree when compared to PU-CS mats.

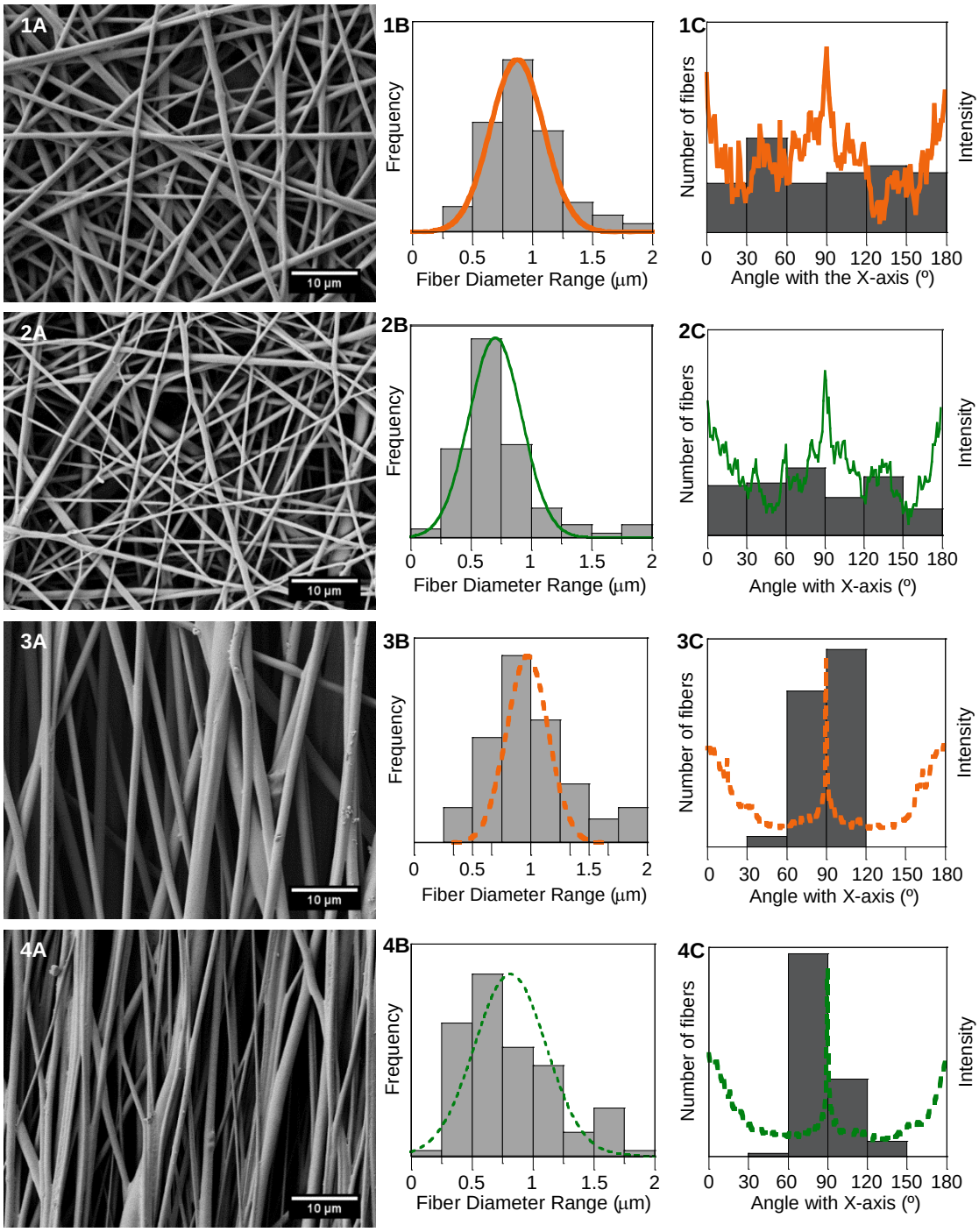

Figure 5.2 – SEM images of the PU-CS (1A, 3A) and PU-Gel (2A, 4A) fibrous mats with random (1A, 2A) and aligned (3A, 4A) morphology. (B) Histogram of the fiber diameter distribution on the mats. (C) Histogram with the angular distribution and the pixel intensity (from FFT analysis) with the acquisition angle for the produced mats.

5.3.2.2 Evaluation of stiffness and wettability

The mechanical properties of random and aligned PU mats were determined by tensile stress-strain tests under dry and wet conditions. Mats' mechanical properties in wet conditions are important to evaluate the applicability of the fibers *in vivo*. In Figure 5.3 is shown the typical stress-strain curves of PU-Gel and PU-CS mats with random (R_PU-CS and R_PU-Gel) and aligned (A_PU-CS and A_PU-Gel) morphology in dry and wet conditions. The behavior of the electrospun mats was described by Lee et al., who found that fibers first slippage over each other and oriented on the direction of the stretching. Then, the load is assured by the inter-fiber interactions and contact bonding points on the fibers. Finally, each individual fiber started to break up to no load can be handled (Lee, Lee et al. 2005).

In dry conditions, the Young modulus (Table 5.1) of PU-CS mats in random and aligned morphology was (3.2±0.3) MPa and (38±2) MPa, respectively, while random and aligned PU-Gel mats have Young modulus of (1.9±0.3) MPa and (17±2) MPa, respectively. Regardless of fiber morphology, PU-CS mats have superior Young modulus when compared to PU-Gel mats. In PUs that phase separate, the hard segment act as physical crosslink, responsible to the increase of PUs Young modulus, while the soft segment confers flexibility to PUs (Saralegi, Rueda et al. 2013). The presence of gelatin in the PU backbone, which has high molecular weight and multiple functional groups, induce chemical crosslink that disturb the phase separation and impair the organization of the PU structure, consequently deteriorating the Young's modulus.

The fiber substrates with aligned morphology had superior Young modulus compared to the randomly oriented fibers (Table 5.1). On the opposite, the elongation at break of the PU-CS and PU-Gel aligned mats, which is (107 ± 9) % and (419 ± 25) %, respectively, is inferior to the elongation at break of random mats (superior to 600 %). Aligned fibrous mats, which are already aligned in the stretching direction, elongate less than the randomly oriented mats, which have first to align in the stretching direction (Yao, Bastiaansen et al. 2014). Aligned PU-CS mats are the ones with higher Young modulus and inferior elongation at break, due to the superior mechanical performance of PU-CS polymer and superior alignment degree regarding aligned PU-Gel mats.

When wet, the mats exhibit different mechanical properties. Wet mats have superior elongation at break and inferior Young modulus when compared to dry mats (Table 5.1). Water penetrates in the fibrous structures and confer mobility to the fibers, which slide over each other under stress (Li, Thouas et al. 2014). The water also change the mobility of the PU chains, destroying the hydrogen bonds and, thus, lowering the Young's modulus (Carlisle, Coulais et al. 2009; Baker, Sigley et al. 2012). The mechanical properties of the PU-Gel mats were less affected in wet conditions due to the superior chemical crosslink in PU-Gel structure, which limit the penetration of water molecules.

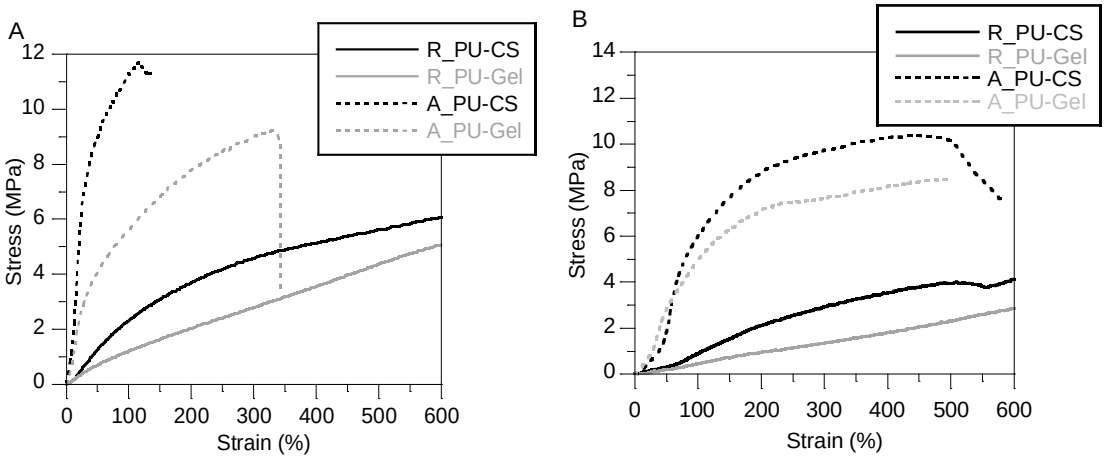

Figure 5.3 – Typical stress-strain curves of random and aligned PU-CS and PU-Gel fibrous mats under (A) dry and (B) wet conditions.

Table 5.1– Mechanical properties: Young's modulus (*E*), elongation at break (ε) and ultimate tensile stress (σ) of random and aligned PU-CS and PU-Gel fibrous mats evaluated in dry and wet conditions.

Fibrous mats	Dry			Wet		
	E (MPa)	ε (%)	σ (MPa)	*E* (MPa)	ε (%)	σ (MPa)
R_PU-CS	3.3 ± 0.3	>600	6.9 ± 0.3*	0.8 ± 0.2	>600	4.6 ± 1.2*
A_PU-CS	38 ± 2.0	107 ± 10	10.4 ± 0.8	5 ± 1	519 ± 59	10 ± 1.0
R_PU-Gel	1.9 ± 0.3	>600	5.3 ± 0.3*	0.8 ± 0.3	>600	5.7 ± 1.5*
A_PU-Gel	17 ± 2.5	419 ± 25	9.3 ± 0.6	6 ± 1	444 ± 42	9.0 ± 2.0

*Tensile stress at 600% elongation

The contact angle measurements and the representative images of the water drop on the fibrous mats are shown in Figure 5.4. The WCA of random and aligned PU-CS fibrous is (153 ± 4) º and (122 ± 2) º, respectively while WCA values of (145 ± 3) º and (143 ± 3) º are obtained for random and aligned PU-Gel, respectively. WCA values are superior to 90 °C, indicating that all substrates are hydrophobic. Although the presence of either CS or gelatin in the PUs structure, which are hydrophilic polymers, they are high hydrophobic structures due to the crosslink of either CS or gelatin in the PUs, which prevent the wetting and spreading of the liquid molecules on the mats (Mahanta, Mittal et al. 2015). However, according to random mats, the PU-Gel mats exhibit inferior WCA when compared to the PU-CS mats. The presence of gelatin, which is more hydrophilic than the CS, can contribute to that difference (Cheng, Chang et al. 2012).

The WCA is also affected by the fiber morphology (alignment degree, fiber diameter and porosity) (Moghadam, Hasanzadeh et al. 2013). The fibrous mats with aligned morphology have inferior WCA compared to the randomly oriented ones. The aligned fibers have different porosities and pore shapes that influence the water drop when it contact the substrate, increasing the contact surface for the water (Kim, Hwang et al. 2016). However, there is no significant difference in WCA measurements between random and aligned PU-Gel mats, indicating that probably other

factors such as surface chemistry, have superior influence in the WCA measurements than the fibers morphology.

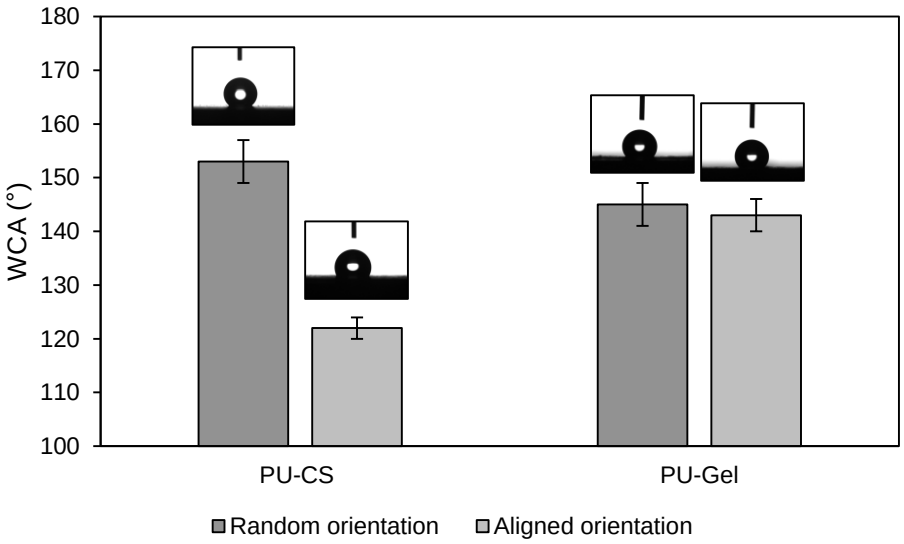

Figure 5.4 – Water contact angle values of the electrospun random and aligned PU-CS and PU-Gel mats and the representative picture of the water drop on the mats' surface.

5.3.3 Proliferation of 3T3 fibroblasts

To evaluate the biocompatibility of the PU-CS and PU-Gel fibrous mats, 3T3 fibroblasts were seeded on the mats with both random and aligned morphology and their proliferation was monitored using the Alamar Blue assay during 7 days in culture (Figure 5.5). At day 1 the absorbance values are about the same for all the mats and for the cell control. After 3 days, the cell density is significantly lower on the randomly oriented PU-CS mats and on the aligned PU-Gel mats when compared to the control. At the end of 7 days, only the cells in the aligned PU-Gel mats reached the same density as the control, while the cells on the other mats exhibited slightly lower values when compared with the results in control. At the end of the culture, the absorbance results of the mats were higher than 75 % of that of the control, indicating that the 3T3 cells adhere and proliferate well on both mats irrespective of the PU type and fibers morphology.

The morphology of the cells on the mats was evaluated after 5 days of culture with fluorescent images from cell cytoskeleton (phalloidin, red) and nuclei (DAPI, blue) (Figure 5.5). The cells are well spread over the surface of the fibrous mats, form stress fibers and make connections between them. On the aligned mats the cell cytoskeleton and nuclei elongated in the direction of the fiber orientation, which is notorious on the aligned PU-Gel mats.

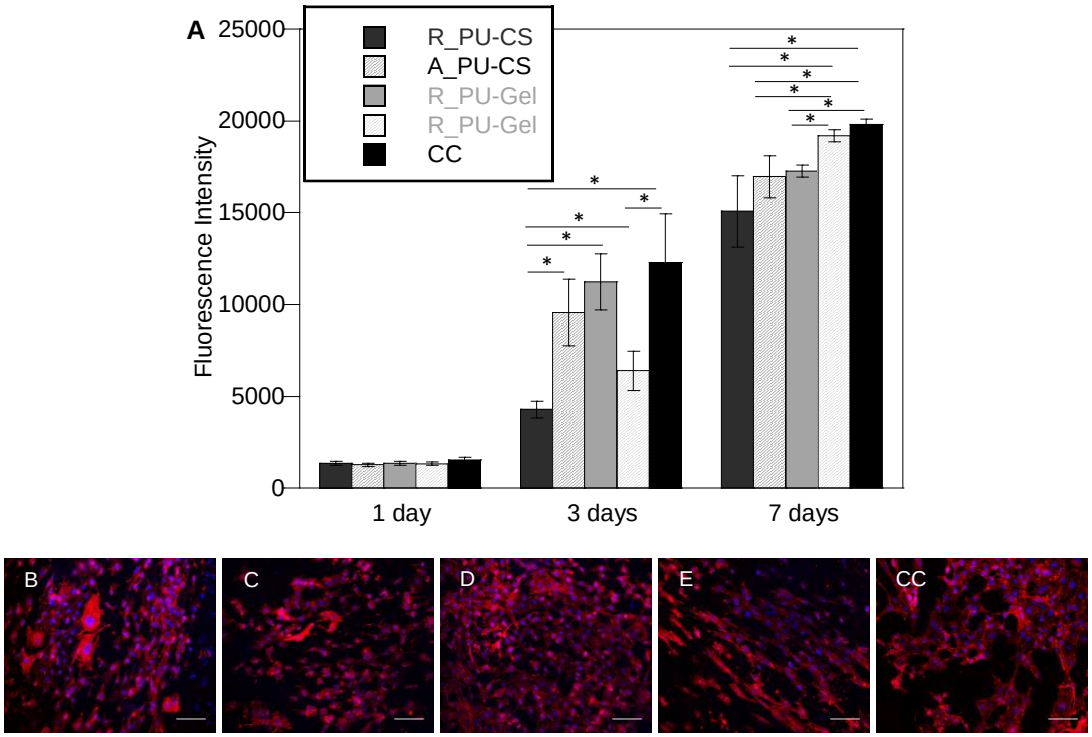

Figure 5.5 – Resazurin proliferation assay of 3T3 fibroblasts seeded on the electrospun PU-CS and PU-Gel random and aligned fibrous mats after 1, 3 and 7 days of culture (mean ± standard deviation, *n=3*). Significance *p<0.05. (A). Microscopic fluorescent images of 3T3 fibroblasts stained for phalloidin (red) and cell nuclei (DAPI, blue) seeded on electrospun fibrous mats from R_PU-CS (B), A_PU-CS (C), R_PU-Gel (D), A_PU-Gel (E) and glass coverslip (CC), during 5 days culture. Scale bar 100 µm.

5.3.4 MSCs adhesion and proliferation on fibrous mats

5.3.4.1 MSCs attachment

The cell growth area and cell density of the MSCs adhered on the PU-CS and PU-Gel fibrous mats with either random or aligned morphology were evaluated after 4 h of culture. The procedure was performed with and without platelet lysate (PL) in the culture medium. Platelet lysates have replaced the use of FBS in the culture of MSCs. The PL have several growth factors that enhance the proliferation of MSCs in culture and maintain their differentiation potential (Hemeda, Giebel et al. 2014). In the culture medium without PL, the real effect of the material chemical structure (PU extended with either CS or gelatin) as well as the morphology (random vs. aligned) on the MSCs was observed.

The number of adhered cells was inferior on the cultures without PL compared to the cultures with PL. The density of adhered cells was similar between all mats in the cultures with PL in culture medium (Figure 5.6A). However, without PL, the number of adhered cells was inferior on PU-Gel with aligned morphology. Therefore, not only the chemistry but also the morphology of the mats influence the MSCs adhesion.

The cell area was similar in all fibrous mats in the absence of PL (Figure 5.6B). However, in the presence of PL, the area of the cells adhered to the mats increase in the following order: A_PU-CS, R_PU-CS, A_PU-Gel and R_PU-Gel, indicating the different ability of the mats to absorb proteins/growth factors from the medium. The cells had superior area on mats with aligned

morphology and with CS in the structure. The presence of PL in the culture medium rendered cells with larger area in all the mats except in the R_PU-Gel mats, in which the cell area values were the same apart from the presence of PL.

According to cell morphology, in the presence of PL the cells were well spread but with few protrusions (Figure 5.6C-F), while without PL, the cells spread with a branched morphology verified by the higher number of actin filaments (Figure 5.6G-J). The cells in mats with aligned morphology followed the direction of the fiber alignment and stretched in the longitudinal direction, which increase the cell area. This results indicated the presence of some adhesion sites on the mats that are recognized by MSCs, allowing the cells to adhere and to spread.

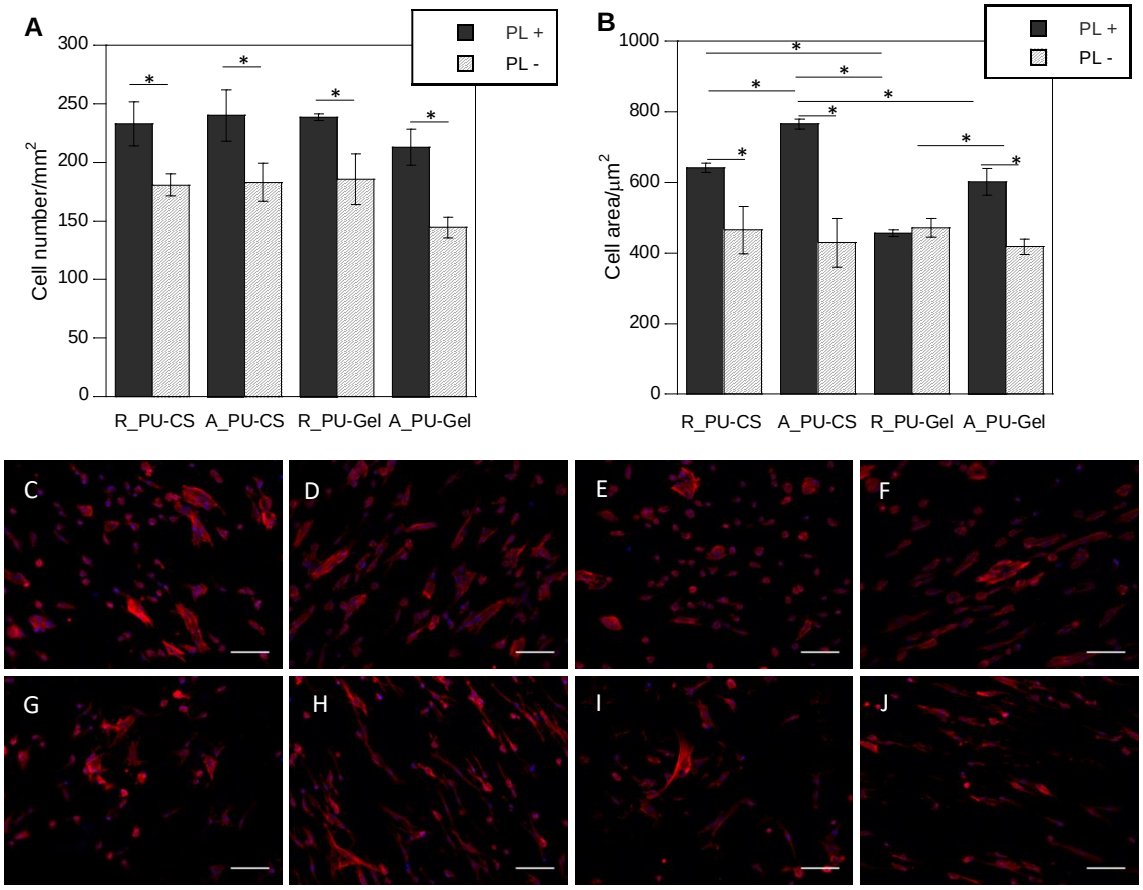

Figure 5.6 – The average values of MSCs number (A) and growth area (B) seeded on the electrospun fibrous mats during 4 h in the presence and the absence of PL in culture medium (mean ± standard deviation, *n=3*), **p*<0.05. Microscopic fluorescent images of MSCs seeded on electrospun fibrous mats from R_PU-CS (C, G), A_PU-CS (D, H), R_PU-Gel (E, I) and A_PU-Gel (F, J) during 4 h in the presence (C, D, E, F) and in the absence (G, H, I, J) of PL in the culture medium. Immunofluorescent staining with phalloidin (red) and for cell nuclei (DAPI, blue). Scale bar 100 µm.

5.3.4.2 MSCs Proliferation

The proliferation of MSCs on the nanofibrous materials was evaluated with the resazurin assay after 1, 3, 7 and 10 days (Figure 5.7K). After 1 day of culture, the cellular metabolic activity was similar for all the fibrous mats as well as for the cell control (glass coverslip coated with gelatin), independently of the morphology and type of PU. After 3 days, no proliferation was noticed for all the mats, demonstrated by the reduced metabolic activity on that day. Nevertheless, an increase in the cell number was verified after 7 and 10 days in culture detected by an increase in the measured fluorescent values, indicating that the cells proliferated only in later days. The delayed MSCs proliferation on electrospun mats compared to the glass coverslip controls can be due to the different 3D structure of the fibrous mats. The porous 3D structure reduced the stress fiber formation. Even more, the cells have to infiltrate and to find contact points, which occurred after some days. On the opposite, the planar stiffer glass coverslip induced higher cytoskeletal stress due to higher focal adhesion formations, improving the proliferation rate (Jiang, Cao et al. 2012; Chang, Fujita et al. 2013). The hydrophobicity of the substrates can also prevent the suitable proliferation of the cells due to the reduced ability of hydrophobic surfaces to attach and adsorb proteins from the culture medium.

The proliferation rates were different between the tested fibrous mats. The PU-Gel present enhanced proliferation rates towards MSCs compared to the PU-CS mats, although the values are inferior to the glass control coverslip. On the PU-Gel mats the presence of gelatin, with the RGD sequence suitable for cell attachment and proliferation, was a determinant factor to enhance the cellular proliferation. Furthermore, the lack or low proliferation rates of MSCs in the presence of substrates with CS is not surprising and was already reported in the literature. The CS is not cytotoxic but it is not a suitable substrate to support the proliferation of cells. According to (Lai, Shalumon et al. 2014), MSCs did not proliferate in the presence of CS fibrous substrates but they were prone to differentiate into the osteogenic lineage. Therefore, PU-CS mats can be used in specific applications to control and induce the differentiation of MSCs.

The proliferation rate of MSCs was superior on the fibrous mats with random morphology compared to the mats with aligned morphology. Some studies (Chang, Fujita et al. 2013; Zandén, Erkenstam et al. 2014) reported that the aligned fibers induced better MSCs proliferation rates mainly due to the similarity of this type of substrates with the flat controls, providing more contact points for cell adhesion and proliferation. However, the fiber diameter also influence the cell behavior. The aligned fibers with diameters around 1 µm, as the fibers studied here, can guide the cells individually over a single fiber, and cells did not cross over the fibers as in the randomly oriented fibers (Bashur, Shaffer et al. 2009). This characteristic associated with less interconnected pores and porosity of the aligned mats relatively to randomly oriented mats, reduced the cell adhesion sites and impaired the cell-cell contact, required for cell proliferation. Thereby, the cells can also be easily removed from the aligned substrates by forces exerted during the change of culture medium (Lü, Wang et al. 2012).

The morphology of the MSCs on the substrates was evaluated after 3 and 7 days of culture by staining the cells with DAPI and phalloidin for nucleus and F-actin filaments, respectively. In Figure 5.7 is shown a representative picture of the MSCs on each mat and glass

coverslip coated with gelatin (control) at 3 days (Figure 5.7A-E) and 7 days (Figure 5.7F-J). The cell number, inferred by the number of nuclei, was inferior in the mats with aligned morphology compared to the mats with random morphology. The reduced cell number was also noted in PU-CS mats compared to PU-Gel mats, corroborating the results of the resazurin proliferation assay. On fibrous mats, the MSCs arrange their cytoskeleton to follow the fibers morphology. This was mainly noticed in the aligned fibers, where the cytoskeleton follow the direction of the fiber alignment and the nucleus have an elongated morphology. On the opposite, the MSCs on the glass substrate are well spread over the surface, exhibiting more contact points for cell attachment, with stronger actin stress fibers formation.

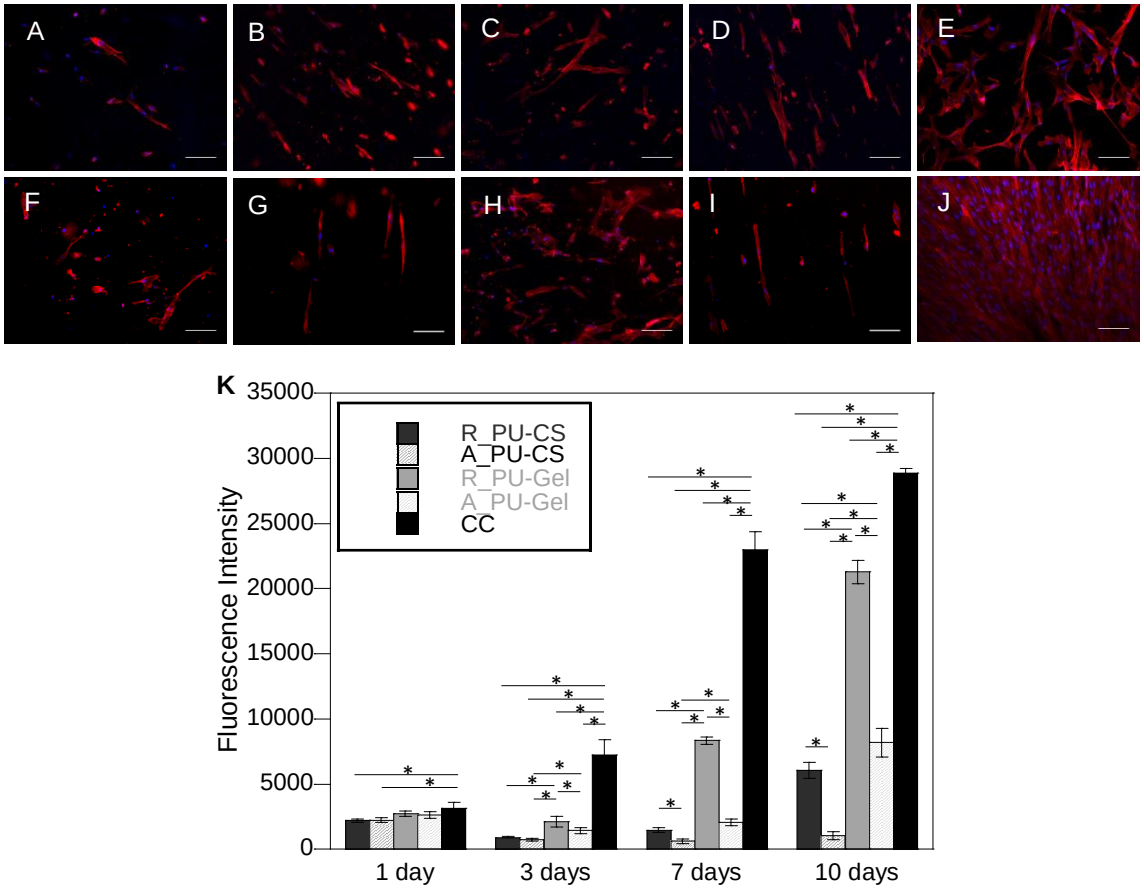

Figure 5.7 – Fluorescent images of immunofluorescent staining for cytoskeleton (phalloidin, red) and cell nuclei (DAPI, blue) of MSCs seeded on electrospun fibrous mats from R_PU-CS (A, E), A_PU-CS (B, F), R_PU-Gel (C, G) and A_PU-Gel (D, H) during 3 days (A, B, C, D) and 7 days (E, F, G, H). Scale bar: 100 µm. (K) Resazurin proliferation assay of MSCs seeded on the electrospun mats after 1, 3, 7 and 10 days of culture (mean ± standard deviation, *n=3*). Significance *p<0.05.

5.3.5 NSCs proliferation on the fibrous mats

The proliferation of NSCs on the mats with random and aligned morphology was evaluated using the WST assay as well as the cytoskeletal markers: phalloidin and two neuronal markers for neurofilaments - NF70 and microtubule associated protein - MAP2. The proliferation was determined by the cell metabolic activity measured with the WST assay after 1, 7 and 14 days of SPC-01 culture on the fibrous mats. The morphological characterization of cells was performed with phalloidin after 7 and 14 days of culture and with NF70 and MAP2 after 14 and 21 days of culture.

After 1 day of culture, the results from WST assay (Figure 5.8K) demonstrated that the density of SPC-01 were similar in PU-CS aligned mats and in the glass coverslips coated with laminin (control). However, in the other mats, the number of adhered cells was significantly inferior to the control. After one week, the NSCs did not proliferate on the mats, maintaining the same number of cells measured at day 1, except on the A_PU-CS mats where the cells proliferated at a small rate. At day 7, the cells on the control were confluent and died; therefore, the measurement of the absorbance values was not possible in this day and further. After 14 days, the cells proliferated on all mats, as verified by an increase in the measured metabolic activity. However, in A_PU-CS mats the NSCs proliferation rate was superior to the other mats. Both the aligned morphology and the presence of CS in detriment of gelatin contributed to that. The cells growing in such a substrate are stretched and elongated parallel to the fibers direction, increasing their proliferation rate. On the other hand, the cells growing in random morphology had a disperse morphology with processes extending in all directions, without a preferential direction, slowing the proliferation rate.

The control glass coverslip was coated with laminin, which is a protein from the ECM essential in the cell attachment, differentiation and survival of cells, including NSCs. Therefore, better adhesion and proliferation was observed in laminin coated substrates compared to the nanofibrous mats (without any coating). Studies from the literature made use of electrospun nanofibrous substrates coated with laminin to evaluate NSCs behavior on the substrates with different morphologies (Christopherson, Song et al. 2009; Lim, Liu et al. 2010; Mahairaki, Lim et al. 2010). Other methods such as, plasma treatment are used to modify the surface of the fibrous mats to add specific chemical groups and to control the adhesion of the adhesive molecules (Zandén, Erkenstam et al. 2014). However, the problem of coating the substrates with laminin is to ensure that all the samples are coated with the same laminin density. In addition, the effect of the chemical composition of the polymers cannot be evaluated because the cells will sense the laminin first. In the study of (Christopherson, Song et al. 2009) the fibrous mats were coated with laminin but the proliferation rate of NSCs was lower on the mats when compared to the tissue culture plate control. The fibrous morphology, different from the flat controls, contributed to slow down the neural cell proliferation.

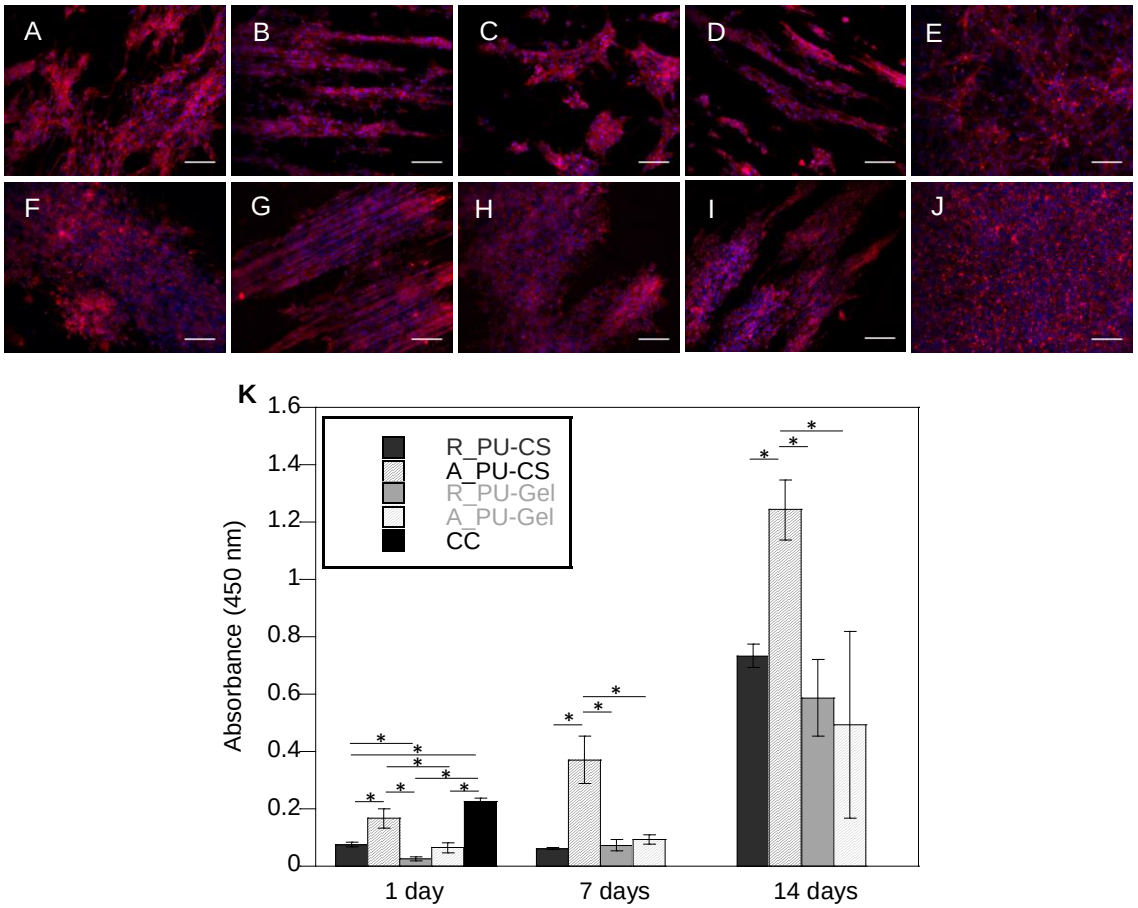

Figure 5.8 - Microscopic fluorescent images of NSCs seeded on electrospun nanofibrous mats from R_PU-CS (a, e), A_PU-CS (b, f), R_PU-Gel (c, g) and A_PU-Gel (d, h) for 7 days (a, b, c, d) and 14 days (e, f, g, h) in culture. Immunofluorescent staining for F-actin (phalloidin, red) and cell nuclei (DAPI, blue). Scale bar 100 µm. (K) WST proliferation assay on NSCs seeded on the electrospun mats after 1, 7 and 14 days of culture (mean ± standard deviation, *n*=3), **p*<0.05.

From the morphologic analysis with phalloidin and DAPI, after 7 days of culture (Figure 5.8A-E), we have observed that the cells grown on the fibrous mats in clusters and do not spread well over all the fibrous surface, in contrast to what was observed in the control where the cells are well spread over all the surface. Within the clusters, the cells are spread and their cytoskeleton is organized along the fibers. This phenomenon was better noticed on the aligned fibers, where the cell cytoskeleton is aligned along the fiber direction. Additionally, some projections are observed at the edge of the clusters with the trend to contact with nearest clusters. After 14 days of culture (Figure 5.8F-J), an increase in the number of cells was visualized by an increase in the number of nuclei, confirming the results from the WST assay. As there are a higher cell number, the cells are in bigger clusters and the projections were barely noticed. After 21 days, SEM images were acquired to evaluate the interaction of the cells with the mats (Figure 5.9). The cells on mats from PU-CS have a spread morphology when compared to the ones in the PU-Gel mats, in which the cells are clustered. Furthermore, the cell protrusions are following the fiber directions in PU-CS fibers with random and aligned morphology, providing contact guidance cues to the cells. On PU-Gel samples, strong interaction between the cells and the fibers were verified by the stretching

of the fibers under the cells. Some infiltration of the cells on the PU-Gel aligned mats were also noticed.

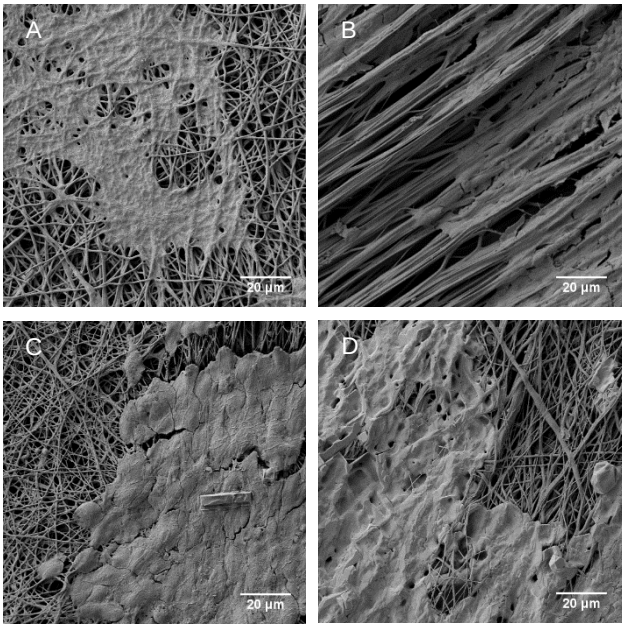

Figure 5.9 – Scanning electron microscopy images of NSCs seeded on electrospun nanofibrous mats from R_PU-CS (A), A_PU-CS (B), R_PU-Gel (C) and A_PU-Gel (D) after 21 days in culture.

NSCs were positive for NF70 and MAP2 after 2 (Figure 5.10) and 3 (Figure 5.11) weeks when seeded on the fibrous mats. However, after 2 weeks the MAP2 marker was poorly detected, indicating the early stage of neurite development at this point. Nevertheless, the NSCs were able to differentiate into the neuronal phenotype without any co-adjuvant. It was observed that the cells were able to elongate and form neurite processes, following the fiber orientation. In aligned mats, the neurites follow the alignment of the fibers, while in the randomly oriented fibers, the neurites follow the substrates in all directions, establishing connections with each other. As observed in cells stained with phalloidin, the cells seeded on the nanofibers mats are growing in individual clusters with more rounded morphology, contrary to cells growing on laminin coated TCP that are spread over all the surface.

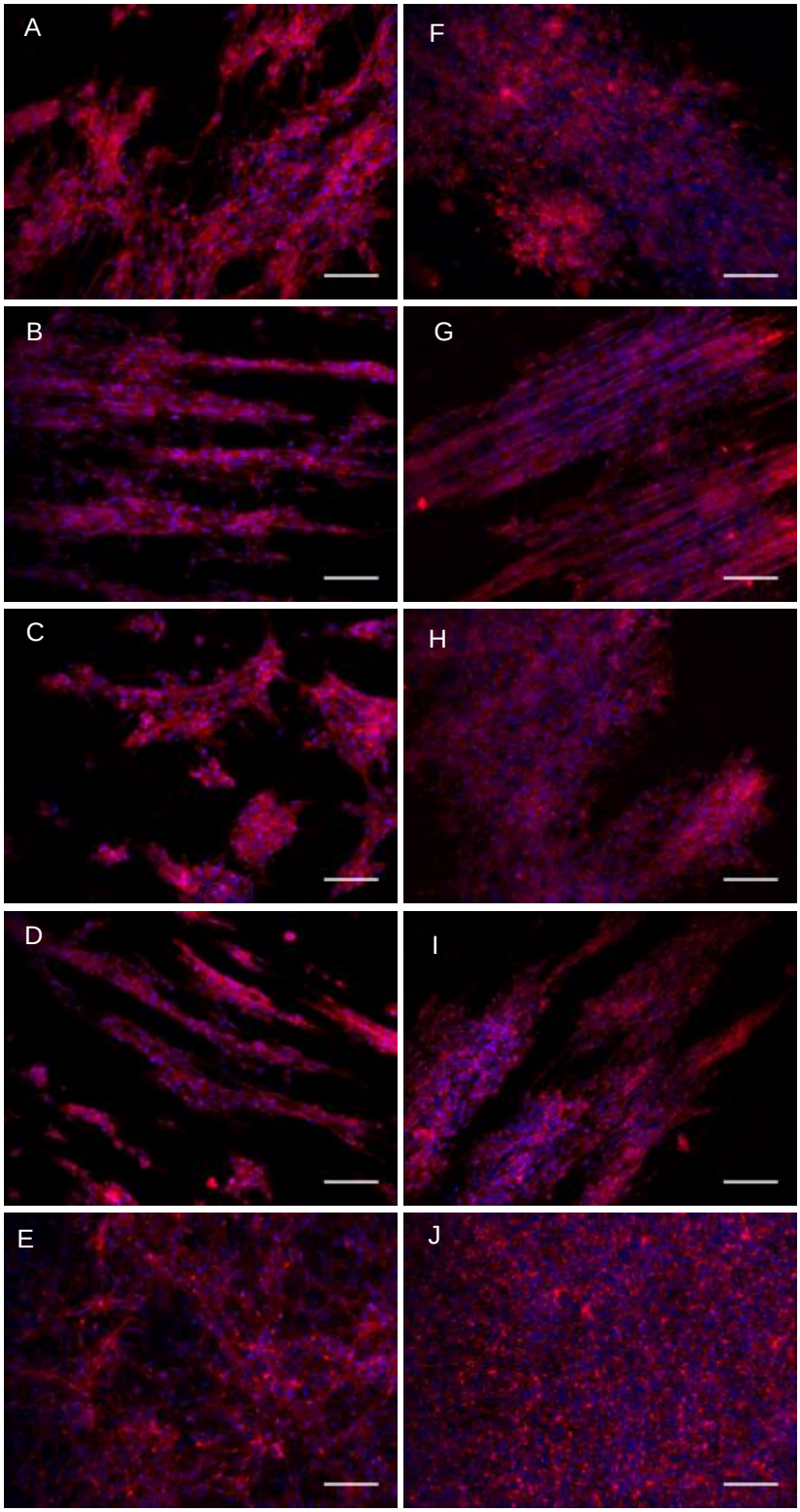

Figure 5.10 – Laser scanning confocal images of NF70 (red) and DAPI (blue) (A – E) and MAP2 (red) and DAPI (blue) (F – J) stained NSCs seeded on electrospun nanofibrous mats from R_PU-CS (A, F), A_PU-CS (B, G), R_PU-Gel (C, H), A_PU-Gel (D, I) and laminin-coated lass (E, J) after 2 weeks. Scale bar: 50 µm.

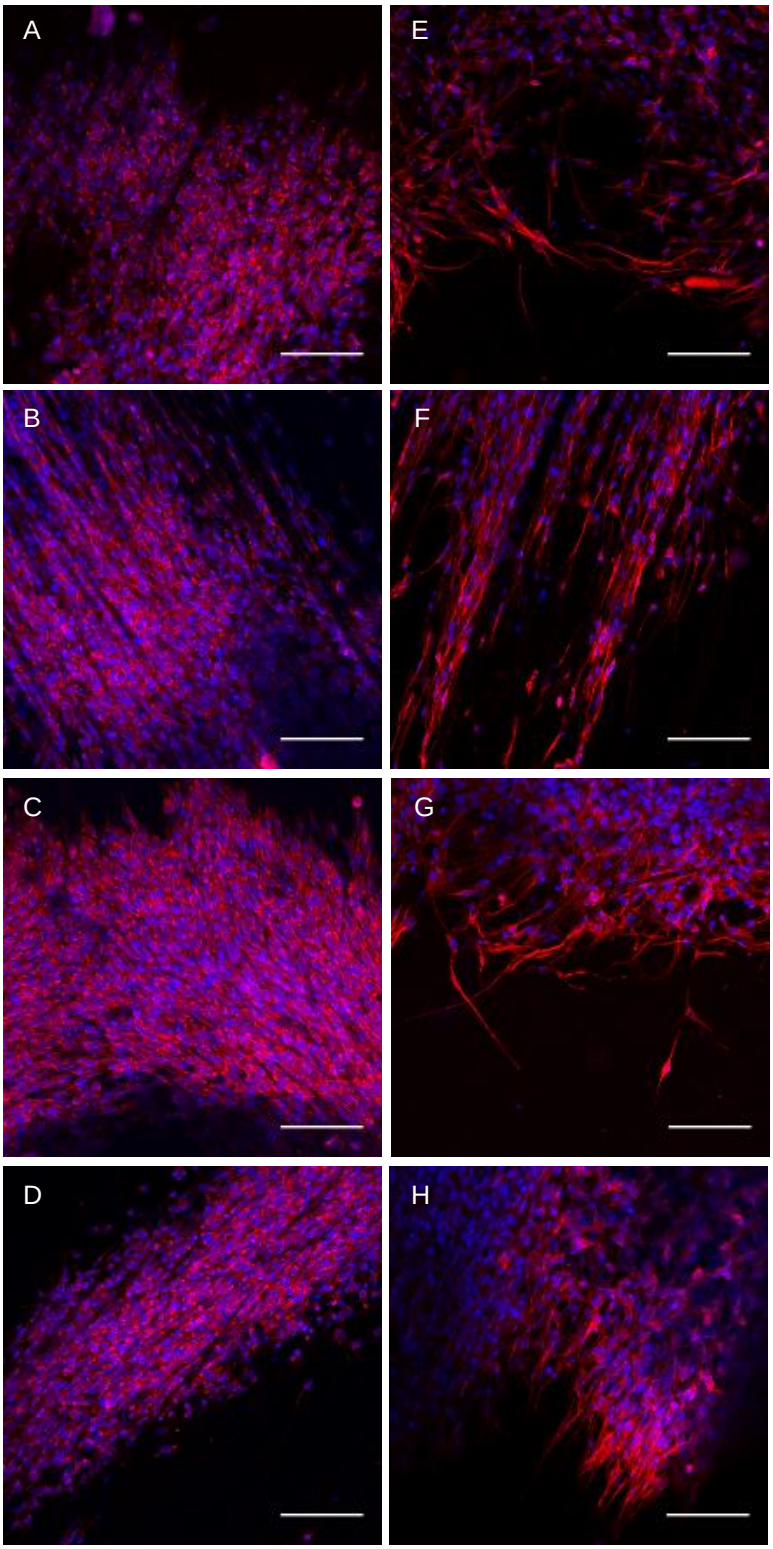

Figure 5.11 – Laser scanning confocal images of NF70 (red) and DAPI (blue) (A – D) and MAP2 (red) and DAPI (blue) (E – H) stained NSCs seeded on electrospun fibrous mats from R_PU-CS (A, E), A_PU-CS (B, F), R_PU-Gel (C, G) and A_PU-Gel (D, H) after 3 weeks. Scale bar: 50 µm.

Controlling the stem cell differentiation is an essential request for their application in regenerative medicine therapies. Usually, growth factors and biomolecules are added to the culture medium to control and induce the differentiation of stem cells into the required lineage.

However, the topography, stiffness and chemistry of the biomaterials have recently been studied as factors that affect cell differentiation.

The A_PU-CS mats supported higher NSCs proliferation and neural differentiation as well as provided guidance cues for cells. Mats of fibers with aligned morphology have been preferred substrates for NSCs since they induce neuronal differentiation as well as the alignment of the neurites (Lim, Liu et al. 2010; Mahairaki, Lim et al. 2010). The fiber diameter also influence the NSCs behavior (Christopherson, Song et al. 2009). In the study of Christopherson and co-workers, fibers with larger diameters reduced the NSCs survival and proliferation, but increased their neuronal differentiation. On the opposite, small diameter fibers support higher proliferation rates but induce the NSCs differentiation into astrocytes.

Differences in the mechanical characteristics of the substrates also influenced the cell fate. The PU-CS mats had superior Young modulus than the PU-Gel mats in both morphologies. Further, the mats with aligned morphology have superior Young modulus than the mats with random morphology. The NSCs proliferate and differentiate better in the mats with superior Young modulus, which is different from what was reported in literature. It was previously reported that soft materials with Young modulus similar to the one of the brain tissue were suitable materials for the proliferation and differentiation of NSCs (Banerjee, Arha et al. 2009). However, in that study, the cells were inside the hydrogel, in a complete different environment. Here, the cells are over the mats, which is an environment similar to the flat coverslips. Looking from this point of view, the mats with superior Young modulus were more similar to the rigid glass coverslips, contributing to the superior performance of these mats on cell proliferation.

According to the material chemistry, the PU-CS mats were suitable substrates for NSCs proliferation and differentiation regarding the PU-Gel mats. The CS has been widely used in scaffolds for neural regeneration and is a suitable substrate to support NSCs (Cheng, Huang et al. 2007; Zahir, Nomura et al. 2008; Yang, Duan et al. 2010; Du, Tan et al. 2014).

The mats influenced the MSCs and SPC-01 cultures in different ways. While in MSCs culture the PU-Gel but not the PU-CS support the cell proliferation, in SPC-01 cultures, the PU-CS mats were the ones that better support the cell proliferation and differentiation. It was also interested to notice the effect of the aligned topography on the different cultures. The alignment prevented the proliferation of the MSCs while, on the opposite, induce better proliferation of SPC-01.

5.4 Conclusion

The development of new scaffolds to support stem cells has been a research topic in tissue engineering. The design of the scaffold is an important step because their characteristics such as, functional groups, topography, hydrophobicity and mechanical properties influence the cell behavior. In this study was evaluated the behavior of human umbilical cord-MSCs and SPC-01 on fibrous mats with different chemistries and morphologies. PUs extended with either chitosan or gelatin were synthetized and processed by the electrospinning technique into fibrous mats with random and aligned morphology. All the mats were hydrophobic and the mats with aligned morphology have superior Young modulus and reduced elasticity regarding the mats with random

orientation. The substrates seeded with MSCs supported MSCs adhesion but only the PU-Gel mats with random morphology supported the MSCs proliferation. The cells barely proliferated on PU-CS mats as well as in mats with aligned orientation. Therefore, soft substrates with gelatin and with randomly oriented fibers were suitable for MSCs.

According to the NSCs, all the mats were able to support their adhesion. However, the PU-CS fibrous mats with aligned morphology were better in supporting the NSCs adhesion, proliferation and neural differentiation. On the opposite to MSCs, the NSCs preferred stiffer substrates with chitosan and aligned fibers.

The results indicated that each cell type behave differently in the presence of each substrate. Therefore, there is a need to customize the scaffold characteristics (physico-chemical, mechanical and topographic) for each cell type and consequently, for each tissue engineering application.

5.5 References

Ayres, C., G. L. Bowlin, et al. (2006). "Modulation of anisotropy in electrospun tissue-engineering scaffolds: analysis of fiber alignment by the fast Fourier transform." Biomaterials **27**(32): 5524-5534.

Baker, S., J. Sigley, et al. (2012). "The mechanical properties of dry, electrospun fibrinogen fibers." Materials Science and Engineering: C **32**(2): 215-221.

Banerjee, A., M. Arha, et al. (2009). "The influence of hydrogel modulus on the proliferation and differentiation of encapsulated neural stem cells." Biomaterials **30**(27): 4695-4699.

Barikani, M., H. Honarkar, et al. (2009). "Synthesis and characterization of polyurethane elastomers based on chitosan and poly (ε-caprolactone)." Journal of Applied Polymer Science **112**(5): 3157-3165.

Bashur, C. A., R. D. Shaffer, et al. (2009). "Effect of fiber diameter and alignment of electrospun polyurethane meshes on mesenchymal progenitor cells." Tissue Engineering Part A **15**(9): 2435-2445.

Cardwell, R. D., L. A. Dahlgren, et al. (2012). "Electrospun fibre diameter, not alignment, affects mesenchymal stem cell differentiation into the tendon/ligament lineage." Journal of tissue engineering and regenerative medicine **8**(12): 937–945.

Carlisle, C. R., C. Coulais, et al. (2009). "The mechanical properties of individual, electrospun fibrinogen fibers." Biomaterials **30**(6): 1205-1213.

Chan-Chan, L., C. Tkaczyk, et al. (2013). "Characterization and biocompatibility studies of new degradable poly (urea) urethanes prepared with arginine, glycine or aspartic acid as chain extenders." Journal of Materials Science: Materials in Medicine **24**(7): 1733-1744.

Chang, J.-C., S. Fujita, et al. (2013). "Cell orientation and regulation of cell–cell communication in human mesenchymal stem cells on different patterns of electrospun fibers." Biomedical Materials **8**(5): 055002.

Chen, P.-H., H.-C. Liao, et al. (2015). "A novel polyurethane/cellulose fibrous scaffold for cardiac tissue engineering." RSC Advances **5**(9): 6932-6939.

Cheng, H., Y.-C. Huang, et al. (2007). "Laminin-incorporated nerve conduits made by plasma treatment for repairing spinal cord injury." Biochemical and biophysical research communications **357**(4): 938-944.

Cheng, N. C., H. H. Chang, et al. (2012). "Efficient transfer of human adipose-derived stem cells by chitosan/gelatin blend films." Journal of Biomedical Materials Research Part B: Applied Biomaterials **100**(5): 1369-1377.

Christopherson, G. T., H. Song, et al. (2009). "The influence of fiber diameter of electrospun substrates on neural stem cell differentiation and proliferation." Biomaterials **30**(4): 556-564.

Du, J., E. Tan, et al. (2014). "Comparative evaluation of chitosan, cellulose acetate, and polyethersulfone nanofiber scaffolds for neural differentiation." Carbohydrate polymers **99**: 483-490.

Hemeda, H., B. Giebel, et al. (2014). "Evaluation of human platelet lysate versus fetal bovine serum for culture of mesenchymal stromal cells." Cytotherapy **16**(2): 170-180.

Huang, C., R. Chen, et al. (2011). "Electrospun collagen–chitosan–TPU nanofibrous scaffolds for tissue engineered tubular grafts." Colloids and Surfaces B: Biointerfaces **82**(2): 307-315.

Jia, L., M. P. Prabhakaran, et al. (2014). "Guiding the orientation of smooth muscle cells on random and aligned polyurethane/collagen nanofibers." Journal of biomaterials applications **29**(3): 364-377

Jiang, T., E. J. Carbone, et al. (2015). "Electrospinning of polymer nanofibers for tissue regeneration." Progress in Polymer Science **46**: 1-24.

Jiang, X., H. Q. Cao, et al. (2012). "Nanofiber topography and sustained biochemical signaling enhance human mesenchymal stem cell neural commitment." Acta biomaterialia **8**(3): 1290-1302.

Kim, J. I., T. I. Hwang, et al. (2016). "A Controlled Design of Aligned and Random Nanofibers for 3D Bi-functionalized Nerve Conduits Fabricated via a Novel Electrospinning Set-up." Scientific reports **6**: 23761.

Lai, G.-J., K. Shalumon, et al. (2014). "Composite chitosan/silk fibroin nanofibers for modulation of osteogenic differentiation and proliferation of human mesenchymal stem cells." Carbohydrate polymers **111**: 288-297.

Lee, K., B. Lee, et al. (2005). "Stress-strain behavior of the electrospun thermoplastic polyurethane elastomer fiber mats." Macromolecular Research **13**(5): 441-445.

Lee, T., S. Kwon, et al. (2014). "Biodegradable sol–gel coatings of waterborne polyurethane/gelatin chemical hybrids." Progress in Organic Coatings **77**(6): 1111-1116.

Li, Y., G. A. Thouas, et al. (2014). "Novel elastomeric fibrous networks produced from poly (xylitol sebacate) 2: 5 by core/shell electrospinning: Fabrication and mechanical properties." Journal of the Mechanical Behavior of Biomedical Materials **40**: 210-221.

Lim, S. H., X. Y. Liu, et al. (2010). "The effect of nanofiber-guided cell alignment on the preferential differentiation of neural stem cells." Biomaterials **31**(34): 9031-9039.

Lü, L.-X., Y.-Y. Wang, et al. (2012). "The effects of PHBV electrospun fibers with different diameters and orientations on growth behavior of bone-marrow-derived mesenchymal stem cells." Biomedical Materials **7**(1): 015002.

Macková, H., Z. Plichta, et al. (2016). "RGDS-and SIKVAVS-Modified Superporous Poly (2-hydroxyethyl methacrylate) Scaffolds for Tissue Engineering Applications." Macromolecular bioscience **16**(11): 1621-1631.

Mahairaki, V., S. H. Lim, et al. (2010). "Nanofiber matrices promote the neuronal differentiation of human embryonic stem cell-derived neural precursors in vitro." Tissue Engineering Part A **17**(5-6): 855-863.

Mahanta, A. K., V. Mittal, et al. (2015). "Polyurethane-grafted chitosan as new biomaterials for controlled drug delivery." Macromolecules **48**(8): 2654-2666.

Moghadam, B. H., M. Hasanzadeh, et al. (2013). "On the contact angle of electrospun polyacrylonitrile nanofiber mat." Bulgarian Chemical Communications **45**(2): 169-177.

Pollock, K., P. Stroemer, et al. (2006). "A conditionally immortal clonal stem cell line from human cortical neuroepithelium for the treatment of ischemic stroke." Experimental neurology **199**(1): 143-155.

Puschmann, T. B., Y. de Pablo, et al. (2014). "A Novel Method for Three-Dimensional Culture of Central Nervous System Neurons." Tissue Engineering Part C: Methods **20**(6): 485-492.

Saralegi, A., L. Rueda, et al. (2013). "Thermoplastic polyurethanes from renewable resources: effect of soft segment chemical structure and molecular weight on morphology and final properties." Polymer International **62**(1): 106-115.

Scadden, D. T. (2006). "The stem-cell niche as an entity of action." Nature **441**(7097): 1075-1079.

Skarja, G. and K. Woodhouse (2000). "Structure-property relationships of degradable polyurethane elastomers containing an amino acid-based chain extender." Journal of Applied Polymer Science **75**(12): 1522-1534.

Trounson, A. and C. McDonald (2015). "Stem cell therapies in clinical trials: progress and challenges." Cell Stem Cell **17**(1): 11-22.

Vatankhah, E., M. P. Prabhakaran, et al. (2014). "Phenotypic modulation of smooth muscle cells by chemical and mechanical cues of electrospun Tecophilic/gelatin nanofibers." ACS applied materials & interfaces **6**(6): 4089-4101.

Watt, F. M. and R. R. Driskell (2010). "The therapeutic potential of stem cells." Philosophical Transactions of the Royal Society of London B: Biological Sciences **365**(1537): 155-163.

Watt, F. M. and W. T. Huck (2013). "Role of the extracellular matrix in regulating stem cell fate." Nature reviews Molecular cell biology **14**(8): 467-473.

Wong, C. S., X. Liu, et al. (2013). "Elastin and collagen enhances electrospun aligned polyurethane as scaffolds for vascular graft." Journal of Materials Science: Materials in Medicine **24**(8): 1865-1874.

Yang, Z., H. Duan, et al. (2010). "The effect of the dosage of NT-3/chitosan carriers on the proliferation and differentiation of neural stem cells." Biomaterials **31**(18): 4846-4854.

Yao, J., C. W. Bastiaansen, et al. (2014). "High strength and high modulus electrospun nanofibers." Fibers **2**(2): 158-186.

Zahir, T., H. Nomura, et al. (2008). "Bioengineering neural stem/progenitor cell-coated tubes for spinal cord injury repair." Cell transplantation **17**(3): 245-254.

Zandén, C., N. H. Erkenstam, et al. (2014). "Stem cell responses to plasma surface modified electrospun polyurethane scaffolds." Nanomedicine: Nanotechnology, Biology and Medicine **10**(5): 949-958.

Zdrahala, R. J. and I. J. Zdrahala (1999). "Biomedical applications of polyurethanes: a review of past promises, present realities, and a vibrant future." Journal of biomaterials applications **14**(1): 67-90.

Zweckberger, K., C. S. Ahuja, et al. (2016). "Self-assembling peptides optimize the post-traumatic milieu and synergistically enhance the effects of neural stem cell therapy after cervical spinal cord injury." Acta Biomaterialia **42**: 77-89.

Chapter 6

Conclusions and Future Work

6. Conclusions and Future Work

6.1 Conclusions

The main objective of this thesis was the development of electrospun mats from biocompatible and biodegradable PUs to support the adhesion and proliferation of Neural Stem Progenitor Cells as well as to induce their neuronal differentiation.

Spinal cord injury is a common disability that occur mainly in young people, resulting in partial or total paralysis and loss of sensation depending on the injury extent. There are no actual treatments for this problem. Therefore, one of the current challenges is the development of a combined therapy using biomaterials, stem cells and biomolecules to fully regenerate the spinal cord. The use of scaffolds that can support the stem cells and modulate their behavior through topographical cues at micro/nanoscale, stiffness and chemical surface has recently received much attention. However, to build the scaffold that get together all the characteristics to accurately control stem cells behavior is still a challenge.

Polyurethanes (PUs) can be easily modulated to have the physical, chemical and mechanical properties that better fit in each specific tissue engineering application. Electrospun mats have been widely used as substrates for cell adhesion, proliferation and differentiation due to their structure similar to the ECM, providing guidance cues to the cells at the submicrometer level. In chapter 3, the synthesis of PUs with chitosan (CS) and their processing in fibrous scaffolds using electrospinning technique is described. PUs extended with dimethylol propionic acid (DMPA) – PU-DMPA, DMPA and chitosan CS – PU-DMPA/CS and CS – PU-CS were synthetized and characterized. Better phase segregation was observed in PU-DMPA/CS followed by PU-CS and by PU-DMPA. The presence of DMPA in PU-DMPA/CS helped to disperse the CS in the PU structure. Without DMPA, CS was crosslinked in PU structure leading to the formation of disordered hydrogen bonds, impairing the phase segregation. The presence of CS in the PU backbone (with or without DMPA) improved the thermal stability and mechanical performance of the PUs when compared to PU without CS.

The three synthetized PUs were electrospun, rendering porous fibrous mats without defects. Films were also prepared by solvent casting. The mats and films had a non-linear stress-strain behavior similar to soft tissues. The Young modulus of the mats and films was superior for PU-CS, when compared to other PUs. The reinforcement effect of the CS crosslinking points and the presence of strong hydrogen-bonds contributed to that. On the opposite, the PU-DMPA mats and films were the ones with inferior Young modulus. In general, the mats have inferior Young modulus relatively to films. Despite of that, the Young modulus of PU-DMPA/CS and PU-CS mats was 3.3 ± 0.3 MPa and 1.5 ± 0.3 MPa, respectively and the elasticity was superior to 600 %. Despite of the difficulty to study the mechanical properties of spinal cord (variability of the regions, age and type of species and variations in mechanical configurations and parameters), some works demonstrated that the spinal cord has a non-linear mechanical behavior similar to filled

elastomers and soft tissues and that their Young modulus ranged from hundreds to thousands Pa (Cheng, Clarke et al. 2008). Despite of these values are lower than the ones reported for PU-CS mats, they are in the range of the values reported for spinal cord dura mater (1.2 ± 0.3 MPa), which have collagen fibers in their constitution (Maikos, Elias et al. 2008).

Both mats and films have a semi-crystalline structure; however, the degree of crystallinity was superior for the mats when compared to the films. The stretching forces applied during the electrospinning process can cause molecular chain orientation along the fiber axis, contributing to the superior crystallinity in the mats. Of the PUs, the crystallinity degree was superior for PU-DMPA/CS substrates due to their superior phase segregation, which let the polycaprolactone soft segment crystallize independent of the hard segment.

According to the hydrophobicity of the PUs, the PU-DMPA/CS films were the ones with the lowest water contact angles value (76 ± 2 º). The presence of dispersed and less crosslink CS left CS free groups available to interact with the water molecules. All the mats were hydrophobic, independent of the CS content, with contact angles superior to 124 º. The structure of the mats with high porosity can lead to the entrapment of air bubbles at the interface, reducing the contact area for water and increasing the water contact angle values.

The passive and enzyme-mediated hydrolysis of the fibrous mats and films was studied. In PBS, PU-DMPA substrates were the only ones that degraded over 60 days. However, all the mats and films were degraded in lipase solution, which attack the esters in the polycaprolactone soft segment. PU-CS mats and films were less susceptible to the enzymatic attack, losing ~20 % of their weight over 40 days. Although the quantity of soft segment was the same for all PUs, the crosslinked structure of PU-CS impaired the diffusion of PBS and/or lipase through the mats/films contributing to inferior degradation rates.

Indirect cytotoxic assays demonstrated the absence of toxicity of all PUs mats and films leachables for HFFF2 cells. However, adhesion and proliferation of HFFF2 cells in all the substrates were not similar. Two factors contribute to that, the chemical structure of the PU (presence or absence of CS) and their structure (films or fibrous mats). PU-DMPA substrates (films and mats) only support the adhesion of the cells but not their proliferation. PU-DMPA/CS and PU-CS substrates support the adhesion and proliferation of HFFF2 cells over 12 days. The proliferation rate was superior on mats than on films. XPS analysis revealed that urethane and urea groups are at the uppermost surface of the fibers while polycaprolactone are at the uppermost surface of the films. Therefore, chemical composition and fibrous morphology of PU-CS mats are better to support HFFF2 cells.

Fiber mats with aligned morphology were also produced from all PUs using a rotating drum. The aligned mats have superior Young modulus in the direction of the alignment and reduce elasticity, when compared to the mats without preferential orientation. The proliferation of HFFF2 cells was inferior in aligned mats when compared to the mats without preferential orientation. The topographical cues presented by aligned electrospun scaffolds induced the alignment and guidance of the HFFF2 cells in the direction of the fiber alignment and the cells presented a more

stretched morphology. Fibers with aligned morphology are preferred for neural tissue engineering to guide neural cells.

The synthesis of PU using gelatin as chain extender/crosslink (PU-Gel) was also performed by replacing CS for gelatin (Chapter 4). Three different gelatin contents (5%, 7.5% and 10%) were used during the synthesis process. The introduction of superior gelatin contents (7.5 and 10 %) in the PU backbone increase the gelatin crosslink degree and the phase mixing, resulting in PUs with amorphous structure and superior thermal stability. PU-Gel with different gelatin contents were processed using the electrospinning to get fibrous mats. The mats obtained from solutions of PU-Gel with superior gelatin content (7.5% and 10%) are full of defects due to the poor solubility of these polymers that are highly crosslinked. Mats from solutions of PU-Gel with 5% of gelatin were uniform without defects. Mats without defects and films, produced from the same solution, are hydrophobic substrates and have an elastomeric behavior similar to the soft tissues. The performance of the mats were evaluated for tissue engineering applications. This was carried out by characterizing the enzyme-mediated and passive hydrolysis of the mats and by accessing the viability of the HFFF2 cells cultured on the mats. The mats and the films did not exhibit any detectable hydrolysis in PBS over 37 days. However, in lipase solution, the ester linkages were cleaved in both substrates, resulting in weight loss that was superior on the mats (~18 % vs. ~7 %). The leachable of the mats and films were not toxic for the HFFF2 cells indicating the safety of using this polymer in biomedical applications. In addition, the mats support the adhesion and proliferation of the HFFF2 cells better than the films and the cells spread uniformly over the mats, establishing contact points. Such a fibrous structure similar to the ECM is a better substrate for cells support than films.

A rotating drum was used to collect PU-Gel mats with aligned morphology. Similar to aligned mats of chapter 3, PU-Gel mats with aligned morphology have superior Young modulus and less extensibility in the fiber direction, when compared to the randomly oriented mats. The HFFF2 cells proliferate better in aligned PU-Gel mats over the first week, compared to the mats with random morphology, on the opposite of what was observed for PU-CS mats in Chapter 3. The topographical cues provided by the aligned mats induce the parallel alignment of the cells in the fiber direction, but still cells establish cell-cell contact points, which can lead to superior proliferation rates.

Mats of PUs extended with either only CS or gelatin have mechanical properties similar to the ones of the soft tissues, have slow degradation rates and support HFFF2 cells adhesion and proliferation. Those mats were used as substrates for umbilical cord-derived MSCs and NSCs (chapter 5). The effect of chemical structure (CS vs. gelatin) and topographical cues (random vs. aligned) were evaluated. MSCs seeded on the mats adhered equally to all substrates but the proliferation rate was different among the mats. The proliferation rate was inferior in mats with aligned morphology when compared to the randomly oriented ones. According to the chemical

structure, PU-Gel mats supported better cellular proliferation. PU-CS mats with aligned morphology were not suitable substrates for MSCs survival and proliferation.

When NSCs were seeded on the mats, the cells adhere and proliferate better in PU-CS aligned mats. On the opposite of what was observed for MSCs, the PU-Gel mats without preferential orientation were less suitable for NSCs support. A confocal microscope was used to observe cell morphology on the mats. NSCs grow in clusters that spread under all surface over time, establishing connections with each other. Importantly, most of the cells differentiate into the neuronal lineage after three weeks in culture without additional factors, being positively stained for NF70 and MAP2 neuronal markers. NSCs in the PU-CS aligned mats aligned well along the fiber direction, following the mats directional cues. After three weeks, the resulting neurites also align along the fibers direction. Each cell type behave differently in the presence of each substrate. Overall, it seems that PU-CS aligned mats are better substrates for neural tissue engineering.

6.2 Future Work

The results from this research are promising and a step forward in order to get a customized scaffold for spinal cord regeneration. However, a lot of research is yet to be done.
In order to complete the PUs analysis, the molecular weight and the viscoelastic properties of the PUs should be determined using gel permeation chromatography and dynamic mechanical analysis, respectively. In the PU-Gel synthesis some adjustments should be performed in order to reduce the extensive gelatin chemical crosslink. To do so, the amine groups of gelatin should be protected before their reaction with the isocyanate terminated pre-polymer with sulfosuccinimidyl acetate (Guo, Bandyopadhyay et al. 2008) or tert-butyloxycarbomil (Li, Davidson et al. 2009). Without the available amine groups, the extensive crosslinking and strong hydrogen bonds between urea groups are prevented, improving the polymer dissolution. At the end of the synthesis, the protective agents are removed leaving free amino groups, which are desirable for NSCs interaction (Ren, Zhang et al. 2009). Another way is to customize the synthesis replacing gelatin by specific aminoacids sequences widely use in neural regeneration and NSCs culture such as IKVAV neural epitope from laminin (Sun, Li et al. 2016).

As the topography of the scaffolds influence cell behavior, further studies should contemplate the production of mats with different diameters and thickness and evaluate their effect on cell behavior (Christopherson, Song et al. 2009). Fibers with different diameters can be obtained by adjusting the solutions polymer concentration, larger fibers can be obtained by increasing the solution concentration. The mechanical behavior of the substrates also influence the stem cell behavior. The mechanical properties of the individual fibers should be tested to understand the mechanical forces that the cells are experiencing, since cells can attach to single fibers. The mats should have pores that allow cellular infiltration, creating a three-dimensional

environment. Cells did not infiltrate, or infiltrate just a few fibers at surface, in the produced mats because of their reduced pore size. Using the co-electrospinning technique where PU fibers are thrown to the collector at the same time of the fibers of a sacrificial polymer (e.g. polyethylene oxide), which are further removed, leaving open pores for cell infiltration (Rnjak-Kovacina and Weiss 2011). When a material is implanted in the body, among other factors, monocytes adhered to their surface, differentiate into monocytes-derived macrophages (release reactive oxygen species) and fused to form foreign body giant cells (McBane, Santerre et al. 2007). The ROS and the enzymes in the macrophages can exacerbate the degradation of PUs (Martin, Gupta et al. 2014). Thus, in order to evaluate the degradation behavior more accurately, the effect of the macrophages in the PUs substrates should be evaluated.

PU-CS support the adhesion, proliferation and neural differentiation of human NSCs without additional biochemical factors or adhesion proteins. As laminin has been used to coat the substrates for NSCs culture, the effect of coating the mats with laminin in the proliferation and differentiation of NSCs should be evaluated and compared to the results of mats without any coating. Further studies should be performed to evaluate the effect of the mats in the differentiation of NSCs into neurons, astrocytes and oligodendrocytes. To do so, flow cytometry and immunocytochemistry can be used to analyze cells stained with different neural markers, such as Vimentin (astrocyte precursors), GFAP and GLAST (differentiated astrocytes), NG2 (oligodendroglial precursors), MBP (differentiated oligodendrocytes).The number of cells positive for each marker must be counted to get the percentage of cells differentiated in each neural phenotype. To determine which genes are more expressed during the differentiation process, quantitative polymerase chain reaction can also be performed. The resulting neurons should be functional, growth over long distances and establish synapses between them and the host neurons. Electrophysiological recordings must be performed to verify if the differentiated neurons can form functional synapses (Yin, Huang et al. 2014).

6.3 References

Cheng, S., E. C. Clarke, et al. (2008). "Rheological properties of the tissues of the central nervous system: a review." Medical engineering & physics **30**(10): 1318-1337.

Christopherson, G. T., H. Song, et al. (2009). "The influence of fiber diameter of electrospun substrates on neural stem cell differentiation and proliferation." Biomaterials **30**(4): 556-564.

Guo, X., P. Bandyopadhyay, et al. (2008). "Partial acetylation of lysine residues improves intraprotein cross-linking." Analytical chemistry **80**(4): 951-960.

Li, B., J. M. Davidson, et al. (2009). "The effect of the local delivery of platelet-derived growth factor from reactive two-component polyurethane scaffolds on the healing in rat skin excisional wounds." Biomaterials **30**(20): 3486-3494.

Maikos, J. T., R. A. Elias, et al. (2008). "Mechanical properties of dura mater from the rat brain and spinal cord." Journal of neurotrauma **25**(1): 38-51.

Martin, J. R., M. K. Gupta, et al. (2014). "A porous tissue engineering scaffold selectively degraded by cell-generated reactive oxygen species." Biomaterials **35**(12): 3766-3776.

McBane, J. E., J. P. Santerre, et al. (2007). "The interaction between hydrolytic and oxidative pathways in macrophage-mediated polyurethane degradation." Journal of Biomedical Materials Research Part A **82**(4): 984-994.

Ren, Y.-J., H. Zhang, et al. (2009). "In vitro behavior of neural stem cells in response to different chemical functional groups." Biomaterials **30**(6): 1036-1044.

Rnjak-Kovacina, J. and A. S. Weiss (2011). "Increasing the pore size of electrospun scaffolds." Tissue Engineering Part B: Reviews **17**(5): 365-372.

Sun, Y., W. Li, et al. (2016). "Functional self-assembling peptide nanofiber hydrogels designed for nerve degeneration." ACS applied materials & interfaces **8**(3): 2348-2359.

Yin, Y., P. Huang, et al. (2014). "Collagen nanofibers facilitated presynaptic maturation in differentiated neurons from spinal-cord-derived neural stem cells through MAPK/ERK1/2-Synapsin I signaling pathway." Biomacromolecules **15**(7): 2449-2460.